Thermométrie submicrométrique par fluorescence:Caractérisation de micro et nanostructures en milieux sec et liquide

Peter Low

T H E S E

en vue de l'obtention du

DOCTORAT DE L'UNIVERSITE DE TOULOUSE

délivré par l'Université Toulouse III - Paul Sabatier

U.F.R. P.C.A.

Discipline: Sciences de la Matière

présentée et soutenue

par

Peter Löw

le 22 février 2008

Titre:

Thermométrie submicrométrique par fluorescence: Caractérisation de micro et nanostructures en milieux sec et liquide

Directeur de thèse:

Christian Bergaud

JURY

Rapporteurs	B.	Cretin
	S.	Volz
Examinateurs	L.	Aigouy
	J.-P.	Bourgoin
	B. J.	Kim
	R.	Plana

Thermométrie submicrométrique par fluorescence: Caractérisation de micro et nanostructures en milieux sec et liquide

Résumé

Ce travail concerne le développement et l'optimisation de la thermométrie par fluorescence en milieu sec et liquide pour caractériser thermiquement des fils de dimensions submicrométriques dont l'échauffement est obtenu par effet Joule. En utilisant des simulations en éléments finis, les paramètres des fils sont étudiés afin d'optimiser leur comportement thermique. Un fort confinement spatial de la température autour des fils en nickel sur un substrat de silicium est observé grâce à des mesures en fluorescence. Concernant le temps de réponse, des constantes de temps thermiques en dessous de la milliseconde sont obtenues expérimentalement. Les résultats présentés dans cette thèse sont d'un grand intérêt pour le développement de nouveaux outils pour la détection, la reconnaissance et l'étude fondamentale des molécules (dépliement et repliement de protéines et d'ADN par exemple) sous modulation thermique rapide.

Mots clés : Fluorescence, thermométrie, analyse submicrométrique, nanofils, simulation en éléments finis, modulation thermique, laboratoire-sur-puce.

High spatial resolution fluorescent thermometry: Thermal characterization of submicrometer structures in dry and liquid conditions

Abstract

This thesis presents the development of an improved fluorescent thermometry approach for the thermal characterization of Joule-heated submicrometer wires in dry and liquid conditions. The design parameters of the wire systems are studied by the use of finite element modeling (FEM) in order to optimize their thermal behavior. A high spatial confinement of the temperature changes is experimentally demonstrated when using a nickel submicrometer wire on a silicon substrate as a heat source. The thermal time constants of the wire systems are shown to lie below one millisecond. The results of this thesis are of great interest in the development of new tools for the sensing, recognition and fundamental studies of molecules (for instance the folding of proteins and DNA) based on fast temperature modulation.

Keywords: Fluorescence, thermometry, submicrometer analysis, nanowires, FEM analysis, temperature modulation, lab-on-a-chip.

PREFACE

The two first years of this thesis was performed at LIMMS-CNRS, IIS, The University of Tokyo, Japan. The third and last year was performed at LAAS-CNRS, University of Toulouse, France. The research activity at LIMMS-CNRS was conducted in collaboration with the laboratory of Professor Beomjoon Kim (IIS, The University of Tokyo).

From the 1st of January 2007, the project was conducted as a part of the ANR project PNANO Nanothermofluo in collaboration with ESPCI (L. Aigouy), ENSCP (M. Mortier) and ECP (S. Volz).

The financing of the thesis was made possible thanks to a BDI grant from the STIC department of the CNRS, France.

All electron beam lithography (EBL) processes described in this manuscript were performed using the Advantest F5112 EBL facilities at the VLSI Design and Education Center (VDEC) at the University of Tokyo, Japan.

ACKNOWLEDGEMENTS

The work that is presented in this manuscript is the result of the contributions from many people and many laboratories. I would like to take the opportunity to acknowledge all of these contributions and attempt not to forget anyone.

Two persons come to mind above all. First of all, I owe particular gratitude to Christian Bergaud, evidently for enabling me to pursue my PhD studies with a long-term stay at The University of Tokyo, but also for his persistence in keeping me on track and for his great support and feedback throughout the entire project without imposing too strict boundaries. I would also like to thank Professor Beomjoon Kim, who was not only the host professor for my research project at The University of Tokyo, but who also provided valuable practical and cultural support and who became a great friend during my stay in Tokyo.

Next, I would like to thank those key persons on which large parts of the experimental activities and fabrication processes relied, in terms of training, licensing and cultural interfacing. I think particularly of Takama-san in Kim lab, Agnes-san in Fujita lab and Kubota-san in Mita-Shibata lab (VDEC) who all showed continuous patience and persistence in their support.

The indispensable support of a range of laboratories is also gratefully acknowledged. The very existence of my PhD thesis is in large parts due to the LIMMS laboratory at IIS, a joint laboratory between the CNRS (France) and the IIS (The University of Tokyo, Japan). LIMMS has been the source of fruitful discussions, interactions and collaborations with its numerous researchers, all of whom I wish to thank. I also wish to thank the permanent staff and secretaries of LIMMS. Further support, particularly in terms of material and equipment, was provided by Fujita lab, Toshiyoshi lab, Takeuchi lab, Fuji lab, Kawakatsu lab and Masuzawa lab at IIS and by Mita-Shibata lab at VDEC. I would like to thank the professors and all of the members of these laboratories for their continuous support during my stay at The University of Tokyo. Thanks also to Professor Karl Böhringer from the University of Washington, who gave feedback on my ideas for nanowire assembly and to Lionel Aigouy & Benjamin Samson at the ESPCI in Paris who made the comparative studies with SThM possible.

Of course I will not forget to mention the people of Kim lab, the lab where I spent the larger part of my PhD project. While many of these students and researchers were great in facilitating the introduction to the various experimental processes (thanks in particular to Janggil-san, Cho-san and Vincent-san), each and everyone became a great friend making my stay in Tokyo as pleasant as it was (thanks to Vincent, Janggil,

Masuda, Hwang, Yamada, Karasaki, Robert, Wang, Jeroen, Saitoh, Cho, Park, Chen, Saitoh, Jacques, Takama and Kim).

Back at LAAS-CNRS in Toulouse, France, I was assisted by numerous research teams. First of all I would like to thank all the members of the NANO group, headed by Christophe Vieu, who provided great support throughout my stay at LAAS. Next, I would like to acknowledge the support provided by the engineers in the TEAM group who facilitated the use of the clean room at LAAS. Further acknowledgements are given to Aurelien Bancaud, Jan Sudor and Corinne Vergnenegre who assisted me in the preparation and performance of the fluorescence-based experimental processes, to Pierre-Temple Boyer who provided silicon substrates for the fabrication of suspended membrane structures and to Nicole Higounet for her support in practical matters.

Last but not least, I would like to say thanks to all the people who made my life in Tokyo so enjoyable. I wish to give an exclusive hug to Shirley, my beloved "room-mate". Then thanks to all the others: Li, Li, Keiko, Thinzar, Sayuri, Keiko, Felix, Maki, Masa, Maud, the Kim-clan (including the Hwangs, Parks and Chos), the Takama-tachis (special thanks to Daisuke for introducing me to Tokyo), Jeroen (thanks for the ping-pong games), Vincent & Tomoko, Jörgen & Magnus (thanks for the pancakes), my Japanese teachers, the people at the IIS international office, etc, etc.

CONTENTS

Abstract iii

Preface v

Acknowledgements vii

Introduction 1

1 Submicrometer thermometry 5

1.1 Thermometry - the measurement of temperature and heat transfer . . . 5

1.1.1 Micro- and nanothermometry . . . 6

1.2 Classifications . . . 7

1.2.1 Contact vs. non-contact techniques . . . 7

1.2.2 Full-field vs. point probe techniques . . . 8

1.2.3 Dry vs. liquid condition thermometry . . . 8

1.3 Contact thermometry . . . 8

1.3.1 Thermistors and RTDs . . . 8

1.3.2 The thermocouple . . . 9

1.3.3 The 3ω-method . . . 9

1.3.4 Contact thermometry in the nanotechnologies . . . 10

1.4 SThM . . . 11

1.4.1 The thermocouple SThM . . . 13

1.4.2 The thermistor/RTD SThM . . . 14

1.4.3 The fluorescent probe SThM . . . 15

1.4.4 The thermal expansion SThM . . . 16

1.4.5 Other SThM techniques . . . 16

1.5 Non-contact thermometry . . . 17

1.5.1 Infrared thermography . . . 17

1.5.2 Thermoreflectance . . . 18

1.5.3 Raman spectroscopy . . . 19

1.5.4 Fluorescent thermometry . . . 21

1.6 Thermometry in lab-on-a-chip systems . . . 34

2 Nanowires as heat sources **37**
2.1 Joule heating in nanowires – a finite element model . . . 37
2.1.1 The FEM model . . . 38
2.1.2 Steady-state analysis . . . 42
2.1.3 Transient analysis . . . 49
2.2 Fabrication of the nanowire heating device . . . 53
2.2.1 Nanowire fabrication . . . 53
2.2.2 Fabrication of suspended membranes . . . 58
2.2.3 Mounting and connection of the nanowire devices . . . 62
2.3 Conclusions . . . 63

3 Selecting a fluorescent probe **65**
3.1 Proposed improvements of fluorescent thermometry . . . 65
3.2 Finding a fluorescent probe . . . 66
3.3 Materials and solvents . . . 66
3.3.1 Quantum dots . . . 66
3.3.2 Rhodamine B . . . 67
3.3.3 Streptavidin – Rhodamine B conjugates . . . 67
3.4 Setup for fluorescence measurements . . . 67
3.5 Assembly of the fluorophores on a surface . . . 68
3.5.1 Evaporation of solvent . . . 69
3.5.2 Immobilization by streptavidin and polylysine . . . 71
3.5.3 pDEP assembly of nanocrystals . . . 71
3.6 Photostability . . . 73
3.6.1 Influence of temperature on the photostability curve . . . 77
3.7 Temperature dependence and reversibility . . . 77
3.7.1 Temperature cycles . . . 78
3.7.2 Temperature calibration curve . . . 81
3.8 Conclusions . . . 83

4 Thermal characterization of the nanowire systems **85**
4.1 Experimental approach . . . 85
4.1.1 Optical setup . . . 85
4.1.2 Global temperature control . . . 87
4.1.3 Equipment for local resistive nanowire heating . . . 87
4.1.4 Sample preparation . . . 88
4.1.5 Acquisition and image treatment . . . 88
4.1.6 Acquisition of time series for transient analysis . . . 91
4.2 Results . . . 91
4.2.1 Dry Conditions . . . 91
4.2.2 Liquid conditions . . . 96
4.2.3 Transient analysis . . . 99
4.3 Preliminary comparisons with fluorescent probe SThM . . . 103
4.4 Conclusions & discussions . . . 104
4.4.1 Discussion on the spatial resolution . . . 106
4.4.2 Discussion on the temperature dependence, range and resolution 106
4.4.3 About liquid conditions . . . 107
4.4.4 The transient thermal analysis . . . 108

5 General conclusions & future directions 109
5.1 Potential further improvements of fluorescent thermometry 109
5.1.1 Alternative fluorescent probes 110
5.1.2 Alternative acquisition methods 110
5.1.3 Improvements of the experimental setup 111
5.1.4 Measurements in liquids 111
5.1.5 Alternative approaches for the transient analysis 112
5.2 Applications of the nanowire heat sources 113
5.2.1 Applications in molecular kinetics studies 114
5.2.2 Localized polymerization and modification of surface properties . 116
5.3 Integration of nanowire heating elements in lab-on-a-chip systems 116
5.4 Possible developments of the nanowire structure 118
5.4.1 Bottom-up fabrication 118
5.4.2 Local heating and FET sensing combined 118

Appendix 119

A Fluorescent probes 119
A.1 Organic fluorescent dyes 119
A.1.1 Rhodamine B 119
A.1.2 Fluorescein 122
A.1.3 Band definition dyes 123
A.1.4 Other thermosensitive organic dyes 125
A.2 Inorganic fluorescent probes 126
A.2.1 Semiconductor nanocrystals 126
A.2.2 Rare-Earth based dyes 131
A.3 Metallorganic dyes 133
A.3.1 Ruthenium 133
A.3.2 Porphyrin 134
A.4 Potential probes 135

B Thermochromic liquid crystals 139

C Microfabrication protocols 141
C.1 Preparing designs for EBL 141
C.2 Basic substrates 141
C.3 Metal nanowire fabrication 142
C.3.1 Protocol 143
C.3.2 Resulting metal nanowires 145
C.4 Creation of the suspended membranes 147
C.5 Silicon nanowire fabrication 149
C.5.1 Protocol 149
C.5.2 Comments on the use of silicon nanowires 152

D TMAH/KOH etch 155

E Streptavidin - Rhodamine B deposition 159

F pDEP assembly of nanocrystals **163**
F.1 Theory behind the DEP effect . . . 163
F.2 Application of the pDEP force for nanocrystal assembly . . . 164
F.2.1 Experimental approach . . . 164
F.2.2 The nanocrystal solution . . . 166
F.2.3 Observation of the assembly . . . 166
F.3 Results & discussions . . . 166
F.3.1 Electrical field assembly on microwires . . . 166
F.3.2 Electrical field assembly on nanowires . . . 167
F.4 Conclusions . . . 170

G Measurement of the optical power densities **171**

Bibliography **175**

Publications **193**

INTRODUCTION

Measuring and controlling temperature on the microscale is an increasingly active area of research and development. While the characterization of temperature is essential for the defect analysis and the design optimization of many conventional microsystems, e.g. microelectronic circuits, the active control of temperature on the microscale can be applied in lab-on-a-chip processes such as the polymerase chain reaction (PCR) [1–6].

The main advantage of the miniaturized on-chip approach to processes such as PCR is the increased capability for fast temperature cycling. Due to the lower thermal mass and heat capacitance, the time required to change between the three different process temperatures (melting, annealing and extension temperature) is significantly decreased. In similarity with the modern PCR devices, current research and development for temperature control in other biological, chemical and biomedical processes frequently aim at the miniaturization of the involved systems. In order to evaluate the thermal behavior at the small spatial and temporal scales of the new devices, it is becoming clear that the performance of the current tools for thermal characterization has to be enhanced and that conceptually new approaches may have to be developed.

Temperature and molecular kinetics A field in which precise spatial and fast temporal control of temperature hold potential for greatly improved efficacy is the field of fundamental molecular studies. A typical area of molecular studies is that of protein folding [7–12]. It is well-known that proteins, as well as other molecular structures such as DNA [13–18], undergo conformational changes upon changes in their environment. Although simulations and structural studies give certain information, the most direct approach to study the pathway and the various transition states of protein folding and unfolding is to perform dynamical studies of the events [19–21]. In these dynamical studies, it is obviously necessary to have access to a characterization method for the analysis of the molecular events, e.g. fluorescence analysis [7,10,22], circular dichroism [11,22] or NMR spectroscopy [19,22]. However, it is also important to have access to a technique which allows for the initiation of the molecular events. Examples of such techniques are rapid mixing (or stopped flow) [23,24], pH-jumping [25,26], pressure-jumping [27] and temperature jumping (T-jumping) [20,23,24].

To allow for accurate studies of the fast kinetic events in molecules, it is generally understood that the disequilibration pulse, which brings the molecule out of its equilibrium state, has to be short in duration and quickly return to its original value in order to resolve the subsequent energy relaxation pathway of the molecule. Among the

aforementioned techniques, T-jumping is the highest performing technique in terms of temporal resolution. It allows for the study of events happening on a time-scale below the millisecond regime due to its short-pulse capabilities [20, 23].

Fast temperature modulation for molecular studies and sensing An additional advantage of short temperature pulses is the possibility to use fast temperature oscillations in combination with a lock-in technique in order to measure the kinetics of a molecule with high noise reduction. This technique was recently demonstrated in the study of the folding properties of a DNA hairpin structure, measuring the kinetics at a temporal resolution of 5 μs [28]. Another similar application making use of fast temperature oscillations has demonstrated the possibility to perform dynamical molecular analysis by studying the displacements of chemical equilibrium as a function of the temperature modulation frequency. Further potential of fast temperature modulation is found in the temperature pulse voltammetry which allows for the identification of different molecular species in a liquid volume [29–31].

Spatial temperature control for sensing applications In the field of molecular sensing, precise temperature control can potentially enhance the sensing mechanisms. This is typically the case in various gas sensors [32–34]. Furthermore, the use of temperature-induced local surface modifications, e.g. the thermal polymerization of molecularly imprinted polymers (MIP) [35–37] and the thermal ablation of resists [38], is promising in the creation of binding and recognition sites on specific sensing elements.

Objectives of this thesis

Fluorescent thermometry Within this thesis, the main target has been to develop a methodology for the effective thermal characterization of micro- and nanoscale temperature control devices, particularly for biological applications. While the achievement of high spatial resolution is a high priority, factors such as cost and simplicity are naturally also of particular importance. In comparing the existing methodologies for small scale temperature measurements, we have identified fluorescent thermometry to be the most suitable method for our purpose. It does not only provide simple and cost-efficient measurements. In addition, since fluorescence microscopy is a well-known tool for most biologists, the method is suitable for quick integration and application in the typical biotechnology laboratories. It is also the only thermometric technology which allows for full-field temperature measurements of samples in liquid conditions. A trade-off which is made is that of the temperature resolution which typically is not better than 1°C for fluorescent thermometry. However, in biological applications this resolution is generally sufficient.

Nanowires as heat sources As we develop an improved methodology for fluorescent thermometry, the performance of the measurements is tested via the parallel development and optimization of an on-chip device for high-speed and spatially confined temperature jumping (Fig. 1). The basic idea of the envisioned device is to use a nanowire to induce temperature changes by resistive heating. Due to the small dimensions and the small heat capacitance of a nanowire, the temporal response of such a heating element can be expected to be very fast and the temperature distribution spatially confined. By

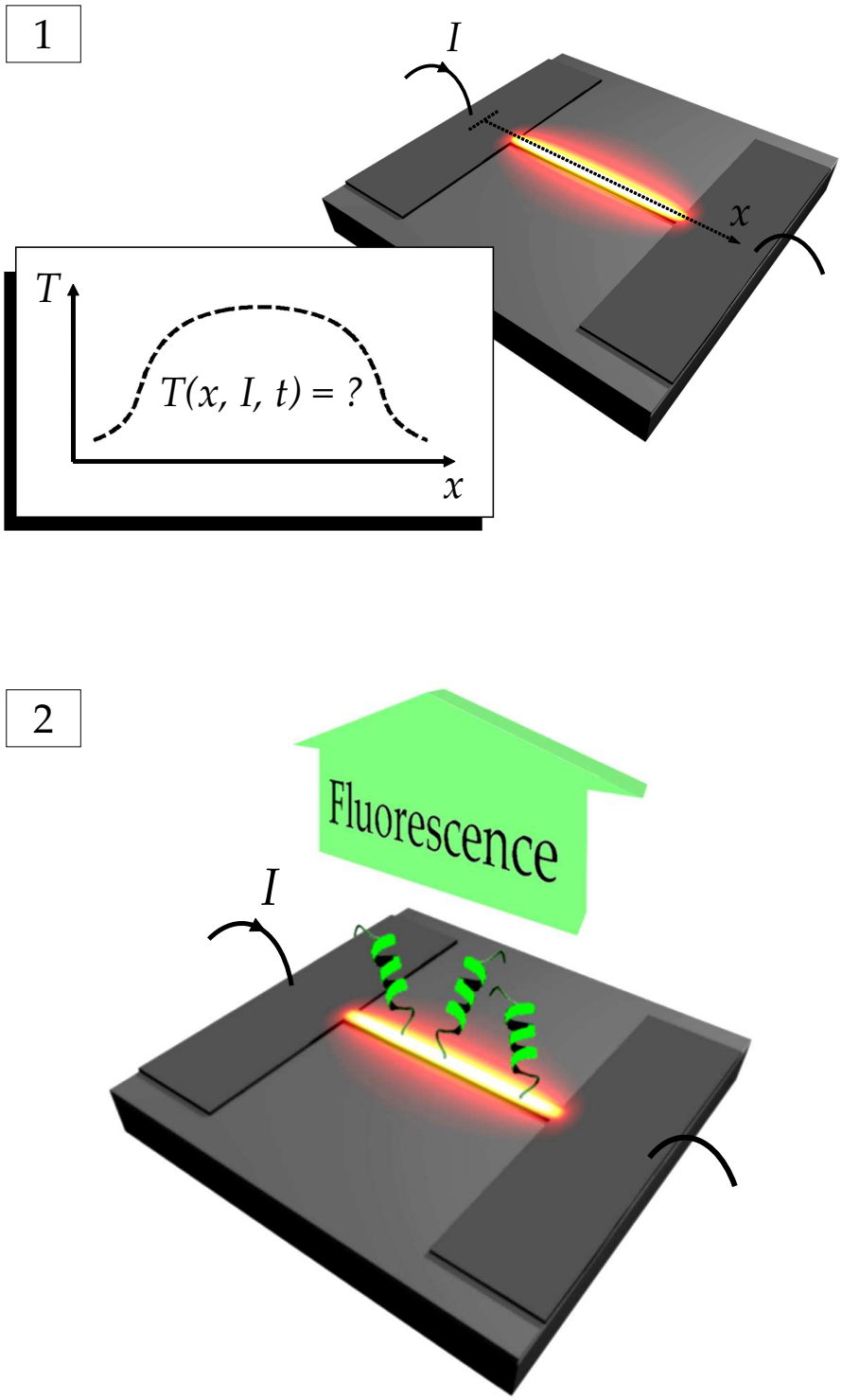

Figure 1: The use of a nanowire as a heating element holds potential for highly localized thermal impact (thus high integration) and fast temporal response. To advance the research on nanowire heaters, the thermal behavior must first be characterized. In a second step, when the thermal behavior is well understood, nanowire heating is expected to find a broad range of applications, e.g. the on-chip study of molecular kinetics and the thermally induced local modulation of surface properties (e.g. in combination with MIP, pNIPAAM etc.).

optimizing the thermal design of the nanowire surroundings, the response times may be significantly improved compared to existing microscale heaters [6, 39, 40] and potentially reach thermal time constants in the lower microsecond regime. An additional advantage of a nanowire-based device lies in the well proved capability of semiconductor nanowires to function as molecular sensors [41–45]. This is appealing regarding the integration of temperature control functions in more complete lab-on-a-chip systems.

A typical application that we have in mind regarding the nanowire heaters is to perform T-jumping for the initiation of molecular folding events. The molecular folding events of different molecules can occur on very different time-scales. Lower time limits are set by the fastest possible formation of local structures, either secondary, such as isolated α-helices (100 ns) and β-turns (6 μs), or tertiary, such as small loops (1 μs) [19, 20]. Observation of folding near these time scales requires effective approaches for detection and the use of ultra-short disequilibration pulses for the initiation of the folding reaction. The shorter the pulse can be made, the better the characterization of the intrinsic equilibration process of the folding event can be resolved.

Typically, T-jumping consists in temperature changes induced by laser heating which allows for pulse durations in the nanosecond regime. However, the complexity and cost of the required laser systems are generally very high. By the use of electrically induced T-jumping by nanowires instead, on-chip integration is made possible and both cost and complexity are decreased with the potential for parallel studies and automated processing. Although not providing pulse durations as short as those in laser T-jumping (nanosecond regime), the envisioned system is likely to provide sufficiently short pulse durations (microsecond regime) for resolving the relaxation mechanisms of most molecules. Considering the added advantages of on-chip handling, the nanowire T-jumping approach will be a highly valuable addition to the existing methodologies.

Disposition of the thesis

Regarding the disposition of the different chapters, we will start by giving a general survey on submicrometer thermometry. This survey is intended to introduce the reader to the principal existing technologies for high spatial resolution temperature measurements and to clarify the reasons behind the choice of fluorescent thermometry within this thesis.

In Chapter 2, the thermal behavior of possible nanowire systems will be studied with the intention of finding appropriate design parameters for an optimal spatial and temporal behavior. To enable the efficient study of relevant parameters, simulations based on the finite element method (FEM) are used. The chapter is completed with a description of the approaches and protocols used to fabricate the simulated systems.

Chapter 3 illustrates the preliminary development process of the fluorescent thermometry, consisting principally in the evaluation of possible fluorescent probes.

After the selection of a fluorescent probe, Chapter 4 deals with the application for high spatial resolution thermometry. Specifically, the nanowire systems developed in Chapter 2 are thermally characterized.

Finally, Chapter 5 is dedicated to a thorough discussion of the results. Possible further improvements will be suggested and the potential applications of the results are discussed.

CHAPTER 1

SUBMICROMETER THERMOMETRY

The aim of the current chapter is to lead the reader through the most common current methodologies in temperature measurement. Considering the position of the thesis within the micro- and nanotechnologies, frequent references will be made to applications in these fields. The performance of the various technologies is also particularly evaluated with small scale temperature characterizations in mind. The chapter will be concluded with discussions on the suitability of the different techniques for the thermal analysis of our particular devices.

Before beginning, it is of value to refer the reader to a couple of related reviews on the same or similar topics. These reviews have been of great value in writing this thesis manuscript and are highly recommended for those seeking to further broaden their knowledge in the field. A thorough review on the entire range of thermometry techniques is found in reference [46]. Reviews focused on microscale thermometry have been given in references [47–49] while a brief review on nanoscale thermometry was given in a recent paper by Lee *et al* [50]. Other interesting reviews with focus on specific technologies are the reviews on nanoparticle fluorescence thermometry [51], scanning thermal microscopes [52], thermographic phosphors [53] and thermochromic liquid crystals [54].

1.1 Thermometry - the measurement of temperature and heat transfer

Temperature is one of the fundamental thermodynamic properties, with fundamental importance for the different properties and behaviors of matter. As such, it is also a parameter which knowledge is of great importance in everyday life as well as in scientific and industrial activities. The term thermometry is normally used when making reference to those technologies devoted to the measurement of the temperature and the heat transfer properties of a system. Over the last centuries, many thermosensing technologies based on different physical properties of materials have been developed, e.g. thermally induced reactions, the expansion/contraction of volume, and thermo-optical and electronic properties. [50]

The importance of measuring and controlling temperature is apparent after a closer look at almost any industrial process. Typically, real-time monitoring of temperature is

essential in order to minimize waste production and energy consumption. Additionally, a broad range of processes requires the implementation of well-defined temperature cycles in order to obtain optimal product qualities [51].

In the field of chemistry and biomedicine, temperature has a great influence on almost all processes and in some cases temperature is the only indication of the progress of the occurring reaction [55]. Furthermore, the handling and investigations of biological cells introduce particular requirements, considering that temperature changes of even a few degrees can mean the difference between life and death of a cell [51]. Temperature measurement is additionally a useful tool in the detection of mechanical weaknesses in components in the aircraft and car industries, e.g. for the identification of faults in high-speed moving parts such as turbine blades [51]. Yet another field where temperature control is essential is in chemical sensor applications. Knowing the temperature is particularly important in fluorescent sensing of oxygen since quenching by oxygen generally is highly temperature dependent [56].

1.1.1 Micro- and nanothermometry

Advances in the nano- and biotechnologies are increasing the demands for precise thermometry, with nanoscale spatial resolution and temporally well-resolved measurements being important for further developments. Accurate temperature measurements on the small scale is a challenging research topic with conventional technologies frequently not having the required performance. Furthermore, due to the possible existence of unforeseen material properties on the nanoscale, e.g. in terms of physicochemical and thermodynamic properties, it is likely that the continued development of thermometric technologies will require the use of new materials and approaches qualitatively different from those typically used today. [50]

One of the first incitements for pursuing what today is referred to as microthermometry was the birth of the semiconductor technologies and the integrated circuits. Due to the dense integration of components and interconnection lines on a small surface, with high heat dissipation as a result, good thermal management has long been a key issue to assure the optimal performance and lifetime of a circuit. Thermal mapping of a circuit board is useful as it gives information about the current densities and the distribution of the current flowing in the interconnection lines. By analyzing these maps, defects can be easily detected by the identification of hot and cold spots, which represent short-circuits and open-circuits, respectively [57–59]. It also gives valuable information about where in a design heat tends to build up, thus giving indications about how to improve the circuit or the cooling system. With the continued drive towards nanoscale electronic components over the last decade, the development of new thermometric technologies as well as the optimization of existing ones have accelerated. Using modern technologies, e.g. scanning thermal microscopy (SThM) and micro-Raman spectroscopy, precise measurements such as the characterization of the asymmetric build-up of heat within single electronic components have become possible [49, 60].

Recent developments in the microelectronic industry towards organic semiconductors have introduced yet higher requirements for good thermal design, owing to the low mobility of carriers in these materials. The high heat dissipation within these devices is paired with a poor thermal conductivity, which results in thermal effects becoming relevant under weaker driving conditions than in inorganic semiconductors. [61]

The tendency of miniaturization is also observed in the biomedical sciences. Minia-

turized systems offer improvements such as reduced consumption of chemicals and higher throughput. In terms of thermal control, the miniaturization also provides advantages, e.g. in the improved response times during temperature cycling processes. For example, in the case of genetic analysis, DNA must first be extracted from cells. This can be accomplished through the destruction of the cell membrane (cytolysis) by heating the cell. The DNA is then amplified through the polymerase chain reaction (PCR), which needs precise thermal cycling between different temperature levels. The cycling process can be done more rapidly in a microfluidic system than in a conventional system due to smaller sample volumes [62, 63]. Thermal cycling is also used for the generation of microbubbles for micromixing [64] and DNA sample transport [65].

There are numerous examples of the importance of temperature effects also in capillary electrophoresis systems and similar devices where electric fields are used to manipulate biological entities. Temperature gradients in capillaries for electrophoresis have long been understood to cause band spreading with a consequent reduction in separation efficiency. Fundamental studies of protein folding and denaturation have also been performed in capillary electrophoresis by controlling buffer temperature. The Joule heating that is induced by the application of electric fields must be taken into account to avoid undesired damage on the biological specimen. [66, 67]

In the field of micro- and nanolithography applications such as nanoimprint lithography and electron beam lithography, the temperature of the resists used for patterning is of great importance. Excessive resist heating in these techniques leads to undesired results such as pattern deformation and failure to reach critical dimensions. There is consequently a great interest in being able to characterize and monitor the temperature of these resists in order to develop optimal process conditions. [68]

1.2 Classifications

1.2.1 Contact vs. non-contact techniques

Before taking on the task of reviewing the various thermometry techniques, it is appropriate to do some classifications. The main distinction that can be made between various techniques concerns whether or not a certain technique involves physical contact with the object being investigated. Typical contact methods include thermocouples, thermistors and resistance temperature detectors (RTD). The most commonly used non-contact method is infra-red (IR) thermography, which due to its simplicity and early development is a popular tool in the microelectronics industry. Other non-contact methods include fluorescent thermometry, thermoreflectance and Raman spectroscopy.

For simple routine measurements of temperature, contact methods are frequently the simplest and most obvious choice. Thermocouples are easily found at a low cost with simple calibration procedures and easy readout of temperature. However, contact methods are badly suited for temperature measurements on small scales. Since the measuring probe of a contact method by definition gets into physical contact with the object of study, the probe will alter the thermal state of the measured area. The probe provides a thermal leakage path to the system leading to false measurements. These errors are more significant for smaller objects due to the relatively big thermal mass that the probe represents. Furthermore, the larger the thermal mass of the probe is, the longer it takes for it to indicate a stable temperature. In the case of high temporal resolution measurements, this presents a significant drawback.

A possible alternative to the application of conventional contact methods is to integrate the thermal probe with the device being measured. For example, a resistive element could be used both as a heat source and as a thermal sensor, using either changes in the resistance or the 3ω-approach to determine the temperature [69–72]. While not allowing for precise spatial resolution, it can in specific cases provide a simple mean to non-invasively perform temperature measurements with potential for high temporal resolutions.

The common way to avoid the typical problems of contact methods is to choose a non-contact method. Non-contact methods function by the analysis of light emitted from or reflected on an object. Due to the need for non-contact methods particularly in the microelectronics industry and in the remote monitoring of various industrial processes in real-time, the development of these techniques have seen great advances over the last couple of decades. In the following sections, contact and non-contact methods will be treated separately, starting with the more basic and simple contact techniques.

1.2.2 Full-field vs. point probe techniques

A second distinction that can be made among different thermometry techniques is whether temperature data is collected in a parallel or serial fashion. Distinguishing between these two types is of particular interest in applications where unknown temperature distributions, e.g. on the surface of an IC circuit, are characterized. Full-field techniques, including mainly a number of non-contact methods, e.g. infrared thermography [73, 74] and thermoreflectance [59, 75], are able to capture the temperature information from several points in one single measurement. On the other hand, point-probe techniques use a probe that measures one point at a time in a serial fashion, thus resulting in significantly longer acquisition times. Typical examples of the latter are scanning thermal microscopy (SThM) [52] and micro-Raman spectroscopy [76].

1.2.3 Dry vs. liquid condition thermometry

Thermometry techniques used in the microelectronics industry do not need the capability to measure the temperature of samples immersed in liquids. The commonly applied techniques, e.g. infrared thermometry and thermoreflectance, perform well for the characterization of dry environments but give poor results for liquid environments. Recent advances in lab-on-a-chip technologies have increased the demands for measurement techniques capable of efficiently characterizing temperatures and thermal properties in liquids.

A technology that has proved to be a simple and efficient tool for the thermal characterization of liquid environments, e.g. microfluidic channels, is fluorescent thermometry [66, 77]. Other techniques that have been applied for similar purposes are Raman spectroscopy [62] and thermochromic liquid crystal (TLC) thermometry [78, 79].

1.3 Contact thermometry

1.3.1 Thermistors and RTDs

The resistivity of basically any kind of conducting or semiconducting material is dependent on a number of parameters. The resistivity of a semiconductor can typically

be modified by the insertion of impurities into the crystal lattice or by the presence of an electric field. More importantly in our context, the semiconductor resistivity also has a strong dependence on the temperature, generally with decreased resistivity upon the increase of temperature. Similarly, although qualitatively different, the resistivity of metals also has a distinct temperature dependence, generally with an increase in resistivity as the temperature is increased. The mechanism behind the temperature-induced changes in resistivity is generally explained in terms of the phonon-electron interactions of a material [46].

Examples of temperature sensors that determine temperature by the measurement of resistivity changes are the thermistor and the resistance temperature detector (RTD). While thermistors typically employ a ceramic or polymer material, the RTD is based on a pure metal, typically platinum. Regarding thermistors, the sensor can be classified as positive or negative depending on whether the resistivity increases or decreases with the temperature. [46, 47]

1.3.2 The thermocouple

Thermocouples are popular tools for everyday temperature measurements. They are commonly used because of their low cost, simplicity, robustness and temperature range. The measurement principle relies on the Seebeck effect, also known as the thermoelectric effect. This effect arises at the junction between two different metals. It consists in the generation of a voltage which is related to the difference in temperature between the measuring junction and a reference junction. Compared to thermistors and RTDs, thermocouples have stable temperature calibration curves and offer higher spatial resolutions. [46, 47, 80]

1.3.3 The 3ω-method

The 3ω-method is a contact mode technique used to evaluate several thermal properties of a sample, in particular thin films [69–72]. Unlike common contact methods for temperature measurements such as thermistors and thermocouples, the 3ω-method operates in the alternating current (AC) regime. In the most simple application of the technique, a line heater is deposited on a sample using an approach that assures a good thermal contact, typically metal evaporation. An AC current with frequency ω, $I(\omega)$, is applied through the line heater. Due to Joule heating, a heat flux at a frequency 2ω is generated. Since the resistance of the metal depends linearly on the temperature, the line heater resistance will oscillate with the temperature changes at the same 2ω frequency. As a result, a 3ω frequency component will be detectable in the voltage drop across the heater. The 3ω component contains valuable information on the thermal properties of the sample. By the use of lock-in detection techniques and four-terminal measurements, a clear detection of the 3ω component can be achieved.

Compared to conventional contact methods, the 3ω-method gives a better signal-to-noise ratio and is particularly well suited for the determination of thermal properties such as the thermal conductivity and the specific heat [81, 82]. In Fig. 1.1, the example of a 3ω-based approach for the determination of thermal conductivity is shown. In this specific case, a four-terminal line heater is deposited on top of a porous anodic alumina membrane. In this case, the 3ω measurement provided information about the thermal conductivity and thermal diffusivity along the channel axis.

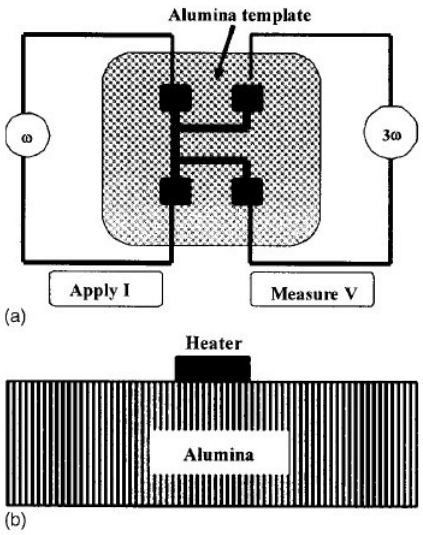

Figure 1.1: Typical configuration for the four-terminal measurement of the 3ω component. The 3ω measurement can be used for the determination of the thermal conductivity of the underlying sample. Here, the sample being investigated is a porous alumina membrane. [71]

The 3ω-method can be used also for the characterization of systems comprising characteristic sizes below the phonon mean free path ($\sim$10 nm), although only in the vertical dimension. In order to properly interpret the acquired signal and to identify the properties of thin layers and interface resistances, specific modeling of the system is required [70].

1.3.4 Contact thermometry in the nanotechnologies

In the context of micro- and nanotechnologies, several attempts have been made to integrate contact measurement probes with micro- and nanostructures [83–86]. Using micropatterning techniques, it is indeed possible to achieve close integration of these probes in the vicinity of the point to be measured. The advantage of such an approach is mainly the simple monitoring of temperature that can be performed once the probe is at place and calibrated. A negative aspect is that, due to the contact nature of the probes, paths for heat leakage are introduced. This is particularly true when measuring highly confined temperature gradients since the thermal probe introduces a relatively large heat capacity in the vicinity of the system [62]. In order to minimize the problem of heat leakage, it is necessary to miniaturize the probe element. In addition, miniaturization is required in order to optimize the response time of the probes [87] and to reach higher spatial accuracy. Miniaturization of this kind is typically seen in scanning thermal microscopes. A particular inconvenience of the thermoelectric contact probes is the influence of ambient electromagnetic noise on the measurement. This is especially problematic in miniaturized thermocouples, where the voltage changes that have to be distinguished are of a very small magnitude.

Contact thermometry is generally only used when temperature distributions do not have to be known, e.g. for the calibration of other thermometry techniques [39]. The solutions to achieve full-field imaging are to either integrate numerous probes on a sample

to form an array of sensing points, which evidently complicates the design of the sample, or to scan a probe over the sample surface. The latter approach is used in scanning thermal microscopy.

1.4 SThM

Scanning thermal microscopy (SThM) is a thermometric method specifically developed for measuring the thermal properties of nanostructured materials at an exceptionally high spatial resolution. It is being addressed in connection with the contact methods for the simple reason that most of the related technologies rely on a probe coming in contact with the investigated object. As the name suggests, the technique makes use of a probe that scans the surface of a sample and senses the local thermal properties. By collecting data from a large amount of points, a thermal map of the sample can be acquired.

The most popular types of SThMs rely on classical contact measurement principles, typically thermocouples and RTDs. The major difference as compared to the conventional techniques is the size of the probes and the capability to precisely position and scan these probes over a surface. The sensing elements of conventional thermocouples and RTDs have dimensions far above the micrometer. Commercially available thermocouples typically come with a minimum junction size of 20 μm. In the case of SThMs, the same physical principles are applied, but the probes are dramatically miniaturized and mounted or directly fabricated on a scanning microscope tip. These tips are commonly of the same kind found on atomic force microscopes (AFMs). Probe sizes are normally on the order of 100 nm.

The development of the SThM began in 1986 with research conducted by Williams *et al* [88], shortly after the invention of the scanning tunneling microscope by Binning *et al* [89]. While high spatial resolution is the SThMs greatest advantage, the typical inconveniences are slow image rendering times and complicated fabrication procedures.

A particular challenge of the SThM methodology, regardless of the kind, lies in understanding the heat transfer mechanisms between the SThM probe tip and the sample being investigated. Improved knowledge in this area holds promise for improved accuracy and reliability by enabling improved probe designs and better interpretation of the measured values. Some of the main advances done since the invention are discussed in articles by Shi *et al* [52] and Luo *et al* [90]. In the article by Luo *et al*, a contact mode SThM was presented, demonstrating that the dominant heat transfer effect taking place between the tip and the surface occurred through a liquid film present at the surface under ambient conditions (see Fig. 1.2). Due to the broadened understanding, they succeeded in demonstrating a spatial resolution of 24 nm. Recent studies by Kittel *et al* on heat transfer in vacuum conditions have continued to shed light on the various mechanisms involved [92].

A fact worth mentioning in the framework of this thesis is the absence of thermal characterizations by SThM made on samples in liquid conditions. Although the implementation of a SThM-based measurement in liquid might be envisioned, the actual implementation is likely to impose significant practical difficulties. These difficulties would consist in problems such as the positioning on an encapsulated liquid systems, the necessity for electric passivation (thermoelectric probes) and the complexity of the optical path (fluorescent probes).

In Table 1.1 , the various types of SThM types proposed to date are presented together with evaluations on their performance in various aspects. In the following, the

Table 1.1: Summary of various SThM techniques.

SThM probe	Heat transfer phenomena	Spatial resolution	Temporal resolution	Temperature resolution	Sensor fabrication difficulty
Thermocouple (coaxial) [88, 93]	Tip-sample heat conduction by air	$\sim 100\,nm$ [a]	$0.1 - 1\,ms$	$10^{-3}\,K$ [b]	Moderate
Thermocouple (crossed wires) [95, 96]	Tip-sample heat conduction by air	$300 - 500\,nm$	$10 - 50\,ms$	$10^{-3}\,K$ [b]	Easy
Thermocouple (micromachined) [90, 91, 97]	Tip-sample heat conduction by liquid film	$20 - 50\,nm$	$0.1 - 1\,ms$	$10^{-3}\,K$ [b]	Difficult
Thermistor/RTD (Wollaston wire) [98–100]	Unknown	$\sim 200\,nm$	Unknown	$10^{-3}\,K$ [b]	Easy
Thermistor/RTD (micromachined) [101, 102]	Unknown	Unknown	Unknown	Unknown	Difficult
Thermistor/RTD (micromachined using FIB & E-beam deposition) [103]	Unknown	$20\,nm$	Unknown	$10^{-3}\,K$	Very difficult
Fluorescent probe [104–106]	Unknown	$100 - 200\,nm$	Unknown	Unknown	Easy
Thermal expansion (bimaterial cantilever) [94]	Unknown	$400\,nm$ [c]	$1\,ms$	$10^{-3}\,K$	Easy
Thermal expansion [107] (SJEM)	No tip-sample heat transfer required	$10\,nm$	$1\,ms$	$10^{-2} - 10^{-1}\,K$	Not required
Contact potential [108]	Tip-sample heat conduction by air	$\sim 100\,nm$ [a]	Unknown	$10^{-3}\,K$ [b]	Easy
NOTN [109]	Photon transfer	$< 100\,nm$	Unknown [d]	Unknown	Moderate
TRSTM [110]	Photon transfer	Unknown	Unknown [d]	Unknown	Easy

[a] Probably limited by gas mean free path. [90]
[b] Limited by electrical noise. [94]
[c] This resolution is argued in reference [100], stating instead a limitation to $200\,\mu m$ due to heat transfer in air.
[d] Potentially very high response time if signal can be kept strong.

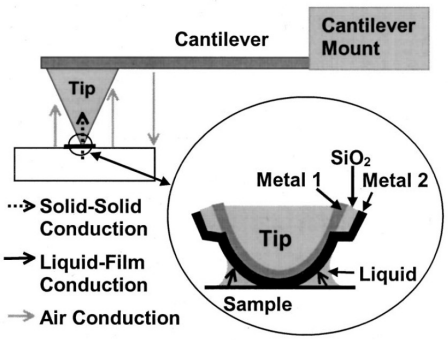

Figure 1.2: The different heat transfer mechanisms for a contact mode SThM. [91]

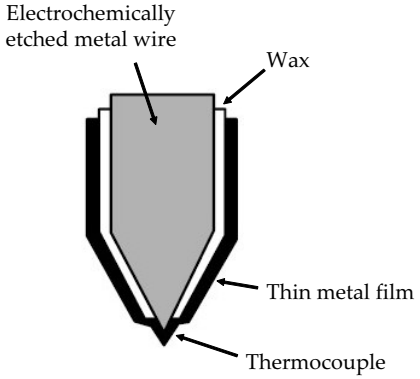

Figure 1.3: Coaxial thermocouple probe with the junction being located at the tip of the wire.

different methods will be further detailed, starting with the two most common types, thermistor/RTD SThMs and thermocouple SThMs.

1.4.1 The thermocouple SThM

In the same way as conventional thermocouples, the thermocouple SThM exploits the Seebeck effect in order to create a temperature dependent voltage at the junction of two metals. A number of approaches have been suggested for the fabrication of miniaturized metal junctions. The first SThM ever fabricated [88] employed a coaxial construction (see Fig. 1.3), providing an effective metal junction size of around 100 nm. The development since then have seen the apparition of tips constructed directly from thin metal wires bent into the desired shape [95] and the use of temperature sensing through diamond tips [96]. More significantly, micromachining technologies have enabled the production of tips in batches and with a more reproducible outcome [90, 91, 96, 97].

The use of thermocouple probes provides advantages such as high spatial resolution and temperature accuracy down to the millikelvin (mK) regime. However, compared to the thermistor probe, the thermocouples may be regarded as less suitable for complete thermal characterizations. This is mainly due to their dependence on external heat sources for the study of properties such as thermal conductivity and specific heat [100].

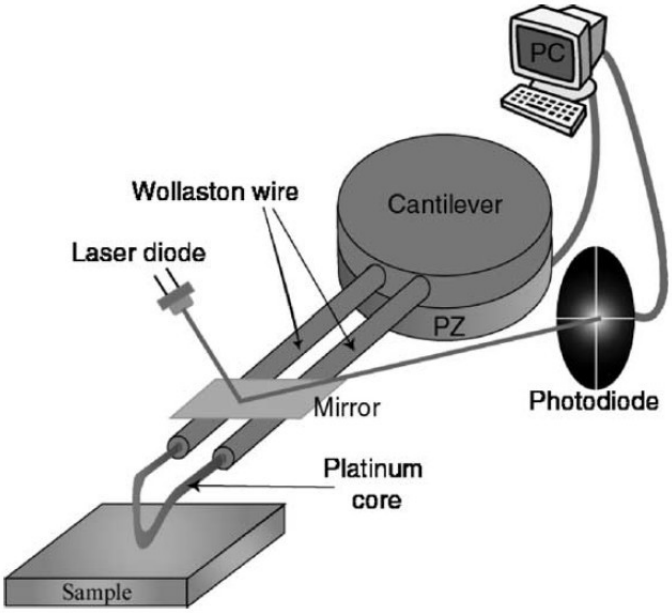

Figure 1.4: The principle of an RTD SThM. [99]

1.4.2 The thermistor/RTD SThM

As described in section 1.3.1, thermistors and RTDs determine temperature by the measurement of electrical resistance in the sensing element. In the SThM version of this technique, platinum is the most common choice of sensor material [98–100, 103]. However, other materials such as palladium have also been employed [101]. The thermistor probe fabrication can be performed in a number of ways. A popular technique is the use of a Wollaston wire that is shaped into a tip and etched partially to remove the protective polymer to uncover its platinum core. Further etching of the platinum results in a miniature sharp edge which can be used as a SThM probe (see Fig. 1.4) [98–100]. Similar to the thermocouple probes, micromachining technologies have provided improved efficiency in the fabrication of thermistor probes [101, 102].

Thermistor probes generally have two functional modes, the passive mode and the active mode. The passive mode is used for temperature measurements. A very small current is passed through the probe, just enough to sense the changes in resistance as the temperature varies. In the active mode, a larger current is applied through the probe, giving rise to local Joule heating. By monitoring how the imposed probe temperature changes upon the contact with a surface, data on thermal properties such as the thermal conductivity and the specific heat can be acquired. Hammiche *et al* used the multiple functions of a thermistor probe in order to perform a complete thermal characterization of metal particles buried in a polymer, including calorimetric analysis and determination of the thermal conductivities and thermal diffusion within the sample. By the use of pulsed heating at the tip of the probe, evanescent thermal waves could be created in the sample, which allowed for the characterization of subsurface properties [98].

As compared to the thermocouple SThM, the thermistor-based SThM has been more popular in total thermal analysis of samples. The main advantage lies in the possibility to use the thermistor probe both as a highly localized heat source and as a temperature sensor. Accordingly, no external heating device, e.g. a laser diode, is needed for the

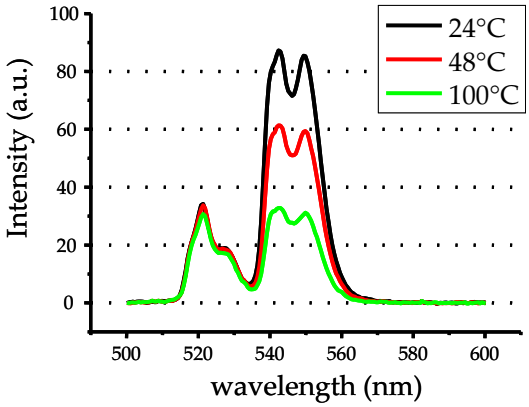

Figure 1.5: Fluorescence spectrum of a fluoride glass particle doped with erbium (Er^{3+}) and ytterbium (Yb^{3+}) ions. The spectrum changes strongly with the temperature.

investigation of thermal conductivity and specific heat.

The disadvantage of the thermistor probes is the slightly lower performance in spatial and temporal resolution. The typical spatial resolution of thermistor probes lies in the range 100 - 300 nm. While a resolution of down to 20 nm has been demonstrated, it should be noted that the successful fabrication of such high performing thermistor probes requires highly sophisticated and costly micromachining equipment [103].

1.4.3 The fluorescent probe SThM

A recent addition to the SThM family is the fluorescent probe SThM [104–106]. This technique is essentially a combination of the fluorescent thermometry technique, which will be addressed in section 1.5.4, and the atomic force microscope (AFM). It proposes the use of a small fluorescent particle glued at the end of an AFM tip. The fluorescence emitted by the particle presents a strong dependence on the temperature (see Fig. 1.5). Scanning a surface while monitoring the changes of the fluorescence gives information on the temperatures throughout the surface. In a recent article by Aigouy *et al* [104], the choice of material and the construction of the probe tip were explained. The fluorescent particle consisted of fluoride glass doped with the rare-earth ions erbium (Er^{3+}) and ytterbium (Yb^{3+}) and had a characteristic size of 300 - 400 nm. With a particle of this size, the technique was claimed to be capable of rendering temperature maps with a lateral resolution of 180 - 200 nm. The lateral resolution is subject to improvement in the near future via a decrease of the fluorescent probe size to a few tens of nanometers.

Compared to the SThM techniques described above, the fluorescent probe SThM has the advantage of being relatively easily assembled in terms of preparing the sensing tip. On the other hand, the technique requires the mounting and the alignment of a laser excitation source in order to induce fluorescence in the fluorescent particle. At this moment, the lateral resolution is comparable to that of the thermistor SThM. Similar to other techniques, a source of inaccuracy is the lack of understanding of the heat transfer mechanisms between the fluorescent particle and the investigated surface. The size of the currently used particles introduces a relatively large heat capacity near the sample which reduces the response time of the measurement. Furthermore, because of

irregularities of the particle shape, the contact area is not well known which is likely to introduce uncertainties in the measurement.

1.4.4 The thermal expansion SThM

This technique relies on the difference in thermal expansion for different materials in order to detect temperature changes. In an article by Nakabeppu *et al* [94], a bimaterial cantilever was realized by simply depositing a thin film of either gold or aluminum on top of a silicon nitride AFM probe. By monitoring the changes in deflection of the cantilever during scanning, using a lock-in detection technique to distinguish thermal and topographic deflection, the probe could be used to map the temperature of a sample with a 400 nm lateral resolution. However, this resolution was questioned in a review by Balk *et al* where the resolution was instead claimed to be limited to 200 μm due to heat transfer mechanisms in the air between the sample and the entire cantilever [100].

Another type of SThM based on thermal expansion is the scanning Joule expansion microscope (SJEM). Here, the thermal expansion being measured is that of a sample heated by a modulated electric current. By modulating the current at a certain frequency, lock-in detection can be used to distinguish topographic features from thermally induced variations in height. The thermal expansion data retrieved by the scanning tip can be used to determine the temperatures on the surface. The SJEM technique has been demonstrated to give a lateral resolution below 100 nm [49, 107, 111].

1.4.5 Other SThM techniques

In addition to the techniques described above, a broad range of other SThM sensing schemes have been proposed. In the following, a short description of some of these approaches will be given.

The contact potential SThM This technique was first proposed in 1992 by Nonnenmacher *et al* [108]. It allows for thermal conductivity measurements and subsurface thermal characterizations on conductors and thin insulating films deposited on top of conductors. Its lateral resolution is about 100 nm. It measures the electrochemical potential difference between the tip and the sample (the contact potential) by probing the electrostatic force field generated by this difference. Heating the tip or the sample causes a change in the electrochemical potential difference, which thus serves as an indicator of the temperature change.

Near-field optics thermal nanoscopy (NOTN) The NOTN technique, as presented by Taguchi *et al* [109], suggests the use of a near-field optical fiber to characterize both temperature and thermal conductivity with high spatial resolution. In order to capture near-field temperature dependent light waves, it relies on the thermoreflectance principle, which will be further explained in section 1.5.2. In short, it measures the change in reflectivity of the surface as a function of temperature. The method is claimed to be a non-contact method. However, the tip-sample distance has to be on the order of a few nanometers for the evanescent waves to be captured and the heat transfer mechanism between tip and sample has not been established. The authors claim a spatial resolution of below 100 nm and potential to reach the vicinity of 10 nm.

Thermal radiation scanning tunneling microscopy (TRSTM) The TRSTM is a recently proposed technique which allows for imaging of thermally excited surface plasmons on an object [110]. The TRSTM is based on a home-made apertureless infrared near-field scanning optical microscope (NSOM) without external illumination. It is an AFM with a hot sample holder combined with an infrared optical microscope and detector. The tip acts as a scattering center that radiates in the far field a signal linearly related to the infrared evanescent fields emitted by the surface.

1.5 Non-contact thermometry

The remaining part of this chapter will be devoted to reviewing what we define as non-contact thermometry techniques. As the name suggests, these methods measure the temperature of an object without the need to get in physical contact with it. In our context, the most obvious advantage of this approach is that the measurement probe won't affect the temperature that is measured. We shall begin by presenting the oldest non-contact method used in microtechnologies, namely IR thermography. Later sections will deal with more recently developed techniques, including thermoreflectance, Raman spectroscopy and fluorescence thermometry. In addition, thermochromic liquid crystal thermometry is briefly covered in Appendix B.

1.5.1 Infrared thermography

All matter emits electromagnetic radiation as a consequence of the movement among charged particles within atoms. This radiation is generally called thermal radiation. The spectrum of the thermal radiation is strongly dependent on the absolute temperature of the object being considered. For a blackbody, i.e. a hypothetical object that absorbs all electromagnetic radiation that falls onto it, the temperature dependence is described by Planck's law of radiation [46, 112]. For increased temperatures, the peak of the thermal radiation shifts towards lower wavelengths and increases in intensity. In the case of real objects, the wavelength and intensity of the peak also depend on the object's emissivity. The emissivity relates the emission characteristics of a specific material to those of an ideal blackbody in order to correct for the lack of total light absorption.

In infrared (IR) thermography, the thermal radiation of an object is captured and analyzed in order to determine its temperature. Electromagnetic radiation is typically captured in the infrared part of light, giving it the name IR thermography. In the microtechnologies, particularly for the non-destructive testing of IC circuits and semiconductor devices, IR thermography has a relatively long history. When used in combination with a microscope to access the microscale features, it is often referred to as micro-thermography. This methodology was proposed already in the 1960s [113, 114], demonstrating its abilities to locate defects on circuits by the identification of hot-spots.

The main advantages of IR micro-thermography are on one hand the simplicity of usage with well-developed commercial solutions available. Furthermore, it provides a quick full-field method of locating hot spots and to characterize temperature on microstructures. It also provides an efficient mean for characterizing fast changes in temperature. The main weakness of micro-thermography lies in its spatial resolution. Since the temperature information is carried by low-energy IR light, the diffraction limit does not allow for a resolution below a few micrometers with conventional optical systems. Typically, the spatial resolution of modern micro-thermography systems lies around

5 μm [57, 74, 115] although recent research has proposed possible solutions for improved resolutions [116, 117]. An additional disadvantage is that the user must know the emissivity of the materials on the sample surface. Without this knowledge, the thermal radiation emitted from the surface can not be correctly interpreted. With the presence of several materials on the sample surface, the measurement is further complicated. Another inconvenience of the method lies in the fact that IR radiation is largely absorbed by water and ordinary glass. This means that thermal mapping through a window or on surfaces immersed in water are made impossible.

1.5.2 Thermoreflectance

A promising alternative to IR micro-thermography is the thermoreflectance technique. The thermoreflectance technique is based on the measurement of thermally induced changes of the reflectivity of a surface. In most solids, the reflectivity is closely associated with thermal expansion. In semiconductors it is also largely affected by the modification of the band gap with temperature [118]. Reflected light coming from the surface of a sample thus carries information about the thermal behavior of the device under test via parameters such as the amplitude, phase and polarization of light. When an electrical current is fed through a device, the device is submitted to a variation of temperature ΔT. This in turn creates a variation of the reflectivity ΔR at the surface of the device:

$$\frac{\triangle R}{R} = \frac{1}{R} \cdot \frac{dR}{dT} \cdot \Delta T = \kappa \Delta T \tag{1.1}$$

where R is the mean reflectivity of the sample and κ is the thermoreflectance coefficient [118, 119]. By capturing and quantizing the variations in reflectivity using a photodiode and a CCD camera, temperature information can be extracted.

Typical applications of thermoreflectance thermometry are seen in the microelectronics field, although it also has been applied for characterizations of for example microelectromechanical systems (MEMS) [75] and laser diodes [120]. Recent developments have furthermore proposed the thermal mapping of buried elements using backside illumination at a wavelength where the silicon wafer is transparent, i.e. light in the infrared region [121, 122].

Thermoreflectance is particularly advantageous in terms of spatial resolution, reaching the sub-micrometer regime, while maintaining a high speed of image capture. Additionally, the setup is relatively cheap and simple. To perform basic measurements, all that is needed is an optical microscope, a CCD camera and a light-emitting diode (LED). However, for optimal performance, additional equipment, e.g. a lock-in detection scheme, is required. [118]

The most critical weakness of the technique is the necessity to precisely know the thermoreflectance coefficients of the involved surfaces. These coefficients are rather difficult to establish because of their strong dependence on several parameters, e.g. the wavelength of the illuminating light (see Fig 1.6) and, in microelectronic devices, the thickness of the passivation layer [75, 119, 123]. In applications for micro- and nanoscale thermometry, the thermoreflectance calibration procedure is particularly complicated due to the high magnification conditions [119]. An additional disadvantage of the thermoreflectance technique is its susceptibility to measurement errors due to imperfections in

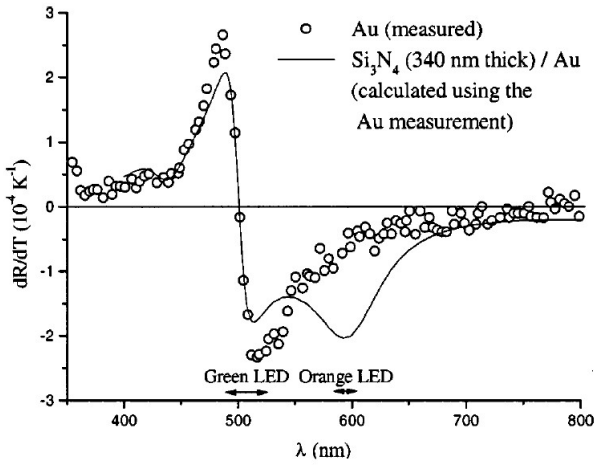

Figure 1.6: Thermoreflectance coefficient on a bare gold surface and a passivated gold surface as a function of the wavelength of the incoming light. A careful choice of the illumination wavelength is necessary in order to ensure a high signal to noise ratio of the measurements [118].

the studied material [124]. Possible solutions for the improvement of the technology are discussed in articles by Dilhaire *et al* [119], Grauby *et al* [125] and Luerssen *et al* [126].

1.5.3 Raman spectroscopy

Raman spectroscopy is a technique in which oscillation frequencies of atoms and molecules are measured. In the case of solid materials, these oscillations are generally known as phonons. Phonons are a quantum mechanical way of describing the lattice vibrations in a material. The nature and amount of possible phonons depend on the type of material that is under consideration. Semiconductor materials, which present symmetric crystal lattices, enable a relatively limited number of possible phonons and therefore give rise to energy spectra, called Raman spectra, containing very distinct peaks. Since even the slightest changes in the lattice structure implies changes in the way atoms oscillate, a range of material properties, e.g. temperature, stress, free carrier concentration and material composition, can be determined by studying the Raman spectrum [124, 127].

Experimentally, Raman spectra can be captured by illuminating an object with a monochromatic laser and detecting the scattered light using a spectrometer and a charge coupled device (CCD). Upon incidence of the laser light on the material lattice, a small portion of the photons, approximately 1 in 10^7 [124], interact with the phonons of the lattice. The interaction can be of two types, either Stokes scattering or anti-Stokes scattering. To understand the nature of these scattering types, it is useful to have a look at a typical vibrational energy level diagram and the corresponding Raman spectrum (see Fig. 1.7). Stokes Raman scattering refers to the case where the resulting state, after phonon-photon interaction, is the excited vibrational energy state. Anti-Stokes Raman scattering on the other hand is the case where a photon interacts with an atom or molecule that already is in the excited vibrational state and which ends up in the unexcited state. The energies of the re-emitted Stokes and anti-Stokes photons are equally different from the incident photon energy, but with different signs (see Fig. 1.7). [60, 124, 127, 128]

There are several ways to determine temperature changes through the analysis of a

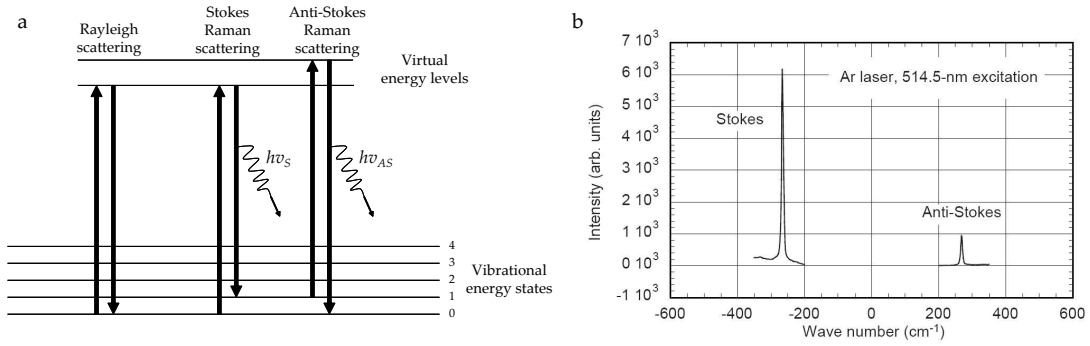

Figure 1.7: a) Vibrational energy level diagram. b) Raman spectrum of GaAs (110). The Stokes and anti-Stokes peaks are equally distant from the excitation laser energy level. [60]

Raman spectrum. A common way to go about it is to study the ratio of the Stokes to anti-Stokes intensities [60, 124, 129]. Another approach is to study the frequency shift, i.e. the positions of the Stokes and the anti-Stokes peaks. This method has been claimed to provide better results for measurements over a broad range of temperature [124, 128]. A third method is to analyze the peak broadening in the Raman spectra. However, to this point, this method has not proved to be as robust as the other two [124, 128].

Under the name micro-Raman spectroscopy, the general Raman spectroscopy technique has been adapted for measurements on surfaces with a high spatial resolution. By illuminating a sample through a microscope objective, the laser illuminates only a limited area. The size of this area determines the spatial resolution of the measurement. Using high power magnification objective lenses, the laser spot size can be limited to a diameter below 1 μm [60]. By the use of XY-tables micro-Raman spectroscopy allows for the analysis of several points on a sample, thus making thermal mapping of a surface possible. Using piezo-stages, the accuracy of the positioning may be as good as 0.1 μm [76, 130].

Micro-Raman spectroscopy presents advantages such as sub-micrometer spatial resolution [76, 131] and the possibility to yield absolute temperature measurements [124]. Furthermore, the technique has a very broad measurement range, from room temperature up to above 1000°C [127]. Another interesting aspect lies in its capability to measure subsurface temperatures due to the penetration of the illuminating laser in the sample by a few micrometers. By the use of confocal microscopy, the temperature of different surface layers can be mapped [76]. An interesting aspect of micro-Raman spectroscopy is that it can be applied to some extent in the measurement of temperatures in water. This is realized by analyzing the O-H stretch vibration modes of the water molecule [62].

Due to the spectral resolution of Raman systems and because of thermal stresses induced in the sample, the temperature accuracy is generally limited to around 10 K [60, 76, 129, 130]. The point-probe nature of the method leads to slow image captures, although high-resolution temporal studies of single points are possible [128, 131]. Using standard micro-Raman systems, the measured temperature in a certain point inevitably represents an average over the penetration depth [124, 129, 132], which obviously decreases the accuracy in case only the surface layer temperature is of interest. Further remarks on the Raman approach should be made regarding its unsuitability for measurements on metals [76]. The main applications lie in the study of semiconductor systems.

Furthermore, calibrations of the micro-Raman system are process dependent, i.e. each new setup and sample material need specific calibrations [124].

1.5.4 Fluorescent thermometry

Fluorescent thermometry relies on the measurement of the photoluminescent light emitted by a probe in order to determine the temperature. The probe is placed at a certain location and reports information on the temperature of its location via changes in its fluorescence. Since the probes used in fluorescent thermometry transmit information via light, the method is useful as a non-contact approach in the characterization of temperature.

Fluorescent thermometry has during the last few decades seen extensive development and found a range of applications. A common use lies in fiber optic fluorescent thermometry where in-process temperature measurements in a wide range of industrial settings have been enabled [55]. For applications in the microtechnologies, the potential of the technique has been the subject of numerous scientific papers [39, 66, 133–135]. For example, fluorescent probes have been used in the defect analysis of electronic circuits by identifying hot spots and for the characterization of temperature distributions in microfluidic channels and on MEMS heating devices [66, 133, 136].

In similarity to micro-Raman spectroscopy and thermoreflectance, the spatial resolution of fluorescent thermometry is fundamentally limited by the diffraction of light. Using low wavelengths and high-performance optics, the spatial resolution could become as good as a few hundreds of nanometers. However, the actual spatial resolution mentioned in the literature so far lies around 1 μm [66]. As for the temperature resolution, specific applications can reach precisions of down to a few millikelvins. However, for applications in the microtechnologies, the best resolutions typically lie in the range 0.1 - 1 Kelvin. Regarding the temporal resolution, the fundamental limit depends on the fluorescent probe used and the response time of the probe's fluorescence to changes in the temperature. Apart from this fundamental limit, the main limiting factor lies in the device used for capturing the fluorescence. When used for full-field studies, CCD cameras are commonly employed for the quick mapping of thermal images. The CCD device generally imposes a maximum temporal resolution of around one millisecond.

As opposed to other non-contact methods, fluorescent thermometry is semi-invasive due to the fact that the fluorescent probes have to be deposited or held at the location of interest. While such a semi-invasive approach may be regarded as a disadvantage, a positive aspect is that the calibration of the probes becomes more or less independent of the sample. This makes fluorescent thermometry relatively simple compared to for example thermoreflectance, where specific calibrations have to be performed for every new sample [119]. As compared to infrared thermography, fluorescent thermometry is not only advantageous in terms of spatial resolution. In addition, it is unaffected by the emissivity of the surface.

Fluorescent thermometry is of particular interest for use in microbiological and biochemical on-chip applications. On one hand, by choosing an appropriate fluorescent probe, measurements can be made through glass and water [51]. Furthermore, the techniques needed, e.g. fluorescent microscopy and fluorescence analysis, are generally well-known to the concerned biologists. The equipment is often also readily available to these researchers, which allows for a relatively fast and cheap implementation of the experimental setup.

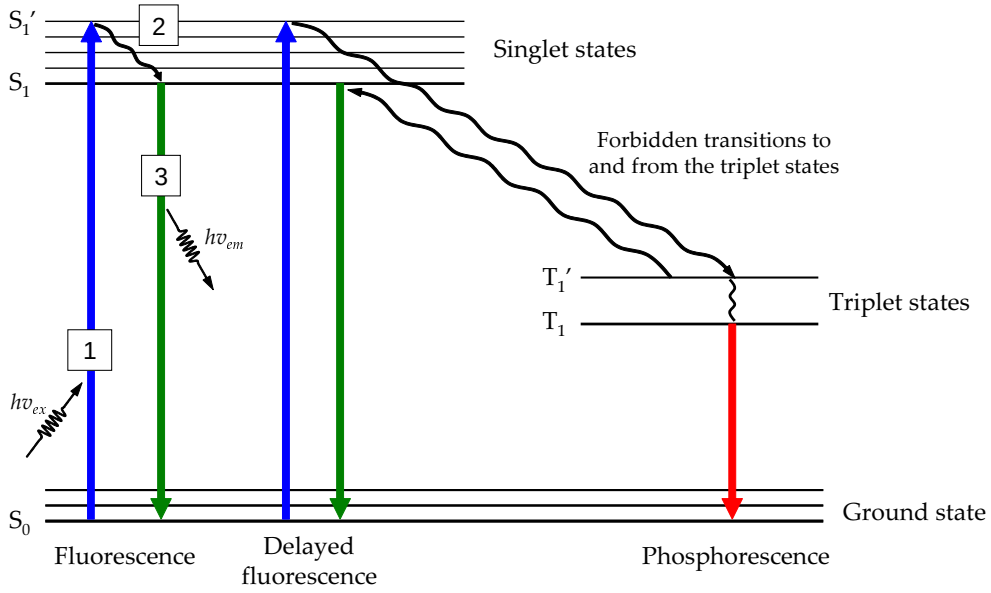

Figure 1.8: The Jablonski diagram is used to diagrammatically illustrate the mechanisms of photoluminescence. The normal fluorescence contains three principal stages; the excitation (1), the excited-state lifetime (2) and the fluorescence emission (3).

1.5.4.1 Theoretical background

Luminescence is the collective name for those processes involving the excitation of a susceptible molecule into an electronically excited state followed by the emission of light upon relaxation of the molecule. The excitation process can occur via a range of mechanical, physical or chemical interactions of the molecule with its environment. In the case where excitation occurs via the interaction of light with the molecule, the luminescence is generally referred to as photoluminescence. The photoluminescence mechanism is further classified into two types, fluorescence and phosphorescence.

Fluorescence is the result of a three-stage process that occurs in the luminescent molecule or particle [137]. It is frequently depicted diagrammatically in the form of a Jablonski diagram as shown in Fig. 1.8.

1. Excitation: A photon of energy $h\nu_{ex}$ is absorbed by the molecule, creating an excited electron singlet state (*S1'*)

2. Excited-state lifetime: The excited state exists for a finite amount of time, typically 10^{-10} - 10^{-7}s [138]. During this time, the molecule may undergo conformational changes and interact with its environment. Due to these processes, the energy of *S1'* is partially dissipated, yielding a relaxed singlet excited state, *S1*, from which the subsequent fluorescence originates. Not all molecules initially excited by the incoming light return to the ground state (*S0*) via fluorescence emission. Nonradiative processes such as collisional quenching and intersystem crossing may assist in the depopulation of *S1'* [138]. Furthermore, competing radiative processes from longer-lived triplet states, called phosphorescence, may also take part in the relaxation process.

3. Fluorescence emission: A photon of energy $h\nu_{em}$ is emitted, returning the excited molecule to its ground state *S0*. Due to the energy dissipation during the lifetime

of the excited state, the energy of the emitted photon is lower than that of the absorbed photon. This means that the emitted photon is red-shifted compared to the absorbed photon. The difference in energy or wavelength between the absorbed and the re-emitted photon, $h\nu_{ex} - h\nu_{em}$, is generally called the Stokes shift.

The difference between fluorescence and phosphorescence The difference between fluorescence and phosphorescence is clarified by considering the different electronic states of a photoluminescent molecule (see Fig. 1.8). Fluorescence is the result of the excitation of the molecule into a singlet state and subsequent relaxation back to the ground state. In the case of phosphorescence, the molecule is primarily excited to the singlet state, after which it is relaxed nonradiatively into a triplet state. Since the electron in this triplet state has the same spin orientation as the ground state electron, transitions to the ground state are forbidden [139]. Relaxation back to the ground state, being a forbidden transition, consequently takes a relatively long time, typically on the order of $10^{-6} - 1$ seconds [138]. As a result, phosphorescence is in most cases weak compared to fluorescence, though with a longer-lasting emission of light. Applications of phosphorescence for thermometry purposes have been proposed in a number of publications [140–142].

The temperature dependence of fluorescence The fluorescence emitted by many fluorescent particles is dependent on the surrounding temperature. The mechanism behind this temperature dependence is slightly different between different fluorophores and shall be discussed in connection with the presentation of each fluorophore in the following text. The most common observation that is made is the decrease of the fluorescence intensity as the temperature is increased. The origin of this behavior is for most fluorophores believed to lie in the increased occurrence of nonradiative processes related to thermal agitation (e.g. collisions with other molecules, intramolecular vibrations and rotations etc.). This leads to shorter fluorescence lifetimes and lower quantum yield [51, 67, 134, 143]. Other effects that can be observed as the temperature is increased are shifts in the wavelength of the emission peaks and broadening of the emission profile [135, 144].

The instability of fluorescence In the use of fluorescent particles and probes, the researcher generally seeks to maximize the stability and repeatability of the measurements. However, in the case of most fluorophores, the emitted fluorescent signal suffers in one way or another from fluctuations and degradations due to interactions with the environment. These effects are particularly disadvantageous when quantitative measurements of the fluorescence are performed. Typical destabilizing effects are those of photobleaching, oxygen quenching, pH quenching, fluorescence intermittency (blinking) and thermal bleaching. The most commonly encountered instability is photoinstability, which can be observed to some extent for all fluorophores [145, 146]. It consists in the change of the fluorescence intensity over time when exposed to the excitation light. It can be observed both as a decrease of the intensity (photobleaching) and as an increase of the intensity (photoenhancement). Fluorescence intermittency is an effect that has been given particular attention in the use of semiconductor nanocrystals [147–150] but which also exists in other fluorophores [151]. It is observed as an on-off behavior of the emitted fluorescence. The mechanism of blinking is still poorly understood, although it has been the subject of numerous articles. Concerning the thermal bleaching, this is a

permanent change of the fluorescence which typically occurs upon the exposure to high temperatures [39, 51, 152].

1.5.4.2 Various fluorescent imaging techniques

The information contained in the fluorescent emission from a fluorophore can be analyzed in a variety of ways. In general, it is of interest to achieve a fluorescence emission that is as strong as possible in order to maximize the signal-to-noise levels. The fluorophores are therefore in most cases excited at the peak of the absorption band. The excitation at a certain wavelength is realized by illumination through optical filters or monochromators, which only transmit light of a narrow band of wavelengths. In the techniques generally referred to as LIF (Laser Induced Fluorescence), laser sources with very well-defined and narrow-banded spectra are used to directly excite a fluorophore [137, 146, 153–159]. For the precise analysis of the emitted fluorescence spectra, a spectrofluorometer can be used. Studies of specific bands are possible by the use of optical filters or a monochromator. In order to capture the filtered signal, devices such as a CCD camera [39, 159] or a PMT (photo-multiplying tube) can be used [105]. To allow for easy and practical separation of the excitation light and the re-emitted fluorescent light, it is generally preferable to choose a fluorophore which possesses a large Stokes shift, i.e. a large gap between the excitation and emission peaks [160].

In the following, different quantitative analysis methods will be further detailed along with descriptions of the typical advantages and inconveniences of each approach.

Intensity-based measurements

The most common method of fluorescence analysis is to measure the integrated intensity of the fluorescent light, either within a certain band of the spectrum, typically in the vicinity of the emission peak, or throughout the entire emission spectrum [66, 77, 133, 134]. This approach allows for a relatively easy setup and enables fast capture times of entire images. Variations in the fluorescence intensity can be captured on a computer using a basic CCD camera. As opposed to several other techniques, the intensity-based measurements generally suffer from losses in accuracy due to factors such as drift of the optoelectronic system and variations in the optical properties of the sample. The optical properties may be affected by photobleaching as well as by changes in fluorophore concentration and the refractive index [161].

FIR – Fluorescence Intensity Ratio As a variation of the intensity-based measurements, FIR relies on the measurement of the intensity at several positions of the fluorescence spectrum. Certain fluorophores are particularly suited for such applications due to the existence of two or more well-defined emission peaks in their spectra. By measuring the ratio of the peak intensities, information can be extracted. Compared to the simple intensity measurements described above, FIR is largely independent of instabilities such as drift of the system or the sample. The intensities of the various peaks certainly change with such drifts but the ratio of the peaks generally stays stable. [105, 106, 162–164]

Two-color thermometry While being similar to FIR in principle, two-color thermometry makes use of two different fluorophores [157, 165]. The technique is sometimes

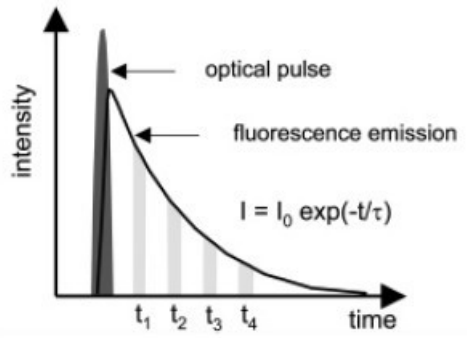

Figure 1.9: The FLIM approach measures the dependence of the fluorescence lifetime on temperature.

employed under the name DELIF (Dual Emission Laser Induced Fluorescence) [137, 154]. The intensities from one spectral band of each fluorophore are measured and the ratio of these two intensities is subsequently analyzed and used to extract information. Typically, one fluorophore has a high intensity dependence on an environmental parameter, in this case temperature, while the other fluorophore possesses a very low dependence on the same parameter. The second fluorophore is then used as an internal reference which takes into account factors such as drifts in the system, e.g. fluctuations of the excitation light source and differences in the optical path.

In the selection of the two fluorophores, it is practical to use fluorophores with similar absorption spectra but with different emission bands. This simplifies the setup required to excite the fluorophores and to separate the resulting emissions.

Two-color thermometry offers more flexibility than FIR in the choice of fluorescence wavelengths, but is more sensitive to intrinsic fluorophore instabilities. Due to the use of two different molecules, differences in for example diffusion rate and photobleaching are not automatically compensated for. Furthermore, in particular for spatially small scale analysis, it may become challenging to make sure that the density of each fluorophore stays constant throughout the field of analysis.

FLIM – Fluorescence Lifetime Imaging

Upon excitation, a fluorophore enters an excited state. The lifetime during which it remains in this state is to a large extent dependent on the environment. In the FLIM technique, this is exploited by determining the dependence between the lifetime and a specific environmental parameter. Temperature in particular tends to affect the lifetime of the excited state. This is due to phenomena such as the changes of the thermal agitation and the presence of charge-transfer states in the surrounding media which offer nonradiative de-excitation pathways that become energetically more favorable with increasing temperature [153].

As compared to intensity-based measurements, FLIM requires a relatively complex experimental setup to be realized. Since the timescale of fluorescence lifetimes typically is on the order of nanoseconds, pulsed lasers are normally employed to precisely control the excitation process. Furthermore, the acquisition of the fluorescence is generally achieved using lock-in techniques in order to precisely select the time window during which fluorescence should be captured. In Fig. 1.9, the approach is visualized by showing

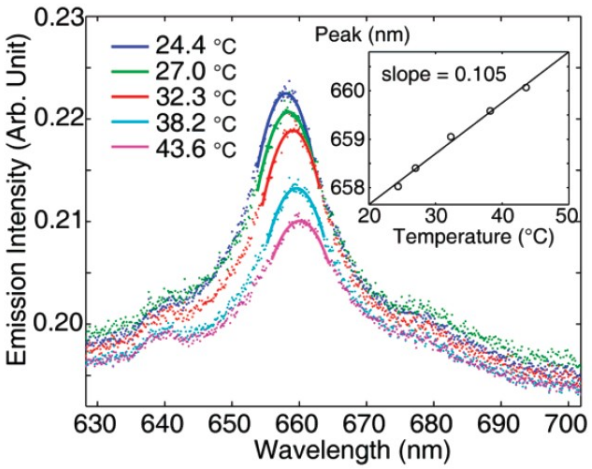

Figure 1.10: Temperature dependence of the spectral position of the CdSe/ZnS nanocrystal emission peak [135].

the time-dependent fluorescence intensity as a result of the excitation by a short laser pulse. In order to determine the lifetime τ, the integrated intensities in two or more specific time windows following the end of the laser pulse are measured. [55, 138]

Since the FLIM approach is a ratiometric measurement technique, it is independent of experimental parameters such as the dye concentration and the excitation/detection efficiency, thereby facilitating quantitative temperature measurements [55, 56, 161]. On the other hand, the method typically requires the acquisition of several data series in order to reach a satisfactory signal-to-noise level. This in turn leads to image capture times which are generally longer than those for intensity-based measurements. In principle, FLIM is not well suited for fast full-field imaging considering that it requires the use of pulsed lasers, lock-in detection and highly sensitive devices to acquire the lifetime data. However, in a recent article by Benninger *et al* [161], three-dimensional imaging of the temperature within a microfluidic channel was illustrated. The technique was based on a relatively complex setup, where FLIM was implemented using an ultrafast, electronically shuttered, wide-field detector based on a gated image intensifier. Furthermore, by the use of multiple parallel laser beams, a fast acquisition time (10 - 30 s) of three-dimensional images was demonstrated.

Spectral shift thermometry

For many fluorophores, the spectral position of the emission peaks changes with the temperature. While in many cases this spectral shift is hardly observable, some fluorophores provide quite easily detectable shifts which in turn can be used to probe temperature changes. Although rarely applied for thermal mapping, a recent paper by Li *et al* demonstrated the use of spectral shifts in semiconductor nanocrystals in order to probe temperatures on a microheater device (see Fig. 1.10) [135]. The technique requires equipment that allows for the capture and analysis of fluorescence spectra. The calibration can typically be performed using a spectrofluorometer while measurements on for example a planar sample require the use of more adaptable instruments, e.g. a spectrograph in combination with a CCD camera. Similar to the FLIM approach, spectral shift thermometry is not affected by system instabilities such as fluctuations of the

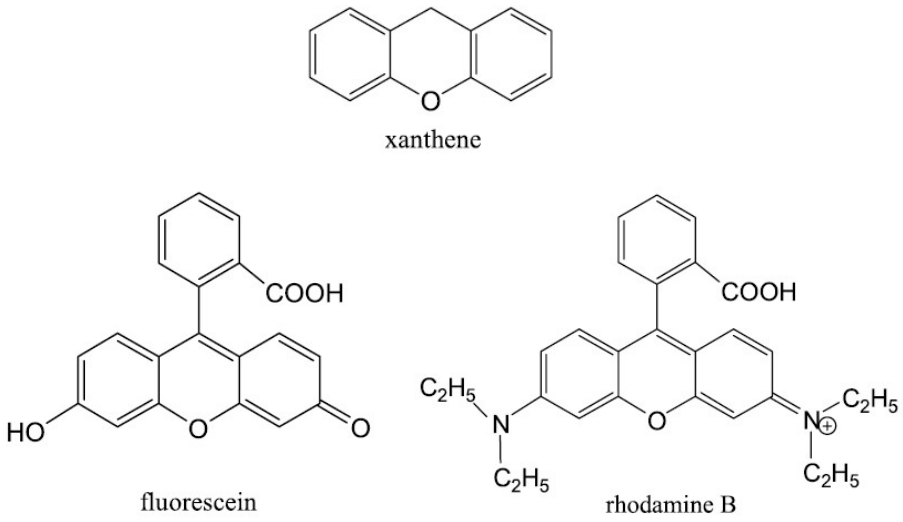

Figure 1.11: Molecular structures of the xanthene molecule and the xanthene-based fluorescent dyes fluorescein and rhodamine B.

excitation light source.

1.5.4.3 Fluorescent probes

Photoluminescent probes can be of very different kinds, e.g. organic (Fluorescein, Rhodamine B, Perylene etc.), inorganic (various rare-earth and semiconductor compounds) and organometallic (Ruthenium and Porphyrin). In the following sections, the fluorescent probes that have been considered for this thesis will be presented, starting with two organic fluorescent dyes, Fluorescein and Rhodamine B. After presenting these dyes, the semiconductor nanocrystals will be addressed followed by rare-earth materials. For a broader survey on the fluorescent materials, the reader is referred to Appendix A, where an additional range of potential probes are described.

A. Organic fluorescent dyes

Among the most commonly employed fluorescent dyes in biological applications we find the Rhodamine and Fluorescein molecules, which are members of the group referred to as Xanthene dyes (Fig. 1.11) [138, 145, 157, 166].

A.1. Rhodamine B One of the most commonly applied organic dyes in fluorescent thermometry applications is the Rhodamine B molecule from the Rhodamine family. It is a dye which absorbs green light and fluoresces in the red-orange part of the visible spectrum. It is commonly used as a laser dye for wavelengths near 610 nm [157]. The Rhodamine B molecule shows a strong dependence on temperature. In the literature, the fluorescence intensity is typically stated to decrease with increasing temperatures at a rate of 1.2 - 2.5% per °C at room temperature [67, 154, 155, 157, 158]. The decrease occurs uniformly over the entire emission spectrum and is strongest in the range of 0 - 100°C [167]. Other molecules of the Rhodamine family have also been applied for temperature characterization, although less frequently [134, 137]. Slyadnev *et al* reported

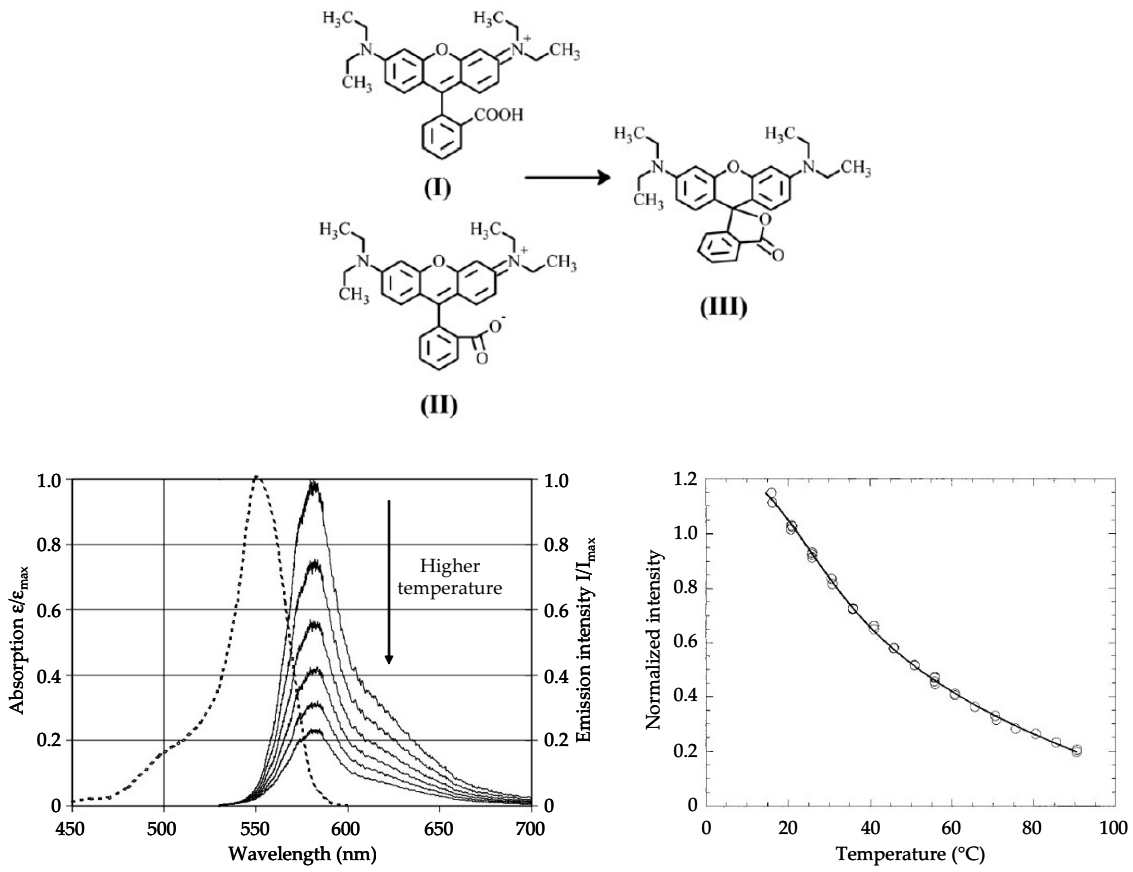

Figure 1.12: a) Molecular structures of the three different conformations that Rhodamine B can take [68]. b) The Rhodamine B spectra at different temperatures. The absorption curve is dashed and the emission curves at different temperatures are solid [146]. c) Temperature dependence of the emission peak intensity [66].

a 5-fold decrease of the fluorescence intensity of Rhodamine 3B when increasing the temperature from 20°C to 90°C [134].

Regarding the mechanism behind the temperature dependence, some papers explain it simply as being a result of the increased amount of non-radiative relaxation processes. However, the mechanism can be explained further in detail by considering the different conformations that the Rhodamine B molecule can take. Depending on the surrounding media and the environmental parameters, there are three possible conformations (see Fig. 1.12). Two of these are strongly emissive, while the third is emissionless due to the interruption of the conjugate π-electron in the chromophore [68]. As the temperature is increased, the transformation from conformation one and two into the third one is facilitated to some extent leading to a decrease in the observed fluorescence intensity. An additional reason for the decrease in intensity is that the Rhodamine B molecule may decompose at elevated temperatures.

Experimentally, the Rhodamine B fluorescence is commonly induced using either a mercury lamp with filters transmitting light in the vicinity of the absorption maximum, i.e. 500 - 550 nm [66]. An appropriate laser source can also be used. The most commonly used laser is the Ar-ion laser with light centered around 514.5 nm [155, 168]. The less employed Nd:YAG laser, with light centered around 532 nm, enables a stronger excitation

as it excites the Rhodamine B molecules closer to the absorption peak [146, 159].

Several approaches for the exploitation of the temperature dependent Rhodamine B fluorescence have been reported. For applications in microfluidics and microsystems, the most common method has been the measurement and analysis of the intensity changes within one spectral band [39, 63, 66, 67, 159, 167]. This is mainly due to the simplicity of these measurements which allow for fast temperature mapping using a standard fluorescence microscope and a CCD camera [66]. Typical temperature resolutions reported for the intensity-based measurements are on the order of 3°C between 20°C and 90°C without spatial or temporal averaging. Spatial resolutions of down to 1 μm have been reported [39, 66]. Slyadnev *et al* reported a temperature resolution of 0.5°C using the alternative Rhodamine dye Rhodamine 3B [134]. Better temperature resolutions have been achieved for temperature measurements on a bigger scale, with resolutions down to 0.4°C [159]. The temporal resolution is typically limited by the acquisition time of the CCD camera in use, i.e. on the order of a few milliseconds.

Except for the single intensity-based measurements, Rhodamine B has also been successfully employed in two-color thermometry applications. The Rhodamine B dye is in this case generally used as a strongly temperature dependent probe while a second fluorophore, e.g. carboxyfluorescein [165], Rhodamine 110 [157] or Pyrromethene 567 [137], is used as an internal reference to compensate for instabilities such as the fluctuations of the excitation light source. The approach requires a slightly more complex setup than single intensity measurements in that it requires the use of two CCD cameras [157] or alternatively a 3-CCD color camera [165] in order to separate the different colors of the two fluorophores. Three-color measurements [156] as well as lifetime measurements have also been investigated [161].

The use of Rhodamine B for temperature characterizations has been extended to several application areas. In the recent past, several papers have been published on its application for temperature mapping within microfluidic channels [63, 66, 67, 167]. Another interesting application is its use for the evaluation of the temperatures within resists used for nanoimprint and electron beam lithography. These processes are highly dependent on the resist staying within a certain temperature range in order to avoid pattern deformation and to achieve specific critical dimensions [68]. Except for its use in microscale applications, Rhodamine B has also been successfully applied in problems such as the characterization of natural convection [146], evaluation of the dynamics of heated submerged jets [156, 168] and the temperature measurements on a monodisperse droplet stream [155].

Except for its strong temperature dependence, typical advantages of Rhodamine B lie in its independence of pH (at pH ranges above 6) and its resistance to high pressures (up to 350 psi) [67, 68, 154]. Furthermore, its temperature dependence has been demonstrated in a number of different media, e.g. ethanol [169], biological buffers [63, 66] and polymer [68], making it a versatile temperature probe. On its downsides, Rhodamine B suffers from relatively strong photobleaching under the influence of the excitation light [67, 146]. Due to the spectral band overlap, its fluorescence has also been shown to be dependent on the dye concentration [170].

A.2. Fluorescein Fluorescein is a commonly used dye for labeling and tracking species in microbiological assays [171, 172]. Additionally, fluorescein has a strongly pH-dependent fluorescence, making it a useful probe in applications where pH must be monitored [154]. In the field of thermometry, fluorescein is useful due to its fluorescence

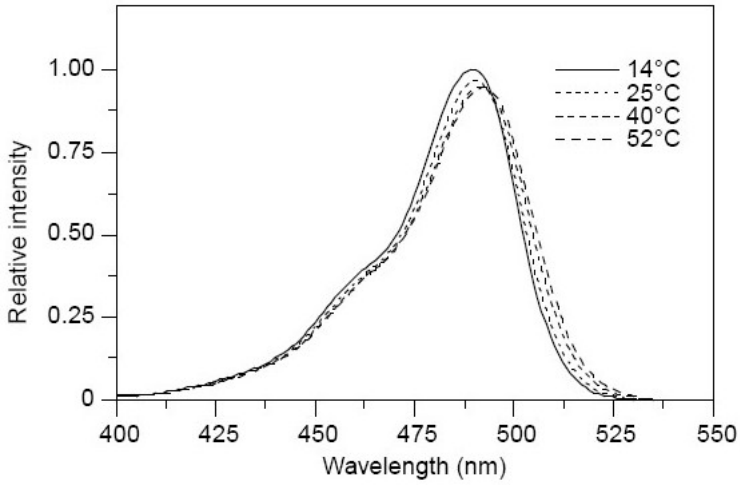

Figure 1.13: Temperature dependence of the absorption spectrum of fluorescein [154].

intensity which decreases as the temperature increases [13, 173]. In contrast to the general observation of decreased intensity with increased temperature, Coppeta *et al* has presented results on the temperature dependence of fluorescein where an increased intensity could be achieved for increases in temperature [154]. The rate of increase was as high as 2.43% per K. This observation could be understood by analyzing the temperature dependence of the absorption spectrum (Fig. 1.13). At an increased temperature, the absorption band is widened. This widening leads to an increased absorption at the flanks of the band. Since the authors of the article used excitation light centered on the flank of the absorption band (514 nm), an increase in temperature led to a dramatically increased absorption which in turn led to a stronger fluorescence intensity. On the other hand, when using excitation light at a lower wavelength (488 nm), the authors measured a temperature dependence of -0.16% per K, i.e. a slight decrease of intensity with an increase in temperature. A typical disadvantage of the fluorescein molecule is that it quickly photobleaches when exposed to the excitation light. The photobleaching process can be alleviated by controlling the environment, e.g. the temperature and the presence of oxygen, both of which influence the photobleaching rate [145].

B. Inorganic fluorescent probes

B.1. Semiconductor nanocrystals A highly interesting new class of fluorescent probes is the semiconductor nanocrystals, also known as quantum dots. Compared to conventional fluorescent dyes, these particles present particular advantages in terms of their high photostability, exceptional quantum yield, broad absorption spectra and narrow emission peaks [51, 174–176]. While being investigated for a range of various applications, e.g. biological labeling [174, 177–181] and semiconductor lasers [182], since 15 - 20 years ago, the application for temperature measurements in the physiologically relevant range is relatively recent. [51, 135, 144, 152]

The nanocrystal photoluminescence dependence on temperature can be observed in several ways. The most significant dependence is that of the emission peak intensity, which decreases when the temperature is increased. Changes can also be observed in the emission band width and in the spectral position of the emission peak. The common observation is a widened emission band and a red-shifted position of the emission peak

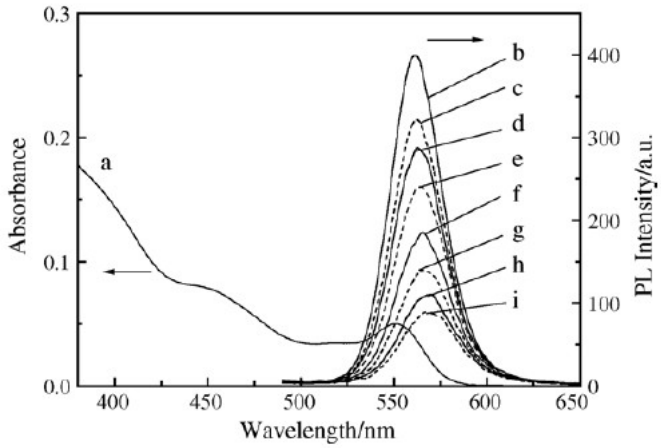

Figure 1.14: Visualization of the CdSe/ZnS spectrum at different temperatures. The spectrum shows several interesting characteristics which can be found in many semiconductor nanocrystals. First of all, the absorption band (curve *a*) is very broad, allowing for a flexible choice of excitation source. Furthermore, the emission peak is relatively narrow. Finally, the emission intensity is strongly dependent on the temperature. The different temperatures of the emission spectra, in the order from *b* to *i*, are 280K, 288K, 298K, 308K, 318K, 328K, 338K and 348K. [152]

for increased temperatures [144].

The mechanisms behind the temperature dependency of the nanocrystal photoluminescence have been the subject of study in several recent publications [183–185]. Due to the quantum confinement, the thermal behavior of nanocrystals has to be analyzed with consideration of the particle size, the processes of nonradiative relaxation via phonon coupling, exciton thermal dissociation, energy transfers, carrier trapping and the temperature dependence of the absorption spectra [51]. Commonly, it is observed that capping layers and organic ligands positioned at the nanocrystal surface play an important role in determining the temperature dependent properties [152, 184, 185]. Yet another contribution to the thermal behavior comes from the thermoluminescence which is caused by a thermally induced recombination of carriers trapped in surface states [51].

Like with other fluorophores used for temperature probing, there are various approaches for the analysis of the temperature dependent fluorescence spectra of nanocrystals. The most common approach until now is single intensity measurements [13, 144, 152]. Another recently demonstrated approach employed the well-known spectral shift of the emission peak of CdSe/ZnS nanocrystals, with a red-shift of 20 nm over a range of 200°C [144, 152], in order to determine the temperatures on a microscale heating strip [135]. FIR techniques are not well suited for semiconductor nanocrystals, as their spectra commonly only contain one very narrow emission peak.

The most commonly studied semiconductor nanocrystals in temperature sensing applications are CdSe and ZnS-capped CdSe (CdSe/ZnS) nanocrystals (Fig. 1.14) [77, 135, 144, 152, 183, 186]. Other nanocrystals of interest are CdTe [51, 185] and ZnS/Mn^{2+} [51, 187] nanocrystals. CdTe has been shown to have a linear reversible fluorescence intensity changes in a range of 30 - 60°C, while for ZnS/Mn^{2+} reversibility has been achieved in the range 30 - 150°C [51].

Semiconductor nanocrystals are advantageous in that they can be customized to a

large variety of applications. By changing the particle diameter, the emission wavelength can be modified. The introduction of impurities during synthesis can also be used to change the nanocrystal properties. Improvements of the performance are often achieved by capping the nanocrystals with a second semiconductor material, e.g. with a different band-gap. Furthermore, to enable the use in various environments, e.g. for biological applications, the particle surfaces are frequently functionalized to provide the probes with specific chemical properties [180].

Because of the high signal yield, often explained by the high electron-hole overlap which results from the quantum size confinement and which leads to an increased oscillator strength [51], semiconductor nanocrystals are particularly useful for quantitative measurements such as fluorescence-based temperature characterization. Furthermore, compared to conventional thermal phosphors, the small size, on the order of 1-10 nm, holds potential for higher spatial resolution measurements because of greatly reduced light scattering [51]. Many semiconductor nanocrystals are also more or less insensitive to oxygen quenching, which makes these probes yet more attractive [144].

A well-known property of semiconductor nanocrystals, mostly regarded as a disadvantage, is the strong fluorescence intermittency, also known as blinking [147–150]. This effect is particularly disadvantageous in applications where quantitative measurement are performed unless averaging of the intensity over relatively long time periods are possible. Another drawback observed for some nanocrystals is the irreversibility of the temperature dependent behavior [39, 152].

B.2. Rare-Earth based dyes A well-known group of photoluminescent materials for thermometry applications is that of rare-earth doped materials. They are commonly known as thermal or thermographic phosphors [53, 153]. The photoluminescence of the thermal phosphors is created as a result of the photo-optical excitation of rare-earth dopants [153]. Thermal phosphors have a relatively long history of applications in thermometry, particularly in high-temperature fiber optic thermometry [55].

In a review by Allison *et al*, the physical mechanism behind the temperature dependence of the thermal phosphors is discussed [53]. The dependence is partly explained by reference to the Boltzmann distribution which governs the partitioning of the populations in the various participating vibrational levels of the ground, excited and emitting states. In a similar manner, Wade *et al* discussed the Boltzmann distribution and its role in the temperature dependent ratio of the population of different excited states of the rare-earth ions [163]. The temperature dependence has further been explained to arise from the presence of charge-transfer states in the host ceramic matrix. These states offer non-radiative de-excitation pathways which become energetically favorable with increasing temperature, thus leading to thermal quenching of the photoluminescent emission [153]. In the case of chelated Eu-ions, where resonant coupling between organic ligands and the rare-earth ions is behind the fluorescence, the decrease in fluorescence intensity at higher temperatures is generally explained as an increased probability for coupling of the excited ligand state to non-radiative states [133, 188, 189]. Changes in the non-radiative relaxation mechanisms have also been discussed as being the reason behind the size-dependent temperature sensitivity of rare-earth doped nanocrystals [190].

Temperature measurements using rare-earth materials are commonly performed by the FIR [162, 163, 190] or FLIM [153] approaches, although single intensity measurements also have been applied [133]. FIR measurements are frequently possible due to the relatively complex emission spectra, often with the existence of several fluorescent and

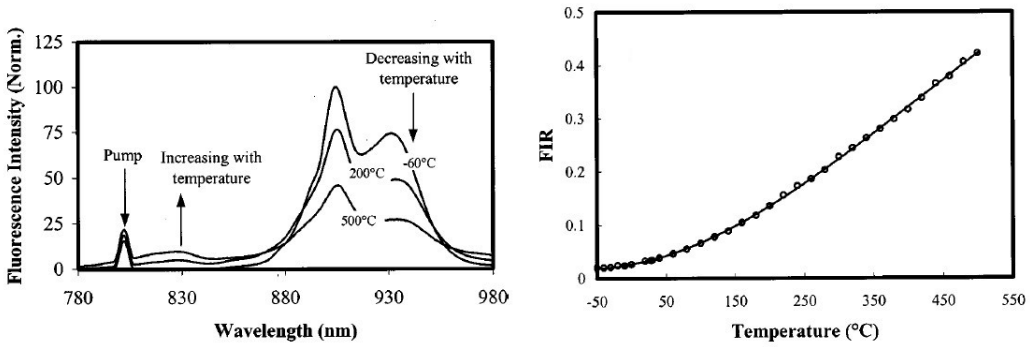

Figure 1.15: The left graph shows the emission spectrum of a Nd^{3+}-doped silica probe.The presence of two emission bands with different temperature dependencies enables the use of FIR-based measurements. In the right figure, a graph relating the ratio of the two emission peaks with temperature is shown. [163]

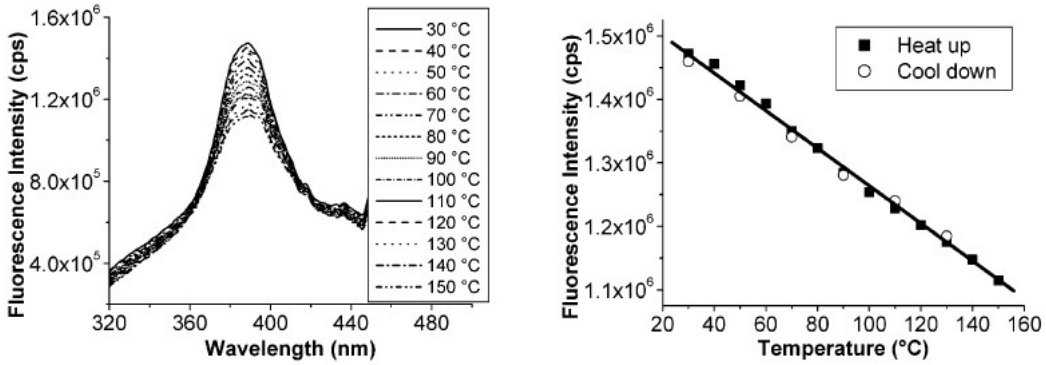

Figure 1.16: Temperature dependence of the europium-doped particle BaFBr:Eu^{2+}. The left graph shows the spectrum at different temperatures. In the right graph, the intensity of the emission peak is plotted as a function of the temperature. [51]

phosphorescent emission peaks originating from one or more rare-earth dopant ions [104]. The often temperature dependent interplay between these peaks provides an excellent tool for temperature determination (see Fig 1.15).

Typical examples of rare-earth probes used for thermometry applications are various europium-based compounds, e.g. Eu:TTA [133, 188] and europium-(III)β-diketonate [56], and europium-doped particles, e.g. Y_2O_3:Eu^{3+} and BaFBr:Eu^{2+} nanoparticles [51, 153]. The europium complexes have demonstrated a high stability and strong temperature dependence in the range of 0 to 70°C [56, 133] whereas the doped particles have shown linear and reversible temperature dependent emission peak intensity between 30 and 150°C (see Fig. 1.16) [51].

Other rare-earth based thermal probes use ions such as erbium [162, 190], terbium [191], neodymium [163] and cerium [153]. High temperature measurements up to 610°C were specifically demonstrated by Camargo *et al* using erbium-doped lead lanthanum zirconate titanate (PLZT) [162]. High-temperature measurements were also presented recently by Aizawa *et al*, using terbium-doped silica as a fiber-optic thermometer for temperature ranging from room temperature up to around 900°C [191]. Another interesting result was presented by Alencar *et al* in the use of erbium-doped

$BaTiO_3$ nanocrystals, showing an exceptionally high temperature resolution of around 0.005°C [190] in the range of 50 to 190°C. This is an order of magnitude better than the commonly reported resolution of 0.05°C for rare-earth based thermal phosphors [53, 153].

Applications of rare-earth doped compounds for temperature measurements have in the past mainly been seen in the field of fiber optic based remote measurements in industrial processes and macro-size temperature monitoring [55, 56]. Typical advantages are their robustness and stability in harsh environments with measurement capabilities ranging from cryogenic temperatures to above 1000°C [53, 55]. Recent developments have seen increased interest of rare-earths in the field of microsystems characterization [105, 133] and microbiological studies [188]. In line with the demands for smaller scale characterization, particular efforts are being invested in the developments of miniaturized rare-earth doped compounds, typically referred to as rare-earth doped nanoparticles or nanocrystals [51, 105, 106, 153, 190].

1.6 Thermometry in lab-on-a-chip systems

We will now conclude the first chapter by giving a brief discussion on the relevance of the submicrometer thermometries with regard to this thesis. As a support to the reader, a selection of the five most significant thermometry techniques are summarized and compared in Table 1.2 .

Temperature control is of great importance in biochemical processes and fundamental biological studies. The potential improvement of temperature control, both in terms of process parallelization and modulation speed, holds promise for a better efficiency of existing processes and the development of new approaches for the study of biomolecular systems.

Within this thesis, the improvement of temperature control has been addressed with specific focus on two indispensable areas of development. On one hand, the heat source and the thermal properties of its environment have to be optimized in order to allow for high spatial confinement and fast stabilization times of the temperature changes. On the other hand, the thermal characterization of the system is essential in order to verify the functionality of the device.

The choice of method for the thermal characterization has in this thesis been given particular importance. With reference to the preceding survey on the existing technologies, we have identified fluorescence thermometry as the most appropriate technology for use in miniaturized biosystems. As opposed to the other techniques, it provides unquestioned capabilities for measurements in liquid environments while being capable of diffraction-limited resolution, i.e. down to a few hundreds of nanometers. In addition, it represents a technology which is well-known to most biologists and which frequently already is available in the concerned laboratories. The main drawbacks lie in instabilities such as photobleaching, thermal bleaching and blinking, which typically reduces the temperature resolution. However, for biological research and processes, the achievable resolutions (0.1 - 1°C) are generally satisfactory.

Naturally, the choice of fluorescent thermometry does not mean that other technologies could not be used as well. In particular, micro-Raman spectroscopy is an interesting technology with certain capabilities of measurements in liquid environments. However, it requires relatively sophisticated equipment and its approach is less straightforward. SThM is also an approach which merits certain attention due to its high spatial resolution capabilities, although the usefulness in liquid conditions has yet to be demonstrated.

Table 1.2: Comparison of micro- and nanothermometry technologies.

Technique	Contact or Non-contact	Point or Full-field	Liquid conditions	Simplicity	Cost
SThM	Contact	Point-probe	Not demonstrated	Moderate - Difficult	Moderate - Expensive
IR thermography	Non-contact	Full-field	No	Simple	Moderate
Thermoreflectance	Non-contact	Full-field	Not demonstrated	Moderate	Moderate
Raman spectroscopy	Non-contact	Point-probe	Yes	Moderate	Expensive
Fluorescent thermometry	Non-contact	Full-field	Yes	Simple	Moderate

Technique	Spatial resolution	Temporal resolution	Temperature resolution	Other remarks
SThM	$10 - 500\,nm$	$0.1 - 50\,ms$	$< 10^{-3}\,K$	The heat transfer between the probe and the sample is often poorly understood and may introduce measurement errors.
IR thermography	$> 5\,\mu m$	$1 - 50\,ms$	$0.1 - 1\,K$	Well-established technology with a wide range of commercial alternatives.
Thermoreflectance	$> 0.5\,\mu m$	$1 - 10\,ms$	$< 1\,K$	
Raman spectroscopy	$> 0.5\,\mu m$	$> 200\,ns$ [131]	$10\,K$	Broad applicable temperature range.
Fluorescent thermometry	$> 0.5\,\mu m$	$1 - 10\,ms$	$0.1 - 1\,K$	Generally limited to narrow temperature ranges.

In conclusion, the development of a device for fast and spatially confined temperature control has led us to pursue the investigation of three principal issues throughout this thesis:

1. Design and fabrication of the heat source. The design and fabrication issues of nanowires as heat sources and the influence of its environment on the thermal response should be specifically addressed. Nanowires have a high potential for the use as heating elements mainly due to their small volume which results in highly localized heating. However, their thermal behavior and the extent of their thermal impact on the environment are likely to be dependent on the thermal design of their immediate surroundings. In Chapter 2, finite element modeling (FEM) will be used in order to investigate some of the possible options in the thermal designs of the nanowire surroundings. The findings will subsequently form a basis for the actual fabrication of nanowire-based heating elements, which will be specifically addressed in the end of Chapter 2.

2. Selection of a fluorescent probe. In Chapter 3, the study of two fluorescent probes in particular, CdSe/ZnS nanocrystals and Rhodamine B, will be presented. These probes were chosen because of their strongly temperature-dependent fluorescence. As explained previously in this chapter, typical challenges of fluorescence thermometry are the various stability issues regarding the fluorescence signal, e.g. photobleaching and thermal bleaching. A large part of Chapter 3 will consequently be dedicated to the evaluation of the fluorescence stability of the two probes. Further essential points of investigation which will also be presented are the acquisition of a temperature calibration curve and the positioning of the probes on the sample to be investigated.

3. Thermal mapping methodology. Various approaches exist for the thermal characterization of a sample using fluorescence. In order to allow for higher spatial resolution, a new methodology based on the confinement of a fluorescent probe in the vicinity of the sample surface is introduced in Chapter 3 and subsequently applied for high spatial resolution thermometry in Chapter 4. Furthermore, in Chapter 4, the experimental aspects of the approach, e.g. in terms of the fluorescence acquisition and analysis, will be illustrated. Choices to be made regarding the experimental approach include those of the acquisition device, e.g. by a CCD camera or a PMT device, and the fluorescence analysis approach, e.g. single intensity measurements or FIR. As shall be seen, for the purpose of full-field imaging capabilities and simplicity, our main approach is based on single intensity measurements of fluorescence captured by a CCD camera.

CHAPTER 2

NANOWIRES AS HEAT SOURCES

After the survey of the existing thermometry techniques presented in Chapter 1, we will now target the development of the nanowire-based heating elements discussed in the introduction. As pointed out in the last section of Chapter 1, the achievement of a system for fast and spatially confined temperature control is largely dependent on the size of the system but also on the materials used and the configuration of the different components. The current chapter will be devoted to deeper considerations on the thermal design of the nanowire system. As a tool in this analysis, the use of computer-aided finite element simulations will be illustrated in detail.

Based on the theoretical considerations and the simulations of the first part, the second part of the chapter will deal with the actual implementation of various nanowire configurations. The fabricated devices will then be used for the experimental analysis and possible validation of the theoretically expected results.

2.1 Joule heating in nanowires – a finite element model

To gain insights into the thermal properties and behaviors of various nanowire configurations without having to perform an experimental trial-and-error procedure, simulations based on the finite element method (FEM) were implemented. All simulations presented here were performed in the commercial software COMSOL® (version 3.3). This software package provides a broad support for the simulation of resistively induced heat generation as well as the different heat transfer mechanisms.

It should be noted that the COMSOL software, like other FEM simulation software, has not been specifically developed for nanoscale thermal transfer. In other words, the software does not take into account nanoscale effects on thermal properties. Such an effect is the possible change of thermal conductivity due to increased phonon boundary scattering [192–195]. Additionally, for dimensions close to the mean free path of electrons (~ 10 nm), the electrical resistivity can be expected to increase due to increased surface scattering. This in turn leads to increased resistive heating and higher temperatures. Although the structures described here are not as small as the mean free paths of the various energy carriers, the sizes are nevertheless relatively near the critical dimensions. All results should thus be analyzed with possible nanoscale effects in mind.

It should also be noted that the FEM simulations performed here are not intended to be used as a tool for the exact prediction of parameters such as the temperature and the power dissipation. The main function of the simulations is instead to provide a simple mean to better understand in which direction certain design changes will affect things such as the resulting temperature distribution, power consumption and response time.

2.1.1 The FEM model

The basic principle of FEM modeling consists in creating a virtual representation of the physical object. In order to achieve this, a number of object properties have to be defined in the FEM software. The first step is to enter the geometry of the object. When doing this, it is necessary to identify appropriate ways to simplify the representation of the different parts. It is generally of interest to minimize the use of largely different-sized parts and complicated geometries. Simplifications can also be made by identifying symmetry lines or planes in the object. If these exist, the volume that has to be analyzed can be largely minimized, allowing for faster calculations of the response. Too large systems frequently lead to the inability of a normal computer to perform the calculations. Lack of memory is a typical reason for uncompleted FEM analysis. To avoid such problems, simplifications of the geometry can help significantly.

Once the geometry is defined, the physics and the material properties of the different parts are defined. These properties will be the basis for the calculation of the physical behavior of the complete model. Furthermore, the boundary conditions of the geometry have to be defined. In the analysis of heat transfer, boundary conditions can typically be the designation of a certain inward or outward heat flow at a surface or the definition of a constant temperature.

Before performing the FEM analysis, the geometry is divided into a large amount of small cells, which are called the finite elements. The assembly of these finite elements is typically referred to as a mesh. The physical behaviors of the object are calculated for each element and with respect of the neighboring elements of each cell. In the COMSOL software, the mesh is created automatically after indicating certain parameters such as the minimum size of each finite element.

In the following, the different steps taken for the implementation of our FEM model will be presented, starting with the creation of an object geometry.

The virtual geometry

The basic nanowire configuration that was analyzed here consisted of a single nickel nanowire which was connected to an external power source by two 10mm-long nickel pads, one at each end of the wire. Since the real-world nanowire is most conveniently realized by conventional lithography methods, e.g. electron beam lithography, the cross-section could be considered to be approximately rectangular. The dimensions of the structure is given in Fig. 2.1, with the nanowire being 20 μm long, 200 nm wide and 40 nm thick.

Regarding the immediate surroundings of the nanowire, we were interested in evaluating the impact of those materials situated both above and underneath it. A closer look at the possible alternatives led us to identify the use of two different materials underneath the nanowire. The most basic alternative was that of a nanowire fabricated on a plain oxidized silicon wafer. Secondly, the impact of using a material of lower thermal conductivity than silicon was investigated. With regard of the existing micromachining

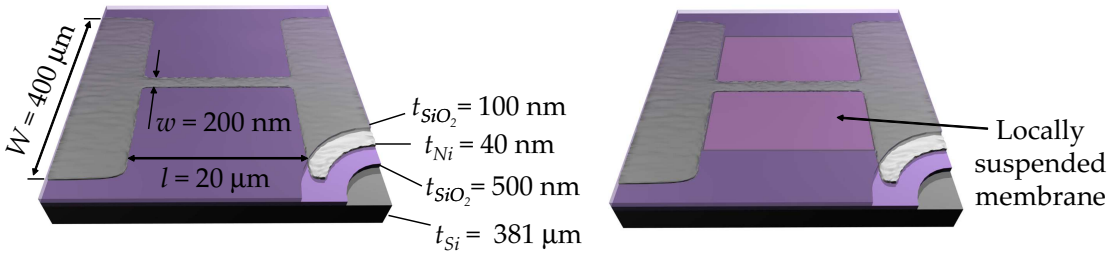

Figure 2.1: The dimensions of the nanowire configurations used in our FEM simulations. As shown in the right figure, simulations were performed also for the case in which the silicon underneath the nanowire was removed. In this case, the nanowire was supported by a thin membrane composed either of only silicon dioxide or of a combination of silicon dioxide and silicon nitride.

technologies, we knew that this could be realized by the removal of the silicon underneath the nanowire and the silicon dioxide layer. Such processing typically leaves a suspended silicon dioxide membrane on top of plain air. The existence of only air and a thin oxide membrane provides a very low thermal conductivity under the nanowire.

Above the nanowire, two alternatives in particular were identified. The nanoheater device will potentially be applied in dry or liquid conditions. In other words, the material on top of the nanowire will typically be a water-like fluid (liquid conditions) or an air-like gas (dry conditions).

In order to create the virtual object, a two-dimensional geometry was initially drawn (Fig. 2.2). In order to simplify the model, the existence of two symmetry lines in the structure was recognized and modeling was done on one quarter of the structure only. The 2D geometry was then extruded several times into a 3D space to create the three-dimensional object shown in Fig. 2.3 . In the bottom of the model, a 50 μm thick block of silicon was created. Parts of this silicon block could be changed to air in order to simulate the case where silicon is etched away. On top of the silicon block, a 500 nm thick layer of silicon dioxide was defined followed by the 40 nm thick nickel structure. Finally, a passivating 100 nm thick silicon dioxide layer and a 30 μm thick block of air/water were created.

Physics of the model

When a voltage is applied to the structure, Joule heating occurs throughout the nickel nanowire and the nickel pads. The heat thus generated is spread from the points of generation to the rest of the sample. The heat transfer through the device can be described by Fourier's law relating the heat generation per unit volume with the power losses per unit volume due to conduction, convection and radiation.

Because of the low temperature range intended for the heater (mainly below 100°C), the radiation losses were considered negligible [196]. Moreover, considering the small characteristic size ($<$ 100 μm) of the chamber on top of the nanowire structure (in a typical microsystem) as well as the absence of an externally imposed flux, the convection losses were also assumed to be negligible. This left us with a simplified and more manageable thermal description of the system which largely depended on the power input for the heat generation and the thermal properties of the materials and the system

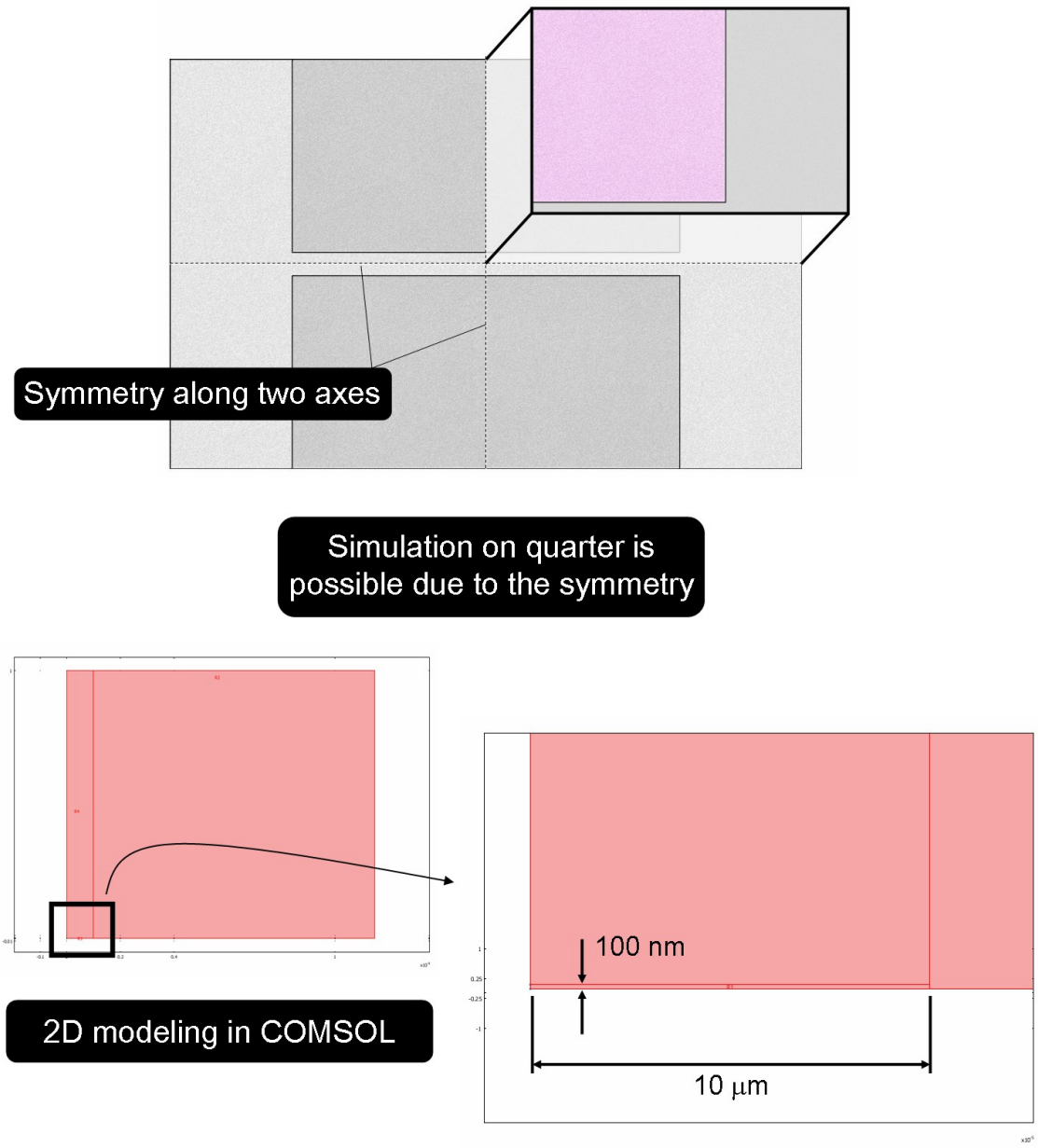

Figure 2.2: Two-dimensional sketch of our nanowire structure realized with the COMSOL interface. Symmetry lines were identified in both horizontal and vertical directions making it necessary only to model a quarter of the structure.

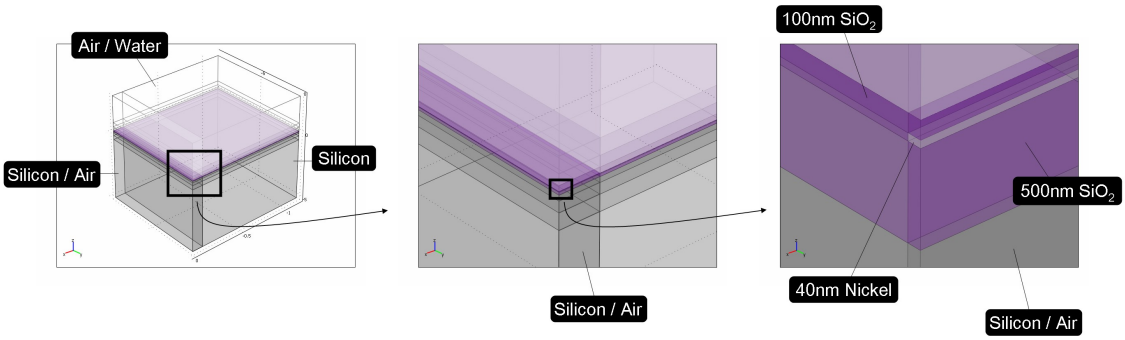

Figure 2.3: Extrusion of the 2D geometry into the 3D space allowed for a simple creation of three-dimensional object. The properties of the various parts could be individually modified by the designation of specific parameters, e.g. thermal conductivity and electrical properties.

Table 2.1: Material parameters concerning the resistive heating and heat transfer.

Material	Nickel	Silicon	SiO_2	Water	Air	SiN_x[a]
Thermal conductivity ($W \cdot m^{-1} \cdot K^{-1}$)	90	130	1.4	0.62	0.026	20
Specific heat capacity ($J \cdot kg^{-1} \cdot K^{-1}$)	450	700	730	4200	1010	700
Density ($kg \cdot m^{-3}$)	8900	2330	2200	995	1.2	3100
Electrical resistivity (ohm·m)	$6.9 \cdot 10^{-8}$	-	-	-	-	-
Temperature coefficient (K^{-1})	0.0059	-	-	-	-	-

[a] Represented in the simulations by Si_3N_4

boundary conditions for the power losses. While making these simplifications, it should be noticed that convection losses may indeed play a certain role in those cases where paths for conductive heat losses are limited. Among the structures we present here, this is mainly the case for the suspended membranes, where convection might increase the power dissipation.

In COMSOL version 3.3 an extensive library of material coefficients is included, covering those materials being employed in our case. While some of the coefficients are slightly temperature dependent and also defined as such in COMSOL, representative values of the parameters used are given in Table 2.1. In the case of nickel, which is to be resistively heated, the electrical resistivity and the temperature coefficient of the resistivity are also of high importance.

The heat generation in the sample occurs entirely in the nickel structure by resistive heating. The amount of resistive heating in each finite element depends on the electric potential drop throughout the element. In the FEM model it is thereby related on one hand to the externally applied current and on the other hand on the resistivity of the metal structure. In the simulations, the fact that the resistivity of metals depends on the temperature was taken into account. The temperature dependent resistivity, $\rho(T)$, can be described by the following formula:

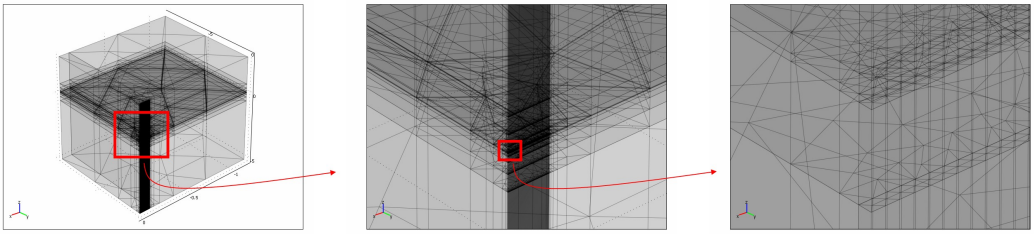

Figure 2.4: A 3D mesh was created to allow for the finite element analysis. The element size is smallest at the nanowire and in its vicinity.

$$\rho(T) = \rho_0(1 + \alpha T) \tag{2.1}$$

where ρ_0 is the resistivity at $T_0 = 20°C$ and is the temperature coefficient of the electrical resistivity. For nickel, the values for the electrical resistivity and the temperature coefficient are $\rho_0 = 6.9{\cdot}10^{-8}$ ohm·m and $\alpha = 0.0059$ K^{-1}, respectively.

Mesh generation

In order to make the mesh structure easy to handle for the computer, a 2D mesh was first created on the top boundary. A minimum element size of 100 nm was defined for the nanowire part in order to assure a good element quality at this essential part of the model. A 3D mesh was subsequently created by sweeping the 2D mesh downwards through the entire volume (see Fig. 2.4) . By the use of the sweeping function, the complexity of the mesh was lowered. This decreased the computer power required for the solution at the expense of the element quality. This trade-off was especially valuable in the transient analysis of the system, where the liberation of extra computer resources is particularly important.

Boundary conditions

As for the outer side boundary conditions of the model, we assumed ambient temperature (30°C) at the interface between the silicon substrate and the surroundings. A temperature of 30°C was also defined at the bottom boundary, assuming here that the sample is placed on a temperature control stage which maintains a constant temperature. Along the symmetry boundaries, thermal insulation was defined since by definition no thermal energy exchange occurs there. On the top boundaries, i.e. between the medium above the nanowire structure (air or water) and the microchamber ceiling, we assumed an outward heat flux. The heat flux was modeled using a heat transfer coefficient, h, giving the heat flux as the power loss per area unit and per °C of temperature difference between the inside and the outside of the boundary [$W{\cdot}m^{-2}{\cdot}°C^{-1}$]. In the case of the air-ceiling interface, a heat transfer coefficient $h_{air} = 5$ $W{\cdot}m^{-2}{\cdot}°C^{-1}$ was used while in the case of the water-ceiling interface $h_{water} = 20$ $W{\cdot}m^{-2}{\cdot}°C^{-1}$ was used.

2.1.2 Steady-state analysis

As we analyzed the simulated temperature distributions in our system, we were particularly interested in the temperatures obtained at the interface between the passivating

oxide and the medium above (air/water). The temperature at this interface is interesting since it is the most likely location of a molecule in the potential applications of the nanowires as sensors and heating elements. As will be explained in Chapter 3, it is also the location of the fluorescent probes when performing the fluorescent thermometry. In Fig. 2.5 and Fig. 2.6, the resulting temperature distributions on the oxide-air/water interface in the four cases identified previously are shown. These results were obtained when passing a constant current of 2 mA through the nickel structure. In Fig. 2.7, the result of increasing the current to 5.5 mA in the case of a bulk-air configuration is shown in order to demonstrate the small influence of the applied power on the characteristic temperature distribution.

Confined and flat temperature profile on silicon

The most striking observation that can be made from these results is the difference in the confinement of the temperature changes when altering the material underneath the nanowire. In the case of a nanowire on top of bulk silicon, the confinement is very high, regardless of the medium on top of the wire. In the case of a nanowire on top of a suspended membrane on the other hand, the temperature increases also at considerable distances away from the wire itself. The explanation for this is the large difference in thermal conductivity between silicon and air. While air isolates the wire very well, the silicon is highly efficient in dissipating the heat that is introduced to the system. Furthermore, since silicon has a higher thermal conductivity than nickel, a larger fraction of heat is dissipated to the silicon substrate than through the nickel wire, which leads to a very flat temperature profile along the wire.

High power dissipation through silicon

The second observation to be made is the large difference in the temperature values obtained when the same current is passed through the different structures. In the case of a membrane-air configuration, the maximum temperature lies above 300°C while for the nanowire on bulk silicon and water on top the maximum temperature is only slightly above 40°C. Evidently, this is due to the fact that silicon is a much better dissipation medium for heat than air. To keep power consumption at low levels it thus favorable to use a nanowire on top of a suspended membrane. In order to reach a maximum temperature above 300°C in the case of a nanowire on bulk silicon, a current of 5.5 mA had to be applied, resulting in a power consumption of 7 mW compared to the power of 0.8 mW for the nanowire on a membrane.

Temperature dependent resistivity

Another interesting feature to point out is that in order to maintain the same current of 2 mA, the different structures requires different voltages. Although there is nothing revolutionary about this observation,[1] it is indeed an effective demonstration of the impact of temperature on the resistivity. The higher the temperature becomes, the more the resistivity will increase, thus requiring a higher voltage to maintain a constant current. The main interest of this temperature dependence is that the resistivity eventually could be used as a simple mean to monitor the average temperature of a nanowire heating element.

[1] The reason for this is simply that we told the software to take the temperature coefficient α into account.

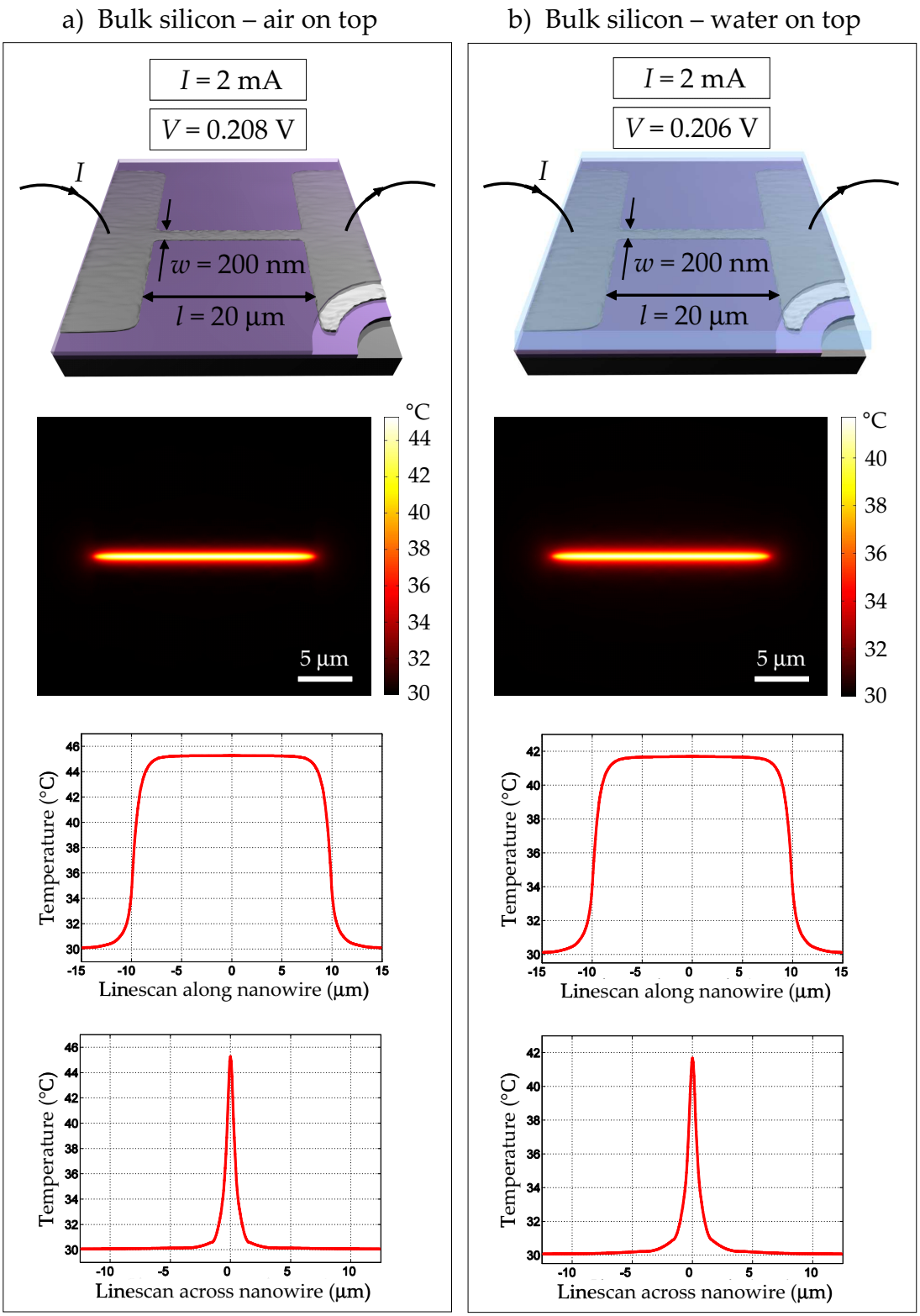

Figure 2.5: Simulation results for a nanowire on bulk silicon in a dry environment (a) and in a liquid environment (b). In both cases, a current of 2 mA was applied. Since the resistivity was temperature dependent, the resulting voltages were not the same for the different cases. The top images show schematics of the geometries used. The second row shows the temperature distributions at the interface between the oxide and the medium above. Finally, the third and fourth rows show linescans along the middle of the nanowire and across the the center of the nanowire, respectively.

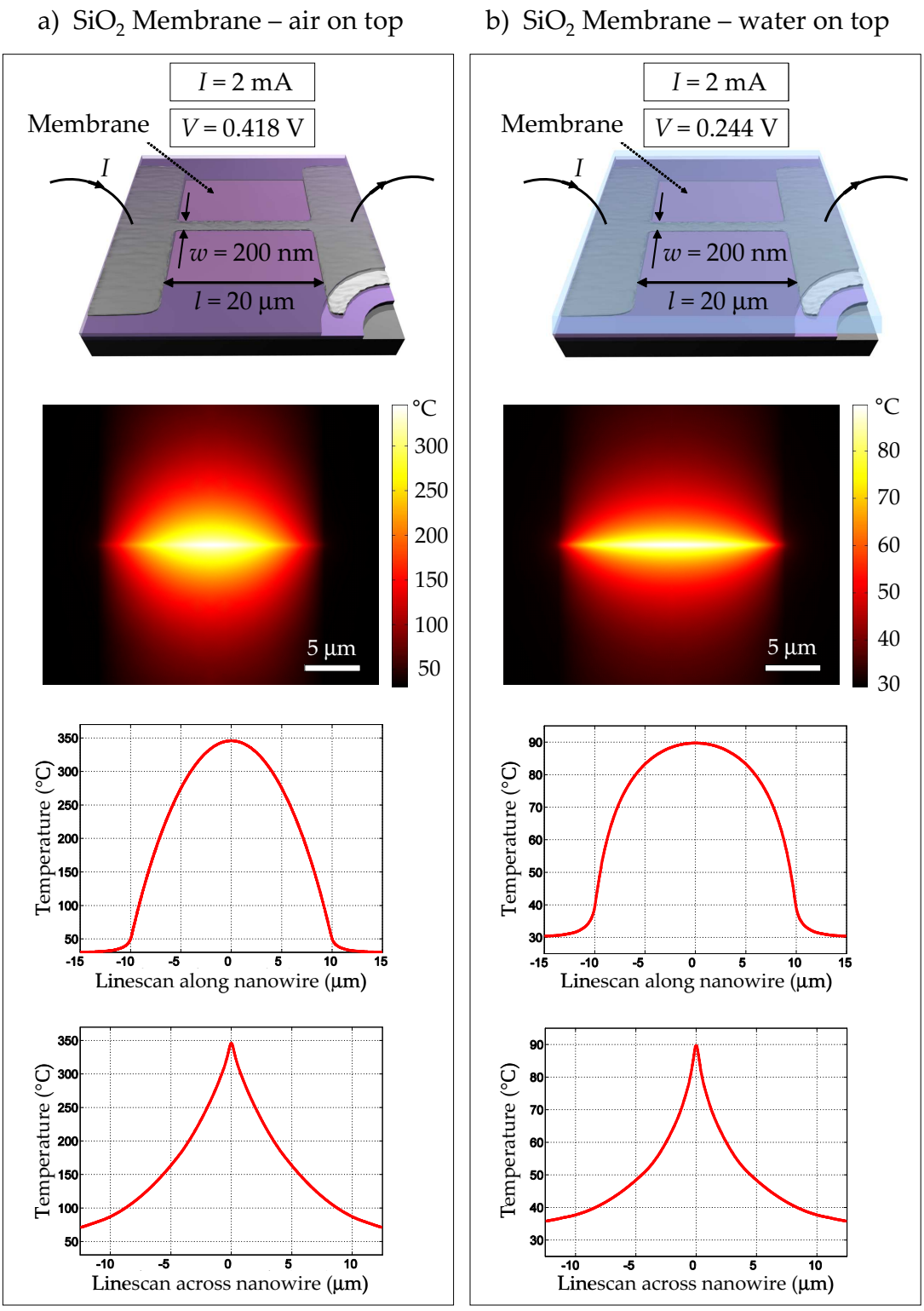

Figure 2.6: Simulation results for a nanowire on a suspended SiO_2membrane in a dry environment (a) and in a liquid environment (b). In both cases, a current of 2 mA was applied. Since the resistivity was temperature dependent, the resulting voltages were not the same for the different cases. The top images show schematics of the geometries used. The second row shows the temperature distributions at the interface between the oxide and the medium above. Finally, the third and fourth rows show linescans along the middle of the nanowire and across the the center of the nanowire, respectively.

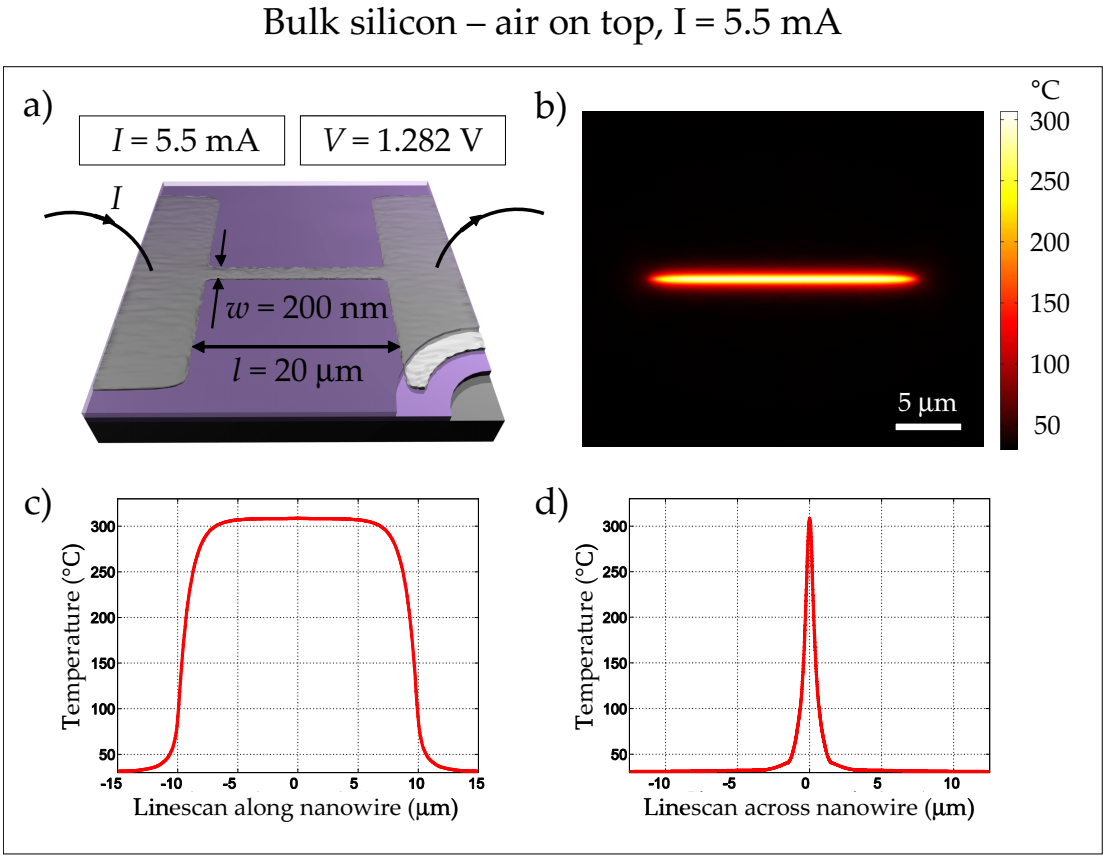

Figure 2.7: Simulation results for a nanowire on bulk silicon in a dry environment. a) Geometry of the sample and the applied current and resulting voltage. b) Temperature distribution at the interface between the oxide and the air. c) Linescan along the middle of the nanowire. d) Linescan across the center of the nanowire. Except for the applied current, which here is 5.5 mA, the parameters are the same as in Fig. 2.5a.

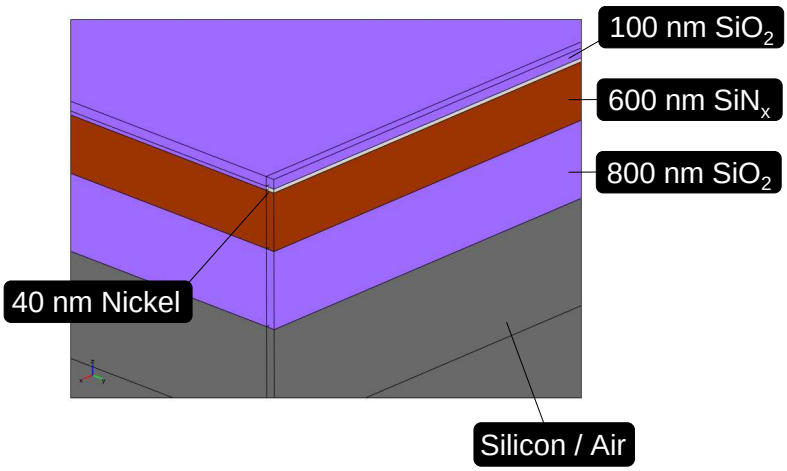

Figure 2.8: In order to study the influence of the membrane composition on the temperature of the system, the previous FEM geometry was modified as shown in this figure. The previous SiO_2 membrane (500 nm thick) was replaced by a SiO_2/SiN_x membrane (800 nm / 600 nm thick).

2.1.2.1 Influence of the membrane composition

The previous section described a simulation regarding a nanowire on top of a standard oxidized silicon wafer. However, as shall be explained in the fabrication section of this chapter, the use of pure silicon dioxide in the realization of suspended membranes is typically not a viable solution. Instead, suspended membranes are typically composed of two or more layers of different materials. The membrane composition that will be of interest for this thesis is the combination of 800 nm silicon dioxide and 600 nm silicon nitride (SiN_x). If we now take a quick look at the thermal properties of silicon nitride, we realize that it possesses a relatively high thermal conductivity (see Table 2.1). By introducing a layer of high thermal conductivity immediately under the nanowire heat source, it is reasonable to ask whether this will have a significant impact on the solutions found previously.

In order to shed some light on this matter, we decided to implement a FEM model based on a slightly modified geometry, introducing a thin silicon nitride layer underneath the nanowire. For simplicity, only the bulk-air and membrane-air configurations were investigated. The geometry of the new structure is shown in Fig. 2.8. Except for the membrane composition, all dimensions were identical to those used in the previous simulations.

The results of the simulations on the modified structures are shown in Fig. 2.9. To simplify the comparison with the case where no SiN_x was used, the linescans from Fig. 2.5a and Fig. 2.6a (nanowire on pure SiO_2 membrane in dry conditions) are included. Additionally, the curves from those figures are normalized with regard to the maximum value of the SiN_x-curves. In other words, the comparison is valid in terms of the characteristic temperature distributions but not in terms of absolute temperature values.

In the two cases shown in Fig. 2.9, a constant current of 2 mA was applied. As can be seen, the temperature changes are less confined compared to the case where no silicon nitride was present underneath the nanowire. This is particularly evident

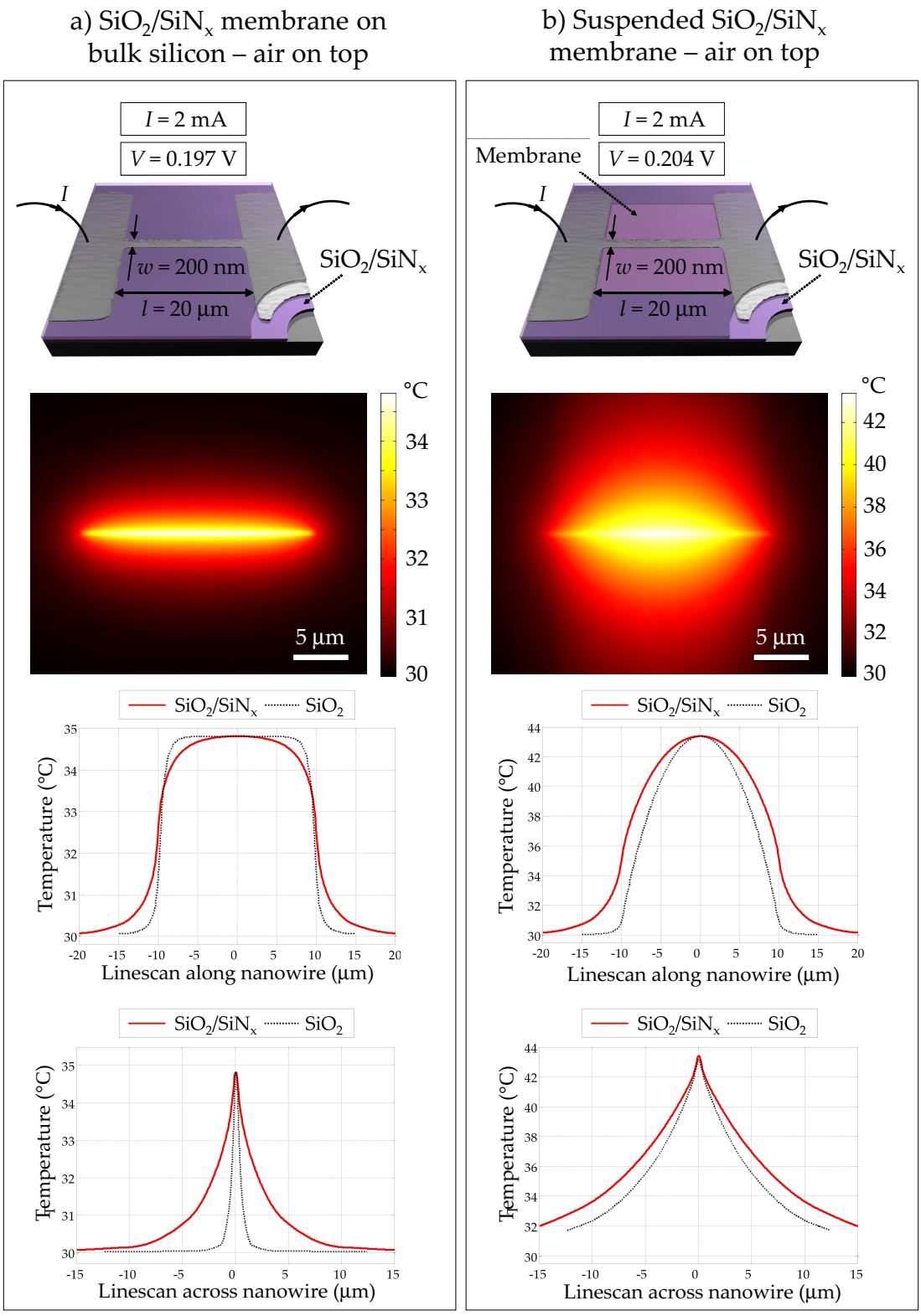

Figure 2.9: Simulation results for a nanowire on an unsuspended (a) and a suspended (b) SiN_x/SiO_2membrane in a dry environment (air). In both cases, a current of 2 mA was applied. The top images show the geometries used. The second row shows the temperature distributions at the interface between the membrane and the air. Finally, the third and fourth rows show linescans along the middle of the nanowire and across the the center of the nanowire, respectively. The linescan graphs include normalized results for the corresponding cases (same geometry and current) for a pure SiO_2membrane.

for the unsuspended SiN_x/SiO_2 layer. If we consider the cross-section plots for the unsuspended SiN_x/SiO_2 membrane, we can also establish that the temperature along the wire in this case is less uniform with a slightly more parabolic shape than for the pure SiO_2 membrane. These results are not surprising, considering that the introduction of a high thermal conductivity layer (SiN_x) underneath the nanowire could be expected to increase the lateral heat transfer.

2.1.3 Transient analysis

Apart from understanding the spatial temperature distributions, there is also particular interest in evaluating the temporal response of a heating device. As discussed already in the introduction of the thesis, the possibility to provide fast response and stabilization times upon resistive heating holds promise for improved efficiency and accuracy in for example fundamental molecular studies. Potential applications lie, for example, in the study of molecular relaxation times by temperature modulation [28,197] and electrochemical analysis of molecules by temperature pulse voltammetry [29–31]. Consequently, we decided to use our finite element model also for the temporal characterizations of the various nanowire configurations.

2.1.3.1 Basic heat transfer considerations

The time it takes for thermal changes to happen can be derived from Fourier's law, which governs the behavior of general heat transfer.[2] In order to broaden the understanding of the transient thermal behavior, various models can be used. Computer-based FEM analysis is clearly a powerful alternative and will be presented below. However, before going into the computer-aided simulations, we will consider the basic principles governing the transient behavior of a thermal system. An interesting analogy of the thermal system can be made with an electrical system. The two systems, thermal and electrical, are governed by the same general equations. By a closer look on how these systems respond to changes of the equilibrium, we can get an indication of what the time constants of our thermal system will look like.

If we consider the sketch in Fig. 2.10, the similarity of our device with a simplified electrical circuit is obvious. The thermal device can be represented by a simple first-order system, consisting of three components: a point of heat generation, some capacity to store the heat and an outward heat flux away from the system.

The heat capacity of the system is capable of holding heat to some extent and is analogous to the capacitor in the electrical circuit. The heat of the thermal system is analogous to the charges of the electrical system. As the resistive heating is turned on, heat is built up in the system to the maximum heat capacity until the thermal resistance allows the heat to leave the system at the same rate as it enters.

By blocking the heat inside the system from flowing out, the thermal resistance is equivalent to the resistor of the electrical circuit. The heat flow through the insulation (equivalent to charge flow through the resistor) increases as the temperature inside the system increases. The thermal resistance is determined by the possible paths of heat

[2] However, for systems with a characteristic size near the phonon mean free path, Fourier's law is not valid. Our systems have a characteristic size of a few hundred nanometer and is assumed to follow Fourier's law.

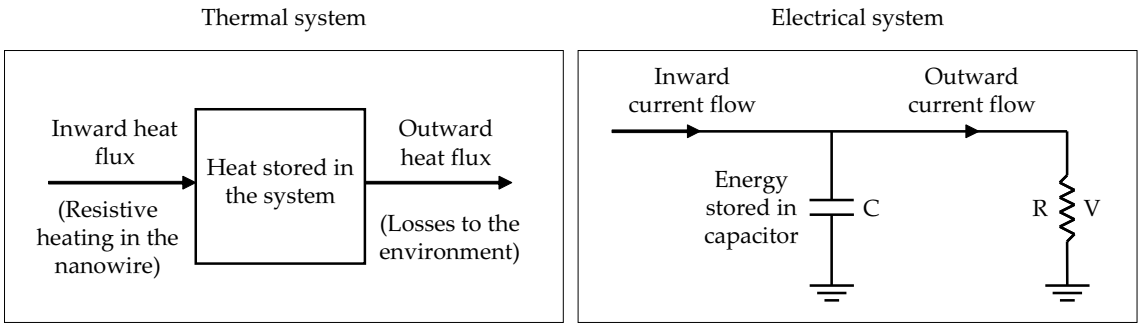

Figure 2.10: Thermal and electrical systems are governed by the same equations. Analogies can therefore be made between their behavior, e.g. in terms of resistance, capacitance and temporal behavior.

loss, i.e. conduction, convection and radiation. In our system we have simplified the losses by saying that the radiation is negligible. Furthermore, the convection losses are considered small in the system and are lumped together to be represented by losses at a certain rate at the system boundaries. Thus, the most significant contribution to the thermal resistance in our system is that of the thermal conductivities of the various materials.

Being governed by the same equations, the two types of systems react equivalently also in terms of temporal behavior. In electrical systems, a time constant is typically used to describe the response of a system to changes in the equilibrium states. The time constant can be conveniently estimated by multiplying the resistance with the capacitance of the system. The same approach can be used for the calculation of the time constant of the thermal system by simply multiplying the thermal resistance with the thermal capacitance of the system:

$$\tau = R \cdot C \tag{2.2}$$

In the case of our system, if convection and radiation transfer of the heat are considered negligible, the thermal resistance can be estimated from the thermal conductivities and the spatial extent of the different materials involved. Regarding the capacitance, it is determined by the densities, the volumes and the specific heat capacities of the materials involved. By changing one or more materials, significant changes in resistance and capacitance are introduced. For example, considering the values of Table 2.1, we expect that the replacement of silicon with air can be expected to slow down the response of the system.

2.1.3.2 Response times – FEM simulations

As we perform transient analysis using a FEM model, the basic concepts described in the previous paragraph are applied to the ensemble of finite elements. With this more complete definition of the system being possible with computer-aided simulations, a more accurate prediction of the temporal response can be expected with the FEM approach.

Since the temporal behavior of the thermal response is largely dependent on the heat capacitance of the system, the specific heat capacities and the density values of the different parts had to be added in the model before running the transient analysis. Apart

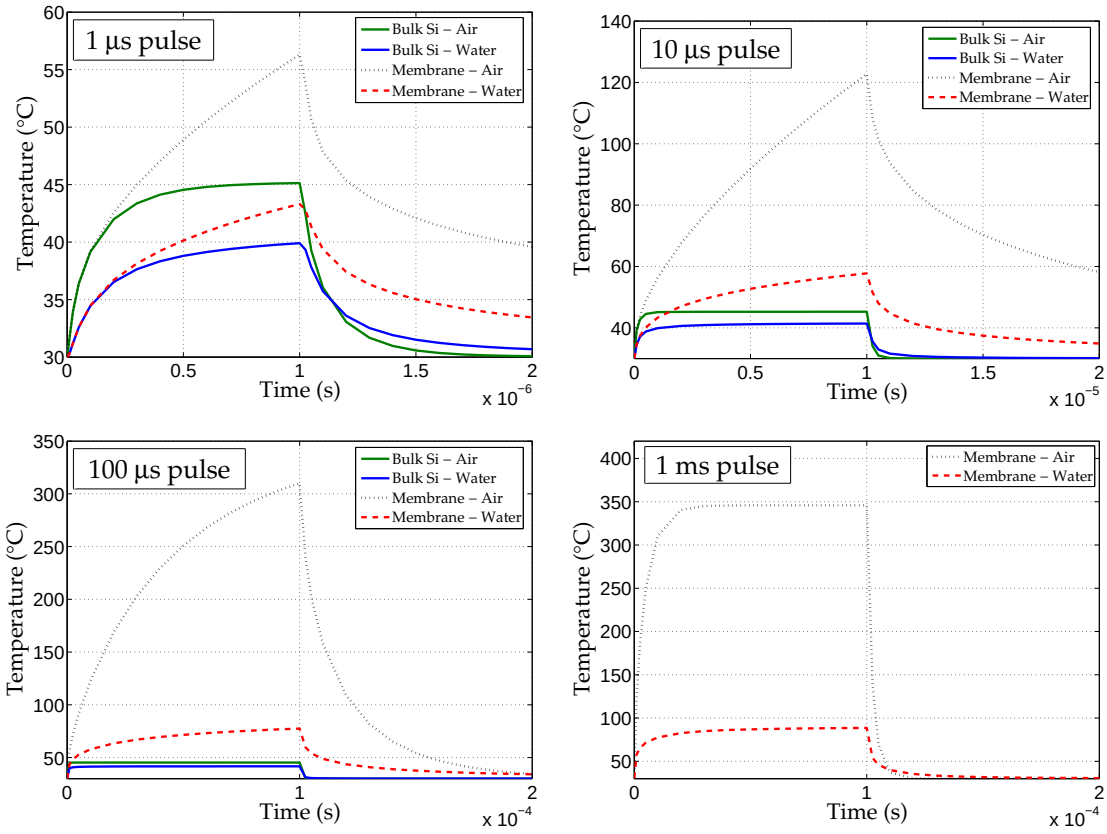

Figure 2.11: Temporal response of the temperature on top of the center of the nanowire and at the interface between the passivating oxide and the medium above (air or water). In the four graphs, four pulse durations of the electrical current were used, ranging from 1 μs to 1 ms (the pulse duration is indicated in the top left corner of each graph). It is clearly observed that the use of a suspended membrane structure gives a slower response. However, the difference of using air or water on top of the structure is not as clear.

from this addition of material parameters, no particular changes or enhancements of the steady-state model were required.

The transient analysis in COMSOL was performed by defining a number of times at which the state of the system should be determined. It was also possible to define when a certain parameter, e.g. resistive heating, should be turned on and off[3]. This presented us with a relatively simple approach for the study of the thermal response of our systems to square current pulses.

In Fig. 2.11, the thermal response to electrical current pulses of different durations is shown. The analysis was in all cases performed at the center of the nanowire on top of the passivating silicon dioxide layer. The graphs clearly show the impact of changing the material underneath the nanowire. The use of silicon underneath implies the use of a very low thermal resistance, which consequently leads to fast equilibration times.

The approximate time constants of the different cases were determined from the

[3]This is done simply by adding the command *(t<t_{stop}) after the parameter entry. This expression will equal 1 as long as it is true and 0 when it is false. t_{stop} should be replaced in the software by the desired stop-time value.

Table 2.2: Simulated thermal time constants for our nanowire systems.

SiO_2 membrane	
Bulk Si-Air	0.15 μs
Bulk Si-Water	0.32 μs
Membrane-Air	44 μs
Membrane-Water	42 μs
SiO_2 / SiN_x membrane	
Bulk Si-Air	0.42 μs
Membrane-Air	6 μs

simulations and are given in Table 2.2. The time constant was defined as the time at which the temperature had reach 67% of its final value.

By the use of silicon, time constants of below one microsecond were found. On the other hand, the use of air or water on top of the structure did not imply a considerable change in the time constant. According to the formula of equation 2.2 and the heat capacities and densities given in Table 2.1, it might be expected that the high heat capacity of water should slow down the response. This is true in the case of the unsuspended membrane configuration but not for the suspended membrane. The reason for this difference is likely to be the difference in the main heat dissipation path. For the nanowire on bulk silicon, the main heat losses occur downwards through the silicon whereas for the membrane configuration the main dissipation path is via the nanowire ends. When using water, which has a higher thermal conductivity than air, the dissipation towards the nanowire ends is facilitated. This leads to a lower total thermal resistance. This effect is big enough to compensate for the higher heat capacity of water.

2.1.3.3 Influence of the membrane composition

Similar to the steady-state simulations, we were interested in knowing the influence of using a membrane partly composed by silicon nitride on the temporal behavior. Since the thermal conductivity of silicon nitride is higher than that of silicon dioxide and since the membrane thickness is different (see section 2.1.2.1), the time constant may evidently be affected.

As indicated in Table 2.2, the time constant for the suspended membrane is about 6 microseconds, i.e. almost one order of magnitude faster for the SiO_2/SiN_x membrane than for the pure SiO_2 membrane. We understand why this is by once again recognizing that the main dissipation channel for the heat is through the silicon at the ends of the nanowire. The introduction of silicon nitride increases the thermal conductivity towards the ends which leads to faster response times.

On the other hand, for the unsuspended membrane, the response for the SiO_2/SiN_x membrane is slightly slower. This is because in the unsuspended case, the silicon underneath the nanowire is the main dissipation path for the heat. When using a silicon

nitride based membrane, a larger thermal barrier is present between the silicon and the nanowire which leads to longer response times.

2.2 Fabrication of the nanowire heating device

In the previously described FEM simulations, we got an idea of what thermal responses could be expected for various nanowire configurations. Of particular interest is the possibility to change the temperature confinement around a nanowire heater by changing the material underneath. One design, with a nanowire on top of silicon, provides high confinement and a flat profile of the temperature distribution while dissipating large amounts of heat to the underlying stage. The other design provides a less confined thermal impact on its environment but consumes considerably less power in order to reach the same maximum temperature. Furthermore, according to the transient analysis, the temporal response is faster when using a nanowire placed on silicon.

In order to verify that the simulated results are in fact valid in reality, it is of great importance to validate them by experimentation, i.e. by actually fabricating the nanowire structures and measuring the thermal behavior. It is of particular interest to do this in order to find out whether there is any kind of nanoscale-related phenomena that may affect the results that are predicted by heat transfer models originally developed for macroscale systems.

2.2.1 Nanowire fabrication

Several techniques exist for the fabrication of nanowires. In general, these are categorized into bottom-up and top-down approaches. Top-down approaches include techniques such as photolithography, electron beam lithography (EBL) and nanoimprint lithography (NIL) [198–202]. The main advantages of the top-down approaches are the ease of positioning nanowires at very exact locations and the possibility to produce large amounts of samples quickly and with a relatively low effort. Bottom-up approaches include techniques like the vapor-liquid-solid (VLS) growth [42, 43, 45, 203–208] and porous anodic alumina (PAA) templating [209–215]. Although the bottom-up approaches can provide better control of the nanowire structure, they present significant drawbacks in terms of positioning and connection to external devices.

2.2.1.1 Our approach: Top-down

If we now look at the structures that we wish to realize, we can establish that we do in fact need the possibility to precisely position our nanowires. We are interested in being able to quickly fabricate large numbers of our nanowire structures and to make them nearly identical each time. The thermal measurements are likely to require repeated experimentation on numerous samples throughout the development and optimization of the targeted fluorescent thermometry technique. Using a top-down approach, there is good potential for relatively quick fabrication of nanowires once the process has been established and optimized. Bottom-up techniques are not capable of this as of today.

To give a further motivation for choosing a top-down approach, the specific requirements of membrane fabrication should be mentioned. In order to realize a suspended membrane at the position of the nanowire, it is a great advantage if the positioning of the wire is well controlled. There are certainly ways to realize a membrane underneath

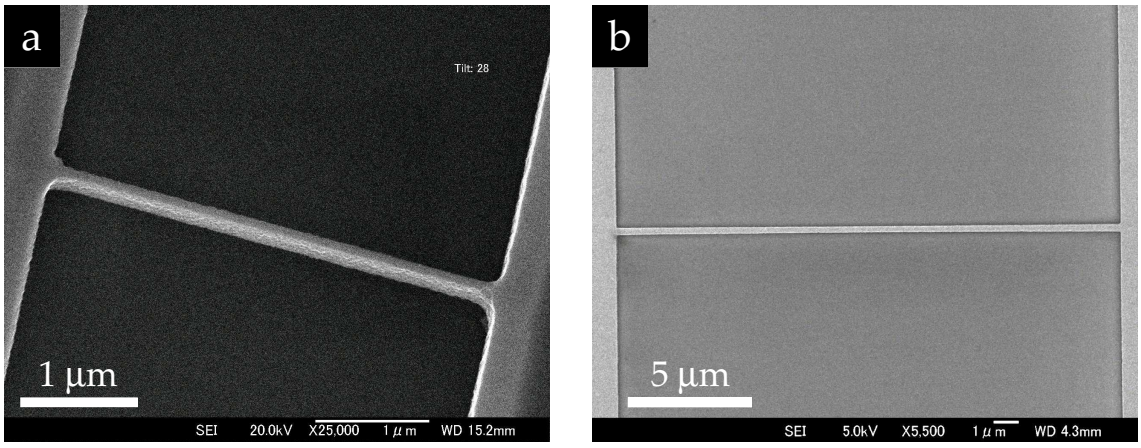

Figure 2.12: a) SEM image of a silicon nanowire fabricated by EBL patterning and dry etching of a SOI wafer. The length of the nanowire is 4 μm and the width 100 nm. This particular nanowire was release-etched from the substrate by removal of the buried oxide. b) SEM image of a nickel nanowire fabricated by EBL patterning and metal lift-off. The length of the nanowire is 20 μm and the width 200 nm.

a randomly deposited "bottom-up" nanowire, but compared to a top-down approach it would be limited in the choice of membrane fabrication technique and furthermore it would be difficult to produce many identical structures.

2.2.1.2 The EBL system

With the motives explained above, a top-down approach was thus chosen for the patterning of nanowires. Due to the relatively quick trial-and-error capability, direct writing in resist was applied using a high-speed electron beam lithography (EBL) system from Advantest Corporation (model F5112+VD01). This system allowed us to write nanostructures of down to 100 nm over entire wafers at a speed of one wafer (4 inch) per hour. Although EBL systems like this require extensive parameter optimization for each application, they are relatively well-performing once a specific process has been developed. Thanks to the direct writing capability, no masks were required and small changes to a nanostructure design could quickly be realized on a wafer.

2.2.1.3 Simplified fabrication protocol

In large, EBL was used in the development of two different nanowire structures, one for the fabrication of silicon nanowires and the other for the fabrication of metal nanowires. In Fig. 2.12, the typical looks of these two types of nanowires are shown. Due to the relative simplicity and lower cost of metal nanowire fabrication, this option was the one finally chosen for mass fabrication and application in the development of fluorescent thermometry. The following simplified protocol concerns exclusively the fabrication of metal nanowires, while the process developed for silicon nanowires is described in Appendix C. Appendix C also contains more detailed descriptions of the fabrication processes that were developed, including more details on the following protocol.

1. Silicon substrates The basic substrates used for the metal nanowire fabrication was either a <100>, 3-inch, 381μm-thick silicon wafer or a <100>, 4-inch, 525μm-thick silicon wafer. The larger 4-inch wafers were used for the development of a suspended membrane structure. The doping type and resistivity of the wafers were in both cases *p*-type and 10-20 Ωcm, respectively. Since the substrate did not take active part in the final device, the doping level had no significance other than the possible influence on EBL scattering effects and on the TMAH etch during membrane fabrication.

2. Nanowire design All structures that were to be patterned by EBL were designed using the Virtuoso module of the CADENCE software package. The designs were exported as stream files in the GDS format. The GDS files were subsequently converted to the BEF format, which is specific for the Advantest EBL system, and decomposed in the software Bexelwin before importing the design in the uTile software of the Advantest EBL system. The uTile software was used to determine the placement of the design on the sample and to define the exposure doses to be used on the different parts of the design.

3. EBL process Spin-coating and exposure of the EBL-specific resist ZEP 520A-7 (Zeon Corp.) was first performed and then followed by the development of the exposed resist in the developing solution ZED-N50 (Zeon Corp.). To assure the good adhesion of the resist to the surface, the adhesion agent HMDS was spincoated on the sample before depositing the resist. To remove possible resist residues that remained on the developed sample, O_2 plasma was used to carefully thin the resist before proceeding to the lift-off process.

4. Lift-off Evaporation of a 40nm-thick nickel layer was realized on top of the patterned resist. Subsequent lift-off of the metal directly transferred the patterned structure to the nickel layer. Since the Advantest EBL system allowed for the patterning of nanostructures as well as larger structures at very short timescales ($\sim$one wafer per hour), the connecting metal pads could be fabricated simultaneously with the nanowires.

5. Passivation In order to electrically passivate the metal structure, the deposition of silicon dioxide was a good choice due to the relative ease of deposition. Since deposition was done on top of metal and thus required a low process temperature, we were limited to two deposition methods. On one hand there was the PVD (physical vapor deposition) method sputtering and on the other hand PECVD (Plasma Enhanced Chemical Vapor Deposition). Due to the availability of sputtering equipment in our laboratory, this technique was chosen. In order to leave windows open in the oxide for wirebonding on the metal, the outer edges of the metal pads were temporarily covered with high temperature-resistant Kapton tape during the sputtering process.

2.2.1.4 Challenges in the fabrication process

A. Resist-related problems

The main requirement for the successful EBL-based fabrication of metal nanowires was the use of an EBL-specific resist that would give good results when used for lift-off processes. During the development of our fabrication process, several problems related

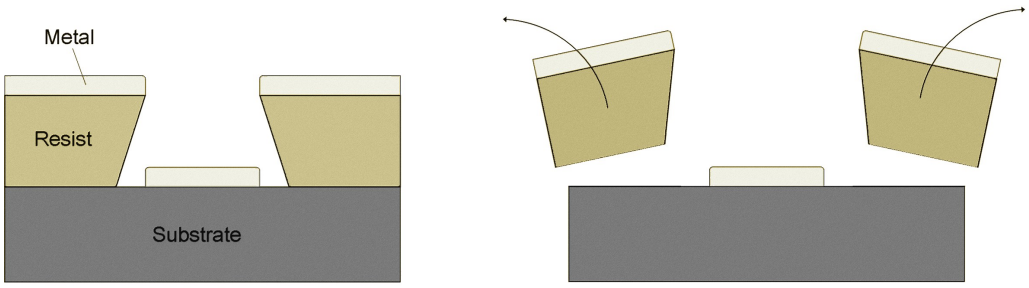

Figure 2.13: In the lift-off process, the resist edges should ideally be inclined inwards as shown in the left image. This increases the chances for a clean lift-off as shown in the right image.

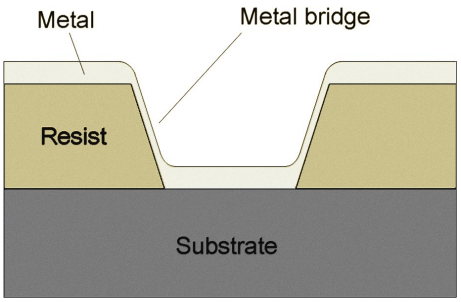

Figure 2.14: An example of a bad resist profile for lift-off is when the resist edges are inclined as in this image. When depositing the metal, the creation of bridges connecting the metal on the sample surface and the metal on the resist surface are very likely to occur. During the lift-off process, these types of bridges may deteriorate the resulting structure or prevent the lift-off to take place.

to the lift-off process were encountered. As shown in Fig. 2.13, the ideal resist for lift-off purposes should give an inwards inclination towards the uncovered sample surfaces. Such a profile allows for a clean lift-off where no unwanted removal of metal occurs. A typically unwanted resist profile is shown in Fig. 2.14. Such a profile makes the lift-off process difficult and normally does not allow for a good control of the resulting metal structures.

Although the resist used in our processes basically provided the desired profile, unwanted metal removal and difficulties in the removal frequently occurred. In the following, the resist-related problems will be discussed in further detail.

Resist residues After the development of the EBL resist, residues of the resist typically remained on the surface (see Fig. 2.15). This was problematic for the lift-off process, particularly because our metal layers were very thin. During lift-off, it happened that residues participated in removing metal that was not intended to be removed. Furthermore, even if unwanted metal removal did not occur at the time of the lift-off, swelling of the resist led to a delayed lift-off in some cases. This effect became apparent only some time after the fabrication. To get rid of the residues, it was efficient to expose the sample to a reactive oxygen plasma etch (sometimes referred to as ashing) for a short time (15 seconds in our case). This process lowered the height of the resist uniformly

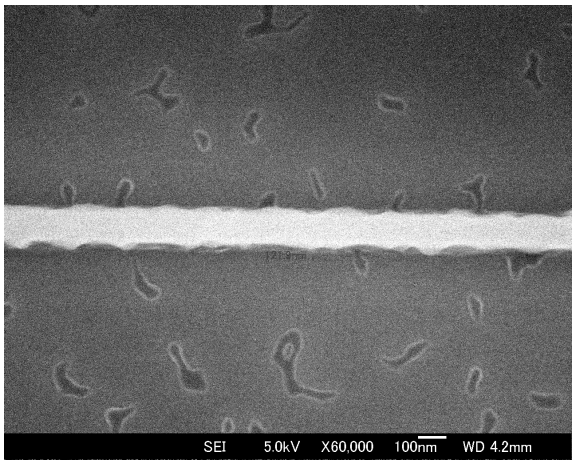

Figure 2.15: After development of the EBL resist, residues of the resist typically remained on the developed areas. Here, the residues are seen as random formations on both sides of the nanowire structure. To prevent negative effects in the subsequent fabrication steps, e.g. unintended lift-off, an O_2 plasma was used to remove the residues.

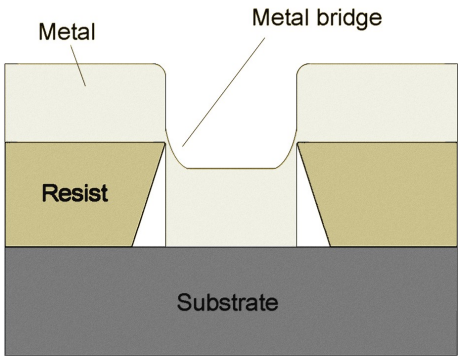

Figure 2.16: It case the EBL resist became too thin, e.g. by excessive application of O_2 plasma for residue removal, metal bridging typically occurred. This normally led to bad results during lift-off.

all over the sample.

Metal bridging While the complete removal of the residues required a certain etch time, it was important not to over-etch the resist. In those cases where too long ashing of the resist was performed, the resist became too thin and the metal on the bare sample surfaces were connected with parts of the metal on top of the resist (see Fig. 2.16). This complicated the lift-off process and even prevented it in some cases. In those cases where lift-off worked in spite of the metal bridging, the resulting metal structures typically presented unwanted geometrical features such as extra metal flakes randomly attached at the edges of the structure.

Resist adhesion problems Although some EBL resist manufacturers claim that their products work without the use of adhesive primers, it is necessary in certain cases to apply a primer such as HMDS to assure the good adhesion of the resist on the sample

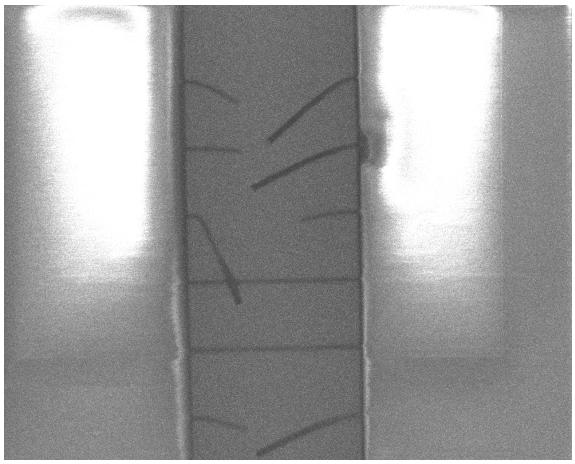

Figure 2.17: Nanowire structures patterned in ZEP 520A resist without the use of HMDS. The intended length of the wires was 4 μm and the width 100 nm.

surface. This is particularly true when patterning very small structures such as those nanowire structures shown in Fig. 2.17, where the fabrication of silicon nanowires was targeted. The intended length of the nanowires was 4 μm and the width was 100 nm. The image was taken by SEM after development of the exposed resist.

In the case of metal nanowire fabrication by lift-off, an inverted nanowire pattern was written in the resist, which meant that the resist adhesion problem was of less significance.

B. EBL-related problems

Stitching errors Stitching errors are related to the way that the EBL system accomplishes exposure of entire wafers. The wafer area is divided into several subfields which are treated serially, one after the other. Typical sizes of these subfields are on the order of 100x100 μm. In the specific case of the Advantest EBL equipment at the University of Tokyo, the size is 80x80 μm. As the system proceeds through the subfields, there is no guarantee that the alignment between neighboring domains is satisfactory. The quality of the alignment depends on the calibration of the system and is normally done by especially trained engineers. While a badly calibrated system can give microscale errors at the subfield edges, a well calibrated system can keep these errors to a few tens of nanometer.

The best way to avoid problems with stitching is to make sure, if possible, that no nanostructures are located at the vicinity of subfield edges. EBL systems normally allow the user to visualize where in a design the subfield edges will appear. By the use of such a function, the design can be modified in a way which assures that no nanostructures are affected by stitching errors. Examples of stitching errors that occurred during the fabrication of our nanowires are shown in Fig. 2.18.

2.2.2 Fabrication of suspended membranes

The fabrication of suspended membranes is not a new concept in the micromachining field. Applications making use of suspended structures are typically seen in microheater elements used in for example gas sensors [32–34,216], PCR devices [3] and microthrusters

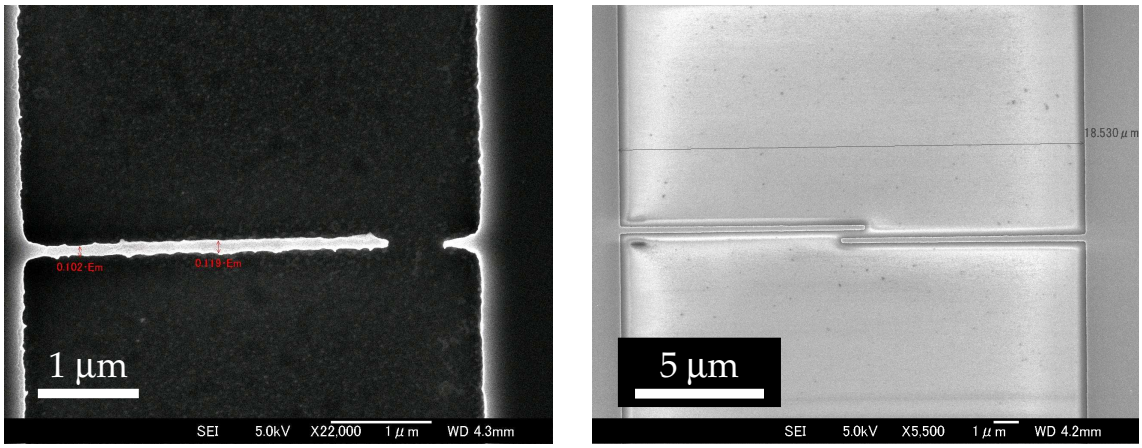

Figure 2.18: Examples of stitching errors in the case of nanowire fabrication.

[217]. Membranes are normally realized by the deposition of the membrane material on the sample followed by local etching of the sample from the back, thus releasing the thin membrane. One of the main challenges in producing the suspended membranes is the intrinsic stresses, either compressive or tensile, that exist within the membranes. The result of a bad design is typically a buckling membrane which easily breaks.

2.2.2.1 Membrane design

The common way of dealing with the intrinsic stresses of the membranes is to use a combination of thin layers made of different materials. By combining the right thicknesses of two materials of opposite stresses (compressive vs. tensile), the resulting observable behavior of the membrane will be that of a stress-free membrane. Within our work we have applied a membrane composition developed a couple of years ago at the LAAS-CNRS [217, 218]. In this process, a combination of silicon dioxide (SiO_2) and silicon nitride (SiN_x) films is used. A plain silicon wafer was first oxidized to render a 800 nm thick layer of silicon dioxide. On top of this oxide layer, 600 nm of silicon nitride was then deposited using a LPCVD process.

The specific challenge of our case was to create a relatively small membrane. The membranes presented in most published works have typical dimensions on the order of a few millimeters. Here, we sought to confine the membrane to an area with a characteristic size comparable to the length of the nanowire, i.e. a few tens of micrometers. In particular, in similarity to the FEM simulations, it was of interest to make the bulk silicon reach close to each end of the nanowire in order to help dissipate the heat upon turning off the resistive heating.

2.2.2.2 Back etching

In order to realize the removal of bulk silicon underneath the SiO_2/SiN_x layers, the classical method is to use one of the anisotropic wet etchants KOH (Potassium Hydroxide) or TMAH (Tetramethyl Ammonium Hydroxide). These etchants attack the silicon with a high selectivity regarding the crystalline planes of silicon, giving rise to pyramidal shapes (see Appendix D for details).

Since about the mid-90s, a process based on reactive plasma etching is also available

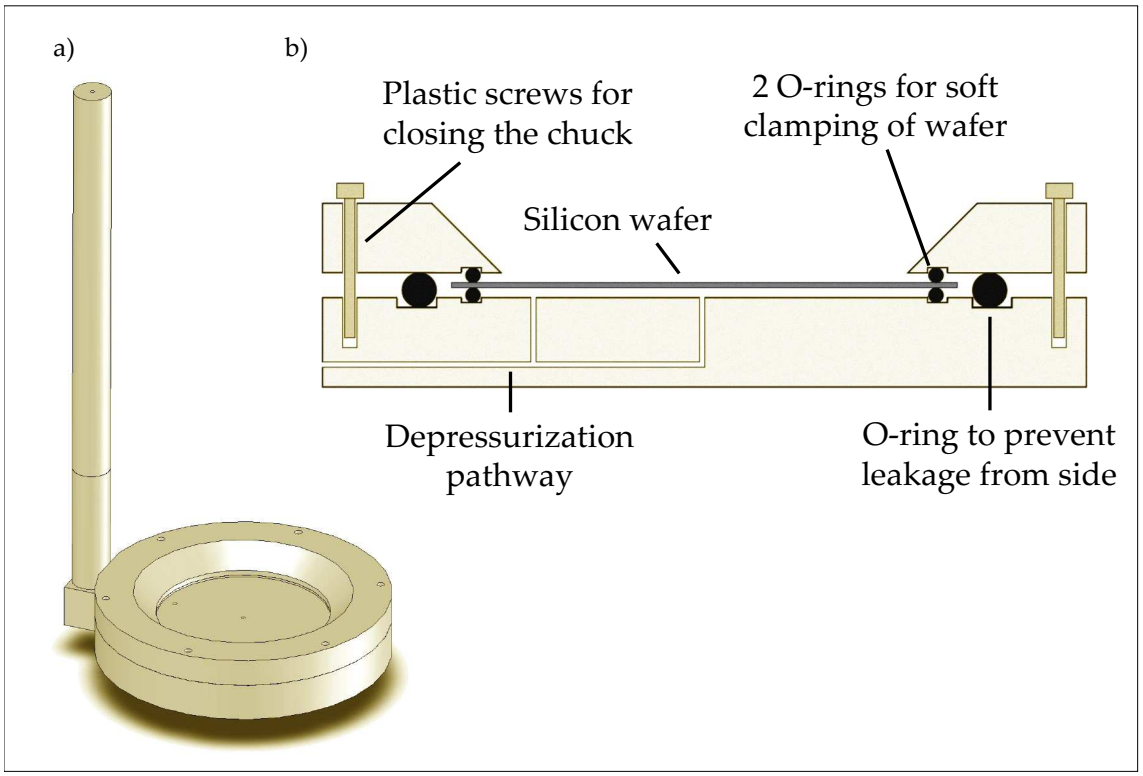

Figure 2.19: An especially made Teflon chuck was used to protect the front side of the wafers during the back-etch process by TMAH or KOH etchant. a) 3D view of the chuck after assembling the parts. b) Cross-sectional side-view of the two lower parts of the chuck.

for the etching of bulk silicon. This process is generally called DRIE (Deep Reactive Ion Etching). The technique allows for the realization of etching profiles without any tapering effect. While the process can be used to create deep holes of high aspect ratios in silicon, the etching rates are highly dependent on the width of the pattern to be etched, particularly for sizes below a few hundreds of micrometers. For the etching of narrow ($< 100\ \mu$m) holes through entire wafers (i.e. 400-500 μm), many DRIE systems do not perform well due to the bad exchange of reactive gases when the etched cavity becomes deeper. The process thus gives its most manageable and predictable results when used for large pattern etching.

The choice of etching method within this thesis was the use of TMAH and KOH etchants. Compared to DRIE, these etching methods were assumed to allow for better control in the fabrication of small suspended membranes ($< 100\ \mu$m). Furthermore, TMAH in particular is advantageous in terms of its lower etching rate of the membrane material. This means that the risk of removing some or all of the membrane is much less during a TMAH process. Furthermore, due to the existence of SiN_x from the preparation of a SiO_2/SiN_x layer, masking of the wafer backside is automatically taken care of for KOH and TMAH etching.

In order to allow for etching of the backside of our silicon without affecting the nanowire structures on the front side, a special chuck made of Teflon was developed (see Fig. 2.19). The mounting of a four inch wafer in this chuck allowed for the protection of the nanowires during long etching times and at the high temperatures (90°C) used

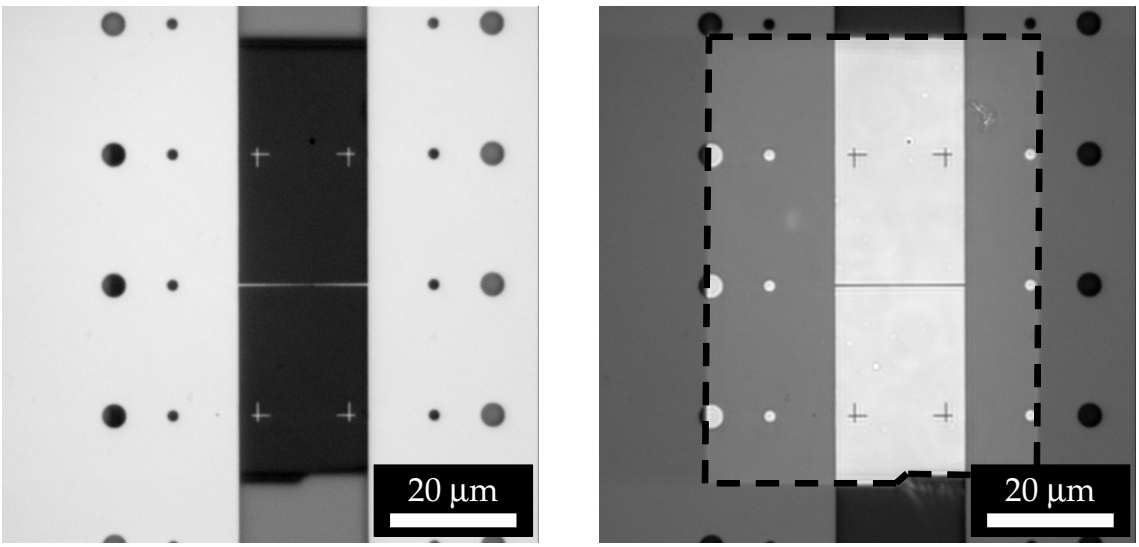

Figure 2.20: Optical microphotographs of a suspended SiO_2/SiN_x membrane. The left photograph was taken using only front illumination. The right image was taken using a combination of back and front illumination, which helped visualizing the membrane position. To further enhance the visibility of the membrane, a dashed line has been added to indicate its position. The circular patterns visible on the metal connection pads have no function except their use for alignment purposes during fluorescence analysis.

during the etch. Further details on this approach as well as the etching parameters are described in Appendix D. An alternative approach that is sometimes used for front side protection is the temporary gluing of a glass wafer on the front side using a special wax. However, the removal of this protecting wafer and wax can easily lead to damage of fine structures unless they are well protected (e.g. by a thick oxide).

A representative membrane structure fabricated with this process is shown in Fig. 2.20. By the use of an optical microscope with backlight function, the visualization of the membrane was made very clear. As can be seen in this representative microphotograph, the resulting membrane position was in many cases not perfect. Although the membrane ended up underneath the respective nanowire in almost all cases, the positioning with regard to the nanowire varied much. The size of the membrane was also quite difficult to control, with the membrane in all cases being larger than planned. As seen in the SEM image of Fig. 2.21, there were clear indications that the etching process did not occur appropriately. A comparison to a normally obtained pyramidal structure after TMAH etch is shown in the same figure. The rough and non-uniform etching profile is believed to be caused by an inefficient exchange of the etchant in the cavities being etched. This in turn was likely the result of bad stirring. Due to practical difficulties, stirring in combination with the use of the Teflon chuck was not perfectly implemented.

In spite of the unexpectedly large membrane sizes and the slightly misaligned positions, these nanowire structures were good enough for the purpose of our thermal investigations.

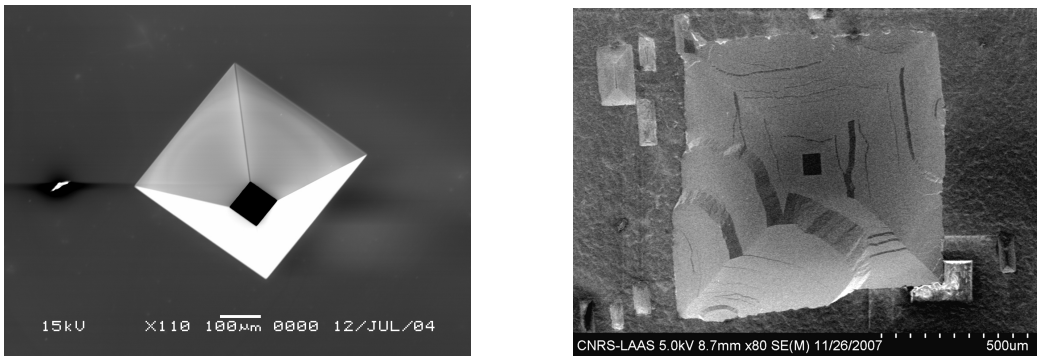

Figure 2.21: The left SEM image shows the result of a regular TMAH etching process. The pyramidal shape is clean and smooth. In the right SEM image, a representative result of the TMAH etch done in our Teflon chuck is shown.

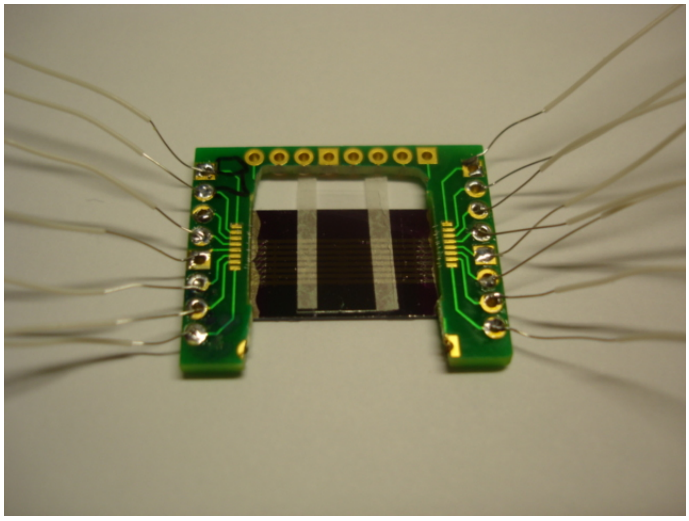

Figure 2.22: A nanowire sample assembled with a customized PCB board.

2.2.3 Mounting and connection of the nanowire devices

All nanowire structures explained above were batch fabricated on silicon wafers. Once the micromachining processes were completed, the wafers were diced into smaller pieces, typically of sizes 20x12 mm, each containing only a small number of nanowires. In order to avoid contamination of the wafer surfaces, a protective resist layer was spincoated on top of the wafer before dicing it. Each piece was then glued to a customized PCB board and connected to the pads of the PCB board using conventional ultrasonic-based wirebonding.

The PCB board contained a cavity in its center and was placed on top of the silicon piece. The placement below the PCB board was done in order to enable direct contact between the silicon piece and the temperature control stage which was used for the thermal manipulation of the sample. An example of a nanowire sample mounted on a PCB board is shown in Fig. 2.22.

2.3 Conclusions

In this chapter, we have addressed the thermal analysis of possible nanowire systems with a FEM-based simulation approach. The results of the simulated systems demonstrated above all that the thermal properties of the materials in the immediate vicinity of the nanowire can be expected to have a great impact on the thermal behavior of the sample. While the small size of the nanowire is the basic requirement for a high spatial confinement of heating, an appropriate design of the entire system is necessary in order to optimize both spatial confinement and response times. In particular it was seen that the positioning of the nanowire on top of a high thermal conductivity material, e.g. silicon, allows for better spatial confinement of the temperature changes and faster equilibration times when subjected to changes in the resistive heating. On the other hand, the achievement of high confinement and fast response is made at the expense of increased power dissipation through the substrate. It also requires the design to incorporate an effective heat sink on the backside of the sample which can continuously remove heat from the sample.

The choice of design should be considered with each specific application in mind. In the case where continuous heat is to be applied, the use of high thermal conductivity substrates such as silicon will inevitably lead to large total energy losses. The use of more isolated nanowires may in these cases be preferred, although it leads to higher distributions of the temperature changes and thus decreasing the possibility for the dense integration of several independent heaters.

In the case that fast response times are the highest priority, the use of high thermal conductivity substrates should be the preferable choice. This is particularly the case, if the heating is applied in pulses of short duration. In this case, the power dissipation is certainly high, but the total energy cost will be less significant due to the short duration of the pulses.

An interesting aspect of using a metal nanowire on a silicon substrate is the remarkably flat temperature profile that is achieved. The temperature is basically constant along the entire length of the nanowire. This kind of profile is appealing in applications such as molecular studies as it simplifies the positioning of the molecules on the nanowire. With the flat temperature profile, there is little importance to where a molecule adheres to the wire. In addition, many molecules sitting on different places on the same wire can with the flat profile be subjected to the same temperature changes.

In the second part of the chapter, the fabrication of the simulated nanowire systems was targeted. Two types of nickel nanowires were fabricated, the first one with nanowires on top of a conventional oxidized silicon wafer and the second one with nanowires on top of a locally suspended SiO_2/SiN_x membrane. Due to its relative simplicity, the EBL technology was applied for the realization of nanowire structures by top-down patterning. For the purpose of membrane fabrication, a back-side etching process based on the wet etchants TMAH and KOH was used. Although the membranes were generally larger than intended and not perfectly aligned under the nanowires, they were considered good enough to take part in the thermal studies of nanowire systems.

Summary of nanowire fabrication

A. *Metal nanowire fabrication*

1. **Wafer cleaning**
   (H_2SO_4:H_2O_2 and BHF)
2. **Thermal oxidation**
   For use in suspended membrane: 800 nm
3. **SiN_x deposition**
   (LPCVD, 600nm)
   Only for fabrication of suspended membrane!
4. **EBL patterning**
   a) *Rinse and dehydration*
   b) *Spincoating*
   (ZEP520A-7)
   c) *Prebaking*
   (180°C, 10 min)
   d) *Exposure*
   (120 C/cm^2)
   e) *Development*
   (ZED-N50, 1 min 30 sec)
5. **O2 ashing**
6. **Metal evaporation:**
   (Nickel, 40 nm thick)
7. **Lift-off**
   (ZDMAC, 60°C, 15 min)
8. **Surface passivation**
   (100 nm SiO_2 by sputtering or PECVD)

B. *Membrane fabrication*

1. **Fabrication of photo-lithography mask**
2. **Backside patterning**
   a) *Frontside spincoating*
   (protective layer: S1818 resist)
   b) *Baking*
   (90°C for 5 minutes)
   c) *Backside spincoating*
   (photoresist: S1818)
   d) *Prebaking*
   (90°C, 5 min)
   e) *Backside alignment & UV light exposure*
   f) *Development*
   (NMD-3, 30 sec)
   g) *Postbaking*
   (130°C, 5 min)
3. **Transferal of resist pattern**
   (SiO_2/SiN_x etching)
4. **Membrane release**
   (Silicon etching by TMAH/KOH)

C. *Final assembly*

1. **Dicing of silicon wafer**
2. **Mounting of sample on PCB board**
3. **Wire bonding**
4. **Soldering of wires**
   (for external connection)

CHAPTER 3
SELECTING A FLUORESCENT PROBE

In the previous chapter, we presented the theoretical considerations regarding the thermal behavior of nanowires in different configurations. Following simulations on the thermal characteristics of two designs in particular, nanowires on bulk silicon and nanowires on suspended membranes, the fabrication of these designs were addressed.

In this chapter, the first necessary steps towards a complete fluorescent thermometry approach will be illustrated. In particular, the evaluation of possible fluorescent probes will be presented. This evaluation deals with various stability issues, e.g. photostability and thermal stability, of the probes and provides us with the information needed to choose the most appropriate fluorophore for application in thermal characterizations. Further investigations that are presented concern the positioning of the fluorescent probes at the locations to be characterized.

3.1 Proposed improvements of fluorescent thermometry

A wide range of techniques are available for the thermal characterization at small scales. Recalling the review given in Chapter 1, the choice of fluorescent thermometry is advantageous due in particular to its potential for high spatial thermal characterizations in liquid environments. In addition, the use of fluorescent thermometry requires a relatively simple setup which is associated with relatively low costs.

Much of the work on fluorescent thermometry to this date concerns the thermal characterization of macro scale systems. Some of the most recent applications of the technique target temperature measurements in microfluidic channels. On the other hand, very few reports have addressed use of fluorescent thermometry for applications reaching the sub-micrometer scale. Considering that the fundamental limit of fluorescent thermometry is the diffraction limit, thus around a few hundreds of nanometers, there is indeed an interest to pursue further developments of the technique.

As compared to earlier work targeting for example temperatures in microfluidic channels, this thesis targets a method where temperature measurements are done specifically on the surface of a sample. To realize this, fluorophores are confined to the vicinity of a sample surface by depositing a layer of the fluorophores directly on the surface without dissolution in a liquid or a resin. Thus, the measured signal will originate completely

from the plane of interest. This is particularly advantageous when investigating temperature gradients of high spatial confinement. The alternative choice of using fluorophores dissolved in a resin or a liquid for the measurement of surface temperatures easily introduce measurement errors since the captured fluorescence originates not only from the surface of the sample and since the temperature is likely to show a gradient throughout the height of the resin or the liquid. In our case, considering the diffraction limit and the use of visible light, we can expect a potential spatial resolution below 500 nm.

3.2 Finding a fluorescent probe

The most important component of fluorescent thermometry is the fluorescence-emitting material used as a temperature probe. As shown in Chapter 1, there is a wide range of fluorophores with potential use for thermal characterizations. In the selection of a fluorophore, the most essential properties to consider are the following.

1. Temperature dependence This could be the temperature dependence of one or several peak intensities of the fluorescence spectra or the dependence of the fluorescence decay time.

2. Photostability Among those particles that possess a temperature dependent fluorescence, it is important that the fluorescence remains stable over time. Ideally, the only factor affecting the fluorescence should be the temperature. However, it is a well known fact that the fluorescence of many fluorophores is degraded under the influence of the excitation light. Many fluorophores also show a dependence on environmental parameters such as pH and the presence of oxygen.

3. Reversibility It is of special interest that the temperature dependence is stable and does not change every time the fluorophore is subjected to a temperature cycle. Instability of the temperature dependence leads to uncertainties in the interpretation of the fluorescence changes.

Within this work, two fluorescent probes have been investigated. The preliminary choice was the use of semiconductor nanocrystals, also known as quantum dots. The other compound that has been targeted is the organic dye Rhodamine B. Both of these fluorophores have in various articles been shown to possess a strongly temperature dependent fluorescence peak intensity [13, 66, 67, 144, 152, 157]. In the following sections, the investigations and evaluations made for the two fluorophores will be presented. For each fluorophore, studies on the fluorescence properties as well as the practical considerations, e.g. the deposition on a micro- or nanostructured surface, will be addressed.

3.3 Materials and solvents

3.3.1 Quantum dots

The specific quantum dots used in our study were the commercially available CdSe/ZnS nanocrystals from Qdot Corporation (now Invitrogen / Molecular Probes). For our investigations we made use of three differently coated CdSe/ZnS nanocrystals. Coated

nanocrystals were used in order to allow for easy handling and solubility. The coatings used were PEG, carboxyl groups or streptavidin. The purchased nanocrystals were diluted 100 times in a biological buffer at pH 7. The fluorescence emission peaks used were 655 nm, i.e. in the red band of the visible light, and 520 nm, i.e. the green band of the visible light.

3.3.2 Rhodamine B

Rhodamine B is a very commonly used fluorescent dye and is thus easily obtained through commercial sources. We purchased regular Rhodamine B as a powder from Sigma-Aldrich (CAS 81-88-9). This Rhodamine B is the sort which is typically used in thermometry applications. The powder is easily dissolved in plain water. For all our applications we dissolved the Rhodamine B powder in deionized water at a concentration of 100 μM.

3.3.3 Streptavidin – Rhodamine B conjugates

In order to enable the binding of Rhodamine B on the sample surfaces, a streptavidin-conjugated Rhodamine B complex was also purchased. This product was found at Molecular Probes (Cat. No. S871) and was delivered as a lyophilized powder. The lyophilized powder was dissolved in a phosphate buffer of pH 7.2, giving a solution with a weight concentration of 1 mg/ml. In order to facilitate the adhesion of streptavidin-Rhodamine B conjugates on the sample surfaces, poly-L-lysine was ordered from Sigma-Aldrich (Cat. No. P8920).

3.4 Setup for fluorescence measurements

All fluorescence measurements were made using a BX-51 upright fluorescence microscope from Olympus. Two different light sources, a conventional mercury lamp from Olympus and an EXFO metal halide lamp, were used. The metal halide lamp generally showed a better performance in terms of intensity stability and also allowed for a uniform illumination field due to the use of a liquid light guide for the connection to the microscope. Selection of the appropriate wavelengths for fluorophore excitation and fluorescence detection was realized by the use of fluorescence filters. Details of the fluorescence filters that we used are presented in Table 3.1 .

The intensity of the incoming light was adjusted by the use of neutral density (ND) filters which were placed in the optical path. The function of the ND filters was to lower the light intensity uniformly all over the spectrum. Standard ND filters from Olympus with transmission values of 6% and 25% were used. Furthermore, when using the EXFO lamp, the intensity could be adjusted stepwise directly on the lamp, with transmission values of 100%, 50%, 25% and 12.5%.

Imaging of the fluorophores was realized by the use of three different objectives, all purchased from Olympus. For low magnifications, a 20X NA0.46 objective was used. For higher magnifications, a 60X NA0.90 objective and a 100X NA0.95 objective were used. All objectives were made for use in dry conditions, i.e. without immersion oil or water as an optical medium. The 60X and 100X objectives had been manufactured and especially adapted for use with glass coverslips. All experiments at these magnifications were therefore performed with a glass coverslip mounted on top of the sample.

Table 3.1: Properties of the fluorescence filters that were used.

Fluorophore	Filter set	Excitation band	Dichroic filter transition wavelength	Emission band
Quantum dots 520 nm (Evident Technologies)	32254a filter set (Chroma Technology)	400-440 nm	470 nm	500-540 nm
Quantum dots 655 nm (Qdot Corporation / Molecular Probes)	XF305-1 filter set (Omega Optical)	402.5-447.5 nm	475 nm	645-665 nm
Rhodamine B	31002 filter set (Chroma Technology)	527.5-552.5 nm	565 nm	582.5-627.5 nm

In order to capture the fluorescence for digital analysis, an EMCCD (electron-multiplying CCD) camera from Andor was used. The EMCCD camera is a recent evolution of the conventional CCD devices. By accomplishing a gain on-chip before the captured signal is sent to the output amplifier, this technique allows for highly reduced readout noise. Although not necessary for large scale measurements where many fluorophores contribute to the signal, the EMCCD cameras are valuable for the capture of very weak signals.

Basic analysis of the acquired fluorescent images was performed in the commercial software IQ from Andor. Further processing of the images was done using mainly MATLAB from MathWorks. Some image treatment was also performed in the software MetaMorph and MetaVue from Molecular Devices and in the freeware ImageJ.

3.5 Assembly of the fluorophores on a surface

In the evaluation of the two fluorophores for the use as temperature probes, we wanted to investigate the properties in an environment similar to that of the final application, i.e. immobilized on the surface of a sample. It should be noted already that this is different from the classical applications of fluorescent thermometry where the probes are normally freely dispersed in a solvent or distributed in a polymer matrix. Furthermore, in a large part of our experiments, we use the probes in a dry environment, which is different from the normal use of most fluorescent probes.

In the following, various approaches for the immobilization of the fluorophores on the sample surface will be presented. Basically, two viable methods were found which worked relatively well both for the Rhodamine B and the nanocrystals. A third approach making use of electric field forces for the assembly of nanocrystals will also be shortly mentioned, although not used for our final applications.

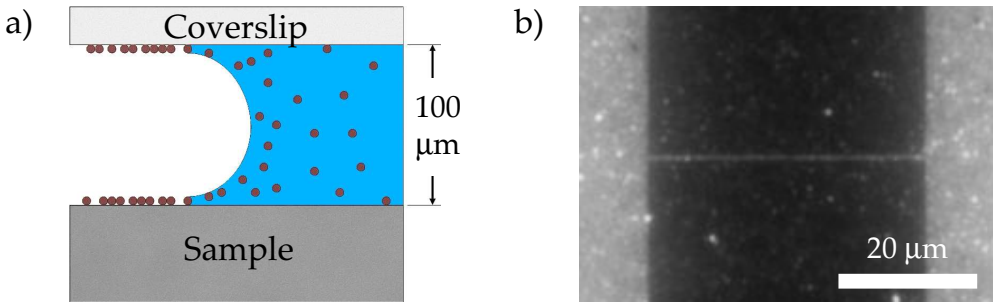

Figure 3.1: a) Principle of the deposition by drying. Upon evaporation of the solvent, the fluorophore is left on the surfaces of the sample and the coverslip. b) A fluorescent image showing the result of quantum dot deposition by drying on top of a passivated 40μm-long and 1μm-wide microwire.

3.5.1 Evaporation of solvent

A simple approach for the deposition of fluorescent probes is to simply try to cover the entire surface with a solvent containing the probe and then let the solvent evaporate. The typical challenges of this approach are to obtain a uniform distribution of the probes after evaporation and to equally cover areas with different surface properties. In case a droplet of the fluorophore solution is simply deposited on the surface, the distribution of the fluorophore on the surface will be highly non-uniform after drying, typically with circular patterns of high concentration around a core circle of disproportionately high concentration.

The best solution found for obtaining a uniform distribution was to mount a glass coverslip above the sample surface, at a height of about 100 μm, thus creating a capillary gap in which the fluorophore solvent could be introduced (see Fig. 3.1). The capillary forces inside the gap, allowed for an efficient distribution of the solution all over the surface. The approach was investigated both for passivated and non-passivated metal nanowire samples. On the samples that had been passivated with a SiO_2 layer, a dense and highly uniform distribution of the fluorophore could be obtained all over the surface upon evaporation of the solvent. However, on the non-passivated samples (with bare metal structures on top of SiO_2), evaporation of the solvent typically led to a much higher density of fluorophores on the SiO_2 surfaces than on the metal structure. On top of the metal, almost no fluorophores could be observed.

The density of the deposited fluorophore layers could be varied by changing the concentration of the fluorophore in the solvent. In the case of the quantum dots, the best coverage was obtained for dilutions of the original solution of around 1:100. Too low concentrations (higher dilution of the original solution) led to bad coverage of the nanowires while too high concentrations (lower dilution of the original solution) led to aggregations and cluster formations at random places on the surface. Also in the case of Rhodamine B, various concentrations were investigated. Due to the relatively low fluorescence strength of Rhodamine B (particularly compared to the quantum dots), we wanted to use the highest possible concentration in order to maximize the fluorescence signal. The best result was found for a concentration of around 0.1 mM. Concentrations of 1 mM and higher gave rise to big cluster formations spread over the surface.

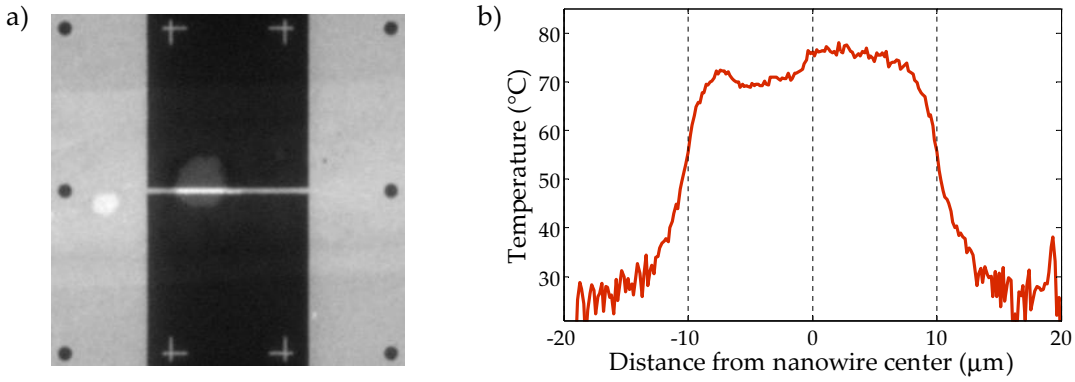

Figure 3.2: The fluorescent image on the left shows a nanowire on which a cluster of high Rhodamine B molecular density can be seen. If the higher density is not taken into account in the thermal characterization by fluorescent thermometry, e.g. by the use of a specific calibration, significant measurement errors occur. In the graph on the right, the influence of the Rhodamine B cluster on the thermal characterization of the resistive heating in the nanowire is clearly visible by an unexpected dip in temperature.

3.5.1.1 Influence of higher concentration and clusters

During the optimization of our fluorescence thermometry, we found that it was important to avoid the creation of fluorophore clusters and aggregations on the areas to be thermally characterized. In Fig. 3.2, an example of the influence of cluster formation is shown. In this case, the drying of Rhodamine B on top of the sample resulted in the creation of a high-concentration stroke of molecules at the nanowire. As seen in the image, a cluster of particularly high molecule density is located on the wire.

As we induced resistive heating in the wire and converted the fluorescence changes to temperature, we found that the temperature at the high-density circle was lower than at the other parts. The reason for this observed drop in temperature is most likely due to the higher molecule density which results in a different temperature dependence. The observed temperature drop is thus a false observation[1].

The fact that the molecule density affects the temperature dependence emphasized the necessity to maintain a good control of the resulting molecule density. Thus, all samples had to be prepared carefully using the exact same protocol each time in order to obtain the same fluorophore density as well as a good uniformity. In case we failed to obtain the appropriate surface coverage on a particular sample, the sample was discarded and not further investigated.

Unless good uniformity is achieved, the calibration of the Rhodamine B must be performed for each pixel before performing the temperature measurements. Using a software such as MATLAB, this approach might indeed be possible to implement, although it would complicate the overall measurement process.

[1] However, there is a possibility that the measured decrease in temperature at the cluster is true. In this case, the dip in temperature would have to be explained by the possible effect of the cluster on the local thermal properties or on the resistive heating in that part of the nanowire.

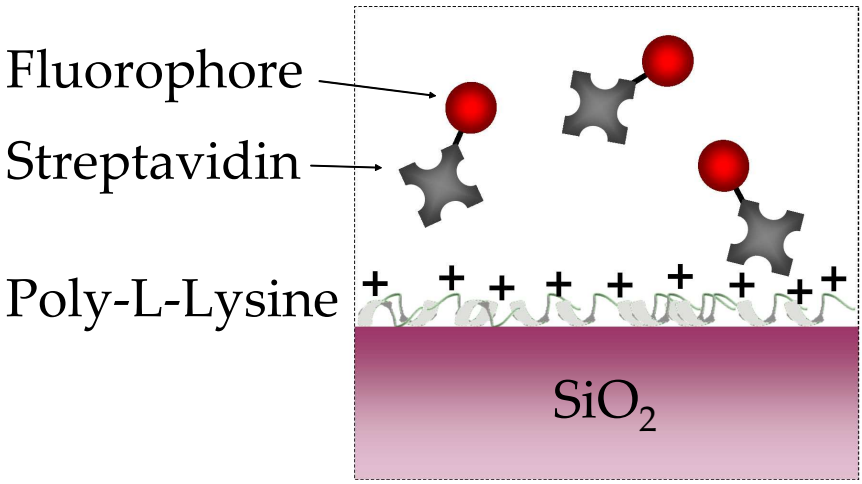

Figure 3.3: Polylysine adsorbs effectively on the SiO_2 surface. At neutral pH and below, the polylysine is positively charged which results in efficient electrostatic binding of the streptavidin conjugates.

3.5.2 Immobilization by streptavidin and polylysine

In order to enable the confinement of fluorophores in the vicinity of the surface also in liquid conditions, a special deposition approach was developed. Using the regular fluorophores did not assure that the probes stayed at the surface upon immersion in a liquid. Instead, a large part of the molecules were typically re-dissolved when the sample was immersed in a liquid. The solution to this problem was to electrostatically bind the fluorophores to the surface. To realize this, a binding protocol based on the interaction between polylysine and streptavidin-conjugated Rhodamine B or nanocrystals was employed.

Since the lysine is a primary amine, the polypeptide is positively charged at neutral pH. This effect can be used for the electrostatic binding of certain molecular species, e.g. streptavidin (see Fig. 3.3). Regarding the thickness of the polylysine layer, it was not measured during our study, but has been reported elsewhere to be approximately 15 Å after 4 minutes incubation under similar conditions. The typical structure of the polylysine chains on the surface has been assumed to be randomly stacked on the surface. [219]

The binding protocol is further explained in Appendix E. After performing the binding of the streptavidin conjugates, the sample was covered with a glass coverslip under which plain DI water or a buffer was inserted. To avoid evaporation of the liquid during experimentation, the sides of the sample-coverslip assembly were encapsulated using a nail polish solution. Drying of the nail polish was allowed for a few minutes, after which no evaporation pathway for the encapsulated liquid was left. A schematic of the assembly is shown in Fig. 3.4.

3.5.3 *p*DEP assembly of nanocrystals

One of the first assembly methods investigated during the work of this thesis consisted in the electric field assisted assembly of nanoparticles on top of micro- and nanowires. The approach was only investigated for quantum dots and presented a possible approach

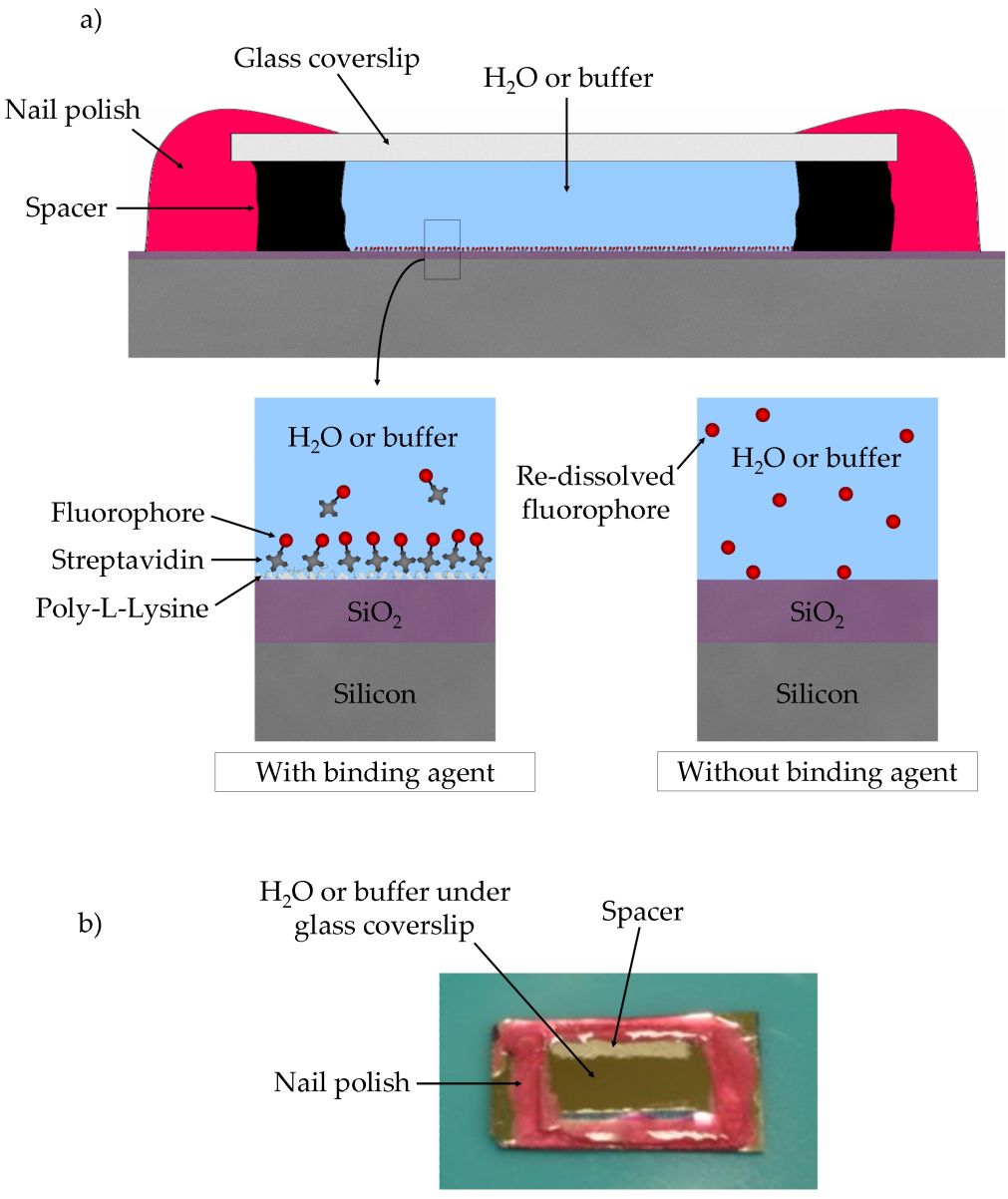

Figure 3.4: a) Sample assembly when using the polylysine/streptavidin electrostatic bond. The purpose of the electrostatic bond is to prevent the re-dissolution of the fluorescent probes. b) Photograph of an actual sample assembly.

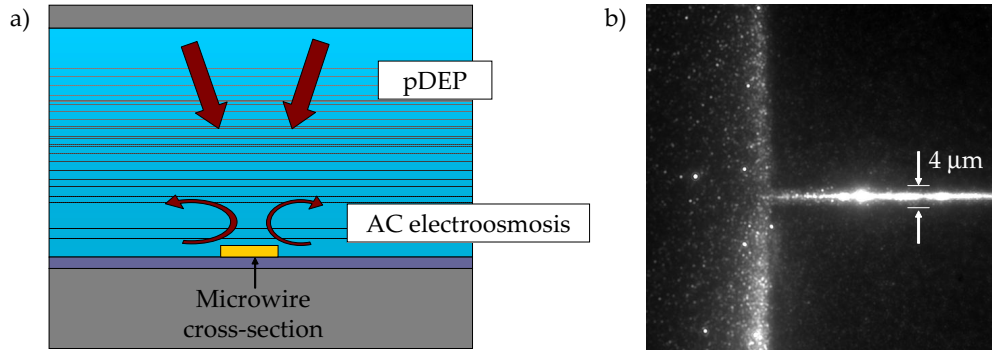

Figure 3.5: a) The electric forces used for the assembly of our quantum dots on micro- and nanowires consisted mainly in pDEP forces. In the case of microwires (width > 1 μm), electroosmotic forces were also observed to assist in the assembly by dragging the particles towards the middle of the wires. b) Quantum dots assembled on a 100μm-long and 4μm-wide microwire.

for the deposition of nanoparticles on non-passivated micro- and nanowires. For a more thorough presentation of the topic, the reader is referred to Appendix F and reference [220].

The basic principle of the approach is to make use of the polarizability of the nanocrystals. Due to this polarizability, positive dielectrophoretic (pDEP) forces can be used to direct the nanocrystals in certain directions throughout a non-uniform electric field (see Fig. 3.5a). A typical result achieved for the assembly of nanocrystals on a microwire is shown in Fig. 3.5b.

3.6 Photostability

A classical problem of fluorescence microscopy is the existence of photoinduced changes of the fluorescence from a fluorophore. The most common effect that is observed is photobleaching, which refers to the gradual decrease of the emitted fluorescence intensity of a fluorophore under the influence of the excitation light. The photostability of our two fluorophores was thoroughly investigated in order to understand its influence on the fluorescence and to allow for compensation of any photoinduced changes of the fluorescence during the temperature measurements.

In order to investigate the response of our fluorophores to the excitation light, a number of dummy samples consisting of nickel surfaces (40nm-thick) passivated with silicon dioxide (100nm-thick) and covered with the specific fluorophore were prepared. The fluorophores were then continuously excited at different intensities for intervals of 30 minutes. During the excitation period, images were captured once every 15 seconds using the EMCCD camera. The average fluorescence intensity of each image was then calculated in the Andor IQ software and plotted as a function of time. These photostability curves were acquired for a range of different intensities and for the use of different microscope objectives. Depending on the numerical aperture and the magnification of the objectives, different optical power densities were transmitted to the sample surface.

Representative photostability curves for the nanocrystals, in dry as well as in liquid conditions, are shown in Fig. 3.6. The corresponding curves for Rhodamine B are shown

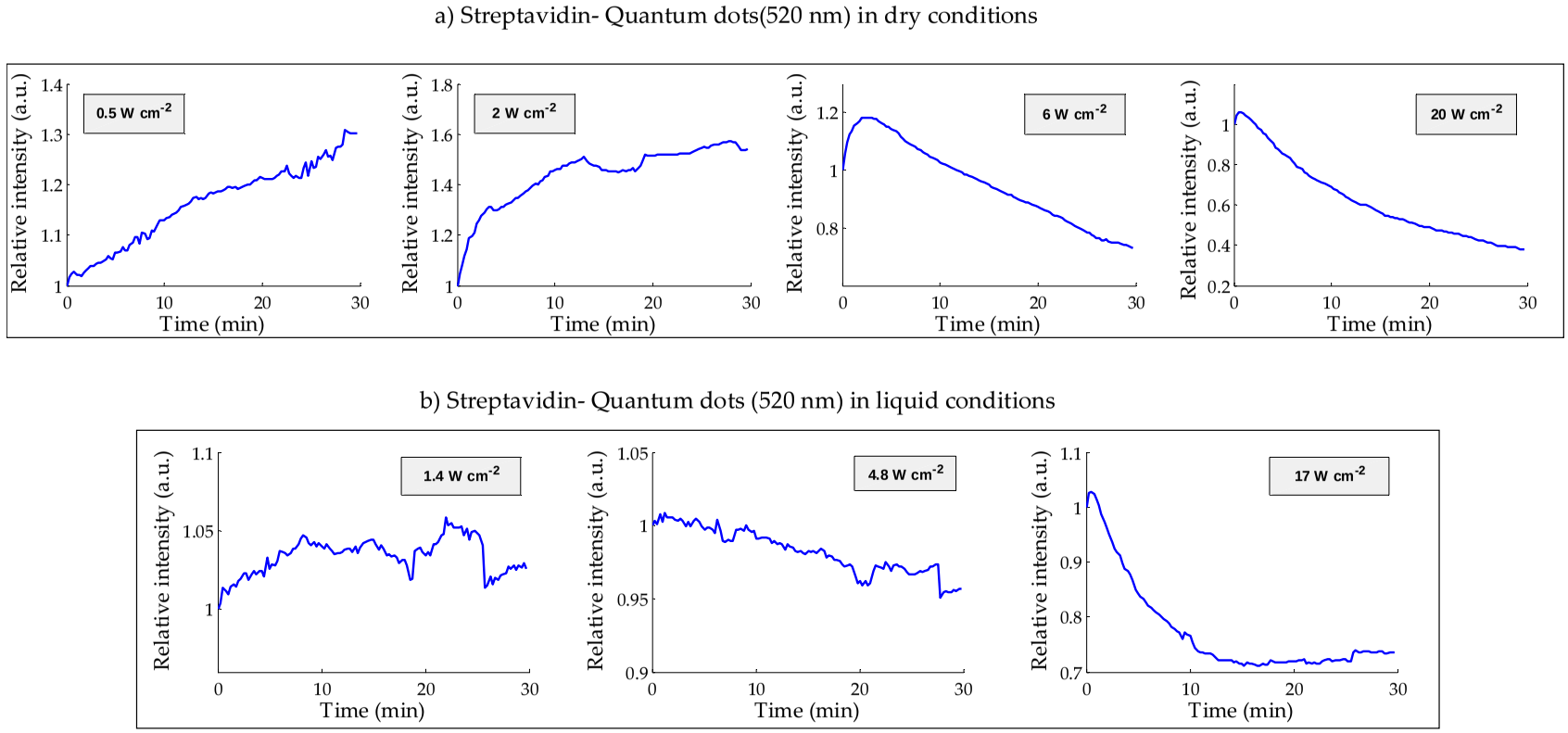

Figure 3.6: These graphs show the photostability of our quantum dots over time and under continuous excitation. In a) the photostabilities for dry conditions are shown and in b) the photostabilities for liquid conditions are shown. The optical power densities which were applied in each case are indicated in each graph. Each curve is normalized with regard to its initial value. It should be be noted that in terms of absolute fluorescence intensity values, the higher excitation power densities give a higher fluorescence.

in Fig. 3.6. In the figures, the optical power density of the excitation light is indicated in W/cm^2 in order to enable a comparison between the different fluorophores. The measurement of the power densities was performed with a Newport 840 Optical power meter and is further described in Appendix G. The fluorescence intensity values are normalized to the initial values of each curve. Although not visible in these curves, it should be kept in mind that the higher the excitation intensity is, the higher the fluorescence intensity becomes. This is the reason for the higher amount of noise and fluctuations in the curves taken at low powers.

As can be seen in the photostability curves, the most typical evolution of the fluorescence intensity under excitation is an enhancement in the beginning of the excitation which fades off until a maximum intensity is passed. Subsequently the intensity starts to decrease with no return to higher levels. Among the curves we find one exception to this behavior, namely the curve for Rhodamine B in dry conditions. In this case, the curve seems to pass through two maxima and one local minimum before entering a final phase of decrease. The first maximum is only observed in the curve obtained at the lowest excitation intensity. In all cases, the effect of increasing the excitation intensity seemed to simply be an acceleration of the movement along the characteristic curve. By investigating a few dummy samples without nickel underneath the nickel, we could also establish a dependence on the surface composition. Interestingly, the movement along the curve was slower on top of the surfaces without nickel underneath. The reason for this is most probably the higher reflectivity of the surfaces with nickel which leads to higher effective illumination of the fluorophores.

When comparing the curves for Rhodamine B and quantum dots, it is obvious that the final photobleaching phase is reached much faster and at lower intensities for Rhodamine B than for the quantum dots. On the other hand, the quantum dots are in fact not particularly photostable, considering the existence of both photoenhancement and photobleaching effects throughout its photostability curve. The main advantage of the quantum dots is instead that they allow for high intensity excitation without excessive photobleaching in contrast to the dry Rhodamine B case.

After the discovery that all curves possess one or more local maxima, it is clear that it would be advantageous to perform all fluorescence measurement at one of these points. Performing measurements here allows for a maximal signal-to-noise level. Therefore, the strategy adopted for our fluorescence measurements involved a preliminary step where continuous excitation of the fluorophore was carried out until reaching the maximum intensity point. In the case of dry Rhodamine B, the second maximum was chosen because of its longer existence. Once reaching the maximum point, the excitation was stopped. All measurements were subsequently performed at the highest excitation intensity. By the use of a computer-controlled optical shutter, the fluorophores were excited only during the capture of an image, which allowed for the minimization of any further movement along the photostability curve. Typically, each captured image required an exposure time on the order of one second. During the investigations presented in the following, a total of 10 to 20 images were typically captured for each sample which equaled a movement of 10 to 20 seconds along the photostability curve. This timeframe did not allow for a significant photoinduced change of the intensity as we started at a point close to and before a maximum.

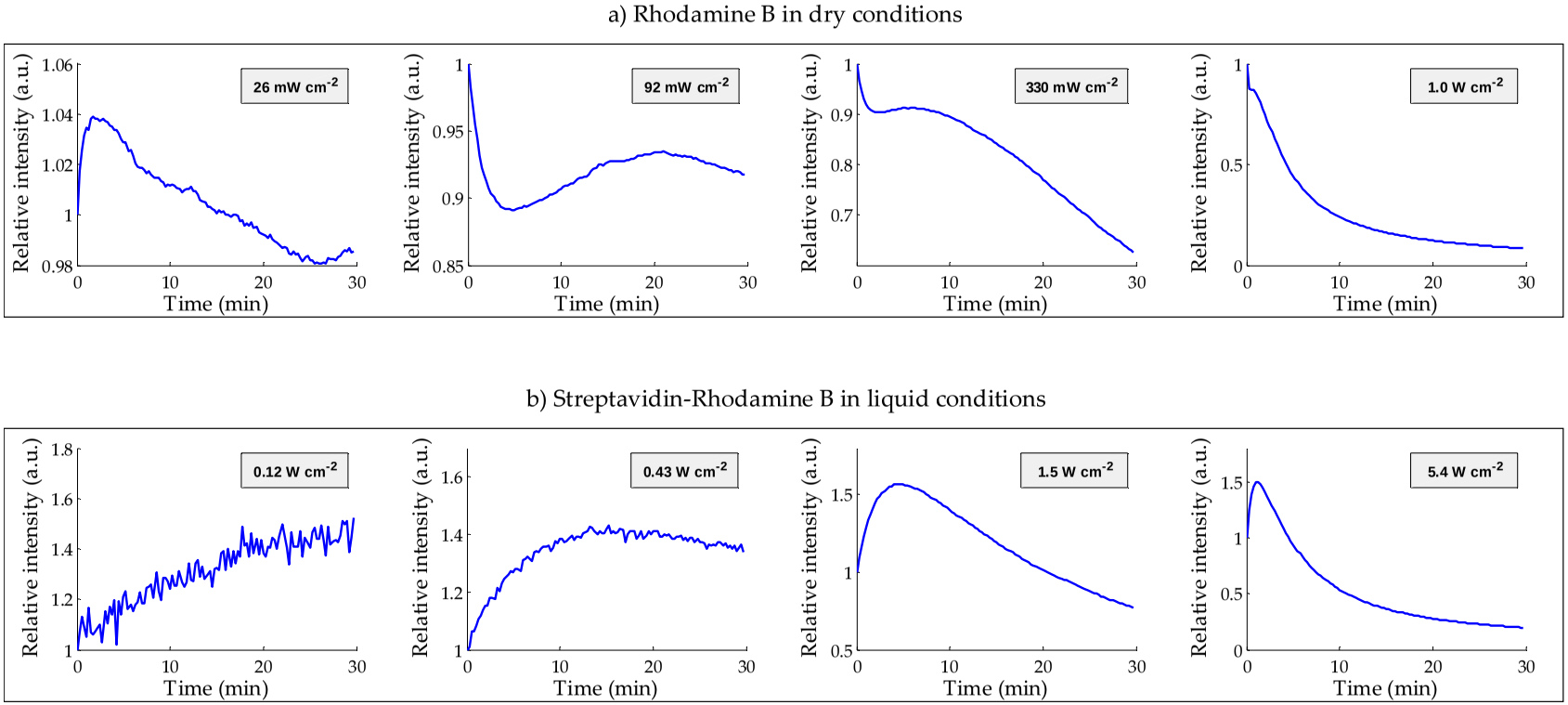

Figure 3.7: These graphs show the photostability of Rhodamine B over time and under continuous excitation. In a) the photostabilities for dried Rhodamine B are shown and in b) the photostabilities for Streptavidin-Rhodamine B in liquid conditions (bound to the surface using the poly-L-lysine electrostatic bond) are shown. The optical power densities which were applied in each case are indicated in each graph. Each curve is normalized with regard to its initial value. It should be be noted that in terms of absolute fluorescence intensity values, the higher excitation power densities give a higher fluorescence.

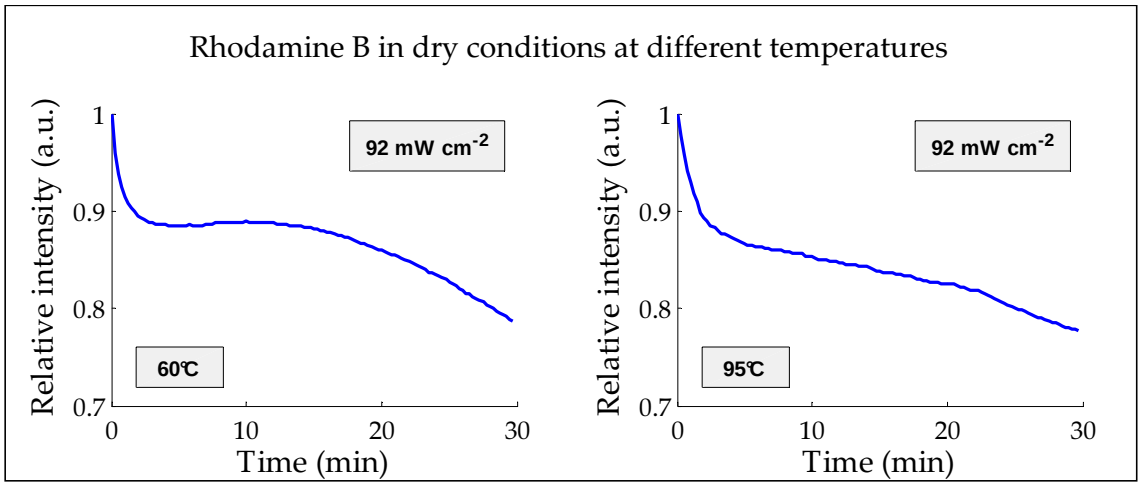

Figure 3.8: These two graphs show the photostability of Rhodamine B over time and under continuous excitation at 60°C and 95°C, respectively. The optical power densities were identical in the two cases. Each curve is normalized with regard to its initial value.

3.6.1 Influence of temperature on the photostability curve

It is interesting to know whether there is an acceleration or a slowdown of the photoinduced fluorescence changes as the temperature is increased. Therefore, the influence of temperature on the photostability was also briefly investigated, although only for dry Rhodamine B. In the previous curves, the temperature was held at ambient conditions, i.e. 25°C. In Fig. 3.8, the results of excitation of dry Rhodamine B at 92 mW/cm^2 at a temperature of 60°C and 95°C are shown. It can be seen that the second maximum is flattened when the temperature is held at 60°C and even disappears in the case of 95°C. Although the reason for this change is not clear, we believe that it might be caused by a difference in susceptibility to photoinduced modification for the different Rhodamine B molecule conformations (see Chapter 1). With a change in temperature, the relative occurrence of the different conformations changes and thereby also the shape of the photostability curve.

3.7 Temperature dependence and reversibility

As we apply a fluorophore for the measurement of temperature, it is obvious that the fluorescence must provide a measurable change upon the change of temperature. The characteristic temperature dependent feature of the fluorescence of our two fluorophores is a decrease of the fluorescence peak intensity when the temperature is increased. In order to enable the use of this dependence for high quality temperature measurements, one of the most important things to do is to carefully characterize its temperature dependence and to accurately describe its behavior. This is best done by simply measuring the fluorescence intensity at several well-defined temperatures imposed by means of a conventional device for temperature control, e.g. a hotplate, a hot bath or an oven. The intensity measurements at different temperatures allows for the establishment of a calibration curve, which relates the relative intensity changes to temperature. In order to optimize the characterization of the calibration curve, it is important to perform the

measurement on a large number of fluorophores and if possible repeat the measurement several times on independent samples. This will minimize the influence of statistical fluctuations during the measurements.

3.7.1 Temperature cycles

Before we proceed to the temperature calibration of the fluorophores, it is worthwhile to take notice of the fact that temperature can have an irreversibly deteriorating effect on the fluorescence of a fluorophore. In the choice of a fluorophore for thermometry, the ideal fluorophore presents the same temperature dependence each time it is subjected to the same temperature changes. Without this thermal stability, the accuracy of the temperature measurements will become poor and unpredictable and the measurements may become useless.

3.7.1.1 Experimental approach

In order to determine the thermal stability of a fluorophore, a range of dummy samples were prepared in the same way as during the photostability investigations. The fluorophores, which were deposited on top of a dummy sample, were subjected to temperature cycles in different temperature ranges by the use of a microscope heating stage to globally heat or cool the entire sample. To improve the thermal contact between the stage and the sample, a thermal grease was applied at the interface.

As for the fluorescence analysis, the sample was allowed to stabilize for 5 minutes at each temperature before capturing 10 images at an exposure time of 200 ms each. The average of these images was then used to determine the fluorescence intensity at that temperature. All measurements performed here were done at a photostable point as described in the previous section and an objective of 20X magnification was used in order to include a large amount of fluorophores in the measurements.

Focus drift Since the entire sample was subjected to the temperature changes, thermal expansion or contraction occurred which led to focus drift and small lateral movement of the sample. Thus, the focus always had to be adjusted to some extent before capturing a new image series. Furthermore, it was useful to find two or three distinctive features in the observed part of the sample in order to allow for re-alignment after possible lateral displacement.

Evaluation of the measurements If the fluorescence variations between the minimum and the maximum temperatures stayed relatively stable over the course of 10 cycles, we accepted the fluorophore and continued to characterize the calibration curve in that temperature range. As we will show in the following, the thermal stability of our fluorophores differed largely both between the fluorophores as well as for the different temperature ranges.

3.7.1.2 Thermal stability – CdSe/ZnS nanocrystals

In Fig. 3.9, representative graphs for the temperature cycles performed for quantum dots, both in dry and liquid conditions, are shown. The results of these cycles show that the thermal behavior of our quantum dots was unpredictable to a large extent,

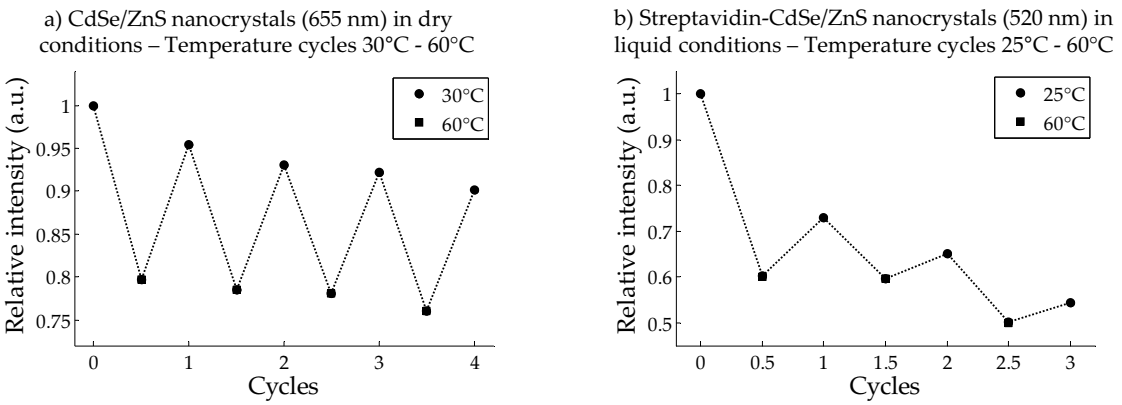

Figure 3.9: a) Temperature cycles of dried quantum dots (CdSe/ZnS, emission at 655 nm) in the range 30-60°C. b) Temperature cycles of streptavidin-conjugated quantum dots (CdSe/ZnS, emission at 520 nm) in liquid conditions and bound to the surface. The range here was 25°C-60°C. None of our quantum dots showed a good thermal stability in the given ranges.

even for relatively small temperature ranges. Similar to our results, several publications have mentioned the strong decrease of fluorescence intensity upon increases of the temperature [13, 144, 152]. However, most of these publications have failed to notice the irreversibility over thermal cycles which is clearly seen in Fig. 3.9.

In our experiments, for every new cycle, the fluorescence was quenched compared to the preceding cycle. In other words it seems that a thermally induced bleaching of the nanocrystals occurred. The reasons behind this are not clearly understood, although it might be caused by surface trap states as discussed in Chapter 1. To broaden the understanding of this effect, specific investigations have to be targeted, which are outside the scope of this thesis.

A few trials on the use of nanocrystals without the polymer coatings (dissolved in Toluene) and with different sizes were briefly investigated in dry conditions, but with the same instability of the fluorescence over temperature cycles.

The instability of the quantum dots implies that they are not well suited as fluorescent temperature probes. Consequently, we chose not to proceed with these probes for the purpose of fluorescent thermometry.

3.7.1.3 Thermal stability – Rhodamine B

In the case of Rhodamine B, the results of temperature cycling in different temperature ranges are shown in Fig. 3.10. Results are presented for both dry and liquid conditions. Compared to the quantum dots, the Rhodamine B allowed for a more stable and repeatable response to temperature changes. This was particularly true for Rhodamine B in dry conditions, where temperature ranges as large as 25-95°C gave a satisfactory repeatability and stability when changing the temperature. When expanding the temperature range above 100°C, the stability was compromised with large departures from the original fluorescence values after temperature cycling.

In liquid conditions, the fact that a water solution was encapsulated on top of the immobilized fluorophore imposed particular conditions which led to a lower viable temperature range in order to maintain stability. The instability at temperatures close to

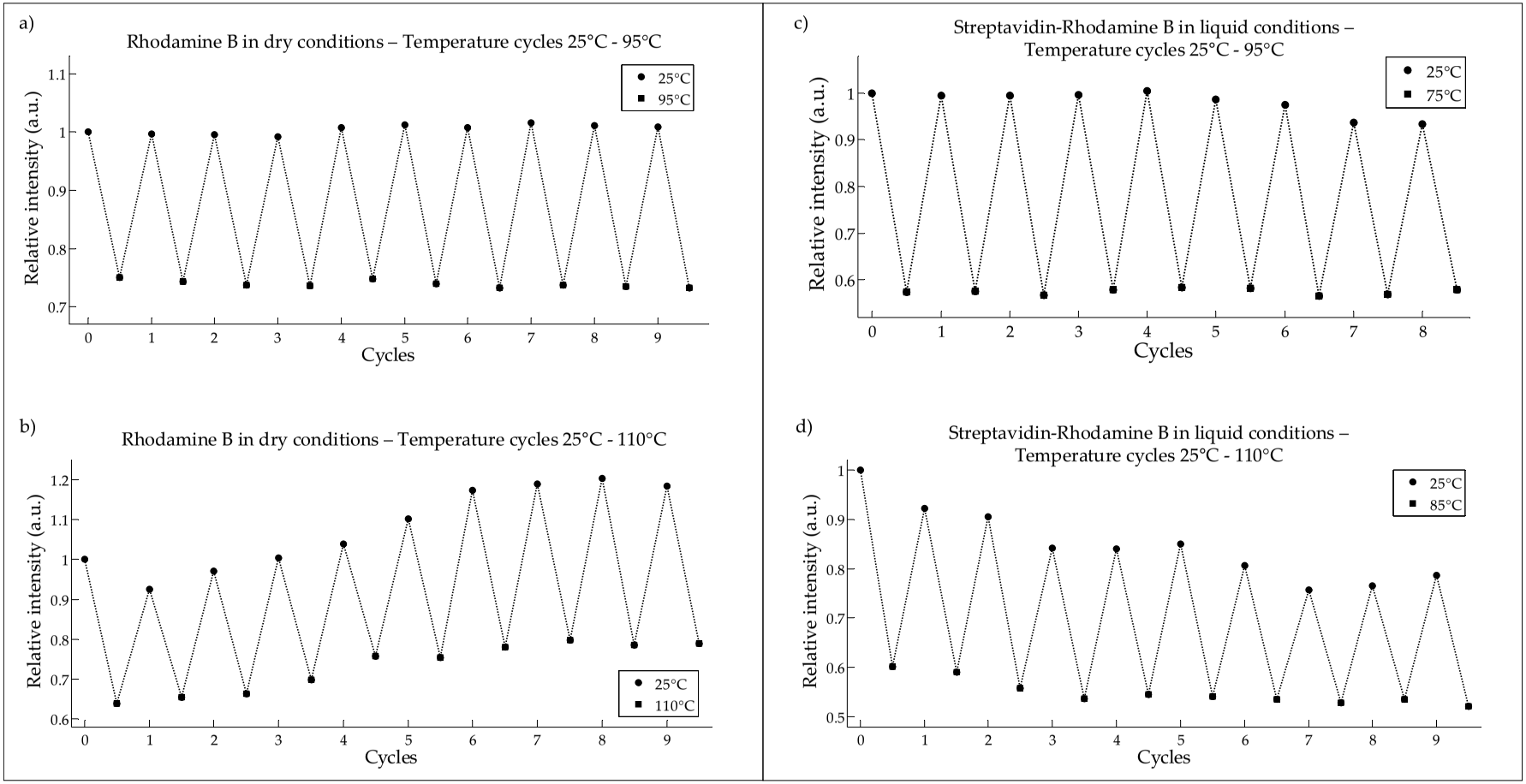

Figure 3.10: Temperature cycles of: a) dried Rhodamine B in the range 25-95°C, b) dried Rhodamine B in the range 25-110°C, c) streptavidin-Rhodamine B in liquid conditions in the range 25-75°C and d) streptavidin-Rhodamine B in liquid conditions in the range 25-85°C. It is clearly seen that the stability over consecutive cycles is much better for lower temperature ranges. In the case of liquid conditions, the instability is observed at a lower range.

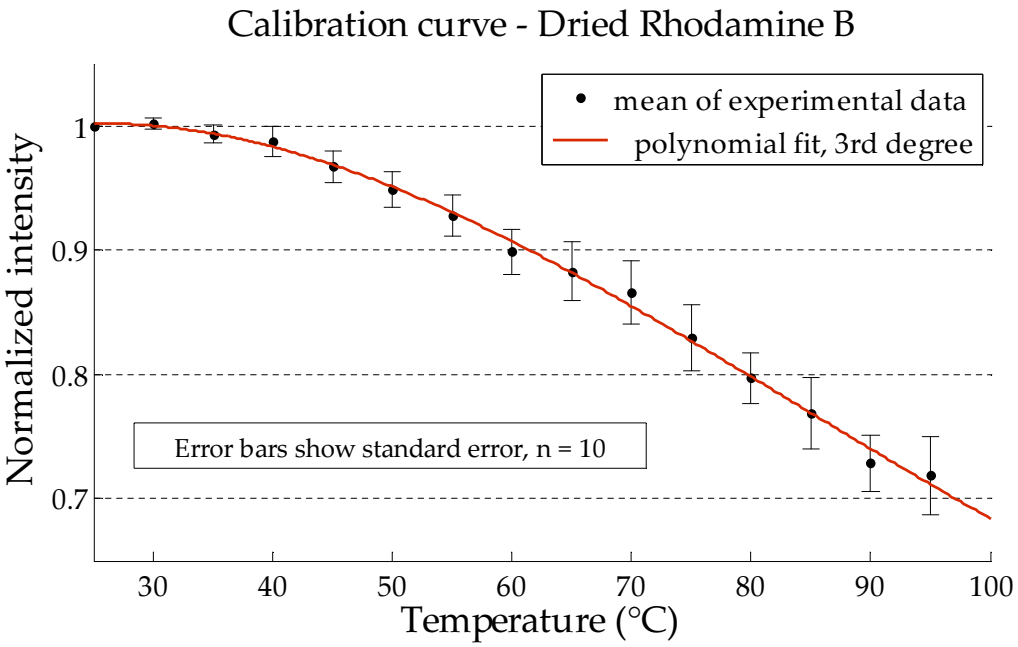

Figure 3.11: Calibration curve for dried Rhodamine B. 10 curves were acquired and the error bars represent the standard error from the mean values.

100°C is most probably due to instabilities of the liquid encapsulation when the water approaches the boiling point. Typical reasons for the difference between dry and liquid conditions, except for the different environments, may be the presence of streptavidin and poly-L-lysine on the surface.

3.7.2 Temperature calibration curve

The result of the temperature cycle experiments led us to focus entirely on Rhodamine B as a probe for the temperature measurements. To realize the acquisition of a calibration curve, a range of samples with fluorophores deposited on top were prepared. Each of these samples was then subjected to one temperature cycle each during which fluorescence intensity data was captured at intervals of 5°C. The temperature range targeted was 25-95°C. At each temperature, the sample was allowed to stabilize for 5 minutes before capturing 10 images with an exposure time of 200 ms each. The average of these images was then used to determine the fluorescence intensity at that temperature. All measurements were made through the 20X magnification objective that was used also for the temperature cycle experiments.

In Fig. 3.11 and Fig. 3.12 the calibration curves for Rhodamine B in dry and liquid conditions, respectively, are shown. The most remarkable thing about the calibration curve in dry conditions is the flat profile over the first 10°C. It should also be noticed that the calibration curve is less pronounced than the corresponding curve for freely dispersed Rhodamine B in water, as shown in some articles [39, 66]. To allow for a direct comparison, a calibration curve acquired in classical liquid conditions (Rhodamine B freely dispersed in water) is shown in Fig. 3.13. The mechanisms behind the difference will not be specifically addressed in this thesis. The difference may be due to such things as the higher likelihood for interaction with oxygen in dry conditions, the different polar

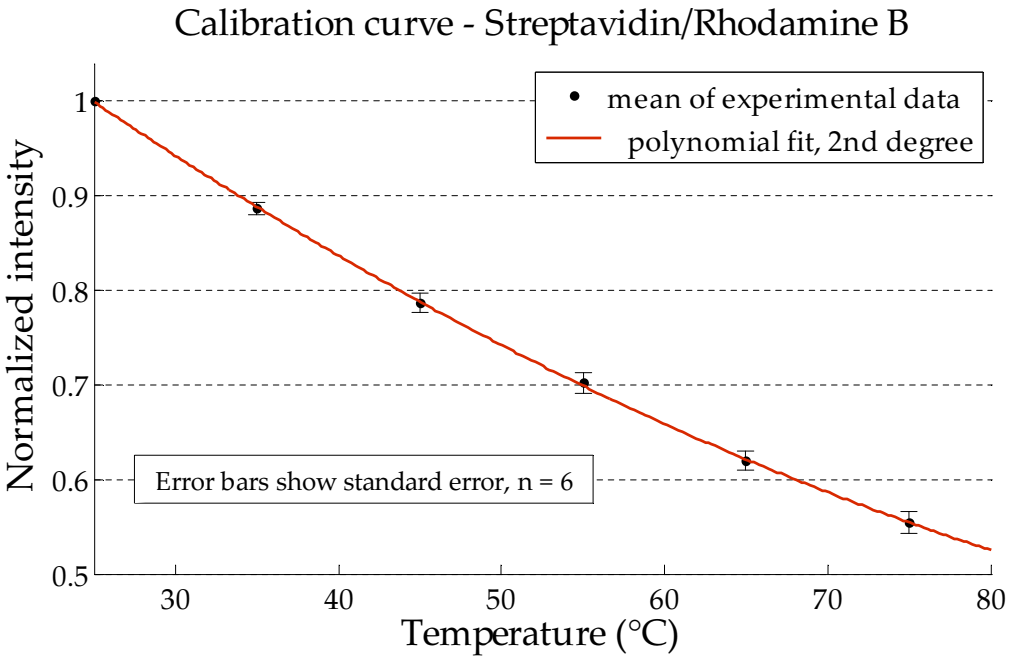

Figure 3.12: Calibration curve for streptavidin-Rhodamine B in liquid conditions. 6 curves were acquired and the error bars represent the standard error from the mean values.

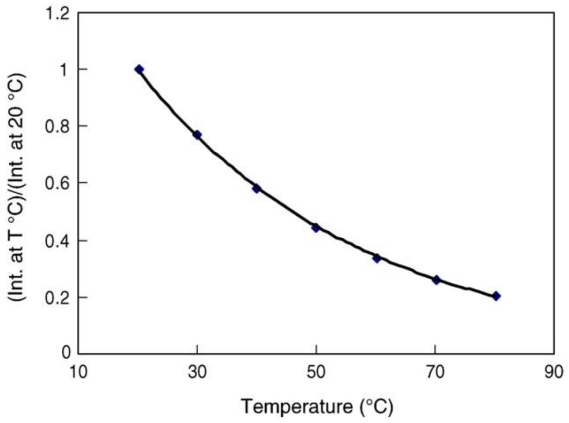

Figure 3.13: Calibration curve for standard Rhodamine B freely dispersed in water (0.1 mM). [39]

environment and the fact that the dried Rhodamine B molecules most probably are more densely packed than in the typical applications of freely dispersed Rhodamine B.

As for the calibration curve taken for the surface-bound streptavidin-Rhodamine B conjugates in liquid conditions, a slightly stronger temperature dependence was found. Furthermore, there was no flat curve profile around ambient temperature as for the dry Rhodamine B. It is seen that the calibration curve of the streptavidin conjugates shows a better correspondence than dry Rhodamine B to the calibration curve of freely dispersed Rhodamine B.

3.8 Conclusions

We have in this chapter illustrated the first steps taken to adapt fluorescent thermometry for surface temperature measurements of high spatial resolution. The main resolution-improving factor is that of confining the fluorophores in the vicinity of the surfaces to be characterized. In dry conditions, the fluorophores could be confined to the surface simply by a deposition and drying process. In liquid conditions, confinement to the surface was attempted by the use of an electrostatic bond. Assembly of fluorophores by electrical field forces was also addressed, although not finally used for our subsequent investigations.

Rhodamine B the best candidate Two potential fluorescent probes, CdSe/ZnS nanocrystals and Rhodamine B, were investigated in order to evaluate their applicability in the specific conditions of our approach for fluorescent thermometry (e.g. in dry conditions or electrostatically bound to the surface). While both of the investigated probes showed a clear dependence on the temperature, only Rhodamine B presented a sufficiently stable and repeatable behavior in the experimental conditions used here. Consequently, Rhodamine B was chosen to be the fluorescent probe in our following thermal characterizations.

Local intensity maximum In the study of the photostability of Rhodamine B, it was found that the temporal dependence of the Rhodamine B photobleaching under continuous illumination contains a local maximum. By performing the fluorescent thermometry at this maximum, the signal can be maximized and the photobleaching more easily controlled. The exploitation of this will be further illustrated in the thermal characterizations presented in the following chapter.

Dependence on the molecular density A challenge that was encountered for the Rhodamine B in dry conditions concerned the impact of the molecular density on the temperature dependence. It is concluded that the deposition of the Rhodamine B molecules on the sample surface has to be carefully performed with the exact same procedure used each time in order to assure the good uniformity of the molecular density and the similar average densities on different samples. In case the achievement of uniform molecular distributions is difficult to obtain, the most efficient way to improve measurement errors is to perform the calibration of the temperature dependence for each individual pixel before performing the temperature measurements on each sample. However, such an approach would imply a significant increase in the complexity of the characterization process.

Temperature dependence Calibration curves were acquired for Rhodamine B in dry and liquid conditions. For dry conditions, it was observed that the temperature dependence was somewhat less strong than for conventional Rhodamine B solutions (Rhodamine B freely dispersed in a solvent).For the streptavidin-Rhodamine B conjugates bound to the surface, the dependence was stronger than for dry conditions but weaker than for the conventional Rhodamine B solutions.

Alternative probes Further investigations dedicated to finding yet better probes for applications in surface temperature measurements are certainly possible and a range of potential fluorophores are mentioned in Chapter 1 and Appendix A. Within this thesis, the investigations stopped at two fluorophores mainly due to time limits and the complexity involved in the development of deposition methods and finding appropriate optical equipment (filters etc.) for each fluorophore. Among the most attractive candidates for further investigations we find various rare-earth doped nanocrystals. Particles of this kind have already been shown to function well in scanning fluorescent probe applications [104–106] and could with high probability be adapted for our full-field approach as well.

CHAPTER 4

THERMAL CHARACTERIZATION OF THE NANOWIRE SYSTEMS

The investigations presented in the previous chapter provided us with the data necessary to choose an appropriate fluorescent probe. By the use of Rhodamine B in a stable temperature range (25-95°C) and at photostable conditions, we have an efficient tool for the thermal characterization of the various nanowire samples presented in Chapter 2. In the following, the application of Rhodamine B for this purpose will be illustrated. The description of the experimental procedure and setup will be followed by a thorough presentation and discussion regarding the obtained results.

In the end of the chapter, in order to further evaluate the reliability of our approach, we will make comparisons with measurements performed using a scanning thermal microscopy approach.[1]

4.1 Experimental approach

An overview of the experimental approach is shown schematically in Fig. 4.1. In the following sections, the various steps of the temperature measurements will be described in further detail.

4.1.1 Optical setup

Regarding the fluorescence imaging, a 100X magnification microscope objective was used. The objective was a dry condition objective, thus avoiding the physical contact with the sample which is the case for immersion objectives. From a thermal point of view, this gives a better control of the global thermal state of the sample since no thermal path (except for the air) is introduced between the sample and the objective. The 100X magnification combined with a high numerical aperture of 0.95 allowed for the best possible acquisition of optical data.

The fluorescence was captured using an EMCCD camera from Andor and preliminary observations on a computer were done using the software IQ, also from Andor. Two

[1]This SThM approach is based on a scanning fluorescent probe and has been developed by Dr. Lionel Aigouy at the ESPCI-CNRS in Paris.

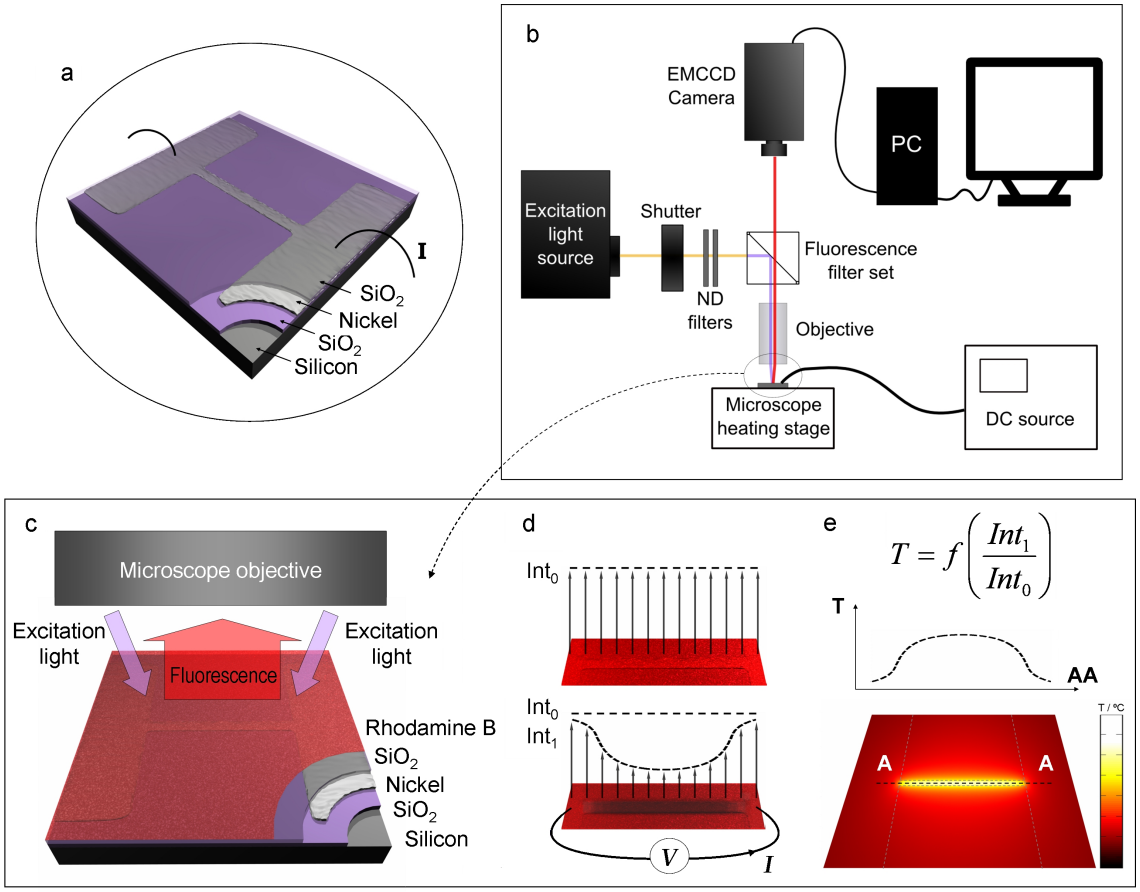

Figure 4.1: a) Resistive heating in a metal micro- or nanowire is used in our case to achieve locally confined temperature changes. b) Setup for fluorescent thermometry using an EMCCD camera to capture fluorescent images. c) The sample is covered by a thin, dense and uniform layer of Rhodamine B molecules. Excitation of the molecules as well as observation of the emitted fluorescence is performed through a high magnification dry objective. d) Local heating occurs when a current is applied to the sample. Depending on the local temperature change, the local emitted fluorescence intensity changes. In the case of Rhodamine B, the intensity decreases when the temperature increases. e) With precise knowledge of the relation between intensity change and temperature change, a given change in intensity can be converted to temperature.

different EMCCD cameras were used during the experiments. For steady-state analysis, the iXon 897 camera was used and for transient analysis, the iXon 860 camera was used. The iXon 860 allowed for higher acquisition rates but used a bigger pixel size and smaller field of capture.

Rhodamine B fluorescence was induced using an EXFO metal halide lamp at maximal intensity. A neutral density filter with 6% transmittance, equaling approximately 1.5 W/cm^2 in combination with the 100X objective, was used. In order to filter out the appropriate excitation and emission wavelengths, a TRITC 31002 filter from Chroma technologies was used. For the purpose of controlling the exposure times, the illumination of the sample was controlled with a computer-controlled shutter (Smartshutter) from Sutter Instruments. Synchronization of the shutter and the camera was possible using the IQ software.

4.1.2 Global temperature control

During all experiments, the nanowire samples were positioned on top of a peltier-based microscope temperature stage from Linkam (PE-120).In order to improve the thermal contact and to minimize movement of the sample during measurements, a high thermal conductivity grease was applied between the sample and the stage. The grease helped in keeping the sample steady. For those samples containing suspended membranes, extra care had to be taken in order not to introduce grease underneath the membranes. A temperature of 25°C was imposed at the bottom of the sample using the peltier element. Dissipation of heat was further facilitated by the use of a water flow through the temperature stage.

4.1.3 Equipment for local resistive nanowire heating

In the experiments targeting temperature measurements in dry conditions, a DC source from Keithley (2430 1KW pulse SourceMeter) was used in a constant current mode. For the experiments in liquid conditions, the use of a DC source typically led to electrolysis, in spite of the passivation layer on top of the nanowires. Therefore, an AC source from Fluke (PM5150 arbitrary waveform generator) was instead used to induce resistive heating. The AC power was applied in a constant voltage mode at a frequency of 10 kHz.

Due to the presence of static charge in the power sources, but also in other equipment such as tweezers, scotch tape and the hands of the operator, special care had to be taken during the manipulation of the smallest nanowires. Although less sensitive to static discharge than for example gold nanowires, the 200-nm wide nickel nanowires were occasionally destroyed when preparing the experiments. To avoid these problems, plastic gloves were used during all experimentation and special care was taken when using scotch tape (scotch tape was typically used to keep the connecting cables steady). Tweezers and other similar objects were discharged to ground before touching the sample.

A possible approach for avoiding destructive static discharge upon connection to the power source was to use a variable resistance between the source and the sample. By maximizing the resistance during connection, any static charge was gently passed through the nanowire. After the connection, the variable resistance could be decreased to zero.

4.1.4 Sample preparation

The deposition of Rhodamine B on the actual samples was achieved in the same way as during the photostability investigations in Chapter 3. In the case of dried Rhodamine B, the fluorophore solution was deposited on the sample, using a capillary gap, the day before the temperature measurements. Evaporation was done overnight at room temperature. Before starting the temperature measurements, the coverslip used during the evaporation was replaced with a clean coverslip. The use of a coverslip was necessary because of the specific optical properties of the 100X microscope objective.

In the case of the streptavidin-Rhodamine B conjugates, binding on the sample surface was performed immediately before the characterizations. A coverslip was subsequently mounted above the sample followed by the introduction of a DI water in the gap. Evaporation of the liquid was prevented by the use of nail polish encapsulation as described previously.

During the liquid measurements, we sometimes had a problem to obtain a clear optical image of the nanowire. This was due to the microscope objective used (100X / NA0.95), which was primarily adapted for measurements in dry conditions. Fortunately, because of the existence of an adjustment ring on the objective, the optical path in the objective could be partly adjusted. This helped in improving the image clarity to some extent. Further improvement of the image required the liquid gap height to be as small as possible in order to minimize the light path through the liquid. We minimized the gap height by the use of parafilm cover paper as a spacer.

4.1.5 Acquisition and image treatment

4.1.5.1 Photobleaching

As seen in the previous chapter, the continuous illumination of Rhodamine B leads to changes in its fluorescence intensity. In the curve relating the intensity with the time under constant illumination, we found that a local intensity maximum exists. Since the intensity changes around the maximum occurred relatively slowly and due to the higher signal at this point, we decided to perform all fluorescence thermometry in its vicinity. To assure that the local maximum of the intensity was always used, each experiment was preceded by the steps illustrated in Fig. 4.2, which shows the example of dry Rhodamine B.

Once the nanowire sample was mounted on the temperature stage and connected to the power source, an area a small distance away from the targeted nanowire was located in the acquisition window. After finding a good focus, a photobleaching curve with a duration of 10 minutes was captured at the experimental excitation intensity (1.5 W/cm^2). This was done in order to determine the exposure time required to reach the local intensity maximum of the photostability curve.

Once having determined the time required to reach the intensity maximum, the targeted nanowire was moved to the center of the acquisition window. During the search for the nanowire, the excitation intensity was kept at a low level in order to avoid unintended photobleaching. After waiting for the sample to stabilize mechanically at the new position, the focus was adjusted. Photobleaching of the Rhodamine B at the nanowire was then performed at the experimental excitation intensity in order to reach the first intensity maximum. Once this point was reached, the excitation light was cut off and no further illumination of the sample was done at the experimental intensity level

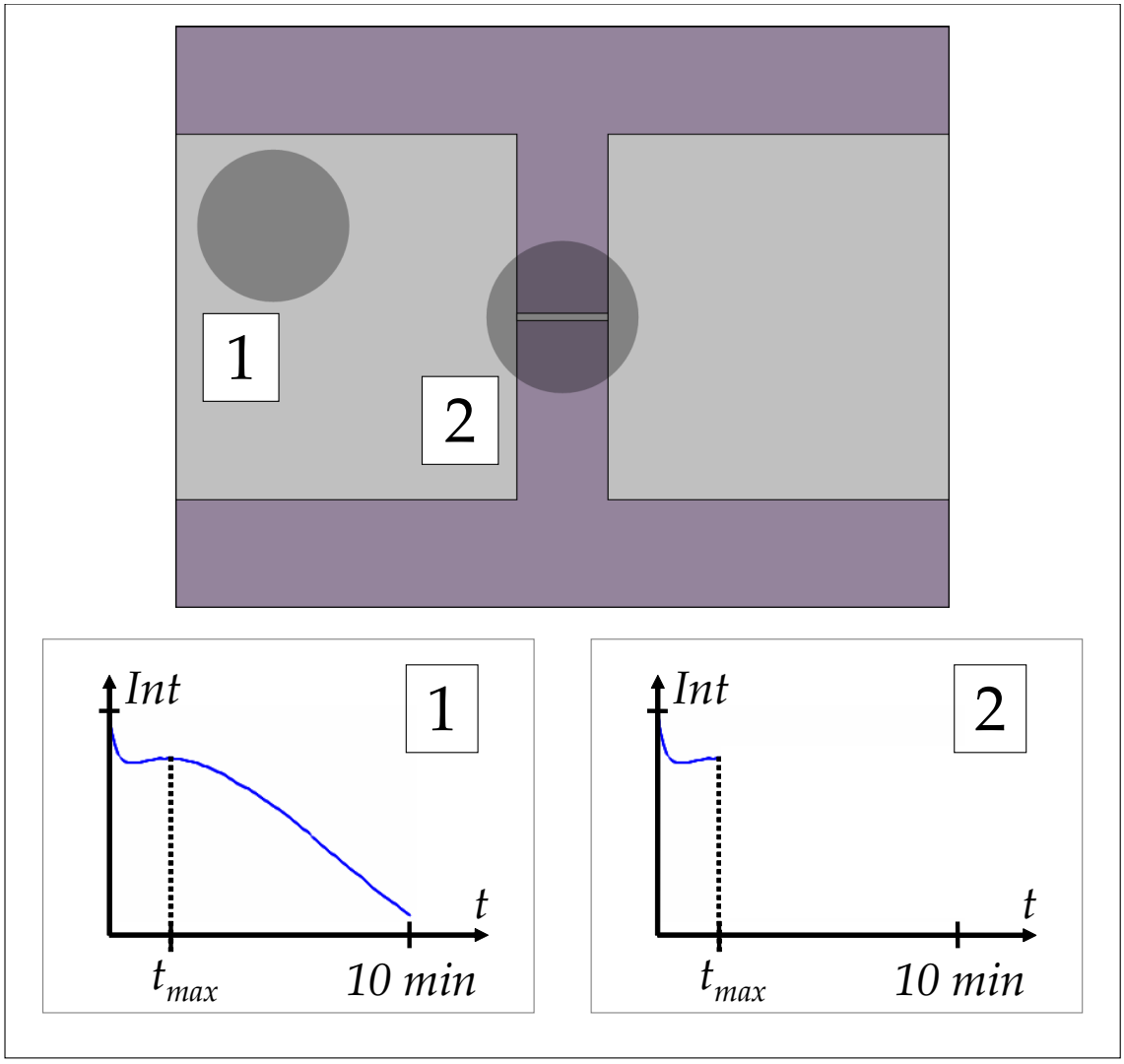

Figure 4.2: Before performing the fluorescent thermometry, the Rhodamine B molecules deposited on the sample to be characterized were shortly investigated regarding their photostability. (1) Firstly, a photostability curve lasting 10 minutes was captured at an area a small distance away from the nanowire. With this curve, the time required to reach the local intensity maximum could be determined. (2) With this knowledge, the nanowire was subsequently centered in the field of view and illuminated by the excitation light for the time determined from the photostability curve. After reaching the intensity maximum, no further excitation was done until the main fluorescence measurement were performed.

until the fluorescence measurements were performed. If additional focus adjustments became necessary, a low excitation intensity was used.

4.1.5.2 Imaging of resistive heating

After reaching the intensity maximum, resistive heating was induced in the nanowire by the application of a DC current (dry conditions) or an AC voltage (liquid conditions). As will be further shown in the results section, the local heating of the nanowires led to decreases in the fluorescence intensity. These decreases could subsequently be converted to temperature values by the use of the previously established calibration curve.

As the fluorescent thermometry approach was developed, we used different ways to perform the acquisition process. Here, two approaches will be illustrated. In both approaches the capture of an image was always preceded by the capture of a background image. The background image was captured while keeping the optical shutter closed.

1. **The first acquisition approach** that we employed consisted in taking a number of images when no resistive heating was applied and subsequently taking a number of images when the resistive heating was turned on. Each of these two series of images was then averaged to give us two images, one without resistive heating and the other with resistive heating. By dividing the latter image with the former one, an image containing the normalized relative intensities of the heated structure could be obtained. The normalized intensity values of this image could then be converted to temperature values by the use of the calibration curve. Typically, 10 images were captured for each image series. To maximize the signal-to-noise levels, the exposure time of each image was set long enough to make use of the entire dynamic range of the camera but without saturating any camera pixel.

2. **The second acquisition approach** that was employed represented a significant improvement with regard to errors induced by fluctuations of the excitation light and possible photobleaching. Instead of taking a series of images once for the off-state and once for the on-state, the resistive heating was repeatedly turned on and off. Each time that the state was changed, a new image was captured. Switching the power on and off was performed manually. Once the images had been captured, each on-state image was divided by the preceding off-state image. This gave an image series containing the normalized relative intensities of the on-state. This series was then averaged to give one single normalized intensity image which was converted to a temperature map by the use of the calibration curve. Since this second approach implied that a new reference image (resistive heating off) was captured for every on-state image, fluctuations over time of the excitation light as well as photobleaching effects were better compensated for. Typically, we took 15 images for each nanowire state.

With both approaches, the acquisition of more images would evidently lead to a better accuracy of the resulting temperature maps. The main problem in both cases was the movement of the nanowire sample during the acquisition. Since we typically captured images at intervals of around 2-3 seconds, the entire process would take more than a minute. In some cases, the sample was relatively steady, but mostly, the sample moved several tens, sometimes hundreds, of nanometers during the acquisition period. This obviously led to a deterioration of the spatial resolution, which became worse for longer

acquisition times. In the first approach, the shortening of the acquisition period can be achieved with relative ease. However, in the second approach, shortening of the entire acquisition period would require the use of a computer-aided synchronization of the optical shutter, the camera and the power source.

The image treatment was mainly performed in MATLAB from MathWorks. Typically, processing of an image in the IQ software led to incompatibilities with other software. In order to avoid problems with image formats, image processing was therefore preferably performed entirely in MATLAB. Possible alternatives to the IQ software which were used for some processing were MetaMorph from Molecular Devices and the freeware ImageJ.

4.1.6 Acquisition of time series for transient analysis

In order to enable a better temporal resolution for the transient analysis of the resistive heating, a high-speed camera (iXon 860 from Andor) was used. With this camera, the smallest possible interval between two consecutive images was 2 ms. The actual acquisition time was 1 ms and the electronic read-out required approximately 1 ms to be completed. During the acquisition of a time series, 3000 images were captured, equaling 6 seconds in total. In order to enable the high acquisition rate, no shutter was used and no background image was captured. Furthermore, the high acquisition rate required the use of a relatively small field of view in the IQ software. A rectangular field covering the location of the nanowire was defined. The average intensity of this field was then analyzed in order to determine the transient behavior of the average nanowire temperature. During the 6 seconds of capture, the on/off state of the resistive heating was changed manually after approximately 2 seconds.

4.2 Results

4.2.1 Dry Conditions

On oxidized silicon substrate

In Fig. 4.3, the results from a measurement on a 20-μm long and 200-nm wide nanowire on an unsuspended pure SiO_2 layer are shown. The different steps of the characterization process are illustrated throughout the figure. In this specific case, the second acquisition approach described above was used. 15 images were captured in total for each state of the nanowire. In Fig. 4.3b, the averages of each image series are shown for the case where a current of 2.3 mA was applied. A slight decrease of the intensity on top of the wire is seen in the on-state image. This decrease is made more obvious by normalizing the intensities of the on-state image with respect to the off-state image. The normalized intensities are shown in Fig. 4.3c, obtained by dividing the on-state image with the off-state image. By applying the calibration curve, the relative intensities of the normalized image can be converted to temperatures. The result of this is shown in Fig. 4.3d. Below the intensity and temperature images, linescans along and across the middle of the nanowire are shown.

The most striking observation that we can make from the resulting temperature map and linescans is the flat profile of the temperature along the nanowire and the strong confinement of the temperature change. Regarding the temperature distribution, the result is in good agreement with those results obtained during the FEM simulations of

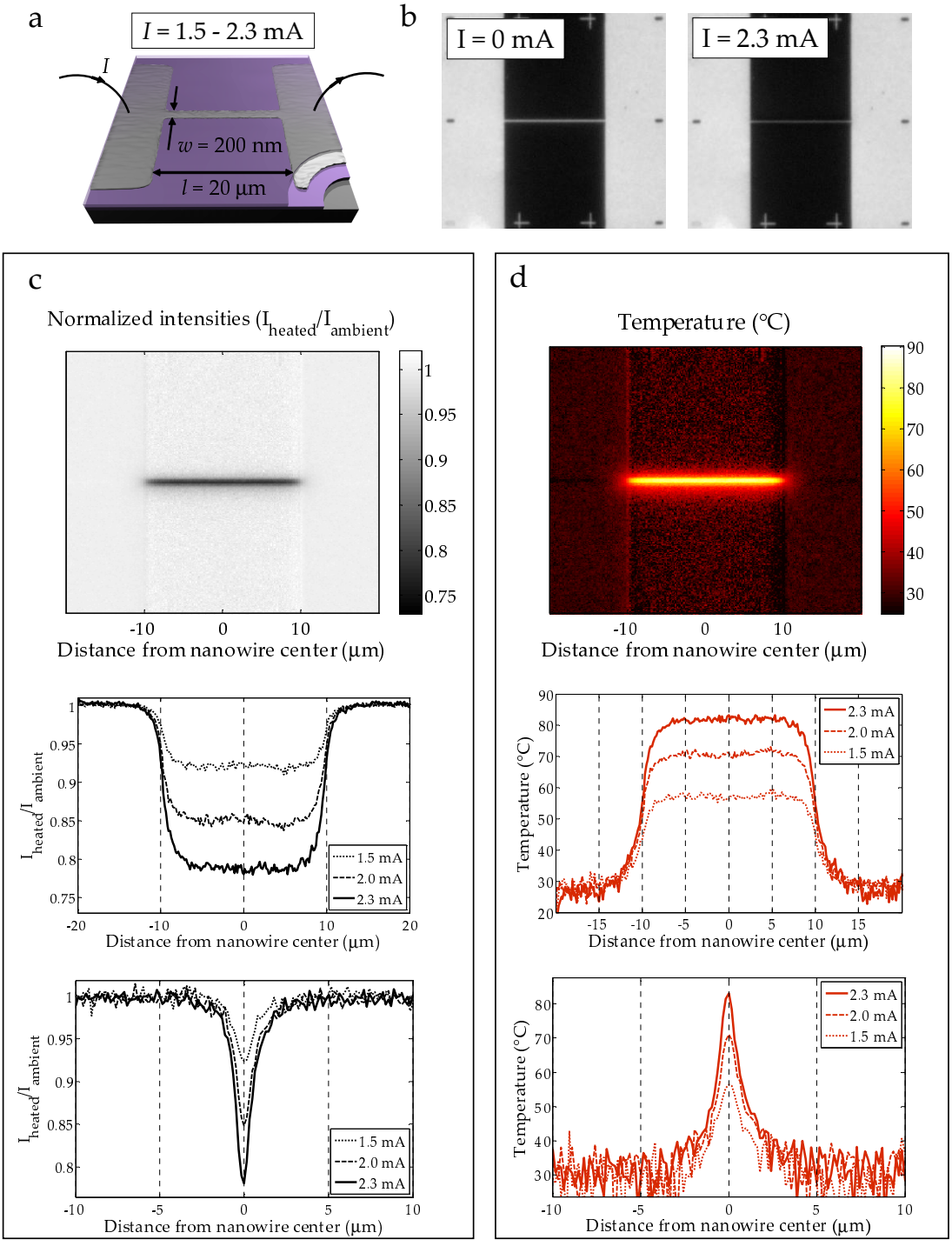

Figure 4.3: Thermal characterization of a nanowire on an unsuspended pure SiO_2 layer in air. a) Geometry. b) Fluorescent images taken for the off-state and the on-state (I = 2.3 mA). c) Normalized intensities of the on-state with regard to the off-state. The images show, from the top to the bottom, a surface map, a linescan along the wire and a linescan across the wire. d) From the top to the bottom, these images show a temperature map of the surface, a linescan along the wire and a linescan across the wire.

Chapter 2. However, by comparing the absolute temperature values, we find that there is a small discrepancy between the simulated and the experimental values. Although this might mean that there is an error in the calibration curve, it may also be an indication of the difficulty in making the appropriate assumptions in the FEM model regarding for example boundary conditions and heat transfer simplifications.

Another observation that is made is the augmentation of fluorescence fluctuations in the low temperature range, e.g. around 25-35°C. This should be no surprise if we recall the shape of the calibration curve for dry conditions. Between 25 and 35°C almost no change in the Rhodamine B fluorescence occurs which obviously leads to the inability to distinguish these temperatures. This is a good demonstration of the need to use a fluorescent probe which possesses a strong dependence on the temperature throughout the entire investigated temperature range. We can see that small fluctuations in the intensity image are magnified in the temperature map for this temperature range. At higher temperatures, the accuracy of the measurement becomes better.

It is also noted that the signal-to-noise levels are higher on top of the nickel areas. As commented previously, this is due to the higher reflectivity of light on those areas where nickel is present.

During the application of different current through the nanowire, we proceeded carefully, starting at low currents and increasing it step by step. It was noticed that if a too high current was applied, the heating of the nanowire would be sufficiently strong to induce thermal bleaching of the Rhodamine B molecules on top of the wire. This could be seen as the fluorescence did not fully recover when turning off the current. The thermal bleaching is estimated to have occurred typically in the range of 100-120°C

On suspended membrane

After the application of our fluorescent thermometry approach to verify the strong confinement of the temperature changes around a nanowire on silicon, we proceed to illustrate the temperatures of a nanowire on a suspended SiO_2/SiN_x membrane. In the case of this specific suspended membrane, the characteristic size of the membrane was more than twice the size of the nanowire length, i.e. relatively large. In Fig. 4.4, the results of the resistive heating in the 20-μm long and 500-nm wide nanowire is shown. The second acquisition approach was used also in this case with a total of 15 images each for the on- and off states. Already in the fluorescent images of Fig. 4.4b, it is seen that the temperature changes are more spread out than for the unsuspended membrane. The fluorescence intensity is decreased at considerable distances away from the wire. By normalizing the intensities of the on-state image and converting to temperature (Fig. 4.4c and d), the spread of the temperature changes is made yet more obvious. It is seen that, although there is a local temperature maximum at the nanowire, considerable temperature changes occurs throughout the entire field of view.

Influence of the membrane composition

As discussed in Chapter 2, the suspended membrane structure required the combination of silicon nitride and silicon dioxide in order to cancel internal stresses and maintain membrane stability. In the FEM simulations, we found that on top of silicon, the membrane composition had a certain influence on the temperature distribution around the nanowire. Experimentally, we could verify the result predicted by the simulations.

In Fig. 4.5, the experimentally obtained temperature distribution around a nanowire

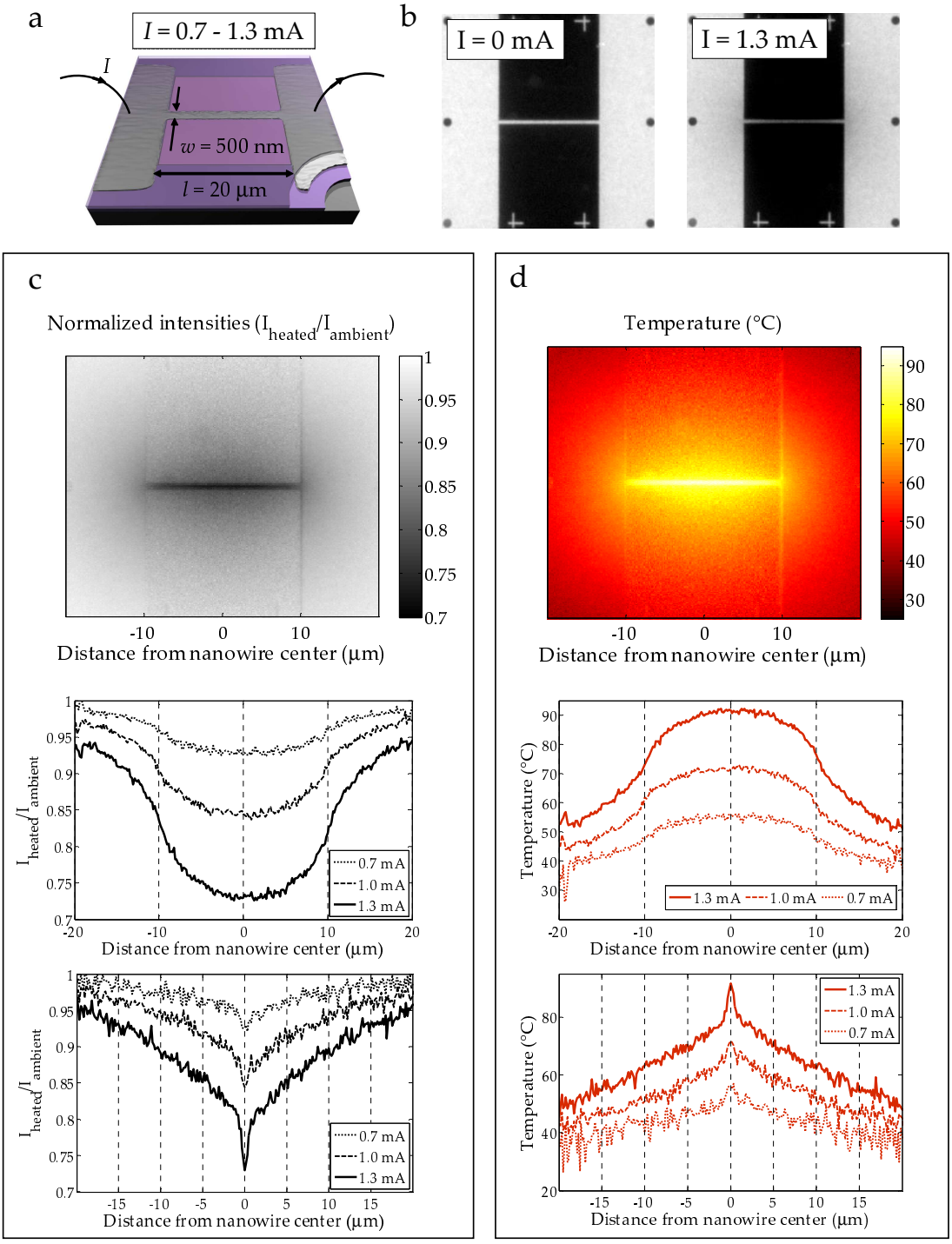

Figure 4.4: Thermal characterization of a nanowire on a suspended SiO_2/SiN_x membrane in air. a) Geometry. b) Fluorescent images taken for the off-state and the on-state (I = 1.3 mA). c) Normalized intensities of the on-state with regard to the off-state. The images show, from the top to the bottom, a surface map, a linescan along the wire and a linescan across the wire. d) From the top to the bottom, these images show a temperature map of the surface, a linescan along the wire and a linescan across the wire.

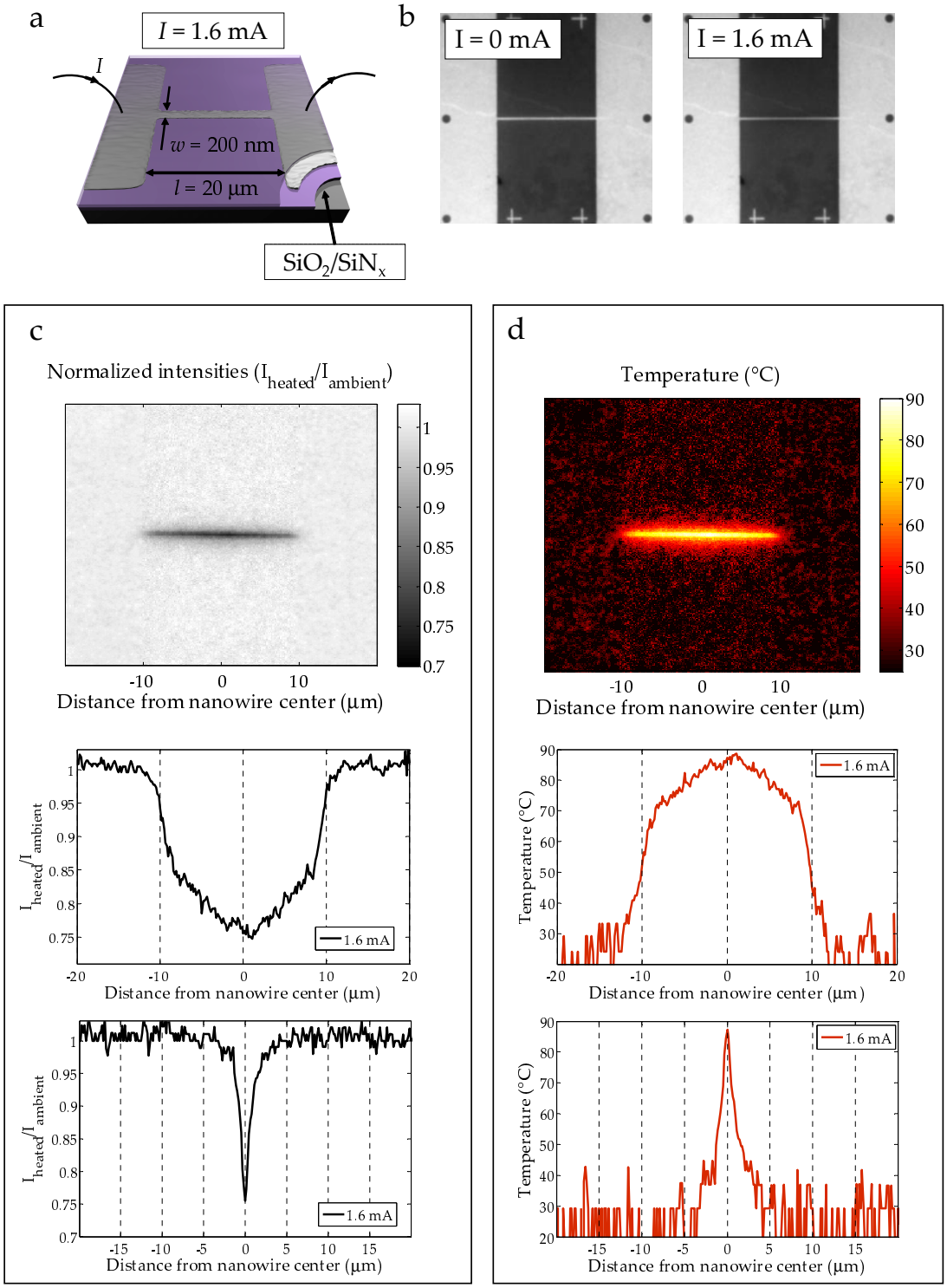

Figure 4.5: Thermal characterization of a nanowire on an unsuspended SiO_2/SiN_x membrane in air. a) Geometry. b) Fluorescent images taken for the off-state and the on-state (I = 1.6 mA). c) Normalized intensities of the on-state with regard to the off-state. The images show, from the top to the bottom, a surface map, a linescan along the wire and a linescan across the wire. d) From the top to the bottom, these images show a temperature map of the surface, a linescan along the wire and a linescan across the wire.

on top of an unsuspended SiO_2/SiN_x layer is shown. The result was obtained using the first acquisition approach described previously. 10 images were captured for the off-state and subsequently 10 images were captured for the on-state. The averages of these two image series were then used to calculate the temperature map. Compared to the results obtained for an identical nanowire on top of a pure SiO_2 layer, the heat is to some extent more spread out. Most obviously, the temperature along the wire is seen to have a more parabolic shape than the very flat profile of the nanowire on top of pure SiO_2. As mentioned already in Chapter 2, the reason for this higher spread of the heat is the high thermal conductivity of the silicon nitride.

While discussing the results in Fig. 4.5, it is noted that the temperature linescans possess a seemingly quantized behavior at the low temperatures. The reason for this was that in this specific case, the image was treated partly in the IQ software. Since we failed to make a backup of the original file, only the treated image was left for further processing. Because of the incompatibility of IQ-processed 16-bit images with other software, we had to make a conversion to 8-bit, which led to a certain loss of information.

4.2.2 Liquid conditions

While much time was spent for the development of the temperature measurements in dry conditions, the results found in liquid conditions are still at this point quite preliminary. However, the obtained results are of great interest for further developments of the technique and will be discussed in the following. As shall be seen, the main problem encountered to this point is the possible re-dissolution of the streptavidin-Rhodamine B conjugates in the immersion liquid which seems to lead to measurement errors.

In Fig. 4.6, the temperature measurements done on a 20-μm long and 500-nm wide nanowire immersed in water and located on an unsuspended SiO_2/SiN_x layer is shown. The temperature distribution along the wire is relatively flat as expected from the FEM simulations and the confinement is high. In the case of this measurement only 4 images were used to create an intensity image. This led to a relatively high noise.

In Fig. 4.7, the heating of a 20-μm long and 500-nm wide nanowire on a suspended membrane is shown. The measurements were performed with the sample surface immersed in water. The spread of the heat is larger than for the unsuspended membrane as predicted by the FEM simulations. Once again, we note that considerable noise is present in the measurement. Like in the previous case, only a few images were acquired, which partly explains the high noise levels.

Discussion on the measurements in liquid conditions

In the case of of the immersed nanowires, it was observed that thermal bleaching of the Rhodamine B molecules occurred at a relatively low temperature, typically already at 45-50°C. This is very different from the bleaching temperature found during the temperature cycles made previously in this chapter. It is also very different from the typical bleaching temperature observed for the dry Rhodamine B molecules. Our current interpretation of this is that, in spite of our efforts to bind the streptavidin-Rhodamine B conjugates at the surface, there is a considerable amount of conjugates which depart from the surface into the solution during the experiment. Such re-dissolution leads to unwanted fluorescent signals from the liquid on above the surface. Since the temperature changes induced by the nanowire are highly localized around the wire, the extra fluorescent

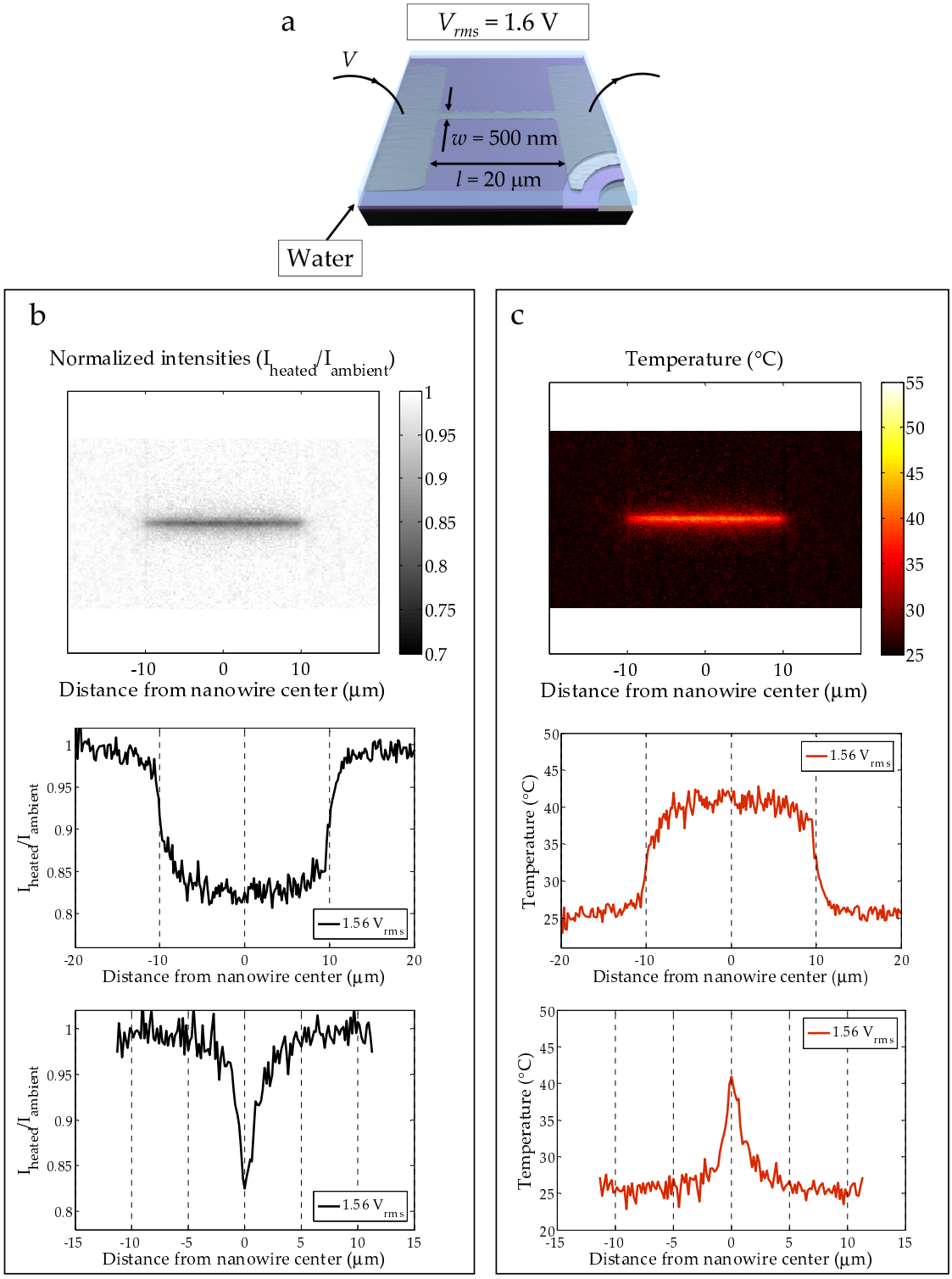

Figure 4.6: Thermal characterization of a nanowire on an unsuspended SiO_2/SiN_x membrane in a water. a) Geometry. b) Normalized intensities of the on-state with regard to the off-state. The images show, from the top to the bottom, a surface map, a linescan along the wire and a linescan across the wire. c) From the top to the bottom, these images show a temperature map of the surface, a linescan along the wire and a linescan across the wire.

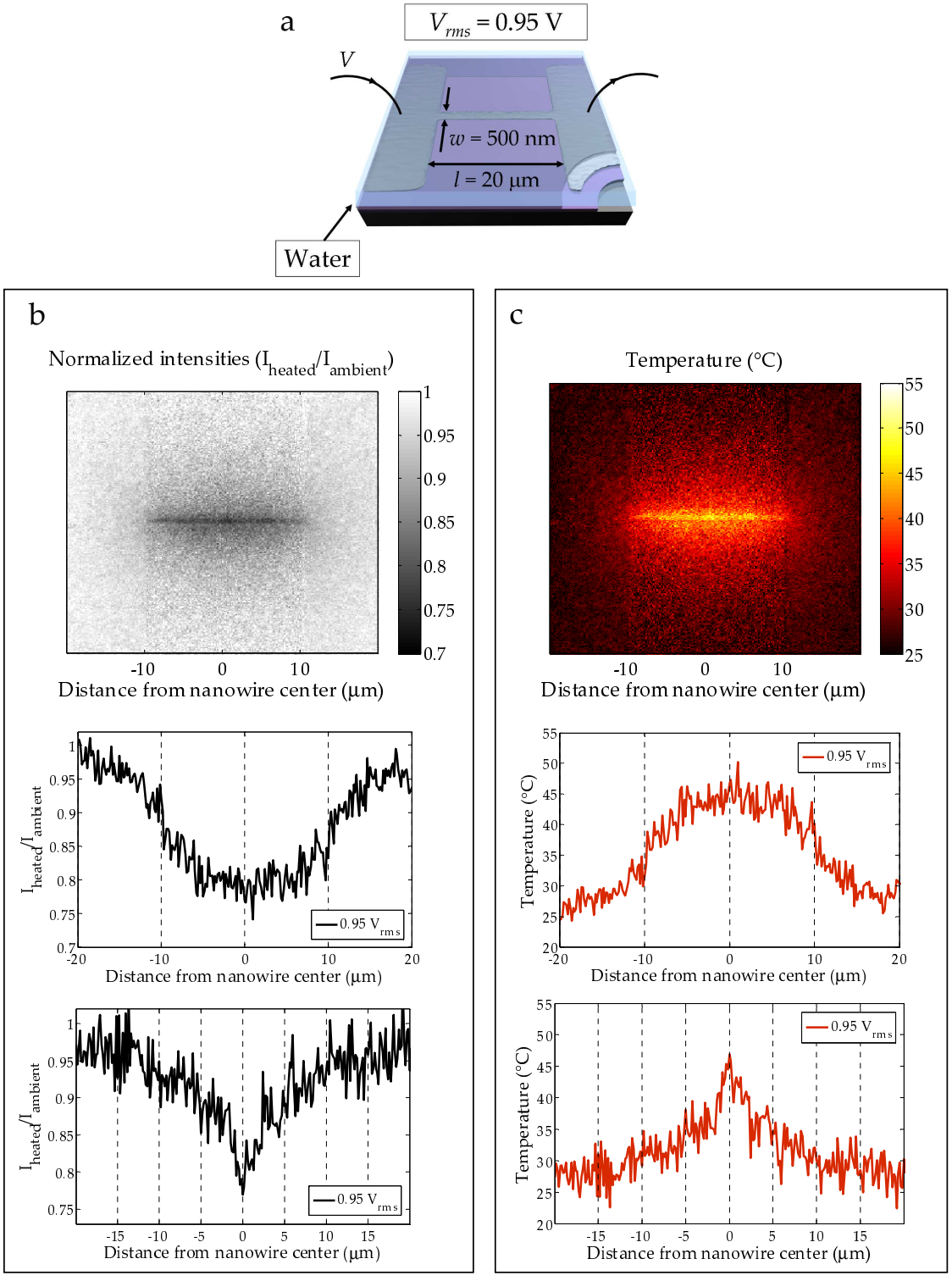

Figure 4.7: Thermal characterization of a nanowire on a suspended SiO_2/SiN_x membrane in water. a) Geometry. b) Normalized intensities of the on-state with regard to the off-state. The images show, from the top to the bottom, a surface map, a linescan along the wire and a linescan across the wire. c) From the top to the bottom, these images show a temperature map of the surface, a linescan along the wire and a linescan across the wire.

signals from the solution will correspond to lower temperatures and thereby introduce measurement errors. Therefore, the thermal bleaching is falsely observed to occur at a lower temperature than is actually the case.

If the assumption that re-dissolution occurs is correct, improvements of the binding protocol will help to improve the measurements. The most urgent change that we propose for further experimentation is the use of a biological buffer instead of the de-ionized water used so far. Considering the electrostatic nature of the surface binding, the importance of keeping the pH stable at a certain level is of particular importance. A different way to improve the situation is to employ a different binding protocol, using for example an aminosilane to chemically bind the Rhodamine B molecules to the silicon dioxide surface.

4.2.3 Transient analysis

In the following, the transient analysis of nanowires in dry conditions is presented. In Fig. 4.8, the transient response of the temperature on a 20-μm long and 200-nm wide nanowire when turning on and off the resistive heating is shown. The nanowire is located on an unsuspended SiO_2 membrane. The next figure, Fig. 4.9, shows the case of a 20-μm long and 500-nm wide wire on top of an unsuspended SiO_2/SiN_x membrane. Finally, in Fig. 4.10, the response time of a 20-μm long and 500-nm wide wire nanowire on top of a suspended SiO_2/SiN_x membrane is shown.

The curves in the graphs show the transient evolution of the average fluorescence intensity on top of the respective nanowire. Due to the direct relation between the Rhodamine B fluorescence and the temperature, the transient thermal behavior of the nanowire can be determined directly form the fluorescence, without the need to convert to temperature first.[2]

Although the noise in the graphs is considerable, it is indeed possible to verify the fast response of the temperature changes, with thermal time constants (the time when 67% of the final value is reached) close to or below one millisecond in all cases. However, the exact temporal behavior is difficult to determine with this amount of noise. In some of the graphs, the temperature stabilization seems to take longer than the length of several frames, i.e. several tens of milliseconds. We conclude that, with the current experimental data, no big difference can be established between the different configurations. Due to the noise and the inconsistency between consecutive measurements, final conclusions on the stabilization times and time constants can not be made.

Possible explanations for the seemingly slower response times, compared to those found in the FEM simulations, may be the use of an excessively simplified FEM model. For example, the assumption that convection plays a negligible role might be bad and the assumption that the peltier-based temperature stage manages to keep the bottom surface of the sample at a constant temperature may also be incorrect. This means that larger heat capacities than foreseen are present in the system, which delays the stabilization time of the system.

The measurements performed here on the temperature stabilization times represent the first of more thorough measurements to be done in the future. It is clear that the use of a CCD camera has major limitations in the use for transient analysis. Better

[2]We assume that the intrinsic changes of the Rhodamine B molecule, which give rise to its temperature dependence, occur much faster than the thermal changes being probed here.

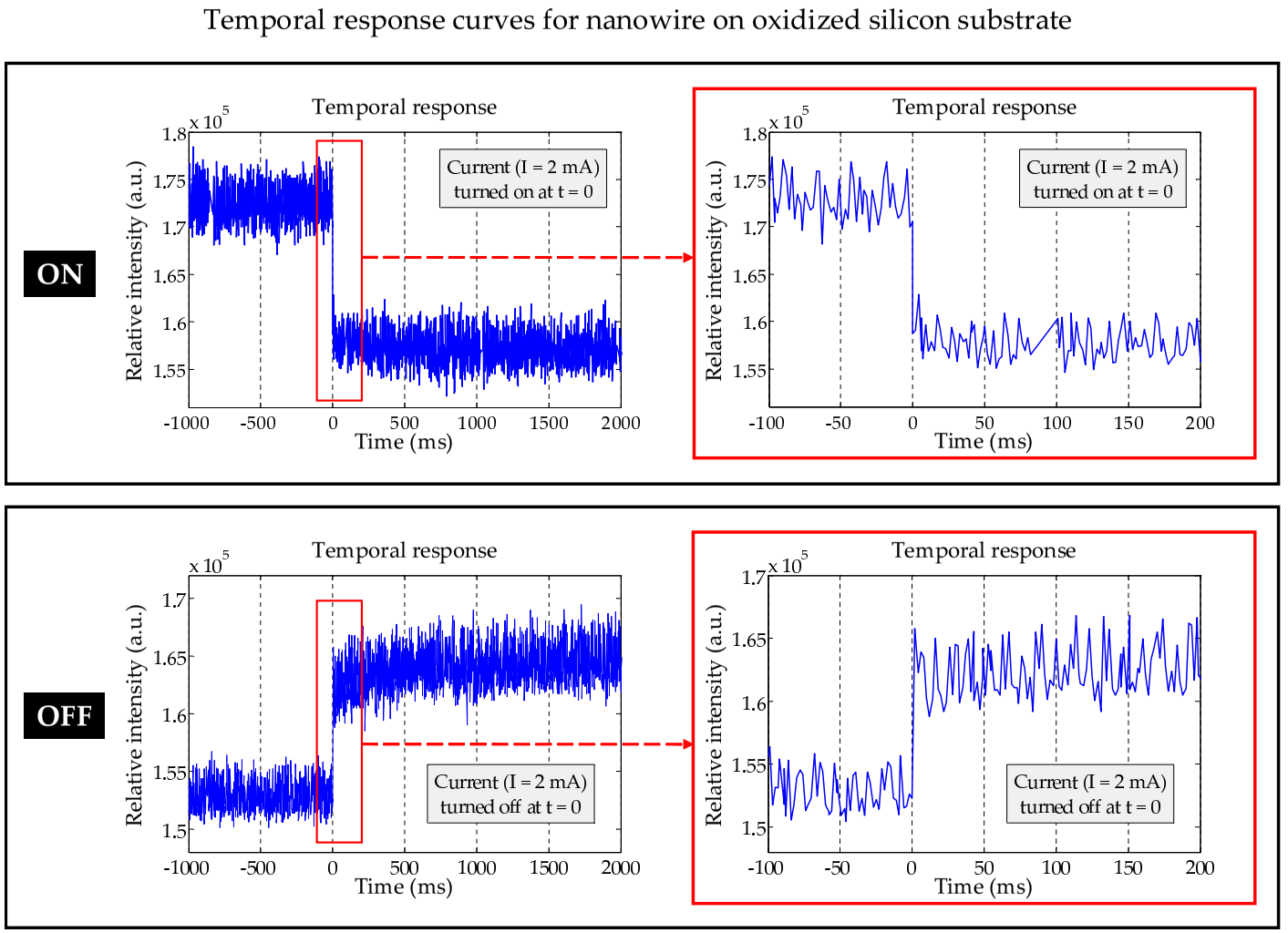

Figure 4.8: Transient response of the fluorescence intensity on a nanowire located on an *unsuspended* SiO_2 layer.

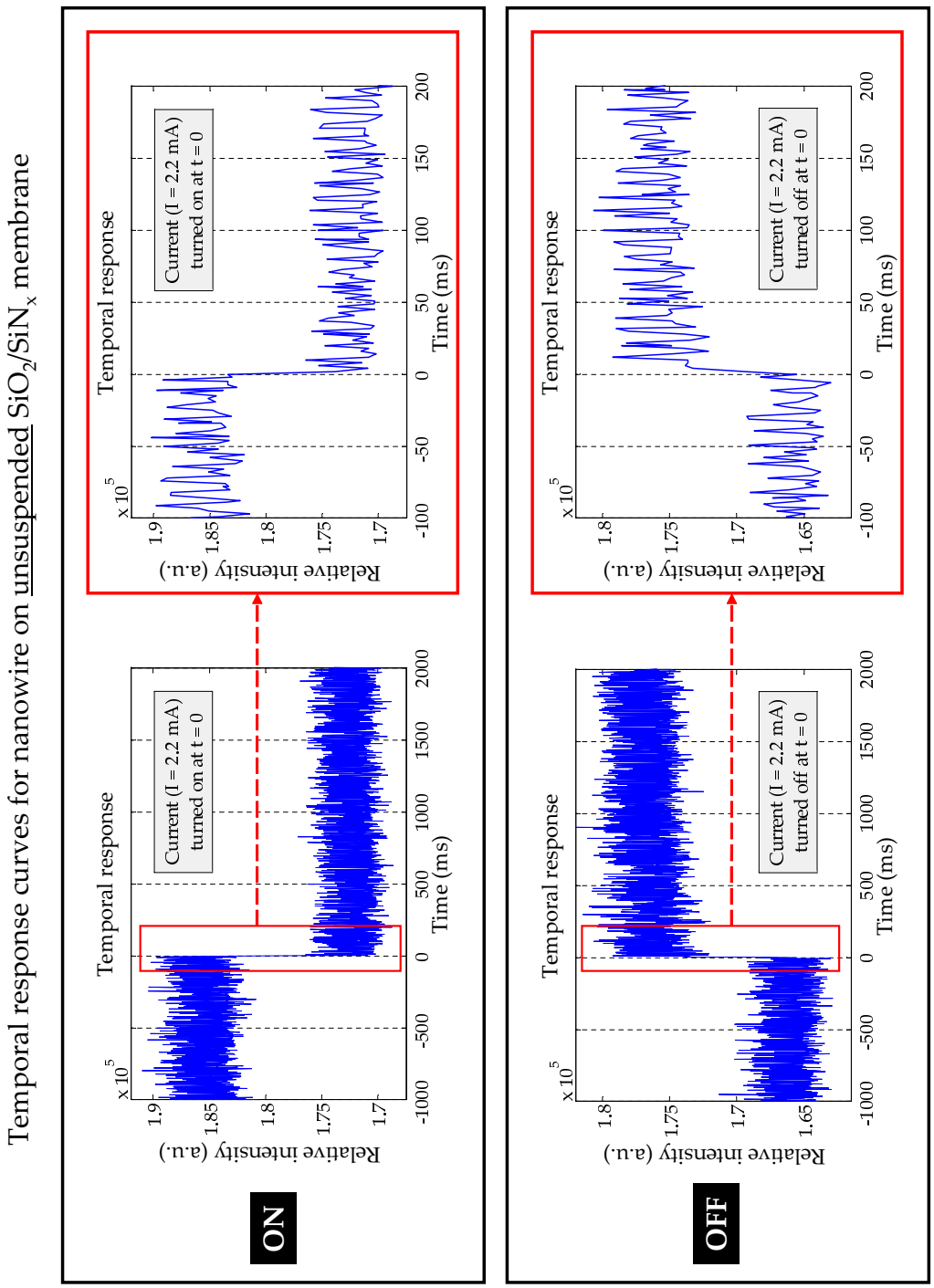

Figure 4.9: Transient response of the fluorescence intensity on a nanowire located on an *unsuspended* SiO_2/SiN_x layer.

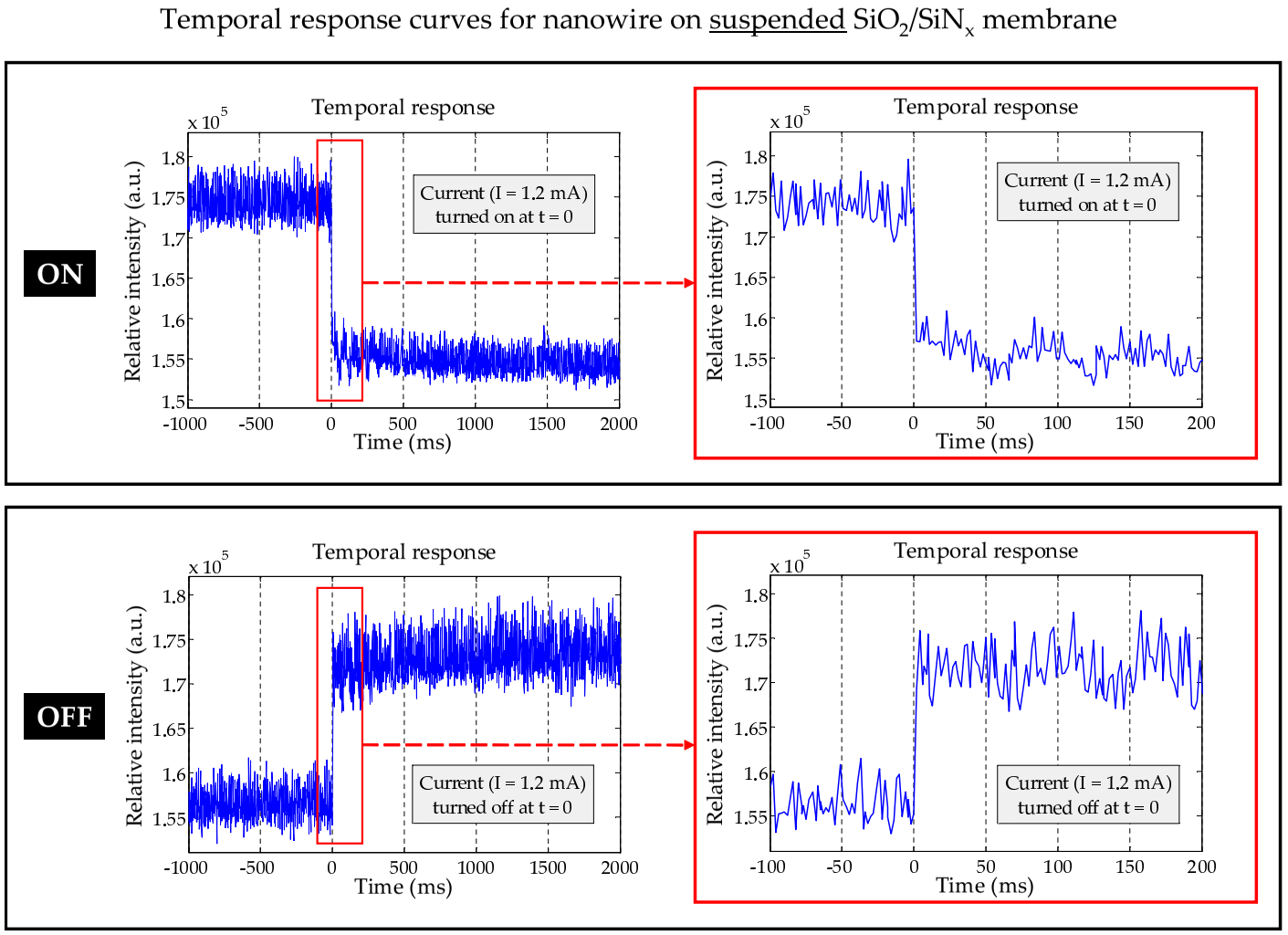

Figure 4.10: Transient response of the fluorescence intensity on a nanowire located on a *suspended* SiO_2/SiN_x layer.

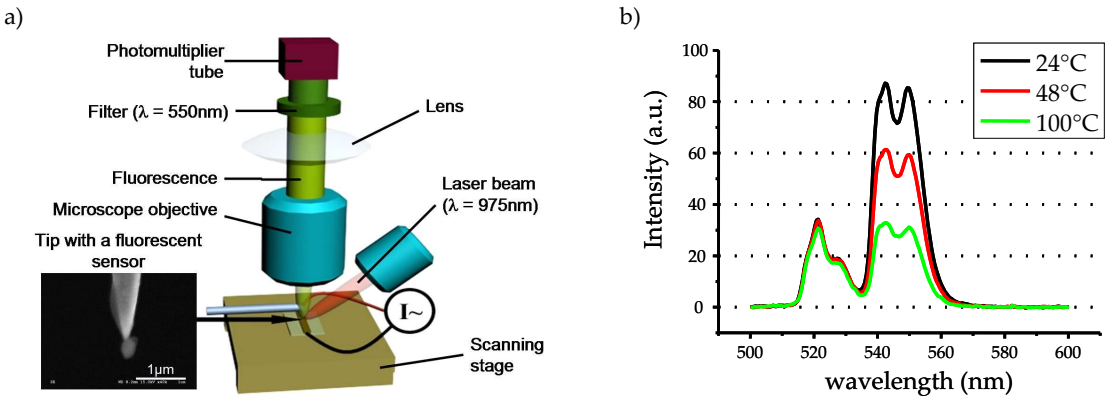

Figure 4.11: a) Setup and principle of the fluorescent probe SThM. A fluorescent rare-earth doped particle is attached at the end of an AFM tip. By scanning the particle over a surface while monitoring the fluorescence changes of the particle, information on the surface temperatures can be extracted. b) The temperature dependence of the ytterbium/erbium co-doped fluoride glass particle used as a probe. The fluorescence contains two peaks, one which is independent of the temperature and another one which is strongly dependent on the temperature. A FIR protocol is used for the fluorescence analysis and the temperature determination. [104–106]

temporal resolution may be achieved by the use of a photomultiplying tube instead. Although this means the sacrifice of spatial resolution, it is an appropriate trade-off to make since the transient analysis only has to be done at one or a few points to give a good understanding of the thermal time constants of the system.

Another approach that could be investigated is the thermal measurements by electronic means. This could, for example, be done by measuring the of the temperature dependent resistance changes of the nanowire. Another possibility may be the use of the 3ω-method which generally gives very accurate thermal characterizations.

4.3 Preliminary comparisons with fluorescent probe SThM

For the purpose of further evaluating the reliability of our fluorescent thermometry approach, two of our nanowire samples were submitted to the ESPCI-CNRS laboratory in Paris, where a SThM technology based on fluorescence measurements is being developed[3]. One of the submitted samples consisted of a 20μm-long and 200nm-wide nanowire and the other was a 80μm-long and 1μm-wide microwire. Both wires were deposited on an unsuspended 500nm-thick SiO_2 layer. Although the SThM measurements are still on-going, some of the results obtained so far will be presented in this section.

The SThM technique, which was partly described in the review of Chapter 1, consists in the use of a fluorescent particle glued at the end of an atomic force microscope (AFM) tip as a nanoscale temperature sensor (see Fig. 4.11a) [104–106]. The fluorescence

[3]The SThM research of the group is directed by Dr. Lionel Aigouy.

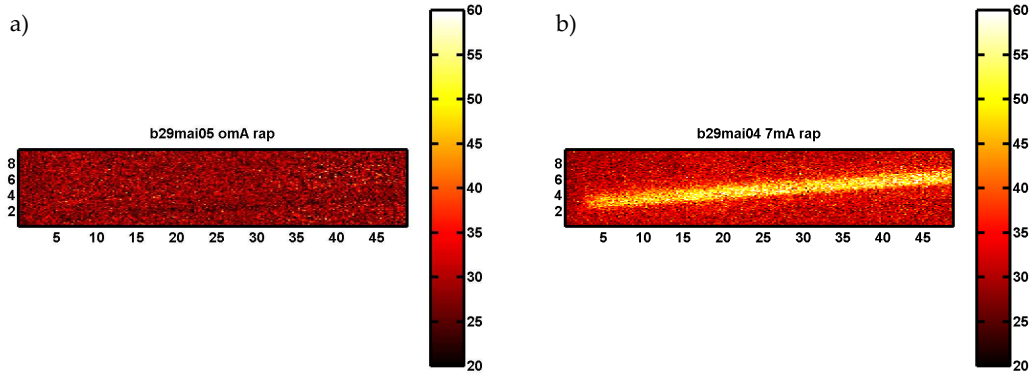

Figure 4.12: Result of the SThM measurement of the changes in fluorescence intensity ratio over a microwire sample. The microwire used here was 40 μm long and 1 μm wide. The intensity ratios are proportional to the temperature changes. Thus, the map represents an image of the relative temperature values throughout the surface. The images in (a) and (b) show the cases where no current and a current of 7 mA (DC) were applied, respectively.

emitted by the particle is modified by temperature changes. Thus, by collecting the emitted light during the scan of a sample, a temperature map of its surface can be acquired. The particle used is an ytterbium/erbium co-doped fluoride glass particle. The temperature is determined by analyzing the ratio of the two fluorescence peaks shown in Fig. 4.11b.

In Fig. 4.12, the result of the SThM measurements on the microwire are shown. The maps show the fluorescence intensity ratios measured throughout the sample surface, which largely correspond to the relative temperature values. When the resistive heating is turned on, it is seen how the temperature changes are confined to the microwire and its immediate vicinity. Similarly, the measurements on the 200nm-wide nanowire (Fig. 4.13) show a high resemblance to the results obtained with our fluorescent thermometry approach (Fig. 4.14). A linescan of the SThM fluorescence intensity ratios across the nanowire show that the temperature change is highly confined to the nanowire and its nearest surroundings (Fig. 4.13b).

4.4 Conclusions & discussions

We have in this chapter illustrated the final steps taken to adapt fluorescent thermometry for surface temperature measurements of high spatial resolution. In line with the results from Chapter 3, Rhodamine B was chosen as a fluorophore for the thermal characterization of our nanowire systems. The main resolution-improving factor of our approach consisted in the confinement of the fluorophores in the vicinity of the surfaces to be characterized. In dry conditions, the Rhodamine B molecules were confined to the surface simply by a deposition and drying process. In liquid conditions, confinement to the surface was attempted by the use of an electrostatic bond between polylysine and streptavidin.

The acquisition approach was exclusively based on single intensity measurements,

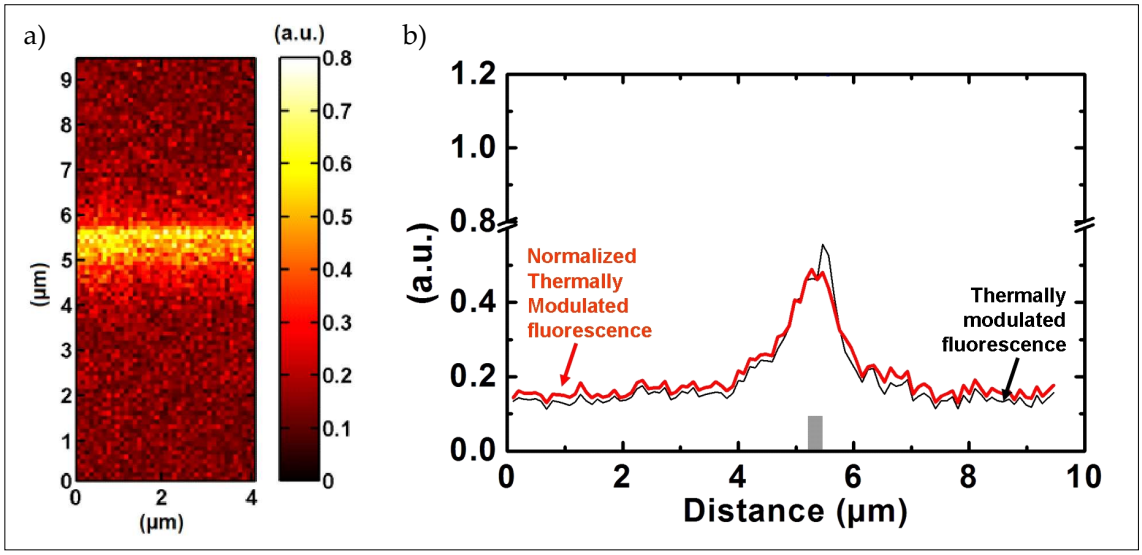

Figure 4.13: a) Image of the thermally modulated fluorescence acquired during the scan of a 200nm-wide nickel nanowire which was resistively heated with an AC current modulated at 543Hz and varying between 0 and 2mA. b) Linescans across the nickel nanowire. The thin black curve represents the raw thermally modulated fluorescence and the thick red curve represents the thermally modulated fluorescence normalized by the room-temperature fluorescence in order to minimize the influence of fluorescence not originating from the probe. The gray rectangle indicates the position of the nickel wire.

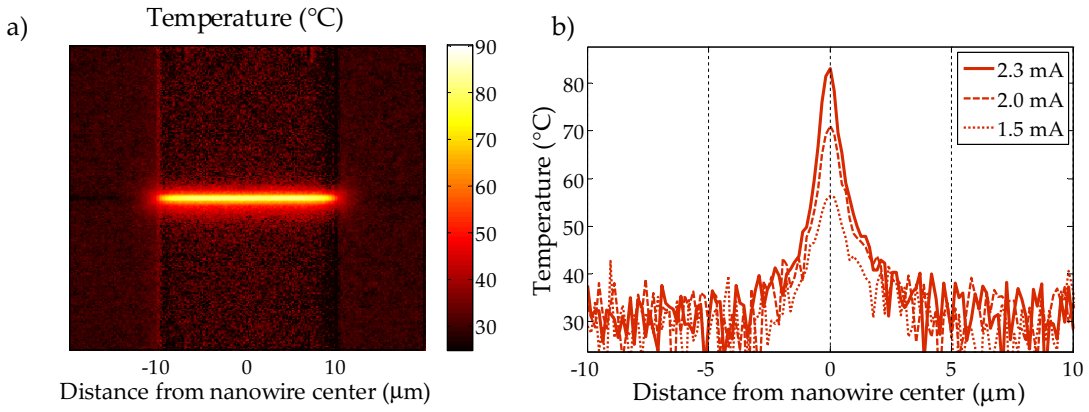

Figure 4.14: a) Temperature distributions on a 20μm-long and 200nm-wide nickel nanowire (identical to the sample studied by SThM) as measured using our approach for fluorescent thermometry. The applied current was in this case 2.3 mA. b) Linescan across the center of the same nanowire.

by the acquisition of the fluorescence peak of each fluorophore. This introduced possible sources of uncertainty in the measurements mainly due to photobleaching effects and fluctuations of the excitation light source. In order to minimize the influence of these effects, an acquisition process where a reference image was acquired before the acquisition of each main image was developed. To increase the signal-to-noise levels, all measurements were done at the local intensity maximum of the photostability curve, which was found in Chapter 3.

An excellent agreement of the experimental results with the simulations of Chapter 2 could be confirmed regarding the spatial temperature distributions on different sample configurations. In addition, comparative studies of the spatial temperature distribution around one of our nanowires using a fluorescent probe SThM supported the obtained results.

4.4.1 Discussion on the spatial resolution

The fundamental limit to the spatial resolution will obviously be the diffraction limit of light. However, from a practical point of view, the main challenge that has to be surmounted in order to assure the best possible spatial resolution is the movement of the sample during the image series acquisition. During our measurements, submicrometer movements were easily induced in the sample by strain originating for example in the electrical connection cables. A solution to this problem could be to further develop the way that the sample is mounted on the microscope stage in order to minimize or completely cancel the existing strains. Another way could be to perform a digital alignment process of the captured images once the entire image series is acquired. However, such an approach would be tedious and time-consuming unless an automatic alignment process can be implemented.

Submicrometer resolution Supported by the results achieved in FEM simulations and with the SThM technique, we believe that the developed fluorescent thermometry allows for spatial resolutions well below one micrometer. To further quantify the spatial resolution it will be of value to continue the comparative studies with SThM and to investigate alternative sample structures with more complex temperature distributions. Interesting alternative samples could for example consist of closely packed nanowires on silicon, which might be used to create submicrometer spatial variations of the temperature.

4.4.2 Discussion on the temperature dependence, range and resolution

High-performing acquisition process The temperature resolution is determined partly by the accuracy of the calibration curve (described in Chapter 3) and partly by the quality of the fluorescence acquisition on the sample to be characterized. As we have seen in this chapter, the quality of the acquired fluorescence images can be very high as long as a rigorous acquisition process is used, with averaging over many images. The further optimization of this should be relatively straightforward with the main issue being the small movements of the sample over the long acquisition times.

Improving the calibration While the acquisition process can give high quality images, the calibration curve is currently assumed to be the main source of inaccuracy in the temperature resolution of our measurements. During the capture of the calibration curve, well-defined temperatures have to be imposed on the fluorophores. However, we do not currently know if the convection of air on top of the sample has a large effect on the fluorophores. In addition, we do not know how large the temperature gradient from the temperature stage to the sample surface is. This leads to inaccuracies in the measurement of the calibration curve. Furthermore, the calibration curve is acquired over a relatively long time which may lead to considerable fluctuations in the excitation light source. This inevitably introduces inaccuracies in the calibration.

The use of a closed temperature control chamber for the calibration may be envisioned in order to better establish the different temperatures. Such chambers are provided as microscope stages by various manufacturers, e.g. Linkam, although at a considerably higher price than the simpler heating stage used in our experiments.

With the current setup, the best way to improve the accuracy of the calibration curve is to repeat the acquisition of the calibration curve many times and analyze the mean values. It would also be interesting to try an approach where the fluorophores are cycled repeatedly between two temperature values in order to determine the relative change of intensity. By repeating this for a range of temperature pairs, the calibration curve could be determined. This approach would allow for an easier identification and distinction of the photobleaching effects, the thermal bleaching effects at certain temperatures and the reversible fluorescence behavior.

Temperature resolution and range Under optimal conditions and by the averaging of a large number of images, the temperature resolution in dry conditions was at its best around 5°C. By the improvement of the calibration of the temperature dependence, this resolution can be expected to reach at least 1°C . From the point of view of typical biological and biomolecular essays, a resolution of a few degrees should be largely sufficient. Considering the suitability of fluorescence measurements in biological applications, this means that there should be a great interest already in the application of our fluorescent thermometry in these fields.

The applicable temperature range in the case of Rhodamine B in dry conditions was 35-95°C. The lower limit was imposed by the lack of temperature dependence below 35°C and the upper limit was imposed by thermal bleaching effects.

4.4.3 About liquid conditions

The polylysine bond The measurements performed in liquid conditions to this point will need further improvement in order to give reliable results. At this point, the results are mainly interesting in determining the spatial temperature distributions but not in determining the actual temperature values. It has been seen here that the proposed binding protocol did not seem to suffice in keeping the fluorophores bound at the surface. This in turn is suspected to have given rise to measurement errors due to the inclusion of fluorescence not only from the surface. For future investigations, it will be important to apply a buffer solution instead of deionized water (which was used so far) in order to keep the pH under strict control. Considering the electrostatic nature of the polylysine bond, a fluctuating pH level may have a substantial negative impact on the streptavidin-Rhodamine B confinement at the surface.

Alternative binding protocol As an alternative to the polylysine protocol, other more robust binding protocols should be investigated, e.g. the use of chemical binding by the silane-biotin-streptavidin bond.

Potential of thermometry in liquid As a final remark regarding the liquid conditions, it is interesting to recall that the calibration curve for the streptavidin-Rhodamine B conjugates was steeper than the corresponding curve for dried Rhodamine B molecules. This holds promise for a better temperature resolution in liquid conditions than in air as soon as the binding of the molecules on the surface can be assured.

4.4.4 The transient thermal analysis

In the end of this chapter, we presented the attempts made to perform transient thermal analysis of the nanowire systems using fluorescent thermometry. It was seen that considerable noise was present in the temporally resolved fluorescent measurements. This made it difficult to draw any final conclusions, although thermal time constants close to or even below one millisecond could be determined. A clear difference between the different sample configurations, as expected from the FEM simulations of Chapter 2, could not be verified.

Signal improvements If we consider improvements of the transient measurements in the immediate future, it should be straightforward to improve the signal-to-noise levels of the current curves simply by performing repeated acquisitions of the same transient event a large number of times. By studying the average of a very large number of curves, the characteristics of the curves will be more easily distinguished. An interesting approach would be to enhance the current experimental setup with a module allowing for the synchronization of the applied currents and the camera system. This way, a large number of curves could be acquired automatically.

Alternative characterization methods Alternative future approaches for the transient analysis of the nanowire systems may be the use of fluorescence acquisition by photomultiplying tube or the analysis of the temperature dependent electrical resistance of the nanowires. Another interesting technique that also could be used to some extent for transient analysis is the 3ω-method.

CHAPTER 5
GENERAL CONCLUSIONS & FUTURE DIRECTIONS

We have in this thesis pursued the development of an improved methodology for fluorescent thermometry. Specific focus has been placed on the improvement of the spatial resolution. The developed technique represents a cost-efficient and simple approach for the quick thermal characterization of surface structures comprising submicrometer features. The current state of the technique allows for high spatial resolution and satisfactory temperature resolution in dry conditions whereas the application in liquid conditions will need further improvement to obtain reliable characterizations. Due to the general familiarity with fluorescence measurements in biological labs and the typical availability of the required equipment, the results are of particular interest for the application in the thermal characterization of microbiological on-chip devices, e.g. lab-on-a-chip systems. Further improvements of the technique for liquid conditions will provide a unique tool for the thermal characterization of nanostructured surfaces immersed in a liquid, e.g. various microfluidic devices.

The developed thermometry approach was used to experimentally perform thermal characterization of nanoscale heat sources based on resistive heating in nickel nanowires. Experimental data from the fluorescent thermometry on these nanowire systems confirmed the high spatial confinement of the thermal impact which had been predicted by the use of FEM (Finite Element Method) simulations. Both simulations and experimental measurements demonstrated clearly the impact of the nanowire environment in determining the thermal behavior of the system. It can be concluded that the use of a high thermal conductivity substrate underneath the nanowire is highly beneficial in terms of confining the thermal impact. Although not clearly confirmed by fluorescent thermometry, the FEM simulations showed clear indications that high thermal conductivity substrates are also beneficial in seeking to optimize the thermal time constant of the system.

5.1 Potential further improvements of fluorescent thermometry

In the development of our fluorescent thermometry approach, a range of potential improvements were identified. Due to time constraints, most of these improvement paths were not deeply investigated within the current work. Nonetheless, for the purpose of

future investigations, the possible paths to improvement will be discussed in the following.

5.1.1 Alternative fluorescent probes

We have seen that the CdSe/ZnS nanocrystals did not provide sufficient fluorescence stability for the use as a reliable fluorescent probe. Instead, Rhodamine B was found to be the most appropriate probe due to the better reversibility when exposed to consecutive temperature cycles. In future applications of our fluorescent thermometry approach it would be of great interest to continue the investigations on alternative probes. While Rhodamine B clearly is useful for temperature measurement, other probes with stronger temperature dependence and larger applicable temperature ranges would naturally provide measurements of higher quality. Among the most promising alternative candidates we find the rare-earth doped nanoparticles, e.g. the same kind used in the SThM device illustrated in Chapter 4. These types of fluorophores are particularly interesting due to the typical existence of several peaks in their fluorescence spectrum. This in turn gives potential for an FIR-based acquisition methodology. Other possible candidates are the Porphyrin and Ruthenium dyes which are briefly described in the extended fluorophore review in Appendix A.

5.1.2 Alternative acquisition methods

The acquisition approach applied so far for our fluorescence analysis has been based on single intensity measurements. When using semiconductor nanocrystals and Rhodamine B, this is the most straightforward approach. However, due to the inherent weaknesses of the single intensity measurements, e.g. the sensitivity to excitation light fluctuations and photobleaching, it is of great interest to make use of methods providing better compensation for these effects. Recalling the review of Chapter 1, four alternative methods exist: FIR (Fluorescence Intensity Ratio), two-color thermometry, FLIM (Fluorescence Lifetime Imaging) and spectral shift thermometry. Among these techniques, we believe that the FIR approach provide the most realistic alternative in terms of suitability for submicrometer measurements and fast full-field studies. FLIM may also be interesting, although it requires a more costly and complex setup and is less well suited for full-field analysis.

In terms of experimental setup, the FIR approach requires the addition of a few extra components in order to allow for the slightly more complex fluorescence analysis. Since two fluorescence peaks are to be measured, two acquisition devices must be used (e.g. two CCD cameras). A beam splitter also has to be inserted in the fluorescence light path in order to deflect half of the fluorescence towards the second camera. Furthermore, a total of two emission filters has to be used in order to allow for the isolation of the two different fluorescence wavelengths. Apart from these extra components, the principles remain the same. The probe (e.g. a rare-earth based fluorophore) should be calibrated in order to relate the intensity ratio to the temperature. Deposition of the fluorophores on the sample surface then allows for the full-field analysis of surface temperatures by converting local fluorescence ratio changes to temperature via the calibration curve.

5.1.3 Improvements of the experimental setup

As pointed out in Chapter 4, one of the most critical challenges to the achievement of high spatial resolution was the non-negligible movement of the samples during the acquisition of fluorescent image series. This issue should be given specific attention in future applications, e.g. by examining alternative mountings of the samples on the microscope stage and by developing a computer-aided method to align consecutive fluorescent images with each other before performing any averaging and temperature conversion. Alternatively, the use of an automatic microscope XY-stage and a feedback loop to the acquisition software might be developed in order to allow for real-time compensation of the movements. However, this would require the use of a very precise XY-stage.

A concrete improvement of the setup could be made by the use of a microscope stage that allows for automatic focus control, e.g. via a feedback loop between the acquisition software and the stage. This might decrease the total photobleaching since it would allow for a faster localization of the optimal focal plane. It would also more effectively assure that consecutive images are acquired at the same focal plane, particularly during the calibration process, as the surface of the sample is displaced to a great extent when changing the global sample temperature.

In the analysis of the local resistive heating on nanowires, the use of a computer-controlled power source would be valuable. By allowing for the synchronization between the camera, the optical shutter and the resistive heating, a large amount of consecutive images could be acquired, thus allowing for significantly reduced noise levels. In combination with automatic focus control and a viable method for the prevention of (or compensation for) sample movements, images with minimal noise and maximal spatial resolution could be acquired.

5.1.4 Measurements in liquids

We saw in Chapter 4 that the fluorescence-based temperature measurements in liquid conditions imposed greater experimental challenges than the measurements in dry conditions. In order to assure a high spatial resolution and the prevention of measurement errors, the fluorescent probes must be confined to the surface of the sample. Within this thesis, a preliminary attempt to confine the probes on the surface was done by the use of electrostatic binding between poly-L-lysine and streptavidin-conjugated Rhodamine B. In the experiments performed to this point, the proposed binding protocol has not so far been proved to be capable of holding the Rhodamine B fluorophores bound to the surface. While the results presented here were achieved in DI water, current essays are focused on the use of more rigorous pH control by appropriate buffers (pH 3-7) in order to increase the positive charge of the SiO_2 surface, which may result in a better electrostatic bond. For future improvements of the fluorescent thermometry approach in liquid conditions, alternative binding protocols may be investigated, e.g. the use of chemical bonds such as the silane-biotin-streptavidin bond.

Fluorescence correlation spectroscopy Another potential approach for the characterization of temperature in liquid may be the use of fluorescence correlation spectroscopy - FCS (see Fig. 5.1). This technique provides high-resolution spatial and temporal analysis of extremely low concentrated biomolecules in liquid conditions. It can be used to determine molecular properties such as diffusion constants and reaction rate constants.

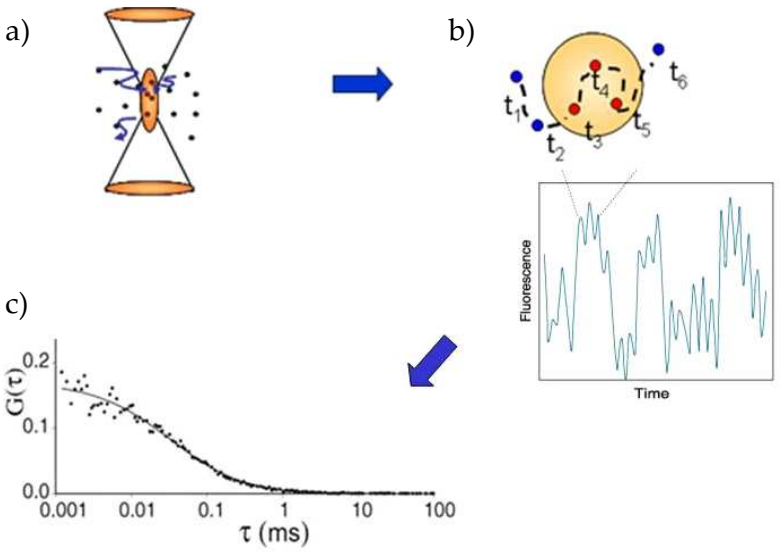

Figure 5.1: Principle of the FCS technique. a), b) The captured signal is determined by the intensity fluctuations which are related to the movement of fluorophores into and out of the observed field. c) The fluctuations result in a temporal correlation of the signal which can be analyzed using the autocorrelation function of the temporal intensity curve.

The technique relies not on quantitative intensity measurements, but rather on fluctuations and deviations from the equilibrium state. In general, all physical parameters that give rise to fluctuations in the fluorescence signal are accessible by FCS. Since the fluorescence fluctuations of fluorescent probes generally follow Boltzmann statistics, the temperature has a significant impact on the fluctuations and can thus potentially be determined by FCS. An example of a potential molecular thermometer for such an application is the green fluorescent protein (GFP) [151].

5.1.5 Alternative approaches for the transient analysis

Transient analysis of the nanowire systems was presented in the end of Chapter 4. Due to the limitation of our CCD camera to an acquisition rate of 500 frames per seconds, the highest possible temporal resolution was 2 ms. Due to high amounts of noise in the measurements at this small exposure time, final conclusions on the temporal behavior could not be made. However, the results did indicate that the final sample temperatures were not reached at a time below 2 ms since certain temperature stabilization seemed to proceed for a few tens of milliseconds. On the other hand, the thermal time constants (defined as the time when the temperature has reached 67% of the final value) are believed to lie close to or below one millisecond.

In order to improve the transient analysis of our nanowire systems, two approaches in particular are suggested. On one hand, the fluorescent thermometry could be applied with the use of a different type of acquisition device that provides a better temporal analysis, e.g. a photomultiplying tube (PMT). A PMT device would allow for both higher sensitivity and higher temporal resolution although largely limiting the characterization to point-by-point analysis. While full-field characterization is of great interest in the determination of spatial temperature distributions, the study of one or a few well-selected

points is most likely sufficient for the determination of thermal time constants and stabilization times of a system. Thus, the use of a PMT tube can most likely be established as the best path towards well-resolved transient analysis based on fluorescence thermometry.

In the case of our nanowires, a convenient alternative to the fluorescent analysis would be to take advantage of the direct relation between the temperature and the resistivity of the nanowire. By monitoring the change of resistance in the nanowire, the temperature changes can conveniently be tracked. Electrical measurements typically provide a much better temporal resolution than that achieved by optical acquisition with for example a CCD camera. Thus, resistance-based measurements can potentially provide a better tool than fluorescent thermometry for the transient analysis of our nanowires.

In order to further optimize the quality of the transient analysis, regardless of the method, it is of value to perform a large number of measurements using identical conditions. Similar to the comments made previously on the amelioration of the experimental setup, the use of an automated approach with synchronization between equipment would be useful. The repetition of the same transient event and the measurement of it for a large number of times would naturally improve the achievable accuracy by the minimization of the random noise in the signal.

5.2 Applications of the nanowire heat sources

Several interesting aspects were found regarding the thermal behavior of our nickel nanowires. The most well confirmed properties, verified both by FEM simulations and fluorescent thermometry as well as by SThM, were those regarding the spatial distribution of the temperature changes on and around the nanowires. The most interesting features were found for those nickel nanowires which were located on top of lightly oxidized silicon wafers. On these substrates, a highly uniform temperature distribution could be observed along the length of the wire. Furthermore, the temperature changes were highly confined with a quick decrease to ambient temperature when moving away from the nanowire. Regarding the temporal response of the nanowires, FEM simulations suggested that the thermal constants would lie at very low values, from below one microsecond to a few tens of microseconds, depending on the sample configuration. Nickel nanowires on lightly oxidized silicon wafers were indicated to give the fastest response. The experimental results did not verify the simulated results, although showing quite fast response with time constants close to or below one millisecond.

The results that we have seen here are of great interest in the development and integration of new functions in on-chip devices based on fast temperature modulation. Although not optimal from a power dissipation point of view, the best spatial and temporal behavior of our nanowire heaters seems to be achieved for the simplest possible configuration, i.e. for nanowires on top of oxidized silicon. With this configuration, the spatial confinement is higher which allows for a better and denser integration of many nanowire heating elements without the problem of excessive cross-talk. Furthermore, the flat temperature profile along the nanowire is appealing since it simplifies the spatial control of temperature in potential applications. Fortunately, these features are best achieved for a configuration which presents no particular fabrication difficulties.

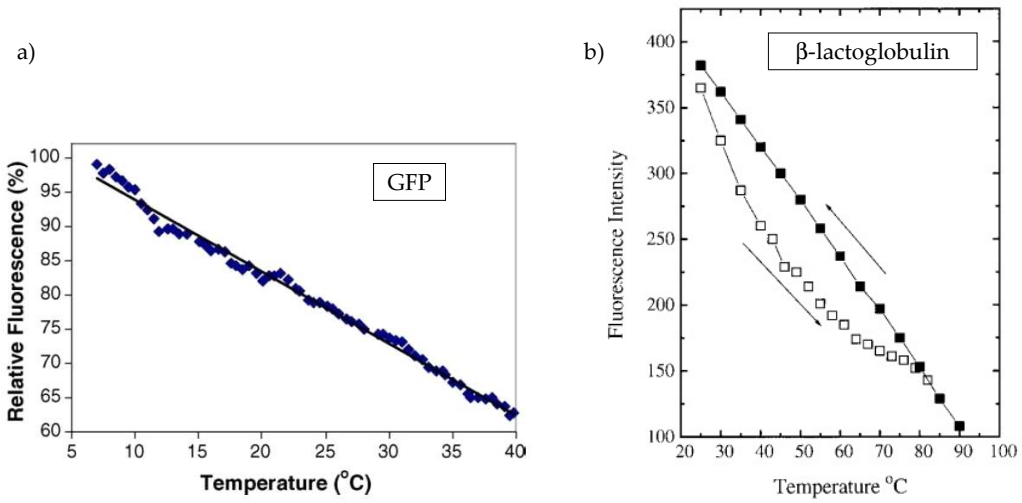

Figure 5.2: a) The temperature dependence of the GFP fluorescence intensity. [12] b) The unfolding and refolding of β-lactoglobulin can be observed through a change of the intrinsic tryptophan fluorescence. The fluorescence intensity is here plotted versus the temperature. [7]

5.2.1 Applications in molecular kinetics studies

Concrete examples of applications where the possibility of fast temperature modulation is likely to have a great impact lie in the efficient on-chip fundamental studies of molecular kinetics by temperature jumping (conformational changes etc.) and the development of sensing schemes based on temperature pulse voltammetry [29–31].

Examples of molecular events that are dependent on temperature are the conformational changes of protein and DNA (folding and unfolding), the activity of molecular motors and the duplication processes of DNA. As explained in the introduction of the thesis, fast temperature jumping (T-jumping) can be used as a tool for such studies. The typical approach is to use complex laser systems to achieve fast T-jumps. By the use of nanowires, we envision instead the use of T-jumps realized on-chip. By further optimization of a nanowire system like this and the development of suitable characterization techniques, researchers studying molecular behavior may be equipped with a revolutionizing tool for the efficient and perhaps automated analysis of molecular events.

In the nearest future, the preliminary task should be to prove the applicability of the nanowire heating elements in the study of model molecules for which the temperature dependent kinetics are already known. Since the temporal response of our nanowire systems have not yet been proved to lie below the millisecond regime, further optimization of the thermal design may have to be performed in order to adapt the system for faster response. However, while continuing the optimization of the system and of the thermometry approach, molecules with relaxation times in the millisecond regime and higher may be investigated. A protein that is well suited for this purpose is the green fluorescent protein (GFP) [12]. Other molecules that may be of interest are the protein Beta-lactoglobulin [7–11] and the molecular motor F1-ATPase [221, 222]. GFP and Beta-lactoglobulin could be observed by means of fluorescence (Fig. 5.2 and Fig. 5.3) while the rotation of F1-ATPase could be visualized in a conventional optical microscope by conjugation to a larger object, e.g. a nanoparticle or a nanorod. The thermally

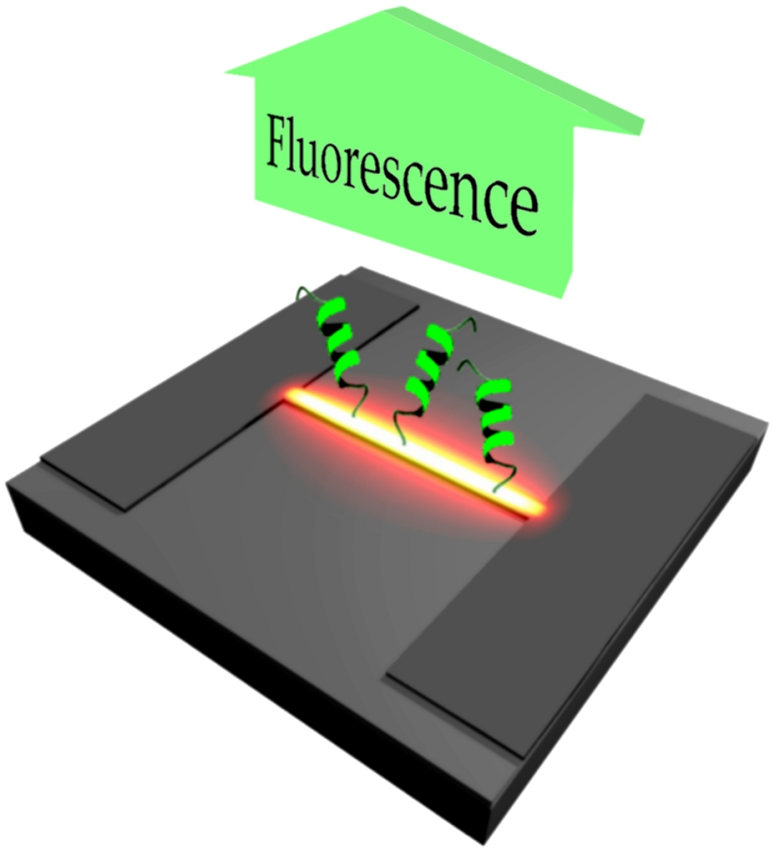

Figure 5.3: Conceptual sketch for the study of molecular kinetics using nanowire T-jumping. The folding behavior of the green fluorescent protein (GFP) could for example be visualized by means of fluorescence.

induced unzipping of DNA strings could also be easily studied by fluorescent labeling, e.g. using the fluorescent dye SYBR Green. Among the molecular motors, microtubules are another type of molecules which possess a temperature dependent activity and which might eventually be studied with the nanowire system [223–226].

5.2.2 Localized polymerization and modification of surface properties

Regarding the highly confined spatial impact of the temperature changes, this will be of value in the highly localized thermally induced modification of surface properties, e.g. the creation of binding and recognition sites by the modification of thin polymer layers such as MIP (Molecularly Imprinted Polymer) [35–37, 227] (see Fig. 5.4) and pNIPAAM [228–231]. This implies that the surface properties of densely packed nanowires can be differently modified by addressing them individually. This is of interest in creating complex sensing devices comprising sensing and recognition sites for a multitude of different molecular species.

Due to the independence of the typical surface modifications on thermal response times, these applications will be targeted in the immediate future. With the thermal characterization of our nanowires, particularly in dry conditions, we know what temperatures and what temperature distributions to expect for certain levels of resistive heating. This will be highly valuable in the development of a process for local surface modification, e.g. the polymerization of MIP and the hydrophilicity change of pNIPAAM.

5.3 Integration of nanowire heating elements in lab-on-a-chip systems

If the nanowires are to be used in integrated systems such as lab-on-a-chip systems, it is of interest to enable precise temperature control without the need to perform fluorescent thermometry. The best way to achieve this control is most likely to use resistance-based measurements of the average nanowire temperature, simply by monitoring the nanowire resistance. Due to the high confinement of the temperature changes to the nanowire (on silicon substrates), there is no need to perform four-point measurement, since all temperature-induced changes in the resistivity throughout the electrical circuit will occur almost entirely at the nanowire.

The main function of the fluorescent thermometry will thus be to perform preliminary analysis in order to understand the exact temperature distributions and to assist in the calibration of the resistance measurements. In the final on-chip system, resistance measurements alone could then be used to monitor the temperature of each individual nanowire.

An alternative to conventional resistance-based measurements could be the use of the 3ω-method which was briefly described in the review of Chapter 1. The 3ω-method allows for accurate and complete thermal characterizations and is therefore an interesting candidate. For transient analysis, the 3ω-method can also be used to determine the time constant of a nanowire system. To resolve very small time constants, a high frequency should be applied. Consequently, certain lower limits to the transient analysis are imposed by the frequencies at which the externally applied power can be modulated.

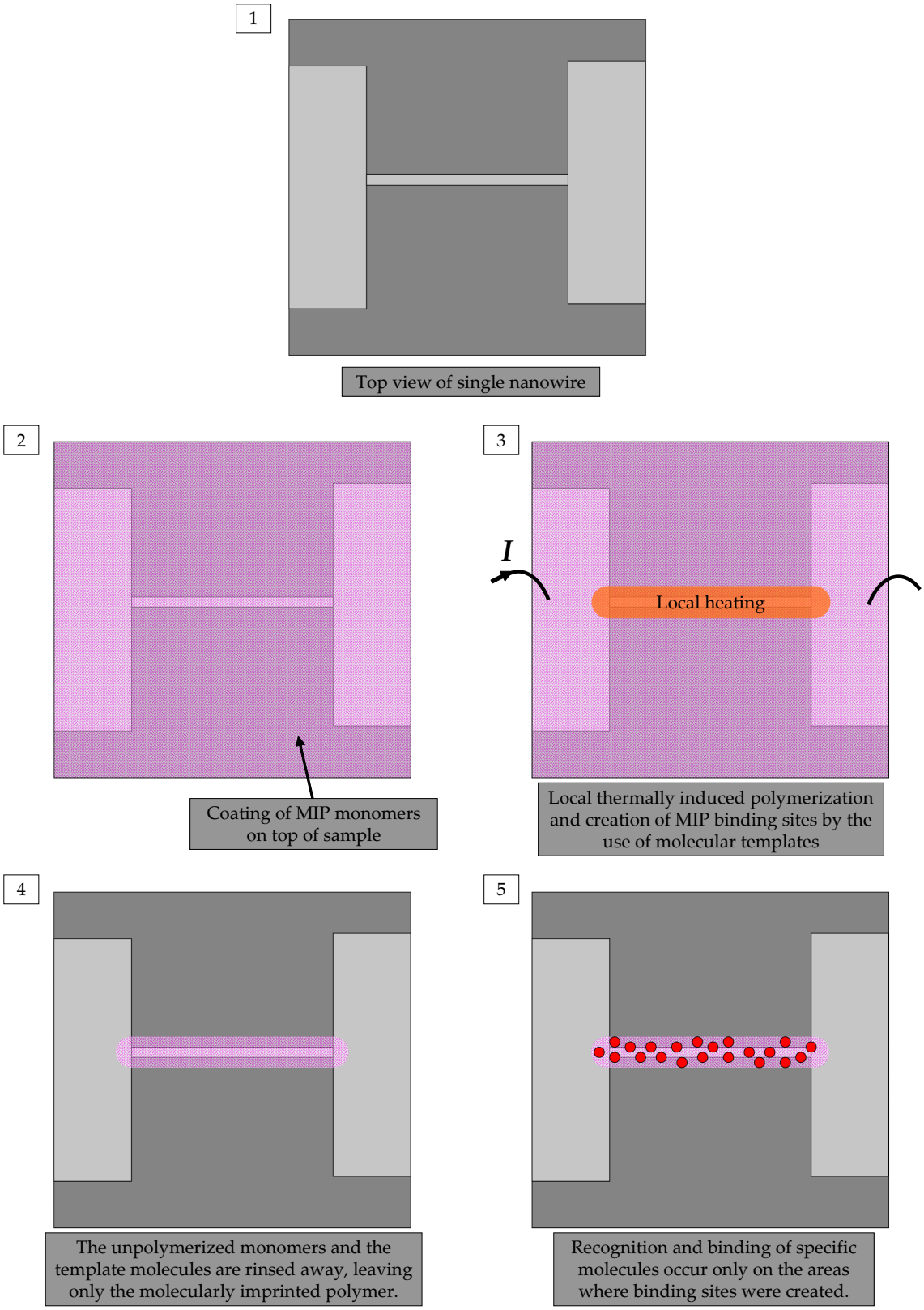

Figure 5.4: Thermally induced local polymerization of MIP monomers. This technique holds potential for the efficient creation of molecular recognition sites on nanowires, e.g. in FET sensing applications.

5.4 Possible developments of the nanowire structure

In the current work we made use of simple metal nanowires fabricated by a top-down approach. While this approach was the appropriate choice for the thermal characterizations performed in this thesis, the future developments of nanowire-based heating devices may potentially benefit from a change to semiconductor nanowires and/or a change to fabrication by a bottom-up technology.

5.4.1 Bottom-up fabrication

The use of bottom-up technologies promises better control of the nanowire structure. Both PAA [210–213,232] and VLS [233] technologies allow for segmentation of the produced nanowires which enables the introduction of high-resistivity parts along the wire. Since high-resistivity segments are expected to heat more than segments with lower resistivity, bottom-up approaches can be used to engineer nanowires with very specific temperature distributions which are determined by the combination of segments. Another interesting aspect of nanowire segmentation is the possibility to create miniaturized junctions in thermoelectric applications, e.g. for the precise measurement of temperature via a nanoscale thermocouple junction.

5.4.2 Local heating and FET sensing combined

The apparent advantage of using semiconductor nanowires is that molecular sensing by the FET effect [41–45] is enabled. Clearly speaking, one single semiconductor nanowire could be used both for fast temperature modulation (by resistive heating) and for molecule sensing (by the FET effect). This allows for the development of very powerful devices for the study of molecular kinetics, as the targeted molecules may be easily detected and monitored electrically. Among the bottom-up approaches, VLS growth is the ideal candidate for the fabrication of nanowire sensors with its high control of the semiconductor structure. Regarding the PAA approach, it is mainly a technique for the fabrication of metal nanowires and is therefore generally not used for sensing applications.

A possible approach for the fabrication of silicon nanowires by EBL has been developed in this thesis and is presented in Appendix C. Improvements of the top-down approach presented in that appendix could be achieved by further shrinking and smoothing of the silicon nanowires by techniques like lateral TMAH etch [202] and size-reduction by thermal oxidation [199–201].

APPENDIX A
FLUORESCENT PROBES

A.1 Organic fluorescent dyes

Among the most commonly employed fluorescent dyes used in biological applications we find the Rhodamine and Fluorescein molecules, which are members of the group referred to as Xanthene dyes (Fig. A.1) [138, 145, 157, 166]. Another group of fluorophores are the band-definition dyes which here will be treated after the Xanthene dyes. A range of less common organic fluorophores will then conclude the part on organic dyes.

A.1.1 Rhodamine B

One of the most commonly applied organic dyes in fluorescent thermometry applications is the Rhodamine B molecule from the Rhodamine family. It is a dye which absorbs green light and fluoresces in the red-orange part of the visible spectrum. It is commonly used as a laser dye for wavelengths near 610 nm [157]. The Rhodamine B molecule shows a strong dependence on temperature. In the literature, the fluorescence intensity is typically stated to decrease with increasing temperatures at a rate of $1.2 - 2.5\%$ per $^{\circ}\mathrm{C}$ at room temperature [67, 154, 155, 157, 158]. The decrease occurs uniformly over the entire emission spectrum and is strongest in the range of 0 - 100 $^{\circ}\mathrm{C}$ [167]. Other molecules of the Rhodamine family have also been applied for temperature characterization, although less frequently [134, 137]. Slyadnev *et al* reported a 5-fold decrease of the fluorescence intensity of Rhodamine 3B when increasing the temperature from 20 $^{\circ}\mathrm{C}$ to 90 $^{\circ}\mathrm{C}$ [134].

Regarding the mechanism behind the temperature dependence, some papers explain it simply as being a result of the increased amount of non-radiative relaxation processes. However, the mechanism can be explained further in detail by considering the different conformations that the Rhodamine B molecule can take. Depending on the surrounding media and the environmental parameters, there are three possible conformations (see Fig. A.2). Two of these are strongly emissive, while the third is emissionless due to the interruption of the conjugate π-electron in the chromophore [68]. As the temperature is increased, the transformation from conformation one and two into the third one is facilitated to some extent leading to a decrease in the observed fluorescence intensity. An additional reason for the decrease in intensity is that the Rhodamine B molecule may decompose at elevated temperatures.

Experimentally, the Rhodamine B fluorescence is commonly induced using either a

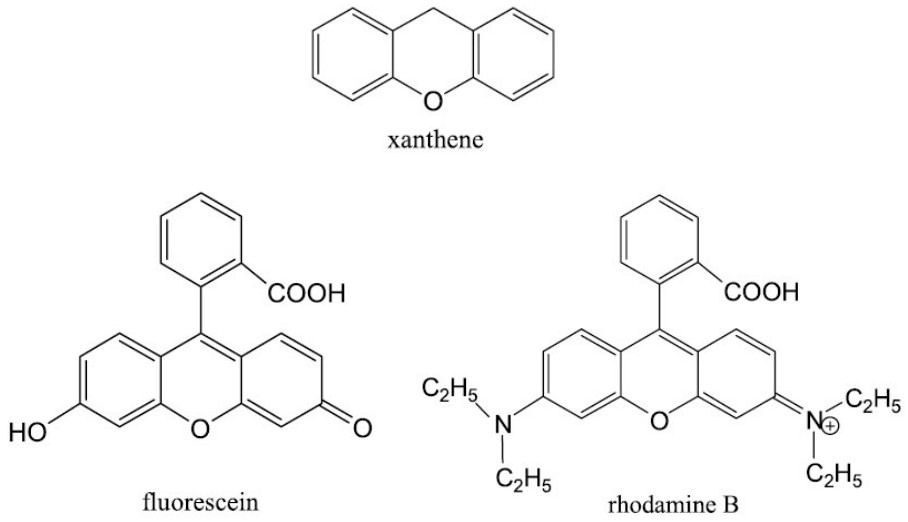

Figure A.1: Molecular structures of the xanthene molecule and the xanthene-based fluorescent dyes fluorescein and rhodamine B.

mercury lamp with filters transmitting light in the vicinity of the absorption maximum, i.e. 500 - 550 nm [66]. An appropriate laser source can also be used. The most commonly used laser is the Ar-ion laser with light centered around 514.5 nm [155, 168]. The less employed Nd:YAG laser, with light centered around 532 nm, enables a stronger excitation as it excites the Rhodamine B molecules closer to the absorption peak [146, 159].

Several approaches for the exploitation of the temperature dependent Rhodamine B fluorescence have been reported. For applications in microfluidics and microsystems, the most common method has been the measurement and analysis of the intensity changes within one spectral band [39, 63, 66, 67, 159, 167]. This is mainly due to the simplicity of these measurements which allow for fast temperature mapping using a standard fluorescence microscope and a CCD camera [66]. Typical temperature resolutions reported for the intensity-based measurements are on the order of 3 °C between 20 °C and 90 °C without spatial or temporal averaging. Spatial resolutions of down to 1 μm have been reported [39, 66]. Slyadnev *et al* reported a temperature resolution of 0.5 °C using the alternative Rhodamine dye Rhodamine 3B [134]. Better temperature resolutions have been achieved for temperature measurements on a bigger scale, with resolutions down to 0.4 °C [159]. The temporal resolution is typically limited by the acquisition time of the CCD camera in use, i.e. on the order of a few milliseconds.

Except for the single intensity-based measurements, Rhodamine B has also been successfully employed in two-color thermometry applications. The Rhodamine B dye is in this case generally used as a strongly temperature dependent probe while a second fluorophore, e.g. carboxyfluorescein [165], Rhodamine 110 [157] or Pyrromethene 567 [137], is used as an internal reference to compensate for instabilities such as the fluctuations of the excitation light source. The approach requires a slightly more complex setup than single intensity measurements in that it requires the use of two CCD cameras [157] or alternatively a 3-CCD color camera [165] in order to separate the different colors of the two fluorophores. Three-color measurements [156] as well as lifetime measurements have also been investigated [161].

The use of Rhodamine B for temperature characterizations has been extended to

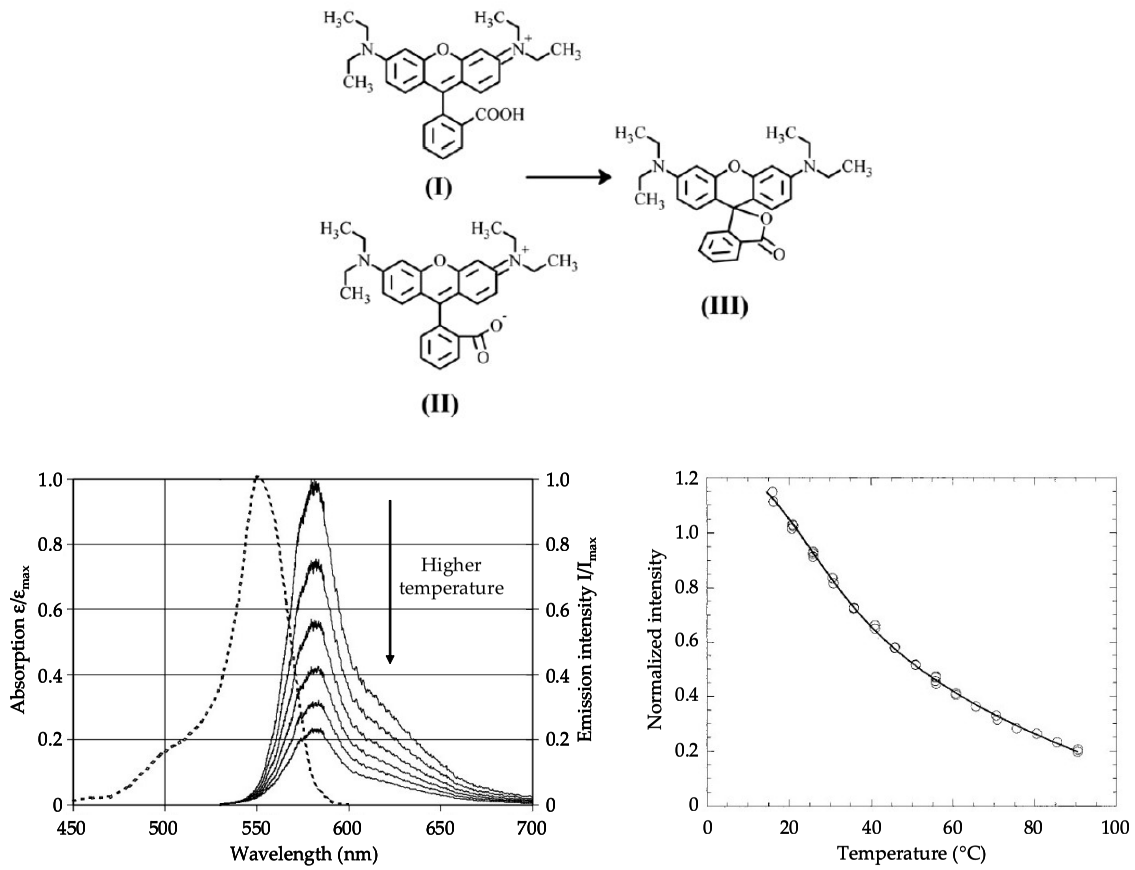

Figure A.2: a) Molecular structures of the three different conformations that Rhodamine B can take [68]. b) The Rhodamine B spectra at different temperatures. The absorption curve is dashed and the emission curves at different temperatures are solid [146]. c) Temperature dependence of the emission peak intensity [66].

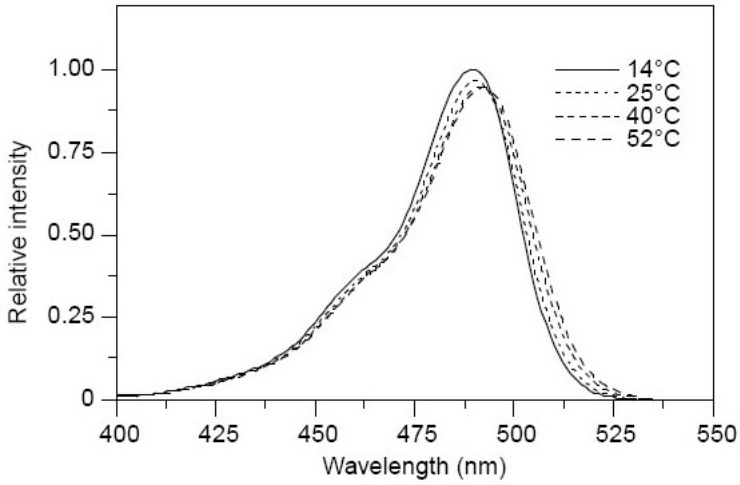

Figure A.3: Temperature dependence of the absorption spectrum of fluorescein [154].

several application areas. In the recent past, several papers have been published on its application for temperature mapping within microfluidic channels [63, 66, 67, 167]. Another interesting application is its use for the evaluation of the temperatures within resists used for nanoimprint and electron beam lithography. These processes are highly dependent on the resist staying within a certain temperature range in order to avoid pattern deformation and to achieve specific critical dimensions [68]. Except for its use in microscale applications, Rhodamine B has also been successfully applied in problems such as the characterization of natural convection [146], evaluation of the dynamics of heated submerged jets [156, 168] and the temperature measurements on a monodisperse droplet stream [155].

Except for its strong temperature dependence, typical advantages of Rhodamine B lie in its independence of pH (at pH ranges above 6) and its resistance to high pressures (up to 350 psi) [67,68,154]. Furthermore, its temperature dependence has been demonstrated in a number of different media, e.g. ethanol [169], biological buffers [63,66] and polymer [68], making it a versatile temperature probe. On its downsides, Rhodamine B suffers from relatively strong photobleaching under the influence of the excitation light [67, 146]. Due to the spectral band overlap, its fluorescence has also been shown to be dependent on the dye concentration [170].

A.1.2 Fluorescein

Fluorescein is a commonly used dye for labeling and tracking species in microbiological assays [171, 172]. Additionally, fluorescein has a strongly pH-dependent fluorescence, making it a useful probe in applications where pH must be monitored [154]. In the field of thermometry, fluorescein is useful due to its fluorescence intensity which decreases as the temperature increases [13, 173]. In contrast to the general observation of decreased intensity with increased temperature, Coppeta et al has presented results on the temperature dependence of fluorescein where an increased intensity could be achieved for increases in temperature [154]. The rate of increase was as high as 2.43% per K. This observation could be understood by analyzing the temperature dependence of the absorption spectrum (Fig. A.3). At an increased temperature, the absorption band is

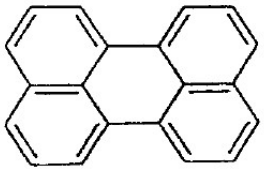

perylene

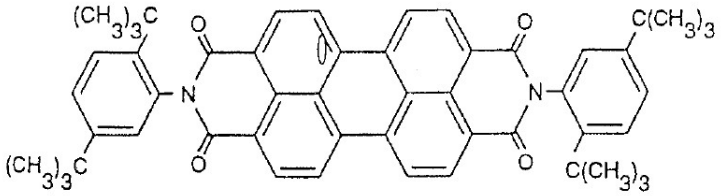

bis(-di-tert-butylphenyl)
-perylenedicarboximide

(BTBP)

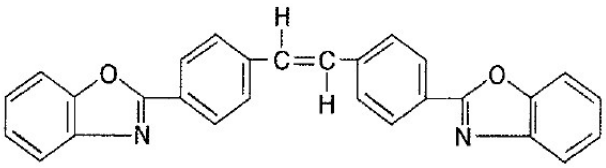

benzoxazolyl stilbene (BOS)

Figure A.4: Molecular structures of the bad definition dyes perylene, BTBP and BOS.

widened. This widening leads to an increased absorption at the flanks of the band. Since the authors of the article used excitation light centered on the flank of the absorption band (514 nm), an increase in temperature led to a dramatically increased absorption which in turn led to a stronger fluorescence intensity. On the other hand, when using excitation light at a lower wavelength (488 nm), the authors measured a temperature dependence of -0.16% per K, i.e. a slight decrease of intensity with an increase in temperature. A typical disadvantage of the fluorescein molecule is that it quickly photobleaches when exposed to the excitation light. The photobleaching process can be alleviated by controlling the environment, e.g. the temperature and the presence of oxygen, both of which influence the photobleaching rate [145].

A.1.3 Band definition dyes

The group of fluorophores here referred to as the band definition dyes comprise compounds such as perylene, benzoxazolyl stilbene (BOS), bis(2,5-tert-butylphenyl)-3,4,9,10-perylenedicarboximide (BTBP) and 2-(1-naphthyl)-5-phenyloxazole (NPO) (Fig. A.4).

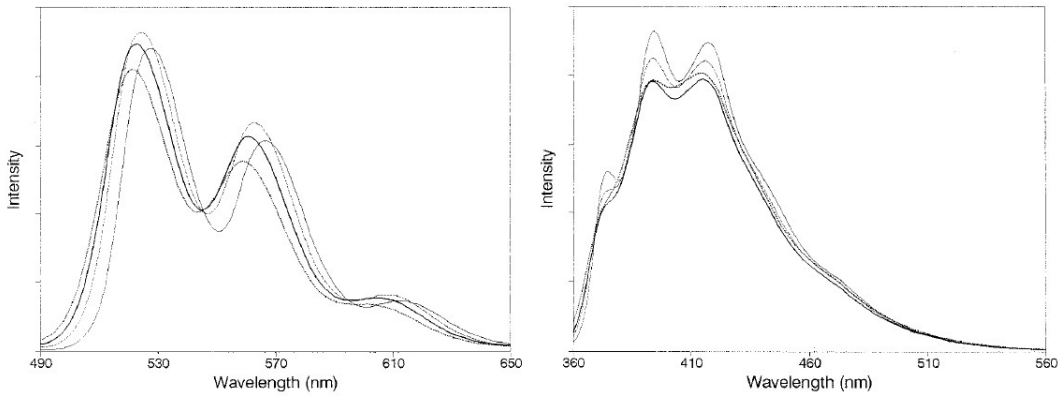

Figure A.5: Emission spectra from the band definition dyes BTBP (left) and NPO (right) [235].

The name of this class of dyes originates in the existence in their fluorescence spectra of two or more distinct intensity peaks [234]. Fig. A.5 shows the specific cases of the temperature dependent spectra of BTBP and NPO, clearly illustrating the multiple peaks of their fluorescence. Due to the presence of these peaks, band definition dyes are typically well suited for FIR-based fluorescence analysis, as demonstrated in several publications, e.g. for BTBP [164, 234–236] and perylene [236, 237]. In the field of fluorescence thermometry, perylene and its derivatives BTBP, BOS and NPO are examples of band definition dyes that are highly applicable thanks to the temperature dependent nature of the ratio between the peaks of their fluorescence spectra. A thorough study on fluorophores suited for thermometry applications was presented by Bai *et al* mentioning particularly the usefulness of the band definition dyes BTBP and NPO as well as the dyes POPOP and BPB, due to their insensitivity to quenching by molecular oxygen, reversible temperature effects and nearly linear temperature calibration curves [235].

The three dyes perylene, BOS and BTBP are furthermore particularly well suited for temperature measurements in polymer processing due to their solubility at dopant levels of concentration in organic polymers and due to the fact that they survive without degradation at polymer processing temperature up to 300 °C [234, 236]. This is useful for example when monitoring the true temperature of a polymer during injection molding and extrusion processing [236, 237]. Furthermore, the BTBP dye has been specifically shown to be independent of polarization effects and the mechanical stress induced on it when applied in polymer processing involving shear flow [236].

The precision of the temperature measurement done with these dyes have been mentioned in the literature as lying in the range of 2 - 4 °C [164, 235]. Applications in the microsystems field have yet to be demonstrated. The mechanism behind the temperature dependence of band definition dyes is generally explained to be of a quantum mechanical origin with a temperature dependence of the decay from an excited state back to the ground state [234]. In the case of BTBP, the temperature dependent changes of the fluorescence spectrum has been explained to be partly due to the thermal excitation of vibronic states in the electronically excited state, termed fluorescence hot-band emission, and partly to the solvent index refraction-induced shifts in the fluorescence maximum [164].

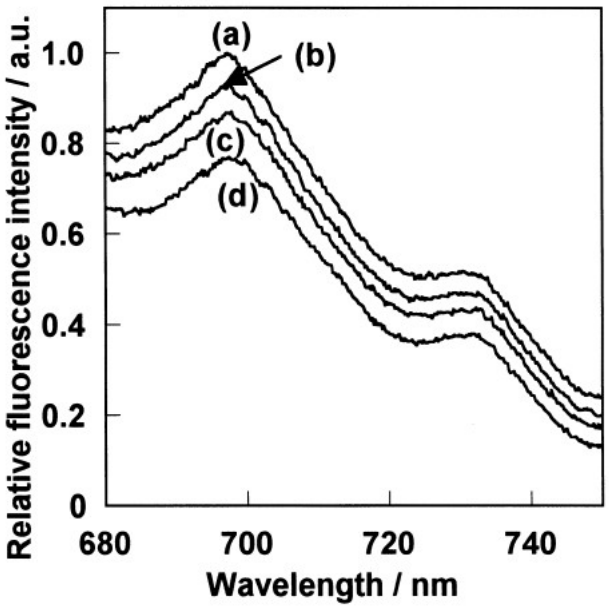

Figure A.6: Temperature dependence of the emission spectra of the ball shaped fullerene C_{60} [238].

A.1.4 Other thermosensitive organic dyes

A.1.4.1 Fullerenes

Fullerenes are molecules composed entirely of carbon. They can take the shape of a hollow ball, ellipsoid or tube. In the shape of a tube, they are generally known as carbon nanotubes (CNT), while the ball shapes sometimes are referred to as buckyballs. In a publication by Amao *et al*, the ball shape of fullerene, C_{60}, was demonstrated to possess a temperature dependent fluorescence intensity [238]. The application involved C_{60} molecules dispersed in a 50 μm thick PMMA film. The authors established the fluorescence intensity to change linearly with temperature in the range of 260 to 373 K (see Fig. A.6).

A.1.4.2 DNA

Two different approaches were recently introduced for using DNA as a means to measure temperature. In an article by Sangmin *et al*, a FLIM method was presented where Rhodamine 6G - labeled DNA oligomers were used [239]. The principle for temperature sensing is based on the fact that the four DNA bases quench fluorescence with variable efficiency. Thymine (T) is the strongest quencher followed by guanine (G), then cytosine (C) and finally adenine (A) which does not quench at all. Therefore, the spacing between a fluorescent dye and a designed sequence of DNA bases is modulated by conformation changes of a DNA chain, and the ability of dye molecules to fluoresce is also modulated. At higher temperatures, the faster the conformational changes occur, and the shorter the fluorescence lifetimes become.

Another approach was presented in a paper by Tashiro *et al*, where a molecular thermometer that uses the different π-stackings of the double-helical β- and Z-DNA was designed [240]. A fluorescent probe was introduced into B- and Z-DNA and the

emission monitored. Since the *Z*-DNA showed a stronger fluorescence than *B*-DNA and since the relative amount of the two forms changes with temperature, the fluorescence intensity could be correlated with temperature. At low temperature, the proportion of the *Z*-conformation is high due to its lower entropy while an increase in temperature increases the proportion of the *B*-conformation. It was found that the intensity of the fluorescence linearly correlated with the temperature.

A.1.4.3 Polyfluorene

The fluorescence from a polyfluorene-based conjugated polymer was recently showed to possess frequency up-conversion fluorescence which intensity depends strongly on the temperature [241]. The up-conversion effect means that two photons are absorbed and subsequently gives rise to fluorescence emission at a higher frequency. The authors described the probe as a potential accurate probe for the measurement of operating temperatures of organic light-emitting diodes (LEDs).

A.2 Inorganic fluorescent probes

A.2.1 Semiconductor nanocrystals

A highly interesting new class of fluorescent probes is the semiconductor nanocrystals, also known as quantum dots. Compared to conventional fluorescent dyes, these particles present particular advantages in terms of their high photostability, exceptional quantum yield, broad absorption spectra and narrow emission peaks [51, 174–176]. While being investigated for a range of various applications, e.g. biological labeling [174, 177–181] and semiconductor lasers [182], since 15 - 20 years ago, the application for temperature measurements is relatively recent. While studies on the temperature dependent properties of nanocrystals in the low temperature range (0 - 300 K) have been investigated for a relatively long time, the properties in the physiologically relevant temperature range (0 - 100 °C) has only recently been given specific attention. Over the past 5 years, an increasing number of papers have addressed this temperature range, frequently with specific focus on the potential application for non-contact temperature probing [51, 135, 144, 152].

Because of the high signal yield, often explained by the high electron-hole overlap which results from the quantum size confinement and which leads to an increased oscillator strength [51], these particles are particularly useful for quantitative measurements such as fluorescence-based temperature characterization. Furthermore, compared to conventional thermal phosphors, the small size, on the order of 1-10 nm, holds potential for higher spatial resolution measurements because of greatly reduced light scattering [51]. Many semiconductor nanocrystals have also shown to be more or less insensitive to oxygen quenching, which makes these probes yet more attractive [144].

Customization of semiconductor nanocrystals can be performed by the introduction of impurities and by changing the particle diameter. Further changes and improvements of the performance are often achieved by capping the nanocrystals with semiconductor materials of different properties, e.g. with a different band-gap. To enable the use in various environments, e.g. for biological applications, the particle surfaces are frequently functionalized to provide the probes with specific binding sites or other chemical properties [180].

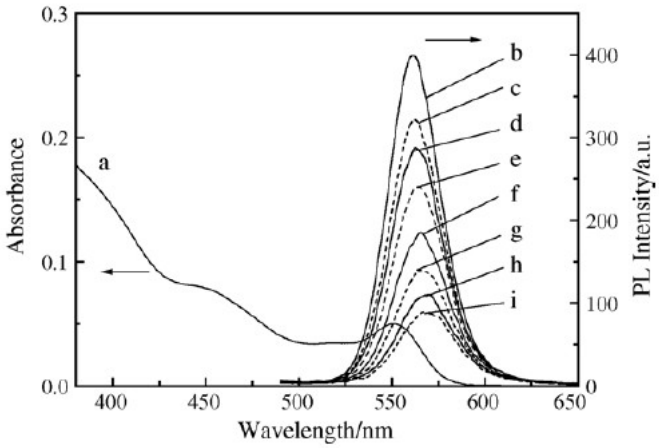

Figure A.7: Visualization of the CdSe/ZnS spectra at different temperatures. The spectra show several interesting characteristics which can be found in many semiconductor nanocrystals. First of all, the absorption band (curve a) is very broad, allowing for a flexible choice of excitation source. Second, the emission peak is relatively narrow and, third, the emission intensity is strongly dependent on temperature. The different temperatures of the emission spectra, in the order from b to i, are 280K, 288K, 298K, 308K, 318K, 328K, 338K and 348K. [152]

The most commonly studied semiconductor nanocrystals in temperature sensing applications are CdSe and ZnS-capped CdSe (CdSe/ZnS) nanocrystals [77, 135, 144, 152, 183, 186]. These nanocrystals have been demonstrated to possess a strongly temperature dependent fluorescence in the range of 100 - 350 K (see Fig. A.7) [144, 183, 186]. Since the temperature dependence stretches over the physiologically relevant temperature range, these nanocrystals are particularly interesting for biomedical applications, e.g. in lab-on-a-chip systems [77, 152]. However, there have been indications showing the irreversibility of the temperature dependent behavior of CdSe-based nanocrystals [39, 152]

Other nanocrystals of interest are CdTe [51, 185] and ZnS/Mn^{2+} [51, 187] nanocrystals. CdTe has been shown to have a linear reversible fluorescence intensity changes in a range of 30 - 60 °C, while for ZnS/Mn^{2+} reversibility has been achieved in the range 30 - 150 °C [51]. However, the exact dependence of the ZnS/Mn^{2+} nanocrystal fluorescence intensity is somewhat unclear. In reference [51], the intensity is stated to decrease continuously with an increase in temperature from 30 to150 °C. On the other hand, in reference [187] the intensity is said to increase from room temperature to 90 °C, after which it starts to decrease until complete quenching at 140 °C. The mechanism behind the intensity increase is explained in the latter reference as being thermoluminescence and thermal curing of the particle surface upon heating. The different behaviors may very well be due to differences in surrounding environmental properties in the two cases.

Like with other fluorophores used for temperature probing, there are various approaches for the analysis of the temperature dependent fluorescence spectra of nanocrystals. The most common approach until now is single intensity measurements [13, 144, 152]. Another recently demonstrated approach employed the well-known spectral shift of the emission peak of CdSe/ZnS nanocrystals, with a red-shift of 20 nm over a range of 200 °C [144, 152], in order to determine the temperatures on a microscale heating strip [135]. FIR techniques are not well suited for semiconductor nanocrystals, as their

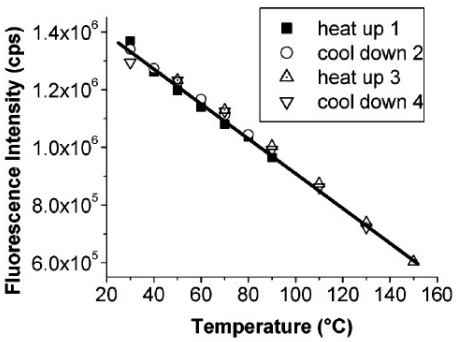

Figure A.8: Temperature dependence of ZnS/Mn^{2+}nanocrystal fluorescence intensity. The temperature dependence of the fluorescence intensity from semiconductor nanocrystals in general is frequently linear. This is different from bulk semiconductors, which generally present an exponential decay with increased temperature. The difference may partly be due to thermoluminescence of the nanocrystals. [51]

spectra commonly only contain one very narrow emission peak.

A.2.1.1 Mechanism behind the temperature dependence of nanocrystals

The nanocrystal photoluminescence dependence on temperature can typically be observed in several ways. While the most dramatic changes with temperature occur in the intensity of the emission peak, with decreased intensity upon the increase of temperature, changes can also be observed in the emission band width and in the spectral position of the emission peak. The common observation is a widened emission band and a red-shifted position of the emission peak for increased temperatures [144].

The mechanisms behind the temperature dependency of nanocrystal photoluminescence have been the object of study in several recent publications [183–185]. Due to the quantum confinement, the thermal behavior of nanocrystals has to be analyzed with particular consideration of the particle size, the processes of nonradiative relaxation via phonon coupling, exciton thermal dissociation, energy transfer, carrier trapping and temperature dependence of the absorption spectra [51]. Commonly, it is also observed that capping layers and organic ligands positioned at the nanocrystal surface play an important role in determining the temperature dependent properties [152, 184, 185].

In a paper by Valerini *et al*, the temperature dependent properties of CdSe/ZnS nanocrystals in the range from 45 to 295 K were specifically investigated [183]. They found the existence of two nonradiative processes, activated in the range 70 - 195 K and 195 - 295 K, respectively. The first, lower-temperature process is a thermally activated carrier trapping in surface states, whereas the main nonradiative process at higher temperatures is thermal escape from the dot assisted by scattering with four LO (exciton–longitudinal-optical) phonons.

Thermoluminescence A typical observation regarding the emission intensity of semiconductor nanocrystals is that it varies linearly with temperature (see Fig. A.8). In bulk materials, however, where the main mechanism is nonradiative relaxation, the corresponding dependence is exponential. A partial explanation for this was given by Wang et al, saying that nanocrystals emit thermoluminescence originating from the thermally

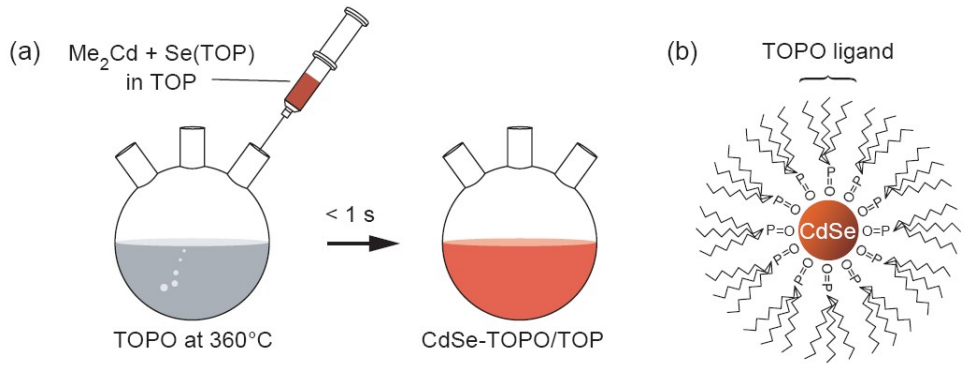

Figure A.9: In many protocols for the fabrication of nanocrystals, specific ligands such as TOPO are used in order to coordinate the synthesis. The ligands subsequently serve to prevent the aggregation of nanocrystals in its colloidal form. [182]

induced recombination of carriers trapped in surface states. This may give rise to luminescence which partly compensates for the exponential decay of fluorescence due to nonradiative recombination. [51]

Capping layer and organic ligands Frequently, nanocrystals are built up in a core-shell structure, with the shell having a stabilizing function on the core semiconductor. Furthermore, nanocrystals are also commonly capped with a layer of organic ligands, the role of which normally is to coordinate the crystal composition and size during synthesis and to prevent aggregation of nanocrystals in the colloidal form (see Fig. A.9). Concerning the role of the organic ligands in the temperature dependent behavior of the photoluminescence, Wuister *et al* presented in two articles the studies of CdTe [185] and CdSe [184] nanocrystals. In the study of CdTe nanocrystals, the ligand role was investigated by freezing of the solvent water molecules surrounding the particles. The presence of specific capping ligands, long-chained thiols in this case, removed the dependence on temperature while other ligands introduced surface quenching states which gave the particle a temperature dependent luminescence. In the other article, the authors stated one important function of the ligand to be the passivation of dangling lone pairs on the nanocrystal surface. Furthermore, they showed that reconstruction of the nanocrystal surface is directly affected by a phase transition in the capping ligand and that, consequently, the ligands can be used as way to gain control over the temperature-dependent luminescent properties of a nanocrystal.

In an article presented by Liu *et al* [152], the effects of the capping semiconductor shell, e.g. the ZnS layer for CdSe/ZnS nanocrystals, were discussed, suggesting that uncapped cores or cores with relatively thinner shells are more exposed to the environment. As a consequence, re-population of mobile electrons and holes on the surface is disturbed when the temperature is increased. This in turn leads to a decrease of the luminescence.

Thermal irreversibility A few publications have mentioned the fact that some nanocrystals have a temperature dependent behavior which is not reversible [39,51,152]. Mostly, this concerns the non-recovery of the original luminescence after heating the nanocrystals to a certain temperature (see Fig A.10). A possible reason for the irreversible

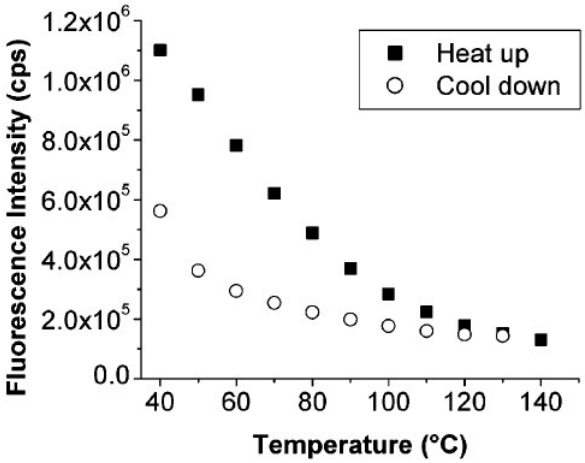

Figure A.10: Many semiconductor nanocrystals suffer from irreversibility of thermal behavior when exposed to thermal cycles. In many cases, the behavior is reversible within a limited temperature range, but irreversible if the temperature is excessively increased. This graph shows the case of CdTe nanocrystals being exposed to a temperature cycle ranging from 40 to 140 C. [51]

thermal response of some nanocrystals may be the thermal curing of surface defects and the thermal oxidization and decomposition of the organic ligands. This leads in turn to permanent changes of the hole and electron re-population properties of the nanocrystal.

A.2.1.2 Nanocrystal clusters

An interesting development in the pursuit of nanocrystal-based temperature probes was recently presented by Biju *et al* [242], showing the use of clustered CdSe nanocrystals. The authors used individual CdSe nanocrystals with diameters of 2 - 5 nm which were used to create aggregates with an average size of 27 nm. The luminescence properties were investigated over a temperature range of 298 - 353 K. It was found that the luminescence was permanently modified over the first four-five temperature cycles, after which the temperature dependence became more or less completely reversible (see Fig A.11). The reason for this effect was explained in terms of the complex interplay between the nanocrystals of each cluster and the influence of the environment on each cluster. The authors attributed the initial less reversible luminescence changes to a passivation effect of the external cluster surface and the subsequent reversible luminescence intensity to the thermal trapping and de-trapping of electrons in the inner surface states of the cluster.

A.2.1.3 Nanocrystal blinking

A well-known property of semiconductor nanocrystals is the fluorescence intermittency, also referred to as blinking [147–150]. This effect is observed as an on-off behavior of the emitted fluorescence. In single dye molecules, on–off behavior results from intersystem crossing into the dark triplet state. While being undesired for certain applications, in particular those involving quantitative measurement of fluorescence intensity, statistical analysis of the blinking phenomenon may in other applications be useful for the deter-

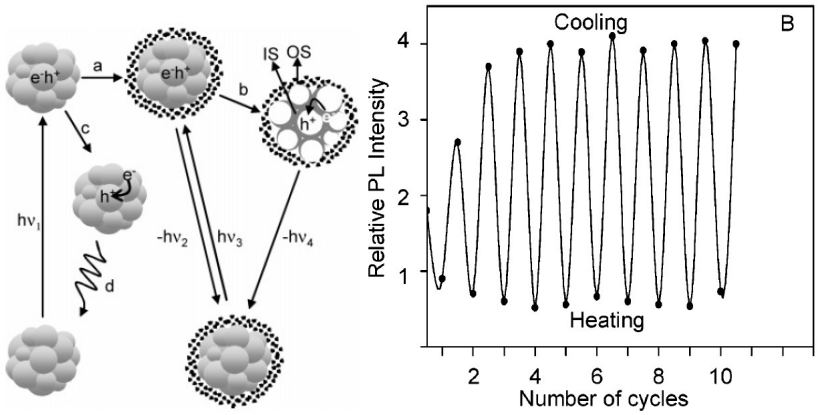

Figure A.11: Thermal curing of CdSe clusters. [242]

mination of environmental parameters. Temperature is found among those parameters affecting the properties of blinking, specifically by affecting number of blinking events in a given time interval. In an article by Banin *et al* [147], the blinking properties of single CdSe/ZnS nanocrystals were investigated. The authors suggested a darkening mechanism that is a combination of Auger photoionization and thermal trapping of charge. In the on state, single electron-hole pairs are photoexcited and subsequently recombine radiatively. The off state on the other hand, is explained as originating from ionized nanocrystals in which the emission is quenched due to trapped charge after simultaneous or sequential absorption of two photons. There are possible trap sites on the particle surface, on the interface between the core and the shell, and in the surrounding matrix. The rate to turn back on is a thermally activated process because the trapped charge is stabilized by local dipoles forming a finite barrier for the jump of charge back into the nanocrystal. Their experimental study revealed on one hand the lengthening of on and off times when the CdSe core was capped with the ZnS layer and on the other hand a substantial reduction in the number of on-off cycles as the temperature was decreased before finally reaching a permanent off state at sufficiently low temperatures.

A.2.2 Rare-Earth based dyes

A well-known group of photoluminescent materials for thermometry applications is that of rare-earth doped materials. They are commonly known as thermal or thermographic phosphors [53, 153]. The photoluminescence of the thermal phosphors is created as a result of the photo-optical excitation of rare-earth dopants [153]. Thermal phosphors have a relatively long history of applications in thermometry, particularly in high-temperature fiber optic thermometry [55].

In a review by Allison *et al*, the physical mechanism behind the temperature dependence of the thermal phosphors is discussed [53]. The dependence is partly explained by reference to the Boltzmann distribution which governs the partitioning of the populations in the various participating vibrational levels of the ground, excited and emitting states. In a similar manner, Wade et al discussed the Boltzmann distribution and its role in the temperature dependent ratio of the population of different excited states of the rare-earth ions [163]. The temperature dependence has further been explained to arise from the presence of charge-transfer states in the host ceramic matrix. These

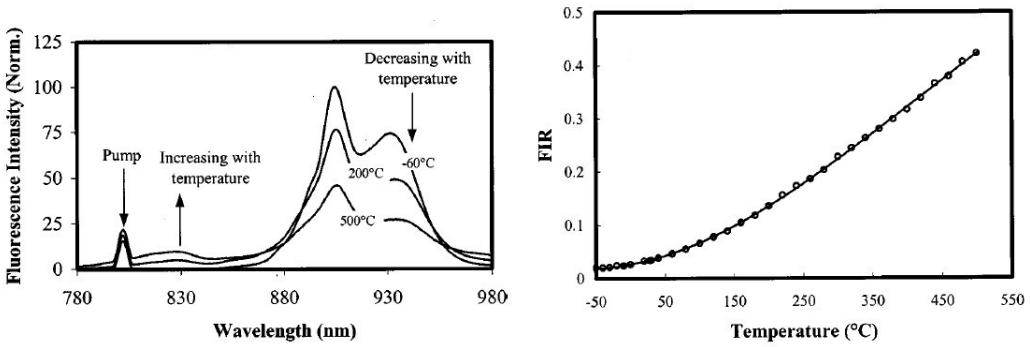

Figure A.12: The left graph shows the emission spectrum of a Nd^{3+}-doped silica probe.The presence of two emission bands with different temperature dependencies enables the use of FIR-based measurements. In the right figure, a graph relating the ratio of the two emission peaks with temperature is shown. [163]

states offer non-radiative de-excitation pathways which become energetically favorable with increasing temperature, thus leading to thermal quenching of the photoluminescent emission [153]. In the case of chelated Eu-ions, where resonant coupling between organic ligands and the rare-earth ions is behind the fluorescence, the decrease in fluorescence intensity at higher temperatures is generally explained as an increased probability for coupling of the excited ligand state to non-radiative states [133, 188, 189]. Changes in the non-radiative relaxation mechanisms have also been discussed as being the reason behind the size-dependent temperature sensitivity of rare-earth doped nanocrystals [190].

Temperature measurements using rare-earth materials are commonly performed by the FIR [162,163,190] or FLIM [153] approaches, although single intensity measurements also have been applied [133]. FIR measurements are frequently possible due to the relatively complex emission spectra, often with the existence of several fluorescent and phosphorescent emission peaks originating from one or more rare-earth dopant ions [104]. The often temperature dependent interplay between these peaks provides an excellent tool for temperature determination (see Fig A.12).

Typical examples of rare-earth probes used for thermometry applications are various europium-based compounds, e.g. Eu:TTA [133, 188] and europium-(III)β-diketonate [56], and europium-doped particles, e.g. Y_2O_3:Eu^{3+} and BaFBr:Eu^{2+} nanoparticles [51, 153]. The europium complexes have demonstrated a high stability and strong temperature dependence in the range of 0 to 70 °C [56, 133] whereas the doped particles have shown linear and reversible temperature dependent emission peak intensity between 30 and 150 °C (see Fig. A.13) [51].

Other rare-earth based thermal probes use ions such as erbium [162, 190], terbium [191], neodymium [163] and cerium [153]. High temperature measurements up to 610 °C were specifically demonstrated by Camargo *et al* using erbium-doped lead lanthanum zirconate titanate (PLZT) [162]. High-temperature measurements were also presented recently by Aizawa *et al*, using terbium-doped silica as a fiber-optic thermometer for temperature ranging from room temperature up to around 900 °C [191]. Another interesting result was presented by Alencar *et al* in the use of erbium-doped $BaTiO_3$ nanocrystals, showing an exceptionally high temperature resolution of around 0.005 °C [190] in the range of 50 to 190 °C. This is an order of magnitude better than the commonly reported resolution of 0.05 °C for rare-earth based thermal phosphors [53,153].

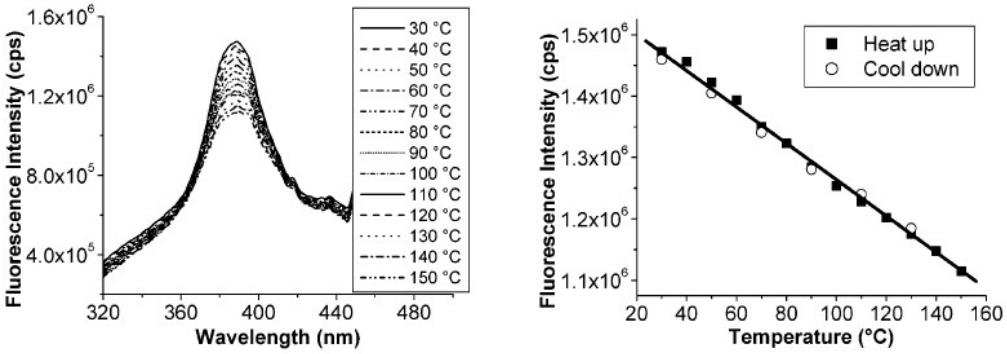

Figure A.13: Temperature dependence of the europium-doped particle BaFBr:Eu^{2+}. The left graph shows the spectrum at different temperatures. In the right graph, the intensity of the emission peak is plotted as a function of the temperature. [51]

Applications of rare-earth doped compounds for temperature measurements have in the past mainly been seen in the field of fiber optic based remote measurements in industrial processes and macro-size temperature monitoring [55, 56]. Typical advantages are their robustness and stability in harsh environments with measurement capabilities ranging from cryogenic temperatures to above 1000 °C [53, 55]. Recent developments have seen increased interest of rare-earths in the field of microsystems characterization [105, 133] and microbiological studies [188]. In line with the demands for smaller scale characterization, particular efforts are being invested in the developments of miniaturized rare-earth doped compounds, typically referred to as rare-earth doped nanoparticles or nanocrystals [51, 105, 106, 153, 190].

A.3 Metallorganic dyes

A.3.1 Ruthenium

The ruthenium complex $[Ru(bpy)_3]^{2+}$ shows several advantages for measurement of temperatures in the range of 20 to 100 °C [160]. Its fluorescence peak is strongly dependent on the temperature and presents a nearly linear dependence in the range 20 to 60 °C (see Fig A.14) [243]. The large Stokes shift makes the dye suitable for fluorescence imaging due to the ease in filtering elastically scattered light [160]. Furthermore, it has been found that the dye has a strong emission following two-photon excitation at 800 nm, making it suitable for two-photon imaging, with its inherent capability of resolving structures in three dimensions [160]. The ruthenium complex shows not only a strong dependence on temperature but also a high sensitivity to oxygen [160, 244]. When measuring temperature, it is therefore generally preferred to cap the dye with an oxygen-impermeable layer. This has been realized either by encapsulation in thin polymer films, e.g. poly(acrylonitrile) (PAN), poly(vinylalcohol) (PVA) or poly(methyl methacrylate) (PMMA) [160, 244], or by incorporation in polymer beads, e.g. PAN beads [244]. Other applications have been presented without the use of such oxygen barriers, e.g. in a publication by Filevich *et al* where temperature distributions in the one-dimensional flow on a dish for biochemical assays were characterized [243]. The authors reported lower signal-to-noise levels due to the presence of oxygen, although still being able to make use

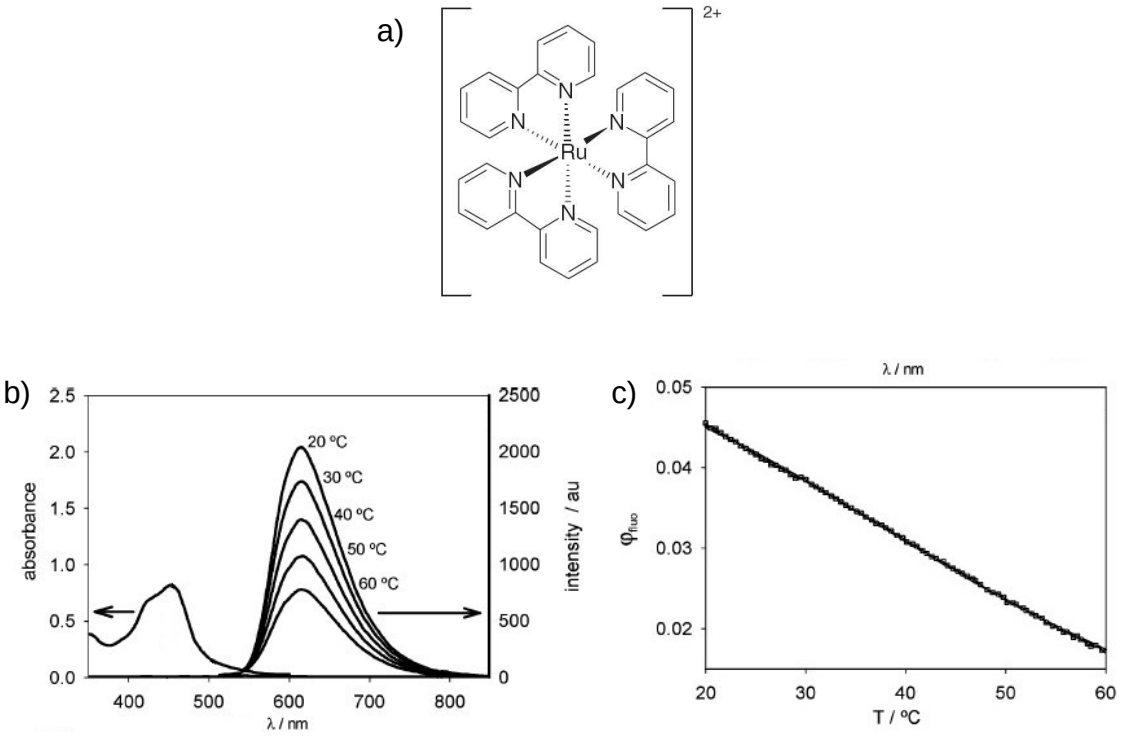

Figure A.14: a) Molecular structure of the ruthenium complex. b) The absorption spectrum and the fluorescence spectrum of ruthenium at different temperature. c) Quantum yield of the ruthenium fluorescence versus temperature. [160, 243]

of the linear temperature dependence of the fluorescence and obtaining a temperature resolution as good as 0.05 °C.

A.3.1.1 Ru(Phen)

A dye related to the $[Ru(bpy)_3]^{2+}$complex is [rutheniumtris- 1,10-phenanthroline], referred to as Ru(phen), which is another highly stable dye which is well suited for thermometry applications. Like $[Ru(bpy)_3]^{2+}$, its fluorescence is strongly affected by temperature in the range of physiological applications. In a paper by Liebsch *et al*, Ru(phen) was established to be capable of measuring temperature with a resolution of 0.05 °C for single point measurements [245]. To avoid oxygen quenching of the fluorescence, the dyes was incorporated into matrices of sol-gel glass and PAN before being deposited as thin films onto different substrates.

A.3.2 Porphyrin

A promising candidate for fluorescent thermometry is the metallorganic dye PtOEP ([2,3,7,8,12,13,17,18-octaethyl-21H,23H-porphyrin platinum(II)]). PtOEP is a dye that has been shown to yield highly efficient organic light-emitting diodes (LEDs) and that recently has been shown to be well suited for FIR based temperature measurements [61, 241]. The molecular structure and the fluorescence spectrum of the molecule are shown in Fig. A.15. The feature at 540 nm, which is significantly weaker in intensity than the main emission peak at 650 nm is strongly thermally activated, which make this dye

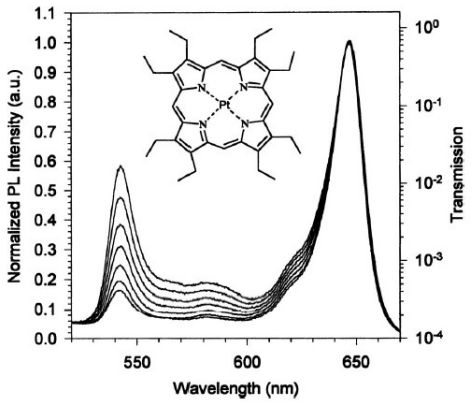

Figure A.15: Temperature dependence of the PtOEP molecule spectrum. The inset shows the molecular structure of the PtOEP dye. [241]

particularly useful for FIR applications. In the first demonstration of this dye for temperature measurements, the PtOEP was dispersed in a conjugated polymer and thermally characterized under vacuum conditions with excitation made with a laser at 380 nm [241]. In another publication, PtOEP was dispersed in polystyrene and spincoated on a surface to form a 130 nm thick film before being studied under vacuum conditions [61]. Using a gated detection technique ultra-fast sub-microsecond fluorescence-based thermal imaging of a conducting strip was demonstrated. Due to the FIR nature of the technique, it is insensitive not only to fluctuations of the excitation light source but also to intrinsic instabilities such as photobleaching.

A.4 Potential probes

Over the last few years, a couple of conceptually new probes for fluorescent-based temperature measurements have been demonstrated. These probes are based on the use of multistructural micro- or nanoscale particles specifically engineered to respond to certain changes in the environment. Although in an early state of development, these kinds of probes show the potential of modern nanotechnologies increased capabilities to structure matter on the nanoscale to fulfill specific needs.

The typical approach to engineering these new kinds of probes is to structure particles with several layers of varying thermal properties. Clear examples of how such engineering can be performed are shown in two articles referring to a new group of probes called molecular springs [246,247]. In these papers, theoretical considerations [247] and experimental results [246] are presented on the use of hybrid complexes composed of semiconductor and metal nanoparticles. The papers address in particular the case of single metal particle cores dressed with a number of semiconductor nanocrystals using polymer linkers for binding (see Fig. A.16). Due to field enhancement and energy transfer between the constituents of the assembly, the fluorescence emission is a complex function of material and geometrical parameters. As a result, due to the thermal sensitivity of the expansion or contraction of the polymer linker, which acts as a molecular spring, the fluorescence emission is changed with changes in temperature. The experimental results show that the assembly of a gold core and surrounding CdTe nanocrystals bound with a PEG linker (Au-PEG-CdTe) undergoes a reversible optically measurable structural

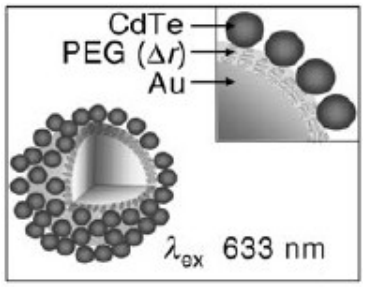

Figure A.16: Metal particle dressed with a number of semiconductor nanocrystals using polymer linkers for binding. [246]

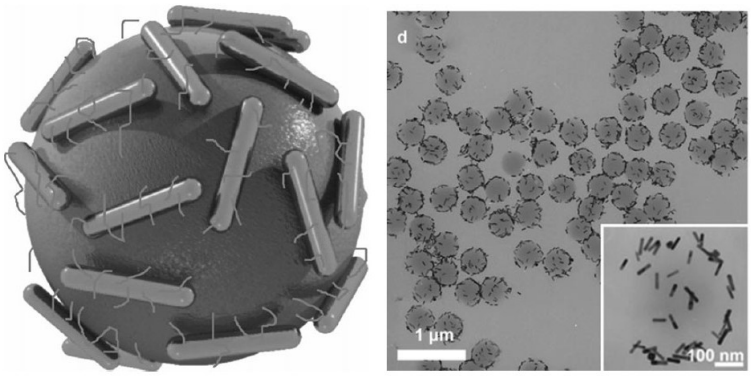

Figure A.17: Sketch of a collapsed pNIPAAM microgel partly covered with polyelectrolyte-coated gold nanorods (left image) and SEM image of the real nanorod-coated microgels. [228]

change as a response to changes in environmental parameters, e.g. temperature changes in the range 20 to 50 °C [246].

With a slightly different assembly of materials, Karg *et al* succeeded in fabricating probes which similarly presents sensitivity to temperature [228]. By assembling gold nanorods on a core of the thermosensitive polymer poly(N-isopropylacrylamide) (pNIPAAM) (see Fig. A.17), spectral changes could be observed as a function of temperature. The reason behind this change lies mainly in the increase of the nanorod density during the shrinking of the polymer with increased temperature, occurring principally at a transition temperature between 30 and 35 °C. Full reversibility was found for temperature changes between 15 and 50 °C.

Similar efforts on the engineering of complex microparticles have resulted in probes which are sensitive to multiple temperature transitions. Li *et al* demonstrated the use of two layers of block co-polymers grafted onto gold nanoparticles, giving rise to a core-shell structure with two thermosensitive points, 33 and 55 °C, due to swelling or contraction of the polymers (see Fig. A.18) [248]. Similar results were presented by Chen *et al* [249] who synthesized core-shell particles entirely of different polymers. Due to the temperature dependent swelling properties of the polymers different transition temperature, the assembled particles showed a two-step temperature dependent swelling behavior.

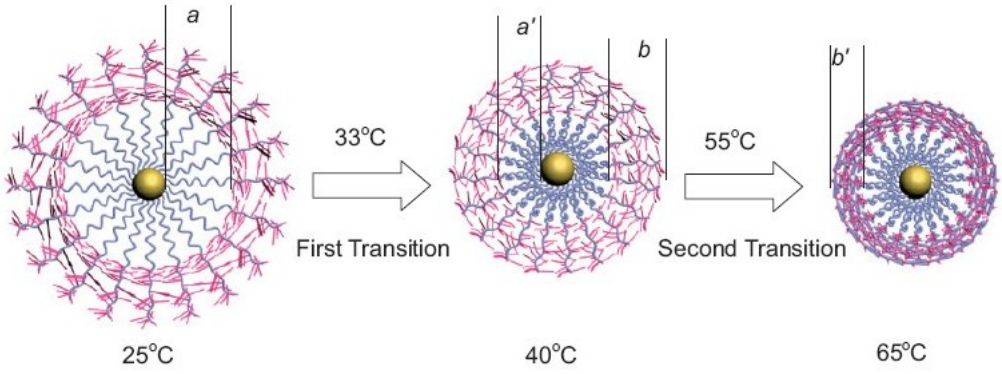

Figure A.18: Schematic illustrating the step-wise temperature sensitivity of gold/co-polymer nanoparticles. [248]

APPENDIX B
THERMOCHROMIC LIQUID CRYSTALS

Thermochromic liquid crystals (TLCs) can be used as temperature sensors due to their change of color with temperature. This feature has been employed for full-field mapping of temperature fields for over three decades [47]. An extensive review of the developments in the application of TLCs was given by Smith *et al* [54], where the experimental aspects of liquid crystals on solid surfaces as well as in fluid suspensions are discussed.

TLCs have found good use both for temperature measurements of liquid volumes [250, 251] and for surface thermometry [252]. Recent developments towards smaller scale have also seen efforts to apply TLCs for the thermal characterization of PCR systems [78,79] and electronic components [253,254], e.g. the detection of hot-spots on IC circuits [255]. The time response of TLC thermometry varies from a few milliseconds to several hundred milliseconds depending on the material and form of TLCs, while the temperature resolution generally is around 1 K [46, 47, 157, 254].

Although TLCs are a non-invasive[1] and cost-effective method for providing full-field temperature information, there are some problems in applying them to temperature measurements in microsystems. The size of the commercially available encapsulated TLCs is typically tens of micrometers, which is impractical for use in micro-sized structures [47], although some papers have claimed spatial resolutions down to 2 - 3 μm using. Furthermore, the coexistence of TLCs with a mixture of fluid, e.g. in PCR systems, may affect the biological activity of the medium [62].

[1] Due to the need for deposition on a sample, however, the technique could be called semi-invasive [46]

APPENDIX C

MICROFABRICATION PROTOCOLS

C.1 Preparing designs for EBL

All structures that were to be patterned by EBL were designed using the Virtuoso module of the CADENCE software package. The designs were exported as stream files in the GDS format. The GDS files were subsequently converted to the BEF format, which is specific for the Advantest EBL system, and decomposed in the software Bexelwin before importing the design in the uTile software of the EBL system. All software was accessed remotely at the *eb3* server of VDEC at the University of Tokyo.

In order to avoid problems related to stitching, the design was inspected in Bexelwin after conversion to the BEF format. In the Bexelwin design viewer, the stitching lines could be visualized. The interval between the stitching lines was 80 micrometers by default in the Advantest EBL system. By inspecting the design, it was assured that no stitching lines coincided with any nanowires. If a stitching line crossed a nanowire, the original design was modified and a new file conversion was performed. Typically, a rectangular structure was added on the side (one side only) of the design in order to shift the relative location of the design with regard to the stitching lines.

During the optimization process of the EBL parameters it was found that excessive exposure occurred of the EBL resist at high doses, due to effects such as electron back-scattering. This in turn led to excessive removal of the resist during development, which could be observed by the widening or narrowing of the intended structures (depending on whether a negative or positive type of design was patterned). Since high doses were effective in minimizing the amount of resist residues after development, we developed an approach where the dimensions of the structures in the software design were pre-compensated for the expected widening or narrowing effects. In Table C.1, a few examples are shown regarding the pre-compensations made when fabricating metal nanowires by lift-off on oxidized silicon substrates.

C.2 Basic substrates

Regarding the EBL process and nanowire patterning, two main fabrication processes were developed. On one hand, a recipe for metal nanowire fabrication was developed and on the other hand the fabrication of silicon nanowires was developed. The basic

Table C.1: Examples of geometrical pre-compensation in the fabrication of metal nanowires.

Desired nanowire dimensions	Dimensions in software design
Length 20 μm & Width 200 nm	Length 20.5 μm & Width 150 nm
Length 10 μm & Width 200 nm	Length 10.3 μm & Width 130 nm
Length 5 μm & Width 200 nm	Length 5.2 μm & Width 80 nm
Length 20 μm & Width 500 nm	Length 20.5 μm & Width 460 nm

substrates used for metal nanowire fabrication was either a <100>, 3-inch, 381 μm thick silicon wafer or a <100>, 4-inch, 525 μm thick silicon wafer. The larger 4-inch wafers were used for the development of a suspended membrane structure. The doping type and resistivity of the wafers were in both cases *p*-type and 10-20 Ωcm , respectively. Since the substrate did not take active part in the final device, the doping level had no significance other than any possible influence on EBL scattering effects and on the TMAH etch during membrane fabrication.

For the purpose of silicon nanowire fabrication, four-inch, 525 μm thick silicon-on-insulator (SOI) wafers were used. The SOI wafers contain a buried thin layer of oxide at a specified depth under the surface. This depth typically ranges from 100 nm to 10 μm while the thickness of the oxide typically ranges from 100 nm to 4 μm. Since the crystallinity and the thickness uniformity of the top silicon layer are very high in commercially available SOI wafers, these substrates are ideal for the fabrication of silicon nanowires with well-defined thicknesses. Our SOI wafers had a top silicon layer thickness of 330 nm and a buried oxide thickness of 400 nm. The conductivity of the top layer was 10-20 Ωcm.

C.3 Metal nanowire fabrication

The fabrication process for our metal nanowires was developed with respect to those results found in the FEM simulations presented in the beginning of Chapter 2. Two main configurations were developed, one with the nanowires on top of passivated solid silicon and one with a suspended membrane structure. In the following, a detailed description on the production of the two configurations will be presented. As shall be seen, the processes are practically identical until after the lift-off process and the subsequent passivation of the nanowires. After those steps, the nanowires on solid silicon are already ready for final mounting on a PCB board, while the nanowires on suspended membranes are further processed to perform the actual realization of the membranes. Details on the suspended membrane fabrications are given in the next section.

C.3.1 Protocol

1. Wafer cleaning

The basic silicon substrate were primarily cleaned in a 1:1 mix of H_2SO_4 and H_2O_2 (also known as a Piranha solution). This process allowed for the efficient removal of possible contamination on the silicon surface. Before proceeding to the subsequent process step, the sample was immersed in a buffered HF solution in order to remove the thin oxide layer which is inevitably created during immersion in the H_2SO_4:H_2O_2 solution.

2. Oxidation

I) *Oxidation of 3-inch wafers (unsuspended structures)*

Wet thermal oxidation was performed at 1100°C for 5 hours using the oxidation chamber of the MEMS cleanroom of Fujita/Toshiyoshi laboratory at IIS, the University of Tokyo. During temperature ramping up and down, a nitrogen flow was applied through the chamber, allowing the oxygen gas to enter only during the 6-hour oxidation window.

II) *Oxidation of 4-inch wafers (suspended structures)*

Wet thermal oxidation was performed by the clean-room engineers at LAAS-CNRS, giving a silicon dioxide thickness of 800 nm as measured by ellipsometer.

3. SiN_x deposition[1]

LPCVD (Low Pressure Chemical Vapor Deposition) was performed by the engineers at LAAS-CNRS in order to render a silicon nitride layer thickness of 600 nm.

4. EBL process

a) *Rinse and dehydration*

In order to remove possible dust and particles from the surface of the substrates, rinsing under running water was done. The rinse with water was likely to leave a thin layer of water molecules on the substrate surface, even after drying with a nitrogen gun. To assure the removal of all humidity from the surface, the wafers were placed on a hotplate at 180°C for 5 minutes.

b) *Spincoating*

An adhesion layer consisting of the primer HMDS was spincoated on the sample followed by the spincoating of the EBL resist ZEP 520A-7 from Zeon Corporation. The spin parameters shown in Fig. C.1 were used in both cases.

c) *Prebaking*

In order to vaporize all remaining solvent in the resist after the coating process, a prebake was performed on a hotplate at 180°C for 10 minutes.

d) *Exposure*

The spincoated samples were inserted in the EBL chamber. The appropriate design files were loaded into the system using the uTile software to define the placement

[1] Only for 4-inch wafers, i.e. suspended structures.

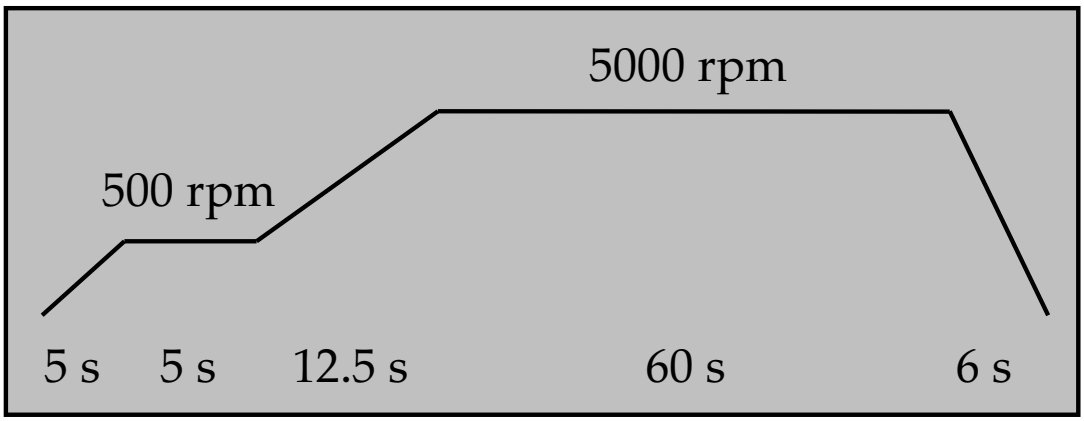

Figure C.1: Spincoating parameters for ZEP 520A-7 when patterning metal nanowires.

of the design on the sample and to define which exposure doses to use. For our optimized process concerning the metal nanowires, a dose of 120 μC/cm^2 was applied.

e) Development

The exposed structures were immersed in the development solution ZED-N50 (Zeon Corp.) for 1 minute and 30 seconds. Subsequent rinsing was performed for 1 minute in the rinsing solution ZMDB (Zeon Corp.). Final rinsing in DI water was also performed before drying the samples by the use of a nitrogen gun. Observation of the developed structures was done under an optical microscope in order to determine whether the result was satisfactory.

f) Resist removal if necessary

If for any reason the exposure had to be started over on the same sample, the remover solution ZDMAC (Zeon Corp.) was used to effectively remove all EBL resist. To allow for an efficient removal process, the solution was heated to 80°C using a hotplate inside a draft booth.

5. O2 ashing

After the development of the EBL-created patterns, the samples were exposed to an oxygen plasma for a short time in an RIE chamber (SAMCO RIE-10NR). This was done in order to minimize the risk of resist residues on the bare substrate areas. The parameters used for the oxygen plasma process are shown in Table C.2 .

6. Metal evaporation

A thin layer of nickel, approximately 40 nm thick, was deposited on top of the patterned resist. Special care was taken to assure a good thermal contact between the wafers and the wafer holder of the evaporation chamber. This was important in order to avoid heat build-up in the sample during the evaporation process, which might lead to the deformation of the resist.

Table C.2: O_2 ashing parameters.

O_2 flow	50 sccm
Pressure	10 Pa
Power	50 W
Time	10 seconds

Table C.3: SiO_2 sputtering process resulting in layer thickness of ∼100 nm.

Background pressure	$< 10^{-5}$ Torr
Total pressure	$2 \cdot 10^{-3}$ Torr
Gas flows	Ar 15 sccm, O_2 20 sccm
Temperature	Room temperature
Power	500 W
Time	25 minutes

7. Lift-off

Lift-off of the evaporated metal was accomplished by soaking the sample in the remover ZDMAC (Zeon Corp.) at 60°C for 15 minutes. In most cases, this was enough to complete the lift-off. However, in some cases, the lift-off had to be completed by immersion in an ultrasonic bath for a few minutes. The length of the immersion in the ultrasonic bath was determined by visual inspection during the process. A disadvantage of having to use the ultrasonic bath was the occurrence of permanent re-deposition of micrometer-size metal pieces on the sample surface. However, due to the unlikelihood for a metal piece to land on the essential parts of the sample, i.e. the nanowires, this was generally only a minor problem.

8. Passivation

The metal nanowires were finally passivated by a silicon dioxide layer using a sputtering process. Sputtering was chosen because of its availability at IIS at the University of Tokyo. An alternative and more regular approach to the deposition of silicon dioxide on top of metals would be PECVD (Plasma Enhanced Chemical Vapor Deposition). The parameters used for the sputtering process are shown in Table C.3 .

C.3.2 Resulting metal nanowires

In Fig. C.2 , examples of the obtained results are shown. As mentioned above, the geometry designed on the computer is not exactly replicated in the patterned resist and the resulting nanowires. In the images of Fig. C.2, the intended geometries as well as the resulting geometries are indicated. If the discrepancy between design and fabricated structures is known, it is possible to achieve certain dimensions by compensating for those narrowing and broadening effects that will occur during the EBL exposure.

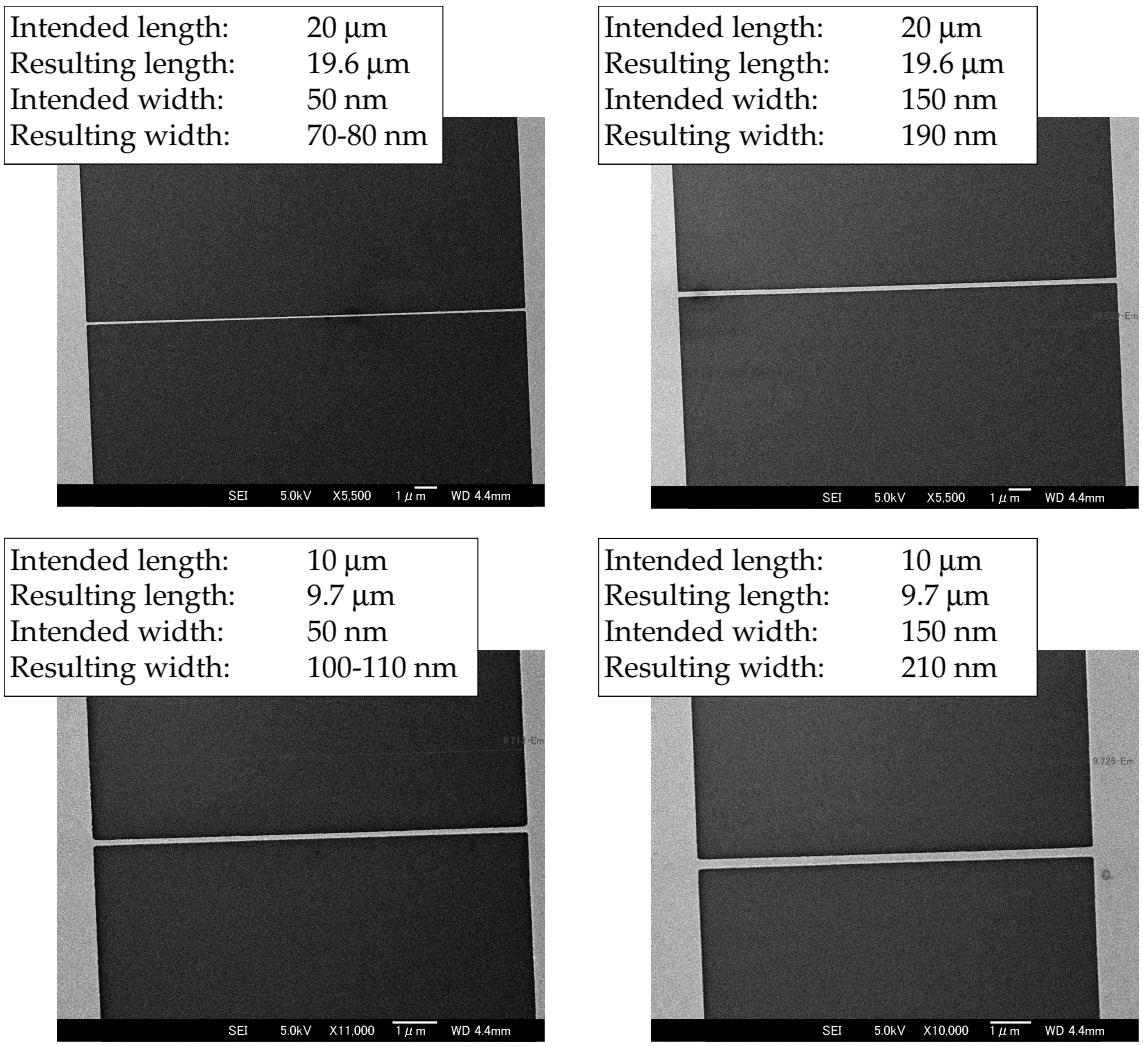

Figure C.2: This figure shows the SEM images of four of our metal nanowires. The resulting nanowire geometries do not perfectly correspond to those defined in the computer design.

C.4 Creation of the suspended membranes

As seen in the results of the FEM simulations of Chapter 2, a considerable difference in thermal behavior is expected for nanowires which are located on different materials. In order to realize a nanowire located on a suspended membrane as simulated in Chapter 2, we applied a back-side etching process based on the wet etchants KOH and TMAH. In order to assure a good stability of the membranes, only the samples with a composite membrane structure were used for this purpose. The composite membrane structure consisted of 800 nm silicon dioxide (SiO_2) and 600 nm silicon nitride (SiN_x) and was fabricated according to steps number 2 and 3 of the previous section. This specific membrane structure is the same as that which was used in earlier applications at the LAAS-CNRS, e.g. for the realization of microthrusters [217]. In the following, the membrane fabrication process is further detailed.

1. Backside patterning

a) *Mask design and fabrication*

The etch patterns to be transferred to the etch mask on the backside of the wafers were designed in the Virtuoso module of the CADENCE package. The design was transferred to a chromium mask for photolithographic use with a laser pattern generator from Heidelberg Instruments.

b) *Frontside spincoating*

Before starting the membrane creation process, a photoresist (S1818) was spin-coated on the front side in order to protect the nanowires. Since the only function of this resist was to protect the front side, the spin parameters were of little importance. It was assured that the entire frontside was well covered after the spincoating process.

c) *Baking*

The protective resist layer was baked on a hotplate at 90°C for 5 minutes in order to vaporize the remaining solvent in the resist.

d) *Backside spincoating*

A photoresist (S1818) was coated on the backside of the wafer using the spin parameters shown in Fig. C.3 . No adhesion agent was applied.

e) *Prebaking*

The frontside resist layer was baked on a hotplate at 90°C for 5 minutes in order to vaporize the remaining solvent in the resist.

f) *Backside alignment & UV light exposure*

Using a backside aligner (Union aligner), the pattern on the chromium mask was aligned with the frontside structures followed by UV light exposure (5 seconds with the Union aligner at IIS, the University of Tokyo).

g) *Development*

Development of the exposed structures was performed in the developing solution NMD-3 for 30 seconds. Rinsing was done in de-ionized water.

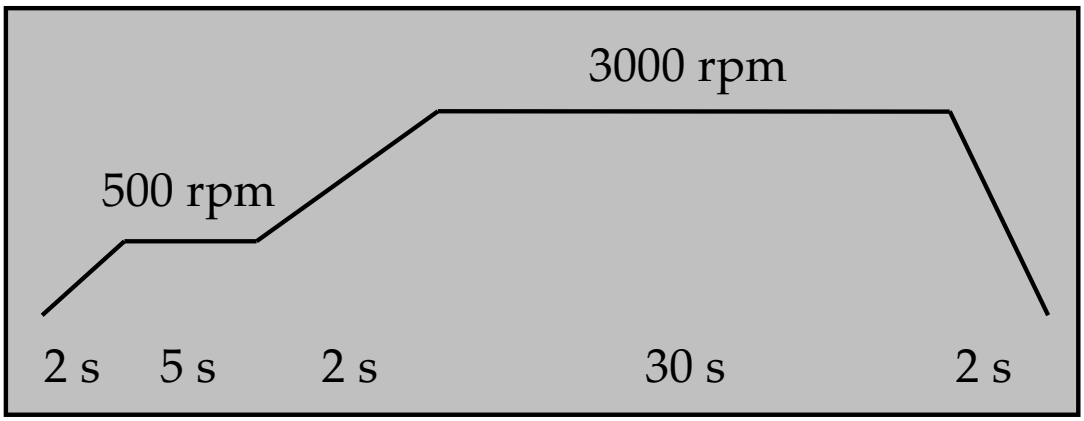

Figure C.3: Spincoating parameters for the photoresist S1818 during the backside patterning.

h) *Postbaking*

A final baking process was performed in order to improve the resistance of the resist. The baking was done on a hotplate at 130°C for 5 minutes.

2. Transferal of pattern to the etch mask

The membrane structure consisting of SiO_2 /SiN_x which had been deposited also on the backside of the wafers could conveniently be used as an etching mask during the KOH and TMAH etch. The following processes were performed to transfer the resist patterns of the previous step to the SiO_2 /SiN_x layer. a) SiN_x etching Dry etching in an RIE (reactive ion etching) chamber from SAMCO (RIE-10NR) was used and a reactive CF_4 gas was applied to perform the SiN_x etching. b) SiO_2 etching The SiO_2 was subsequently etch using a wet etch approach. The etchant used was buffered HF.

3. TMAH/KOH etch[2]

a) *Preparation of the etchant solution*

An especially modified glass beaker was used to contain the TMAH and KOH etchants. In the case of TMAH etching, the beaker was directly filled with a commercially available 15% TMAH solution. In the case of KOH etching, KOH pellets were poured into the beaker followed by the replenishment of water. The concentration was made to be approximately 30%.

b) *Heating of the etchant solution*

The beaker was placed on a hot plate. By the use of a feedback loop between the hot plate and a thermometer inserted in the solution, the temperature of the solution was increased to and kept at 90°C.

[2] More details on the TMAH/KOH processes are given in Appendix D

c) Mounting the sample in the chuck

As explained in Chapter 2, the frontside of the wafer had to be protected by the use of a Teflon chuck in order to avoid the deterioration of the nanowire structures. The wafer was mounted in the Teflon chuck, taking special care not to fasten the screws asymmetrically. Instead of fastening the screws completely one after the other, all screws were fastened in steps, addressing diametrically opposed screws after each other. After carefully mounting the wafer, the chuck was inserted into the hot etchant solution. Due to the depressurization path through the bottom and the handle of the chuck, thermally induced destructive shocks could be avoided.

d) Etching process

During the entire duration of the etching process, vigorous stirring was performed. Due to the size of the Teflon chuck, good stirring at the wafer surface could not be achieved by the regular hot plate stirring function. Instead, the most efficient method was to use a rotating blade inserted from above. Since the beaker had to be closed to prevent evaporation of the etching solution, a small hole was drilled in the lid of the glass beaker through which the rotating blade could be inserted. The etching process took up to 10 hours with the TMAH etchant and approximately 5 hours and 30 minutes with the KOH etchant. As the end of the process was getting close, the chuck was taken out of the etchant solution and the progress of the etching was inspected under an optical microscope without removing the wafer from the chuck. In the case of KOH, due to the considerable etching rate also of SiO_2, it was particularly important to stop the etching as soon as possible after completing the process in order not to etch into the membrane.[3]

C.5 Silicon nanowire fabrication

C.5.1 Protocol

1. Doping

In order to avoid the need for high voltages and consequently low currents, when performing resistive heating and sensing with the nanowires, the top silicon layer of the SOI substrate was doped to a relatively high level. The doping level used was $10^{19}cm^{-3}$. In order to avoid a metallic behavior and unpredictable behavior of the semiconductor behavior, doping levels above $10^{19}cm^{-3}$ were not considered. The doping was implemented by ion implantation of boron ions (p-type).

2. Wafer cleaning

The SOI substrate was cleaned in a 1:1 mix of H_2SO_4 and H_2O_2 (also known as a Piranha solution). Native oxide and oxide created during the cleaning process were subsequently removed using a buffered HF solution.

[3] For future etching of this kind, it could be of interest to try an approach where KOH is used for removing the larger parts of the silicon followed by etching in TMAH in order to proceed more slowly the last tens of micrometers and avoid unwanted etching of the membrane

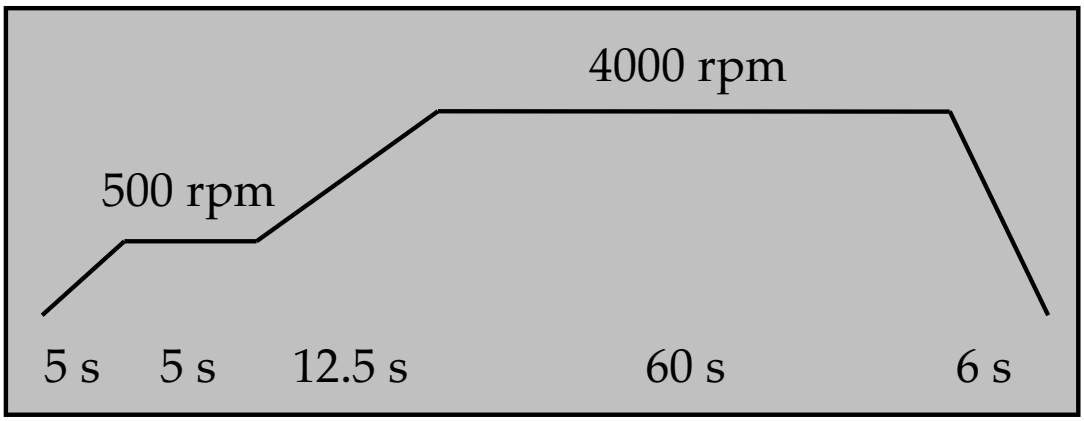

Figure C.4: Spincoating parameters for ZEP 520A when patterning silicon nanowires.

3. EBL process

a) *Rinse and dehydration*

In order to remove possible dust and particles from the surface of the substrates, rinsing under running water was done. The rinse with water was likely to leave a thin layer of water molecules on the substrate surface, even after drying with a nitrogen gun. To assure the removal of all humidity from the surface, the wafers were placed on a hotplate at 180°C for 5 minutes.

b) *Spincoating*

An adhesion layer consisting of the primer HMDS was spincoated on the sample followed by the spincoating of the EBL resist ZEP 520A from Zeon Corporation. This resist was more viscous than the ZEP 520A-7 used for the metal nanowires. This in turn resulted in a slightly thicker resist layer. The spin parameters shown in Fig. C.4 were used both for the HMDS and the resist.

c) *Prebaking*

In order to vaporize all remaining solvent in the resist after the coating process, a prebake was performed on a hotplate at 180°C for 5 minutes.

d) *Exposure*

The spincoated samples were inserted in the EBL chamber. The appropriate design files were loaded into the system using the uTile software to define the placement of the design on the sample and to define which exposure doses to use. For silicon nanowire with widths below 200 nm, a dose of 86 μC/cm^2 was and for widths larger than 200 nm, a dose of 88 μC/cm^2 was used.

e) *Development*

The exposed structures were immersed in the development solution ZED-N50 (Zeon Corp.) for 4 minutes and 30 seconds. Subsequent rinsing was performed for 1 minute in the rinsing solution ZMDB (Zeon Corp.). Final rinsing in DI water was also performed before drying the samples by the use of a nitrogen gun.

Table C.4: O_2 ashing parameters.

O_2 flow	50 sccm
Pressure	10 Pa
Power	50 W
Time	10 seconds

Observation of the developed structures was done under an optical microscope in order to determine whether the result was satisfactory.

f) *Resist removal if necessary*
If necessary, the remover solution ZDMAC (Zeon Corp.) was used to effectively remove all EBL resist. To allow for an efficient removal process, the solution was heated to 80°C using a hotplate inside a draft booth.

4. O2 ashing

After the development of the EBL-created patterns, the samples were exposed to an oxygen plasma for a short time in an RIE chamber (SAMCO RIE-10NR). This was done in order to minimize the risk of resist residues on the bare substrate areas. The parameters used for the oxygen plasma process are shown in Table C.4 .

5. Dry anisotropic etching

Dry anisotropic silicon etching based on a reactive SF_6 ion plasma assisted by O_2 and C_4F_8 gas was used to etch the top silicon layer of the SOI wafer. The process was performed with a ICP-RIE machine STS (recipe *SOI10040* for the machine in the MEMS cleanroom of Fujita laboratory). By protecting only the covered areas, the EBL resist assured the transfer of the resist patterns into the silicon layer. The buried SiO_2 layer acted as an etch barrier due to its relatively low etching rate. Because of the anisotropic character of the dry etch, the nanowire cross-section was rectangular. The resulting structure in the top silicon layer was a central nanowire part with two big connecting pads, one at each end.

6. Removal of EBL resist

In order to remove the remaining EBL resist, the ZEP remover ZDMAC (Zeon Corp.) was used. The sample was soaked in the remover at 80°C for 5 minutes. If residues remained on the sample surface after this process, oxygen ashing was performed for a minute at high power to assure a clean surface. The ICP-RIE machine was used for this ashing process.

7. Optional nanowire release

On some samples, the nanowires in the top silicon layer were release-etched by immersion in a buffered HF solution for a few minutes. This etching process was only suitable for relatively short nanowires. For nanowires longer than approximately 10 μm, permanent stiction between the nanowire and the underlying silicon structure would easily occur

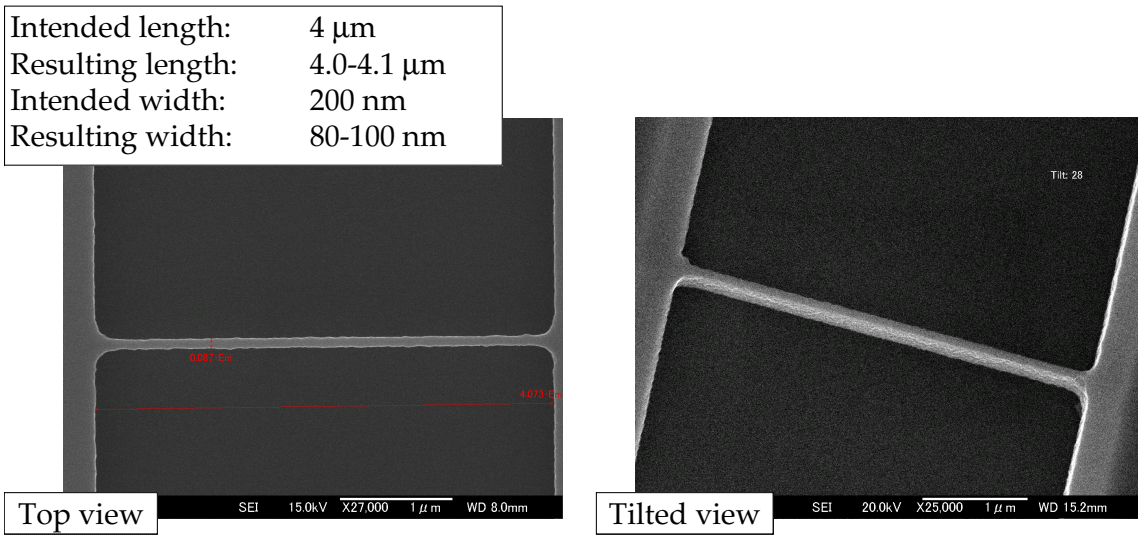

Figure C.5: SEM images of a release-etched silicon nanowire. The left image shows a top view and the right image shows nanowire from a slightly inclined perspective. The length of the nanowire is 4 μm and the width 100 nm. At the edges of the connecting pads, the underetch by the BHF solution can be seen. The underetched areas are brighter than the unetched areas.

during the evaporation of the rinsing solution (DI water).[4] An example of a successfully release-etched silicon nanowire is shown in Fig. C.5 .

8. Deposition of metal electrodes

In order to facilitate the external connection of the silicon pads by wirebonding, a metal layer was deposited on top of the pads using a conventional photolithography and lift-off process (not detailed here). The size of the metal electrodes was such that they reached very near the ends of the silicon nanowires. This was done in order to allow for a further increased relative resistance of the nanowire compared to its connection paths. This is interesting from a thermal point of view, considering that the resistive heating would become yet more localized this way. The metal of choice was aluminum, which interfaces well with *p*-type semiconductors. The important thing to consider was to choose a metal which would not give rise to a Schottky barrier at the semiconductor-metal interface. In order to enhance the contact between the aluminum and the silicon, the sample was additionally cured in an oven at 360°C for 20 minutes.

C.5.2 Comments on the use of silicon nanowires

The two main reasons for discontinuing the use of silicon nanowires within this thesis were related to the time-demanding doping process needed to reach an appropriate conductivity level and the connection to an external power source. Standard commercial SOI wafers come with a typical doping level of 10^{15}cm^{-3} (*p*-type), corresponding to

[4] This critical length is obviously dependent on the thickness of the buried oxide layer. In the case of our SOI wafer, this thickness was 400 nm.

a resistivity of approximately 10-20 Ωcm. Using substrates with these relatively high resistivity values means that relatively high voltages will be needed in order to obtain resistive heating in the structure and that low current values have to be analyzed when performing FET-based sensing. To enable the use of lower voltages, doping of the silicon structure should be made to render it closer to metallic behavior. Good doping values lie around 10^{18}-10^{19} cm^{-3}. Above this point the behavior becomes more unpredictable and less manageable. The practical realization of doping is well established in the microelectronics field. However, in micromachining laboratories, doping is less common and the introduction of doping means having to prolong the fabrication process. A convenient alternative would be to buy commercial pre-doped SOI wafer, although such customized solutions are expensive for a research laboratory. A second inconvenience with the silicon nanowires is the general need to deposit a layer of metal on top of the silicon pads in order to enable wirebonding on the structure and connection to an external power source. While some wirebonding machines allow for direct bonding of wires onto bare silicon surfaces, the more common machines are typically limited to bonding on metal layers.

APPENDIX D

TMAH/KOH ETCH

In order to realize the removal of bulk silicon underneath the SiO_2/SiN_x layers, we used the anisotropic wet etchants KOH (Potassium Hydroxide) and TMAH (Tetramethyl Ammonium Hydroxide). These etchants attack the silicon with a high selectivity regarding the crystalline planes of silicon. Due to the higher etch rate of the <100> planes compared to the <111> planes, a pyramidal shape is achieved in the etched substrate. The inclination of the <111> planes with regard to the <100> plane of the wafer surface is 54.7deg. The exact etching rates of KOH and TMAH are given in Table D.1 and Table D.2 . Due to the low etching rate of SiO_2, masking is commonly done with this oxide. An alternative is to use SiN_x, which is hardly etched at all by KOH and TMAH.

A drawback of TMAH is the relatively high etch rate of the <111> plane. This means that unless the process is stopped in time, broadening of the membrane width may occur. KOH on the other hand has a much lower <111> plane etch rate but etches SiO2 faster than TMAH. Therefore, when using KOH, special care has to be taken when the end of the etching process is near in order to ensure that the membrane is not excessively etched.

In order to allow for etching of the backside of a silicon wafer without affecting the structures on the front side, the etchant solution must somehow be stopped from reaching these structures. In the case of wet etchants in general, protection is provided by covering the surface with a resist or wax. However, the regular resists and waxes are not able to withstand the attack of TMAH and KOH. Instead, the protection of the front side requires the use of a specific chuck in which the wafer can be placed before being immersed in the etchant. This chuck should leave only the backside exposed to the liquid environment while the front side should be shielded from the entrance of any

Table D.1: Etching rates for a 33% KOH solution at 90°C.

Silicon <100>	2 μm/min
Silicon <111>	$\sim$ 0 μm/min
SiN_x	< 1 nm/min
SiO_2	0.015 μm/min
Si <100> / SiO2 = 133	

Table D.2: Etching rates for a 15% TMAH solution.

Silicon <100>	1.4 μm/min at 90 °C 0.9 μm/min at 80 °C
Silicon lateral underetch	0.075 μm/min at 90 °C
SiO_2	0.001 μm/min at 90 °C
Si <100> / SiO_2 = 1400	

liquid.

The development of a protection chuck was performed with the following specifications in mind. First of all, the chuck should be able to protect the backside from the TMAH and KOH etchants. Second, the mounting of the wafer should be done in a way that does not induce excessive mechanical stress in the wafer. Third, since the etching process is performed at a temperature of 90°C, it is important that pressure changes in the air enclosed in the cavity at the wafer backside do not lead to the destruction of the thin membranes as the silicon etching is finished or close to finishing. These consideration led us to develop a chuck made of Teflon as shown schematically in Fig. D.1. The Teflon resists the etching action of TMAH and KOH solutions at high temperatures. In addition, it is relatively cheap and easy to process. An alternative material that could be used is PEEK, which generally provides a better thermal stability and longer lifetime but which is up to 10 times more expensive than Teflon.

As shown in the schematic of Fig. D.1, the chuck contains circular grooves for the positioning of O-rings. Two O-rings are positioned on opposite sides of the wafer in order to assure a soft clamping of the wafer and to prevent the passage of the etchant solution to the wafer front side. A third O-ring of larger diameter is additionally used to help preventing the passage of TMAH solution through the sides of the chuck. Six screws made of PEEK are used to keep the chuck closed. When closing the chuck, the screws are tightened by addressing diametrically opposed screws at the same time in order to avoid the introduction of asymmetric mechanical stress in the wafer. An important design feature is also the existence of an air pathway from the enclosed chamber at the wafer front side. This pathway is realized by the drilling of a narrow cylindrical hole reaching from the middle of the chuck towards the connection point of the handle and then from one end of the handle to the other. The handle is securely attached to the main part of the chuck using PEEK screws and a small O-ring to avoid leakage. This way, the enclosed chamber at the front side of the wafer is connected to the atmosphere, which allows for a continuous stabilization of the temperature-induced pressure changes in the chamber.

During etching, the chuck was placed in a horizontal position with the wafer surface to be etched facing upwards. An especially manufactured glass beaker with a lid was used. The lid of the beaker contained three holes, one allowing for the handle to reach out to the atmosphere, another one enabling the introduction of a rotary stirring blade from above and the last one enabling the introduction of an thermometer into the etchant solution. Stirring of the TMAH solution during etching is of high importance in order to maintain a uniform etching rate. The approximate etching time for the 525 μm thick

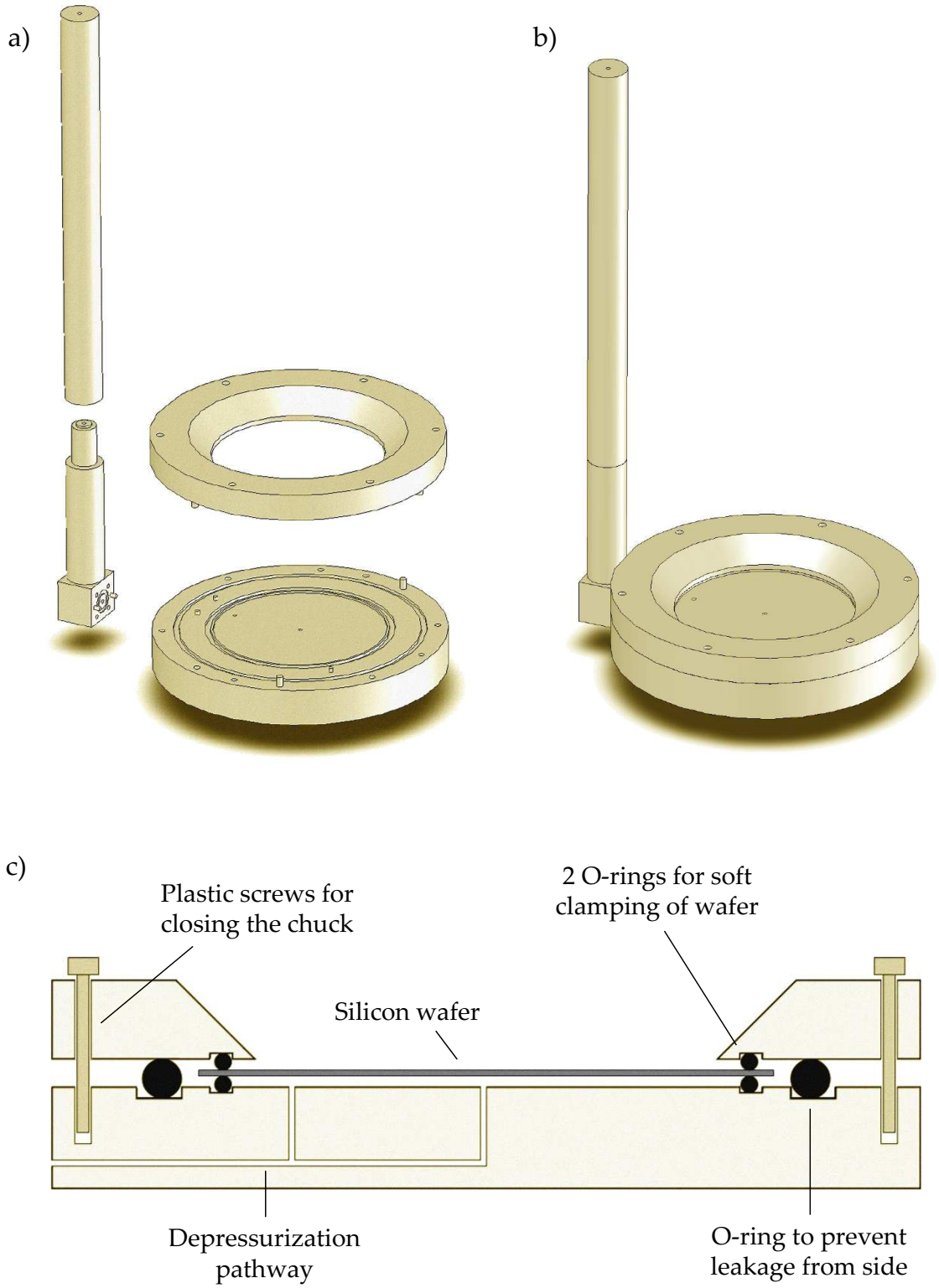

Figure D.1: a) 3D view of the TMAH/KOH chuck with the four main parts separated. b) 3D view of the TMAH/KOH chuck after assembling the parts. c) Cross-sectional side-view of the two lower parts of the TMAH/KOH chuck.

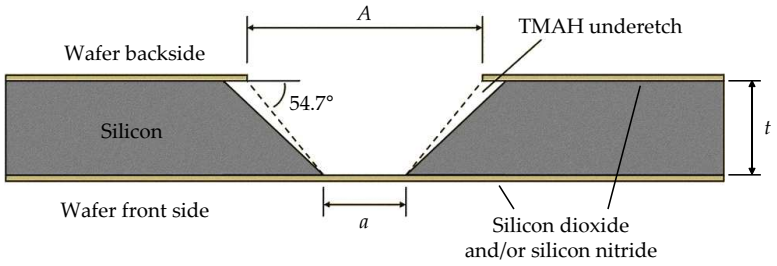

Figure D.2: Geometry of the resulting TMAH holes. The size of the bottom side orifice can be calculated using a simple geometrical relation between the parameters in the figure.

wafers used here was 5h 30min for KOH and above 10 hours for TMAH. Due to the long etching time using TMAH, most samples were prepared using KOH etching. To avoid etching of the membrane close to the end, the chuck was repeatedly taken out of the etchant and the progress of the etching process was observed under an optical microscope while still in the chuck. Approximate measurement of the etch depth was done using the focal distance measurement function of the optical microscope. For future fabrication of suspended membranes, an alternative approach is to etch most of the bulk silicon with a KOH etchant and then change to a TMAH bath for the last few tens of micrometers. This would keep the total etching time relatively short while lowering the risk of unintentional membrane etching.

Due to the pyramidal shape of the KOH and TMAH etching profiles, the thickness of the wafers has to be known in order to calculate how large the unmasked areas of the backside should be. This principle is illustrated in Fig. D.2. In order to achieve the size *a* on the front side, the unmasked length *A* on the backside can be calculated by the following formula.

$$a = A - \frac{2t}{tan(54.7)} \tag{D.0.1}$$

In order to actually achieve the predicted size a on the front side, it is important to align the unmasked areas as well as possible to the crystalline planes wafer. Practically speaking, this means aligning the square patterns of the mask with the flat edge of the wafer. In the case of TMAH etching, because of the somewhat higher etch rate of the <111> plane, the wall inclination will change continuously during the etching time. This results in a slightly different etching profile. However, the formula above is still accurate if the etching process is stopped immediately after the etchant reaches the other side.

APPENDIX E

STREPTAVIDIN - RHODAMINE B DEPOSITION

1

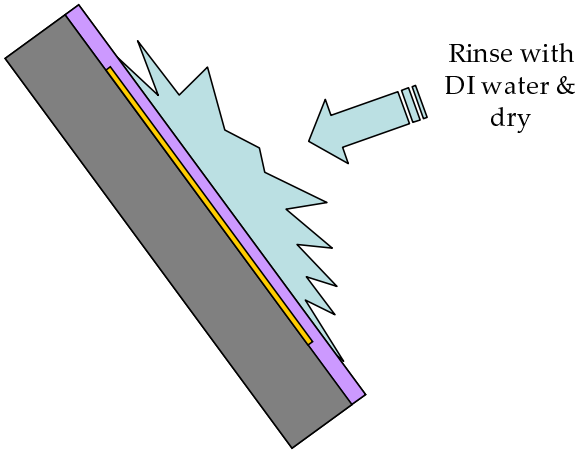

2

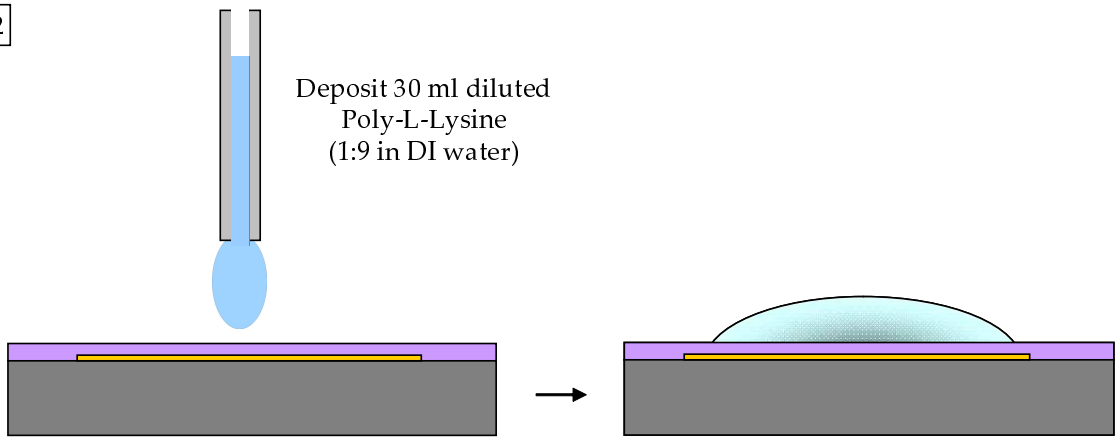

3

Place a Parafilm piece on top of the Poly-L-Lysine droplet in order to distribute the liquid over the surface.
Leave the Poly-L-Lysine for **t = 5 min**, with the Parafilm on top.

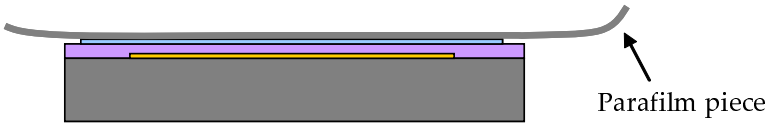

4

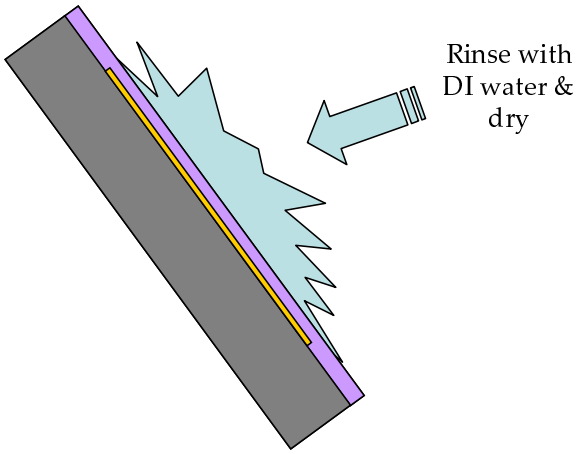

5

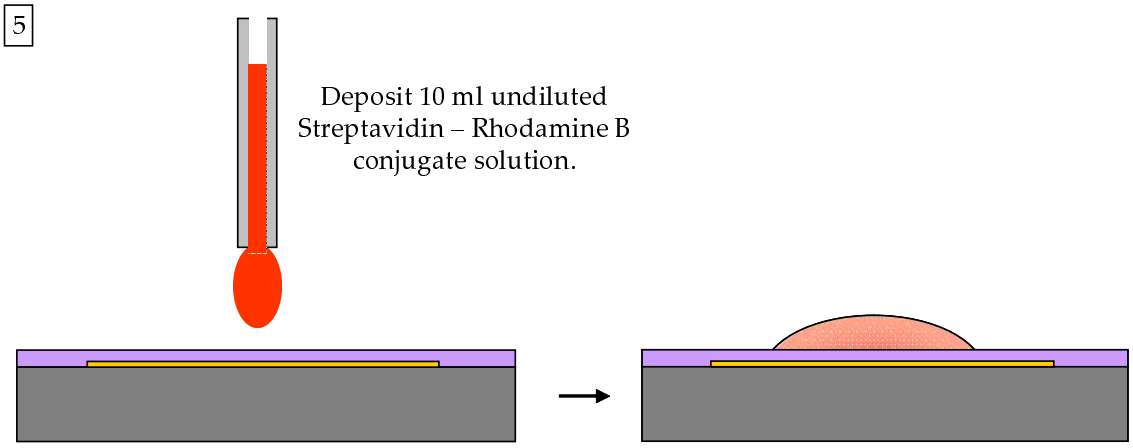

6

Place a Parafilm piece on top of the Streptavidin - Rhodamine B droplet in order to distribute the liquid over the surface. Leave it for **t = 15 min**, with the Parafilm on top. Place a small Petri dish above the sample in order to minimize solvent evaporation. Protect the solution from direct light by covering the Petri dish with aluminum foil.

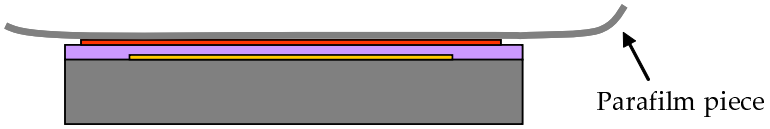

7

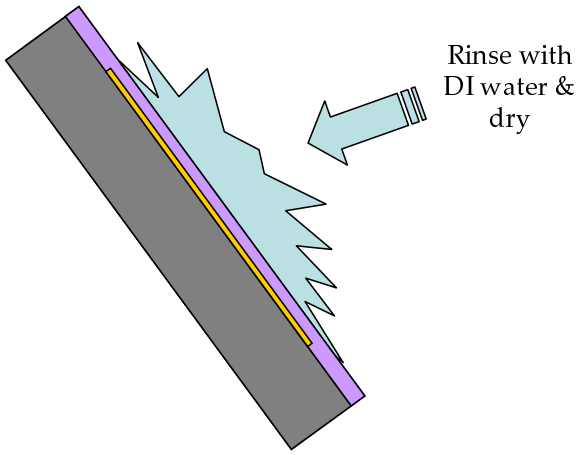

APPENDIX F

PDEP ASSEMBLY OF NANOCRYSTALS

One of the challenges that were faced in this thesis was that of locating the fluorescent temperature probes at the locations to be characterized, i.e. on top of the nanowires. One of the investigated approaches for the probe deposition consisted in the assembly of semiconductor nanocrystals on our micro- and nanowires using electric fields. While finally not being used for our fluorescent thermometry technique, the results are of significant general interest and will therefore be presented in this appendix.

The basic mechanism of the electric field assembly relies on those forces that act on polarizable particle when exposed to a non-uniform AC electrical field. These forces are generally known as dielectrophoretic (DEP) forces. Over the last decade, the DEP forces have been exploited in a range of applications, in particular biological ones, e.g. for the manipulation and positioning of molecular species [256–258]. While the DEP effect has been the main focus of our studies regarding the electric field assembly, other electrical effects, in particular AC electroosmosis [259], are likely to play important roles in the results that we have found.

F.1 Theory behind the DEP effect

The DEP force acts on a polarizable particle in case it is immersed in a medium of a different polarizability and is exposed to a non-uniform AC electrical field. The time-averaged DEP force can be approximated in terms of dipole effects as: [257, 260]

$$\langle F_{DEP} \rangle = 2\pi a^3 \varepsilon_m Re\left[f_{CM}\right] \nabla \left|E_{rms}\right|^2 \tag{F.1.1}$$

$$f_{CM} = \frac{\varepsilon_p^* - \varepsilon_m^*}{\varepsilon_p^* + 2\varepsilon_m^*} \left(the\, Clausius - Mossotti\, factor\right) \tag{F.1.2}$$

In this formula, E_{rms} is the root mean square of the electric field, a the radius of the particle, ε_m the complex permittivity of the medium and ε_p the complex permittivity of the particle. Considering this formula, we can see that the DEP force depends on the particle size, the magnitude of the applied field and the frequency of the applied field. Depending on the frequency, the so-called Clausius-Mossotti factor, f_{CM}, will have different signs and thereby the direction of the force will change. In the case that the factor is positive, as in Fig. F.1 , the particle is more polarizable than the surrounding

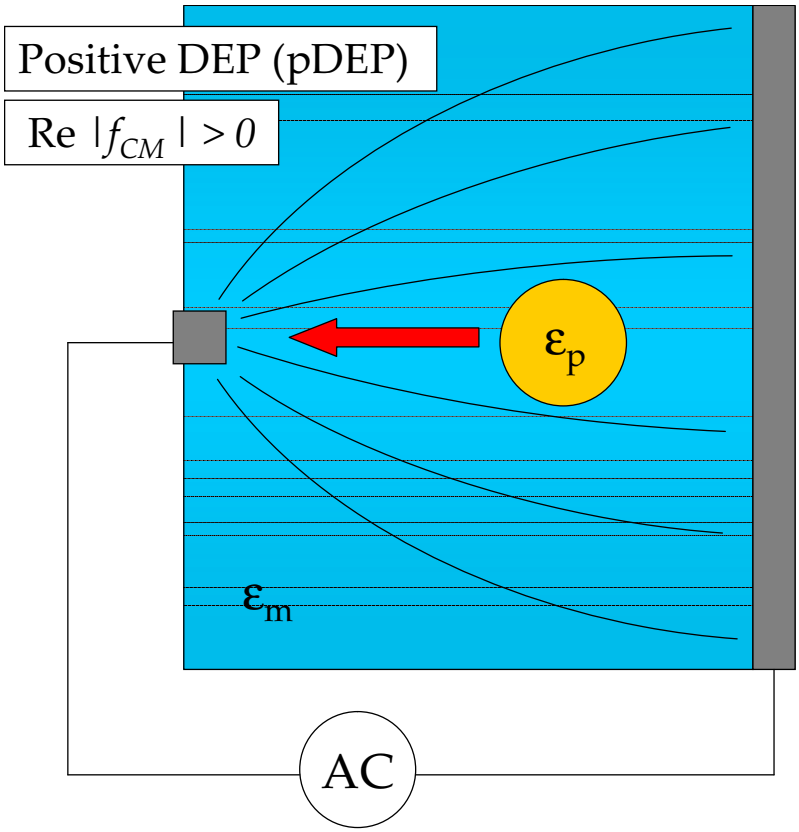

Figure F.1: Positive dielectrophoresis - pDEP.

medium and the particle will be attracted towards the maxima of the electrical field, i.e. towards the left in the figure. This is called positive dielectrophoresis (pDEP) and is the type of DEP force that has been investigated in this work.

F.2 Application of the pDEP force for nanocrystal assembly

If we consider the geometry of our micro- and nanowire structures and we imagine the positioning of a large and flat electrode above the wire structure, it is easy to realize how a non-uniform electric field can be created between the large electrode and the small wire. By the application of an AC field between the large electrode and the wire, maximum electric field strength will be located at the vicinity of the wire. By the use of an appropriate frequency, polarizable particles dispersed in the medium between the large electrode and the wire the will be attracted towards the wire. Under the assumption that the semiconductor nanocrystals are polarizable to some extent, the assembly of the nanocrystals on our wires can thus be expected.

F.2.1 Experimental approach

As shown in Fig. F.2 , we applied the previously explained principles by the positioning of an ITO (Indium Tin Oxide) covered glass coverslip above our wires at a distance determined by a double-sided adhesive tape spacer (thickness$\sim$100 μm). The ITO is

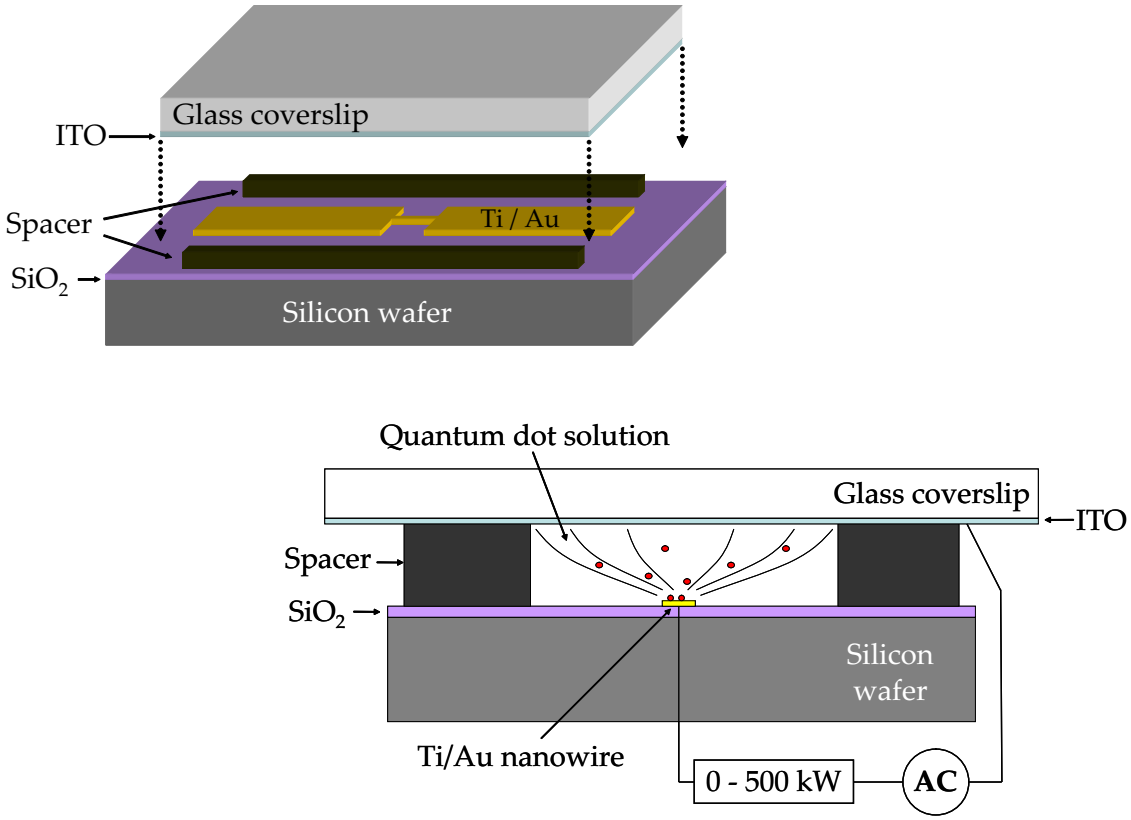

Figure F.2: Sample setup for pDEP assembly of nanocrystals. An ITO-covered glass coverslip was placed above the wire using an adhesive tape as a spacer. This way, a non-uniform electrical field could be obtained between the flat ITO electrode and the wire, with a field maximum in the vicinity of the wire.

a transparent and electrically conductive oxide. Thus, it could be used as an electrode while simultaneously allowing for optical observation from above.

The wires that were used for the assembly experiments were non-passivated metal wires, typically Ti/Au wires or Ni wires with a thickness of 40 nm. The length varied from 10 to 100 μm and the width from 200 nm to 4 μm. The samples were mounted on a PCB board and wirebonded to allow for external connection. For the use of the smallest wires (width$\lesssim$500 nm), variable resistances in the range 0-500 kΩ were connected in each end of the wires and turned to their maximum value. This protected the nanowires from static shock and burnout when connecting them to the AC power source. After connection, the variable resistances were turned to zero. The AC field was applied using an Agilent 33220A wave generator with an effective voltage range of 0-10 V peak-to-peak and a frequency range of 0-20 MHz.

F.2.2 The nanocrystal solution

After having prepared the experimental setup, a quantum dot solution was introduced into the gap between the ITO slide and the sample surface. The quantum dot solution consisted of carboxyl functionalized CdSe/ZnS core-shell nanocrystals with emission peak at 655 nm (from Quantum Dot Corp.). The diameter of these particles was around 10 nm and the particle concentration of the original nanocrystal solution was 8.2 μM. Regarding the experimental solution, a 25 mM MES buffer of pH 5.0 was used as the solvent medium and the dilution of the quantum dots was 1:5000 with regard to the original solution. To facilitate the insertion of the solution in the gap, the hydrophilicity of the ITO slide was increased by ashing in O_2 plasma before mounting.

F.2.3 Observation of the assembly

The electrical field assembly process was observed from the top using a BX-51 fluorescence microscope from Olympus with appropriate filter sets. In order to capture and record fluorescent images on a computer, a Cascade II:512 CCD camera from Photometrics in combination with MetaMorph software from Molecular Devices Corp. was used.

F.3 Results & discussions

The results turned out to be somewhat different in the case of microwires and nanowires. These two cases will therefore be treated separately.

F.3.1 Electrical field assembly on microwires

In the case of microwires, electrical field assembly was successful as can be seen in Fig. F.3, where a 4 μm wide and 100 μm long Ti/Au wire was used. Nanocrystals lined up along the middle of the wires and on the edges of the connecting electrode areas. To achieve this assembly, a frequency of 100 kHz and a voltage of 10 V peak-to-peak were applied. As for the voltage, assembly could be seen already at a few volts. Increased voltage accelerated the assembly process.

The movement of the nanocrystals during the assembly process seemed to have two components. On one hand, pDEP forces dragged the nanocrystals towards the microwire

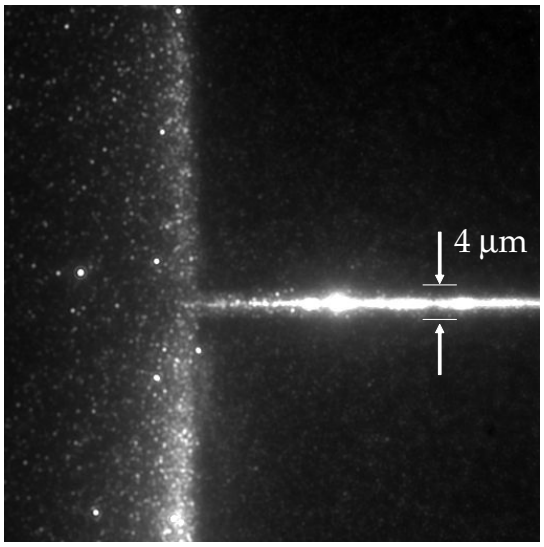

Figure F.3: Fluorescent image showing electrically assembled nanocrystals along the middle of a 100-μm long and 4-μm wide wire.

as expected. Secondly, a semicircular movement of the nanocrystals was observed at the vicinity of the wire, as illustrated in Fig. F.4. This second movement dragged the nanocrystals to the middle of the wire. We believe that this flow was induced by AC electroosmotic forces [259] which appeared due to the potential difference between the microwire area and the surrounding SiO_2 surface.

In some experiments the resulting assembly looked like in Fig. F.5. This typically occurred when old nanocrystal solutions were used. As the solutions got older, clustering of the nanocrystals occurred and the effective particle size thereby increased. During the assembly, the movement was the same as in the former case. On the other hand, attachment occurred at the edges of the wire. We believe that nanocrystal clusters were attracted to the edges in a similar way as the former case. However, due to their size, they got in contact with the underlying SiO_2 onto which they easily adhered. Fewer particles would therefore continue to the middle of the wire.

F.3.2 Electrical field assembly on nanowires

As for assembly on nanowires, assembly could not be observed for a setup similar to the one used for microwires. At no available voltage or frequency did assembly occur in the nanowire case. On the other hand, assembly could be achieved through a slight change in the electrical connections (See Fig. F.6). In the case of the microwires, one pole of the AC source was connected to the ITO slide and the other pole to both ends of a microwire. In the case of nanowires, only one nanowire end was connected to the AC source. Due to the high resistance that the nanowire represented, different potentials were thereby obtained at the two ends of the nanowire.

Using this modified connection, assembly was obtained also in the nanowire case. During the assembly, a slow global movement of the particles from one side of the nanowire to the other was observed. At the vicinity of the wire, nanocrystals were attracted relatively fast towards the nanowire as illustrated in Fig. F.7. During this movement, some nanocrystals attached while others rapidly bounced back off. Assembly

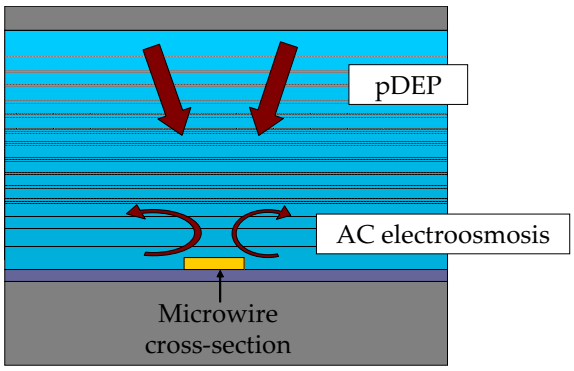

Figure F.4: As the non-uniform AC field was applied, movement of the nanocrystals appeared as indicated by the arrows in this figure. Two components could be seen. On one hand pDEP forces dragged the particles towards the wire. Secondly, a semicircular flow of nanocrystals was observed at the vicinity of the wires. This is believed to be caused by AC electroosmosis.

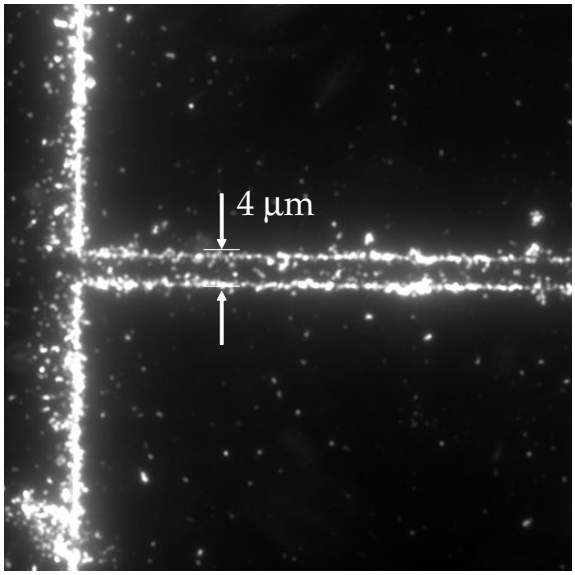

Figure F.5: Fluorescent image showing nanocrystals and nanocrystal clusters which are mainly assembled along the sides of the 100-μm long and 4-μm wide wire.

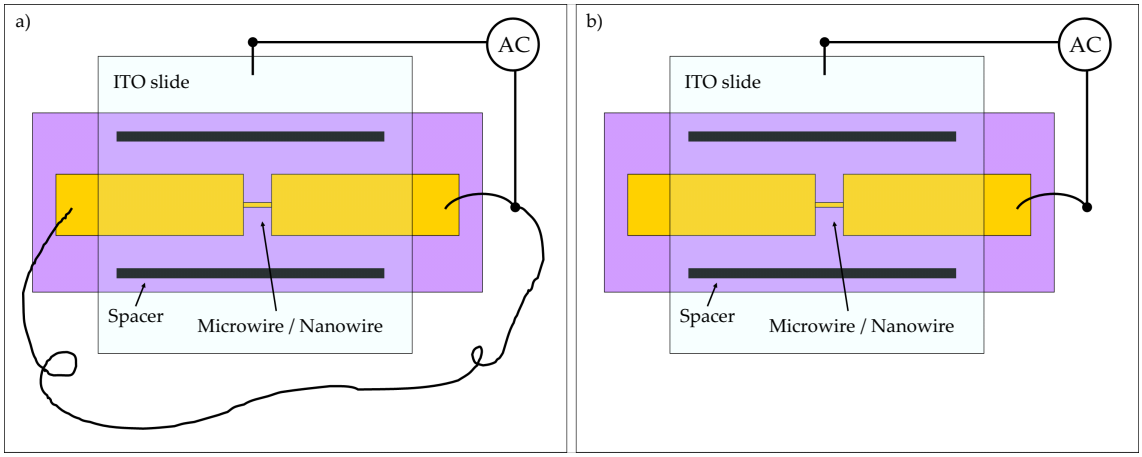

Figure F.6: a) In the case of the microwires, one pole of the AC source was connected to the ITO slide and the other pole to both ends of a microwire. b) In the case of nanowires, only one nanowire end was connected to the AC source.

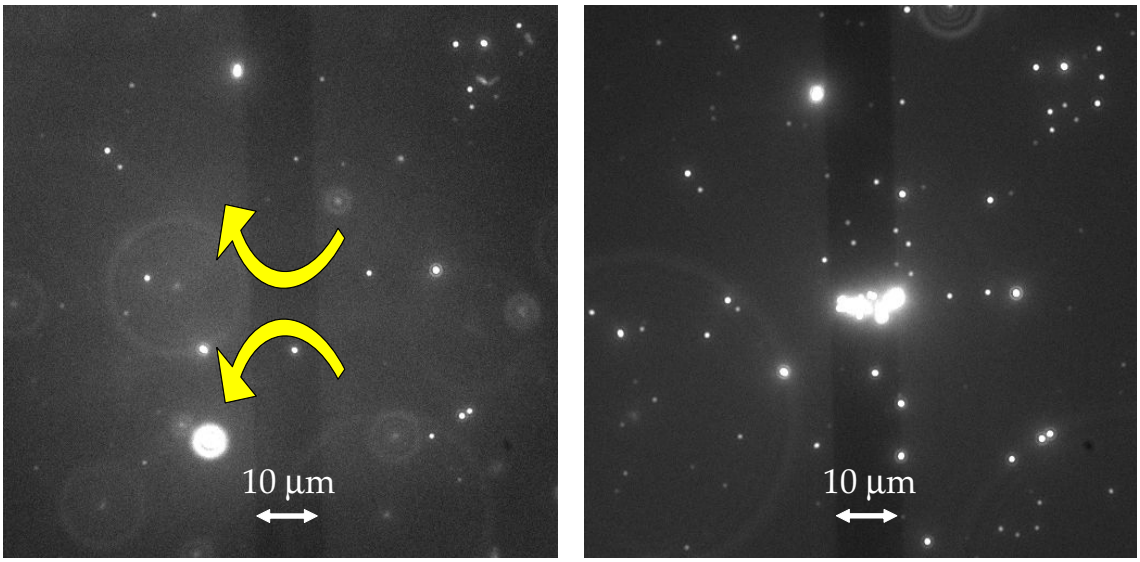

Figure F.7: Fluorescent image showing a 200 nm wide nanowire structure. Due to its small size it is hardly visible. The arrows indicate the movement of the nanocrystals during electrical assembly (left). Nanocrystals assembled on top of the nanowire (right).

in the nanowire case occurred most effectively at a frequency around 5 MHz and at a voltage around 4 V. Too high applied voltage, typically 5 V or higher, led to burnout of the nanowire.

The observed movement is still not fully understood. We believe it to be a rather complex superposition of different forces. The difference in potential on the two sides of the nanowire seemed to induce an AC electroosmotic flow of particles in the vicinity of the wire. At the same time, the formerly discussed pDEP forces were most likely altered due to the new electrical field component that appeared between the two sides of the nanowire. This probably resulted in the particles being dragged in one direction at the vicinity of the gap between the connecting electrodes.

F.4 Conclusions

The electrical field assembly of semiconductor nanocrystals on micro- and nanowires presented a rather complex behavior. The involved phenomena need further investigations before making final conclusions. At this point, the main assembling force is believed to be a positive DEP force, while other effects such as AC electroosmosis also seem to be involved.

APPENDIX G
MEASUREMENT OF THE OPTICAL POWER DENSITIES

When performing the photostability tests on the different fluorophores (see Chapter 3), neutral density (ND) filters were used to alter the transmitted excitation intensity. When using the EXFO metal halide light source, an additional intensity control was available on the lamp. Furthermore, the intensity finally reaching the sample surface also depended on the objective and the excitation filter for the specific fluorophore.

In order to get a quantitative indication of the optical power densities reaching the sample surface for the various combinations of light source intensity and ND filters, the transmitted powers were measured under the objective using a Newport 840 optical power meter[1]. Optical power densities were subsequently obtained by dividing the total optical power (which was measured by the power meter) with the illuminated surface area.

In order to estimate the size of the illuminated surface area for the different microscope objectives being used, strong photobleaching was performed by illuminating the fluorophore-covered surface for an hour at maximum intensity. By subsequently shifting to an objective of lower magnification, the formerly illuminated area could be seen as a dark circular spot. Since the transition between the bleached and the unbleached portions of the surface was not sharp, but rather gradually changing from dark to bright, the middle of the gray zone was used to estimate the diameter of the bleached spot. The principle is illustrated in Fig. G.1 . Images were taken with an iXon 897 EMCCD camera from Andor and analyzed in the IQ software, also from Andor.

Throughout the power density measurements, the transmission values of the attenuation devices were determined as shown in Table G.1 . The measured optical power values and densities for different configurations are shown in Table G.2 . The inaccuracy of the optical power density values is at least 10% of the given values, due to uncertainties especially in the determination of the illuminated area. It should also be noted that the lamp intensities change with the aging of the lamps and thus have to be reevaluated periodically.

[1]Corinne Vergnenegre at the LAAS-CNRS assisted in the optical power measurements and her help is gratefully acknowledged.

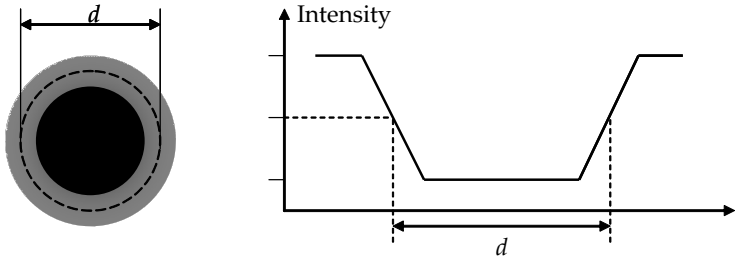

Figure G.1: The diameter d of the photobleached spot was determined by considering the position of the gray-zone where the intensity was halfway back to its maximum.

Table G.1: Transmission values of optical power with various attenuation devices.

	Given value	Measured value
ND filter "ND25"	25%	28%
ND filter "ND6"	6%	8%
EXFO Top level	100%	100%
EXFO Top level - 1	50%	51.1%
EXFO Top level - 2	25%	24.2%
EXFO Top level - 3	12%	14.0%
EXFO Bottom level	0%	0%
Liquid light guide inserted to outer notch only	-	5%

Table G.2: Optical power values for different configurations.

Lamp type:	EXFO metal halide lamp
Intensity level:	Top level (100%)
ND filters:	ND6 & ND 25
Excitation filter:	Chroma TRITC 31002 filter (Rhodamine B)

Objective →	20X / NA 0.46	60X / NA 0.90	100X / NA 0.95
EXFO diameter of field, d	0.91 mm	0.38 mm	0.23 mm
EXFO field area	0.65 mm^2 = 0.0065 cm^2	0.11 mm^2 = 0.0011 cm^2	0.042 mm^2 = 0.00042 cm^2
Total optical power under objective	0.780 mW	0.340 mW	0.176 mW
Optical power density (power per unit area)	0.12 W/cm^2	0.31 W/cm^2	0.42 W/cm^2

Lamp type:	EXFO metal halide lamp
Intensity level:	Light guide inserted to outer notch (5%)
ND filters:	No ND filters
Excitation filter:	Chroma TRITC 31002 filter (Rhodamine B)

Objective →	20X / NA 0.46	60X / NA 0.90	100X / NA 0.95
EXFO diameter of field, d	0.91 mm		0.23 mm
EXFO field area	0.65 mm^2 = 0.0065 cm^2		0.042 mm^2 = 0.00042 cm^2
Total optical power under objective	2.135 mW		0.437 mW
Optical power density (power per unit area)	0.33 W/cm^2		1.0 W/cm^2

Lamp type:	Olympus BX-51 mercury lamp
Intensity level:	- (only one level available)
ND filters:	ND6 & ND 25
Excitation filter:	Chroma TRITC 31002 filter (Rhodamine B)

Objective →	20X / NA 0.46	60X / NA 0.90	100X / NA 0.95
Mercury lamp diameter of field, d		0.46 mm	
Mercury lamp field area		0.17 mm^2 = 0.0017 cm^2	
Total optical power under objective		1.655 mW	
Optical power density (power per unit area)		0.97 W/cm^2	

Lamp type:	EXFO metal halide lamp
Intensity level:	Top level (100%)
ND filters:	ND6 & ND 25
Excitation filter:	Chroma Adirondack Green 32254a filter (Evidots 520nm)

Objective →	20X / NA 0.46	60X / NA 0.90	100X / NA 0.95
EXFO diameter of field, *d*	0.91 mm	0.38 mm	0.23 mm
EXFO field area	0.65 mm^2 = 0.0065 cm^2	0.11 mm^2 = 0.0011 cm^2	0.042 mm^2 = 0.00042 cm^2
Total optical power under objective	0.99 mW	0.42 mW	0.20 mW
Optical power density (power per unit area)	0.15 W/cm^2	0.38 W/cm^2	0.48 W/cm^2

Lamp type:	EXFO metal halide lamp
Intensity level:	Top level (100%)
ND filters:	ND6 & ND 25
Excitation filter:	Chroma ET-GFP (FITC/Cy2)

Objective →	20X / NA 0.46	60X / NA 0.90	100X / NA 0.95
EXFO diameter of field, *d*	0.91 mm	0.38 mm	0.23 mm
EXFO field area	0.65 mm^2 = 0.0065 cm^2	0.11 mm^2 = 0.0011 cm^2	0.042 mm^2 = 0.00042 cm^2
Total optical power under objective	0.73 mW	0.29 mW	0.15 mW
Optical power density (power per unit area)	0.11 W/cm^2	0.26 W/cm^2	0.36 W/cm^2

BIBLIOGRAPHY

[1] Zhang, C., Xu, J., Ma, W. & Zheng, W. PCR microfluidic devices for DNA amplification. *Biotechnology Advances* **24**, 243–284 (2006).

[2] de Mello, A. J. DNA amplification: does 'small' really mean 'efficient'? *Lab on a Chip* **1**, 24N–29N (2001).

[3] Lee, D.-S. *et al.* Bulk-micromachined submicroliter-volume PCR chip with very rapid thermal response and low power consumption. *Lab on a Chip* **4**, 401–407 (2004).

[4] Kopp, M. U., de Mello, A. J. & Manz, A. Chemical amplification: Continuous-flow PCR on a chip. *Science* **280**, 1046–1048 (1998).

[5] Kricka, L. J. & Wilding, P. Microchip PCR. *Analytical and Bioanalytical Chemistry* **377**, 820–825 (2003).

[6] Liu, C. N., Toriello, N. M. & Mathies, R. A. Multichannel PCR-CE microdevice for genetic analysis. *Analytical Chemistry* **78**, 5474–5479 (2006).

[7] Bhattacharjee, C. & Das, K. P. Thermal unfolding and refolding of β-lactoglobulin: An intrinsic and extrinsic fluorescence study. *Eur. J. Biochem.* **267**, 3957–3964 (2000).

[8] Nölting, B. Temperature-jump induced fast refolding of cold-unfolded protein. *Biochemical and Biophysical Research Communications* **227**, 903–908 (1996).

[9] Sava, N., Van der Plancken, I., Claeys, W. & Hendrickx, M. The kinetics of heat-induced structural changes of β-lactoglobulin. *J. Dairy Sci.* **88**, 1646–1653 (2005).

[10] Iametti, S., Cairoli, S., De Gregori, B. & Bonomi, F. Modifications of high-order structures upon heating of β-lactoglobulin: Dependence on the protein concentration. *J. Agric. Food Chem.* **43**, 53–58 (1995).

[11] Fessas, D., Iametti, S., Schiraldi, A. & Bonomi, F. Thermal unfolding of monomeric and dimeric β-lactoglobulins. *European Journal of Biochemistry* **268**, 5439–5448 (2001).

[12] Copty, A. *et al.* Probing of the microwave radiation effect on the green fluorescent protein luminescence in solution. *Synthetic Metals* **155**, 422–425 (2005).

[13] Mao, H., Holden, M. A., You, M. & Cremer, P. S. Reusable platforms for high-throughput on-chip temperature gradient assays. *Analytical Chemistry* **74**, 5071–5075 (2002).

[14] Balss, K. M., Ross, D., Begley, H. C., Olsen, K. G. & Tarlov, M. J. Dna hybridization assays using temperature gradient focusing and peptide nucleic acids. *Journal of American Chemical Society* **126**, 13474–13479 (2004).

[15] Flechsig, G.-U., Peter, J., Hartwich, G., Wang, J. & Gründler, P. Dna hybridization detection at heated electrodes. *Langmuir* **21**, 7848–7853 (2005).

[16] Russom, A. *et al.* Genotyping by dynamic heating of monolayered beads on a microheated surface. *Electrophoresis* **25**, 3712–3719 (2004).

[17] Gonzalez, J. M. & Saiz-Jimenez, C. A simple fluorimetric method for the estimation of DNA-DNA relatedness between closely related microorganisms by thermal denaturation temperatures. *Extremophiles* **9**, 75–79 (2005).

[18] Gonzalez, J. M. & Saiz-Jimenez, C. A fluorimetric method for the estimation of G+C mol content in microorganisms by thermal denaturation temperature. *Environmental Microbiology* **4**, 770–773 (2002).

[19] Schanda, P., Forge, V. & Brutscher, B. Protein folding and unfolding studied at atomic resolution by fast two-dimensional NMR spectroscopy. *PNAS* **104**, 11257–11262 (2007).

[20] Gruebele, M., Sabelko, J., Ballew, R. & Ervin, J. Laser temperature jump induced protein refolding. *Accounts of Chemical Research* **31**, 699–707 (1998).

[21] Shea, J.-E. & Brooks III, C. L. From folding theories to folding proteins: A review and assessment of simulation studies of protein folding and unfolding. *Annual Review of Physical Chemistry* **52**, 499–535 (2001).

[22] Righetti, P. G. & Verzola, B. Folding/unfolding/refolding of proteins: Present methodologies in comparison with capillary zone electrophoresis. *Electrophoresis* **22**, 2359–2374 (2001).

[23] Nölting, B. *Protein Folding Kinetics: Biophysical Methods* (Springer, 2006), 2 edn.

[24] Volk, M. Fast initiation of peptide and protein folding processes. *European Journal of Organic Chemistry* **14**, 2605–2621 (2001).

[25] Nabuchi, Y., Murao, N., Asoh, Y. & Takayama, M. Probing the unfolding and refolding processes of carbonic anhydrase 2 using electrospray ionization mass spectrometry combined with ph jump. *Anal. Chem.* **79**, 8342–8349 (2007).

[26] Sato, S., Luisi, D. L. & Raleigh, D. P. pH jump studies of the folding of the multidomain ribosomal protein l9: The structural organization of the n-terminal domain does not affect the anomalously slow folding of the c-terminal domain. *Biochemistry* **39**, 4955–4962 (2000).

[27] Font, J. *et al.* Pressure-jump-induced kinetics reveals a hydration dependent folding/unfolding mechanism of ribonuclease A. *Biophysical Journal* **91**, 2264–2274 (2006).

[28] Braun, D. & Libchaber, A. Lock-in by molecular multiplication. *Applied Physics Letters* **83**, 5554–5556 (2003).

[29] Voss, T., Gründler, P., Kirbs, A. & Flechsig, G.-U. Temperature pulse voltammetry: hot layer electrodes made by ltcc technology. *Electrochemistry Communications* **1**, 383–388 (1999).

[30] Voss, T., Kirbs, A. & Gründler, P. Basics of temperature pulse voltammetry. *Fresenius Journal of Analytical Chemistry* **367**, 320–323 (2000).

[31] Gründler, P. Phenomena at hot-wire electrodes. *Fresenius Journal of Analytical Chemistry* **367**, 324–328 (2000).

[32] Iwaki, T. *et al.* Design and simulation of resistive SOI CMOS micro-heaters for high temperature gas sensors. *Journal of Physics: Conference Series* **15**, 27–32 (2005).

[33] Sberveglieri, G., Hellmich, W. & Müller, G. Silicon hotplates for metal oxide gas sensor elements. *Microsystem Technologies* **3**, 183–190 (1997).

[34] Briand, D., Heimgartner, S., Grétillat, M.-A., van der Schoot, B. & de Rooij, N. F. Thermal optimization of micro-hotplates that have a silicon island. *Journal of Micromechanics and Microengineering* **12**, 971–978 (2002).

[35] Haupt, K. & Mosbach, K. Molecularly imprinted polymers and their use in biomimetic sensors. *Chemical Reviews* **100**, 2495–2504 (2000).

[36] Haupt, K. Creating a good impression. *Nature Biotechnology* **20**, 884–885 (2002).

[37] Haupt, K. Imprinted polymers - tailor-made mimics of antibodies and receptors. *Chemical Communications* **2**, 171–178 (2003).

[38] Park, I., Li, Z., Pisano, A. P. & Williams, R. S. Selective surface functionalization of silicon nanowires via nanoscale joule heating. *Nano Letters* **7**, 3106–3111 (2007).

[39] Arata, H. F. *et al.* Temperature distribution measurement on microfabricated thermodevice for single biomolecular observation using fluorescent dye. *Sensors and Actuators B* **117**, 339–345 (2006).

[40] Yamamoto, T., Takahiko, N. & Fujii, T. PDMS-glass hybrid microreactor array with embedded temperature control device. application to cell-free protein synthesis. *Lab on a Chip* **2**, 197–202 (2002).

[41] Patolsky, F. & Lieber, C. M. Nanowire nanosensors. *Materials Today* **8**, 20–28 (2005).

[42] Patolsky, F. *et al.* Electrical detection of single viruses. *Proceedings of the National Academy of Science* **101**, 14017–14022 (2004).

[43] Patolsky, F., Zheng, G. & Lieber, C. M. Nanowire-based biosensors. *Anal Chem.* **78**, 4260–4269 (2006).

[44] Wang, W. U., Chen, C., Lin, K.-h., Fang, Y. & Lieber, C. M. Label-free detection of small-molecule-protein interactions by using nanowire nanosensors. *Proceedings of the National Academy of Science* **102**, 3208–3212 (2005).

[45] Zheng, G., Patolsky, F., Cui, Y., Wang, W. U. & Lieber, C. M. Multiplexed electrical detection of cancer markers with nanowire sensor arrays. *Nature Biotechnology* **23**, 1294–1301 (2005).

[46] Childs, P. R. N., Greenwood, J. R. & Long, C. A. Review of temperature measurement. *Review of Scientific Instruments* **71**, 2959–2978 (2000).

[47] Yoo, J. Y. Recent studies on fluid flow and heat transfer in thermal microdevices. *Nanoscale and Microscale Thermophysical Engineering* **10**, 67–81 (2006).

[48] Price, D. M., Reading, M., A., H. & Pollock, H. M. New adventures in thermal analysis. *Journal of Thermal Analysis and Calorimetry* **60**, 723–733 (2000).

[49] Pollock, H. M. & Hammiche, A. Micro-thermal analysis: techniques and applications. *Journal of Physics D: Applied Physics* **34**, R23–R53 (2001).

[50] Lee, J. & Kotov, N. A. Thermometer design at the nanoscale. *Nanotoday* **2**, 48–51 (2007).

[51] Wang, S., Westcott, S. & Chen, W. Nanoparticle luminescence thermometry. *Journal of Physical Chemistry B* **106**, 11203–11209 (2002).

[52] Shi, L. & Majumdar, A. Recent developments in micro and nanoscale thermometry. *Microscale Thermophysical Engineering* **5**, 251–265 (2001).

[53] Allison, S. W. & Gillies, G. T. Remote thermometry with thermographic phosphors: Instrumentation and applications. *Review of Scientific Instruments* **68**, 2615–2650 (1997).

[54] Smith, C. R., Sabatino, D. R. & Praisner, T. J. Temperature sensing with thermochromic liquid crystals. *Experiments in Fluids* **30**, 190–201 (2001).

[55] Grattan, K. T. V. & Zhang, Z. Y. *Fiber optic fluorescence thermometry* (Chapman & Hall, 1995).

[56] Borisov, S. M. & Wolfbeis, O. S. Temperature-sensitive europium(iii) probes and their use for simultaneous luminescent sensing of temperature and oxygen. *Analytical Chemistry* **78**, 5094–5101 (2006).

[57] Jorez, S., Laconte, J., Cornet, A. & Raskin, J.-P. Low-cost optical instrumentation for thermal characterization of mems. *Measurement Science and Technology* **16**, 1833–1840 (2005).

[58] Pomeroy, J. W. *et al.* Thermal mapping of defects in AlGaN/GaN heterostructure field-effect transistors using micro-raman spectroscopy. *Appl. Phys. Lett.* **87**, 103508 (2005).

[59] Chan, P. K. L., Pipe, K. P., Qin, G. & Ma, Z. Thermoreflectance imaging of current dynamics in high power sige heterojunction bipolar transistors. *Applied Physics Letters* **89**, 233521 (2006).

[60] Yamaguchi, T., Ohkubo, M., Ikeda, N. & Nomura, T. Measurement of semiconductor surface temperature using raman spectroscopy. *Furukawa Review* **18**, 73–77 (1999).

[61] Stehr, J. *et al.* Sub-microsecond molecular thermometry using thermal spin flips. *Advanced Materials* **16**, 2170–2174 (2004).

[62] Kim, S. H. *et al.* Micro-raman thermometry for measuring the temperature distribution inside the microchannel of a polymerase chain reaction chip. *J. Micromech. Microeng.* **16**, 526–530 (2006).

[63] Fu, R., Xu, B. & Li, D. Study of the temperature field in microchannels of a pdms chip with embedded local heater using temperature-dependent fluorescent dye. *International Journal of Thermal Sciences* **45**, 841–847 (2006).

[64] Deng, P., Lee, Y.-K. & Cheng, P. The growth and collapse of a micro-bubble under pulse heating. *International Journal of Heat and Mass Transfer* **46**, 4041–4050 (2003).

[65] Deng, P., Lee, Y.-K. & Cheng, P. Micro bubble dynamics in dna solutions. *Journal of Micromechanics and Microengineering* **14**, 693–701 (2004).

[66] Ross, D., Gaitan, M. & Locascio, L. E. Temperature measurement in microfluidic systems using a temperature-dependent fluorescent dye. *Analytical Chemistry* **73**, 4117–4123 (2001).

[67] Seger-Sauli, U., Panayiotou, M., Schnydrig, S., Jordan, M. & Renaud, P. Temperature measurements in microfluidic systems: Heat dissipation of negative dielectrophoresis barriers. *Electrophoresis* **26**, 2239–2246 (2005).

[68] Ko, F.-H., Weng, L.-Y., Ko, C.-J. & Chu, T.-C. Characterization of imprinting polymeric temperature variation with fluorescent Rhodamine B molecule. *Microelectronic Engineering* **83**, 864–868 (2006).

[69] Cahill, G. D. & Pohl, R. O. Thermal conductivity of amorphous solids above the plateau. *Physical Review B* **35**, 4067–4073 (1987).

[70] Tong, T. & Majumdar, A. Reexamining the 3-omega technique for thin film thermal characterization. *Review of Scientific Instruments* **77**, 104902 (2006).

[71] Borca-Tasciuc, D.-A. & Chen, G. Anisotropic thermal properties of nanochanneled alumina templates. *J. Appl. Phys.* **97**, 084303 (2005).

[72] Kim, W. *et al.* Thermal conductivity reduction and thermoelectric figure of merit increase by embedding nanoparticles in crystalline semiconductors. *Physical Review Letters* **96**, 045901 (2006).

[73] Webb, P. Thermal imaging of electronic devices with low surface emissivity. *IEE Proc. G* **138**, 390–400 (1991).

[74] Kozlowska, A. *et al.* Analysis of thermal images from diode lasers: Temperature profiling and reliability screening. *Applied Physics Letters* **86**, 203503 (2005).

[75] Grauby, S., Dilhaire, S., Jorez, S. & Claeys, W. Temperature variation mapping of a microelectromechanical system by thermoreflectance imaging. *IEEE Electron Device Letters* **26**, 78–80 (2005).

[76] Kuball, M. *et al.* High spatial resolution micro-raman temperature measurements of nitride devices (fets and light emitters). *phys. stat. sol. (a)* **202**, 824–831 (2005).

[77] Mao, H., Yang, T. & Cremer, P. S. A microfluidic device with a linear temperature gradient for parallel and combinatorial measurements. *Journal of American Chemical Society* **124**, 4432–4435 (2002).

[78] Chaudhari, A. M., Woudenberg, T. M., Albin, M. & Goodson, K. E. Transient liquid crystal thermometry of microfabricated pcr vessel arrays. *Journal of Microelectromechanical Systems* **7**, 345–355 (1998).

[79] Liu, J., Enzelberger, M. & Quake, S. A nanoliter rotary device for polymerase chain reaction. *Electrophoresis* **23**, 1531–1536 (2002).

[80] Allen, P. B. *et al.* Selective electroless and electrolytic deposition of metal for applications in microfluidics: Fabrication of a microthermocouple. *Analytical Chemistry* **75**, 1578–1583 (2003).

[81] Lu, L., Yi, W. & Zhang, D. L. 3ω method for specific heat and thermal conductivity measurements. *Rev. Sci. Instrum.* **72**, 2996–3003 (2001).

[82] Dames, C. & Chen, G. 1ω, 2ω, and 3ω methods for measurements of thermal properties. *Rev. Sci. Instrum.* **76**, 124902 (2005).

[83] Jiang, L., Wang, Y., Wong, M. & Zohar, Y. Fabrication and characterization of a microsystem for a micro-scale heat transfer study. *Journal of Micromechanics and Microengineering* **9**, 422–428 (1999).

[84] Yoon, D. S. *et al.* Precise temperature control and rapid thermal cycling in a micromachined DNA polymerase chain reaction chip. *J. Micromech. Microeng.* **12**, 813–823 (2002).

[85] Jiang, L., Wong, M. & Zohar, Y. Unsteady characteristics of a thermal microsystem. *Sensors and Actuators A* **82**, 108–113 (2000).

[86] Jang, S. P., Kim, S. J. & Paik, K. W. Experimental investigation of thermal characteristics for a microchannel heat sink subject to an impinging jet, using a micro-thermal sensor array. *Sensors and Actuators A* **105**, 211–224 (2003).

[87] Bourg, M. E., van der Veer, W. E., Grüell, A. G. & Penner, R. M. Electrodeposited submicron thermocouples with microsecond response times. *Nano Letters* **7**, 3208 –3213 (2007).

[88] Williams, C. C. & Wickramasinghe, H. K. Scanning thermal profiler. *Applied Physics Letters* **49**, 1587–1589 (1986).

[89] Binning, G., Rohrer, H., Gerber, C. & Weibel, E. Surface studies by scanning tunneling microscopy. *Physical Review Letters* **49**, 57–61 (1982).

[90] Luo, K., Shi, Z., Varesi, J. & Majumdar, A. Sensor nanofabrication, performance, and conduction mechanisms in scanning thermal microscopy. *J. Vac. Sci. Technol. B* **15**, 349–360 (1997).

[91] Shi, L., Plyasunov, S., Bachtold, A., McEuen, P. L. & Majumdar, A. Scanning thermal microscopy of carbon nanotubes using batch-fabricated probes. *Applied Physics Letters* **77**, 4295–4297 (2000).

[92] Kittel, A. *et al.* Near-field heat transfer in a scanning thermal microscope. *Physical Review Letters* **95**, 224301 (2005).

[93] Oesterschulze, E., Stopka, M., Ackermann, L., Scholz, W. & Werner, S. Thermal imaging of thin films by scanning thermal microscope. *Journal of Vacuum Science and Technology B* **14**, 832–837 (1996).

[94] Nakabeppu, O., Chandrachood, M., Wu, Y., Lai, J. & Majumdar, A. Scanning thermal imaging microscopy using composite cantilever probes. *Applied Physics Letters* **66**, 694–696 (1995).

[95] Majumdar, A., Carrejo, J. P. & Lai, J. Thermal imaging using the atomic force microscope. *Applied Physics Letters* **62**, 2501–2503 (1993).

[96] Majumdar, A. *et al.* Thermal imaging by atomic force microscopy using thermocouple cantilever probes. *Review of Scientific Instruments* **66**, 3584–3592 (1995).

[97] Small, J. P., Shi, L. & Kim, P. Mesoscopic thermal and thermoelectric measurements of individual carbon nanotubes. *Solid State Communications* **127**, 181–186 (2003).

[98] Hammiche, A., Hourston, D. J., Pollock, H. M., Reading, M. & Song, M. Scanning thermal microscopy: Subsurface imaging, thermal mapping of polymer blends, and localized calorimetry. *Journal of Vacuum Science and Technology B* **14**, 1486–1491 (1996).

[99] Lopez, L. D. P. *et al.* Characterization of the thermal behavior of pn thermoelectric couples by scanning thermal microscope. *Microelectronics Journal* **35**, 797–803 (2004).

[100] Balk, L. J., Cramer, R. M. & Fiege, G. B. M. Thermal analyses by means of scanning probe microscopy. In *Proc. of 6th IPFA* (1997).

[101] Aubry, R. *et al.* SThM temperature mapping and nonlinear thermal resistance evolution with bias on AlGaN/GaN HEMT devices. *IEEE Transactions on Electron Devices* **54**, 385–390 (2007).

[102] Gu, Y. Q., Ruan, X. L., Han, L., Zhu, D. Z. & Sun, X. Y. Imaging of thermal conductivity with sub-micrometer resolution using scanning thermal microscopy. *International Journal of Thermophysics* **23**, 1115–1124 (2002).

[103] Rangelow, I. W., Gotszalk, T., Abedinov, N., Grabiec, P. & Edinger, K. Thermal nano-probe. *Microelectronic Engineering* **57-58**, 737–748 (2001).

[104] Aigouy, L., De Wilde, Y., Mortier, M., Giérak, J. & Bourhis, E. Fabrication and characterization of fluorescent rare-earth-doped glass-particle-based tips for near-field optical imaging applications. *Applied Optics* **43**, 3829–3837 (2004).

[105] Aigouy, L., Tessier, G., Mortier, M. & Charlot, B. Scanning thermal imaging of microelectronic circuits with a fluorescent nanoprobe. *Applied Physics Letters* **87**, 184105 (2005).

[106] Samson, B. *et al.* Scanning thermal imaging of an electrically excited aluminum microstripe. *Journal ofApplied Physics* **102**, 024305 (2007).

[107] Varesi, J. & Majumdar, A. Scanning joule expansion microscopy at nanometer scales. *Applied Physics Letters* **72**, 37–39 (1998).

[108] Nonnenmacher, M. & Wickramasinghe, H. K. Scanning probe microscopy of thermal conductivity and subsurface properties. *Applied Physics Letters* **61**, 168–170 (1992).

[109] Taguchi, Y., Horiguchi, Y., Kobayshi, M., Saiki, T. & Nagasaka, Y. Development of nanoscale thermal properties measurement technique by using near-field optics. *JSME International Journal B* **47**, 483–489 (2004).

[110] De Wilde, Y. *et al.* Thermal radiation scanning tunnelling microscopy. *Nature* **444**, 740–743 (2006).

[111] Igeta, M., Banerjee, K., Wu, G., Hu, C. & Majumdar, A. Thermal characteristics of submicron vias studied by scanning joule expansion microscopy. *IEEE Electron Device Letters* **21**, 224–226 (2000).

[112] Zielinski, A. E., Niles, S. & Powell, J. D. Current and heat conduction during a pulsed electrical discharge. *Journal of Applied Physics* **86**, 3943–3952 (1999).

[113] Schlegel, E. S. Apparatus for determining temperature profiles in microstructures. *Review of Scientific Instruments* **34**, 360–361 (1963).

[114] Griffin, D. D. Infrared techniques for measuring temperature and related phenomena of microcircuits. *Applied Optics* **7**, 1749–1756 (1968).

[115] Kozlowska, A., Wawrzyniak, P., Tomm, J. W., Weik, F. & Elsaesser, T. Deep level emission from high-power diode laser bars detected by multispectral infrared imaging. *Applied Physics Letters* **87**, 153503 (2005).

[116] Fletcher, D. A. *et al.* Near-field infrared imaging with a microfabricated solid immersion lens. *Appl. Phys. Lett.* **77**, 2109–2111 (2000).

[117] Ippolito, S. B. *et al.* High spatial resolution subsurface thermal emission microscopy. *Applied Physics Letters* **84**, 4529–4531 (2004).

[118] Tessier, G., Holé, S. & Fournier, D. Quantitative thermal imaging by synchronous thermoreflectance with optimized illumination wavelengths. *Applied Physics Letters* **78**, 2267–2269 (2001).

[119] Dilhaire, S., Grauby, S. & Claeys, W. Calibration procedure for temperature measurements by thermoreflectance under high magnification conditions. *Applied Physics Letters* **84**, 822–824 (2004).

[120] Ochalski, T. J. *et al.* Complementary thermoreflectance and micro-raman analysis of facet temperatures of diode lasers. *Applied Physics Letters* **89**, 071104 (2006).

[121] Tessier, G., Bardoux, M., Boué, C., Filloy, C. & Fournier, D. Back side thermal imaging of integrated circuits at high spatial resolution. *Applied Physics Letters* **90**, 171112 (2007).

[122] Thorne, S., Ippolito, S., Ünlü, M. & Goldberg, B. High-resolution thermoreflectance microscopy. In *Mat. Res. Soc. Symp. Proc. Vol. 738* (2003).

[123] Grauby, S. *et al.* Qualitative temperature variation imaging by thermoreflectance and sthm techniques. In *THERMINIC 2005*, 284–289 (2005).

[124] Abel, M. R. *et al.* Thermal metrology of silicon microstructures using Raman spectroscopy. In *21st IEEE SEMI-THERM Symp.* (2005).

[125] Grauby, S., Forget, B. C., Holem, S. & Fournier, D. High resolution photothermal imaging of high frequency phenomena using a visible charge coupled device camera associated with a multichannel lock-in scheme. *Review of Scientific Instruments* **70**, 3603–3608 (1999).

[126] Lüerssen, D., Hudgings, J. A., Mayer, P. M. & Ram, R. J. Nanoscale thermoreflectance with 10mk temperature resolution using stochastic resonance. In *21st IEEE SEMI-THERM Symp.* (2005).

[127] Kuball, M. Raman spectroscopy of GaN, AlGaN and AlN for process and growth monitoring/control. *Surface and Interface Analysis* **31**, 987–999 (2001).

[128] Serrano, J. R., Phinney, L. M. & Kearney, S. P. Micro-raman thermometry of thermal flexure actuators. *Journal of Micromechanics and Microengineering* **16**, 1128–1134 (2006).

[129] Aubry, R. *et al.* Temperature measurement by micro-raman scattering spectroscopy in the active zone of algan/gan high-electron-mobility transistors. *Eur. Phys. J. Appl. Phys.* **27**, 293–296 (2004).

[130] Kuball, M. *et al.* Measurement of temperature in active high-power AlGaN/GaN hfets using raman spectroscopy. *IEEE Electron Device Letters* **23**, 7–9 (2002).

[131] Kuball, M. *et al.* Time-resolved temperature measurement of AlGaN/GaN electronic devices using micro-Raman spectroscopy. *IEEE Electron Device Letters* **28**, 86–89 (2007).

[132] Rajasingam, S. *et al.* Micro-Raman temperature measurements for electric field assessment in active AlGaN/GaN HFETs. *IEEE Electron Device Letters* **25**, 456–458 (2004).

[133] Van Keuren, E. *et al.* Temperature profiles of microheaters using fluorescence microthermal imaging. *Sensors and Materials* **17**, 001–006 (2005).

[134] Slyadnev, M. N., Tanaka, Y., Tokeshi, M. & Kitamori, T. Photothermal temperature control of a chemical reaction on a microchip using an infrared diode laser. *Analytical Chemistry* **73**, 4037–4044 (2001).

[135] Li, S., Zhang, K., Yang, J.-M., Lin, L. & Yang, H. Single quantum dots as local temperature markers. *Nano Letters* **7**, 3102–3105 (2007).

[136] Meyer, C. W., Meier, D. C., Montgomery, C. B. & Semancik, S. Temperature measurements of microhotplates using fluorescence thermometry. *Sensors and Actuators A* **127**, 235–240 (2006).

[137] Hidrovo, C. H. & Hart, D. P. Dual emission laser induced fluorescence technique (delif) for oil film thickness and temperature measurement. In *Proc. of ASME FEDSM 00* (2000).

[138] Valeur, B. *Molecular Fluorescence: Principles and Applications* (Wiley-VCH, 2002).

[139] Lakowicz, J. R. *Principles of fluorescence spectroscopy* (Kluwer Academic / Plenum Publishers, 233 Spring Street, New York, N.Y. 10013, 1999), 2nd edn.

[140] Tsuboi, T. & Aljaroudi, N. Temperature dependence of phosphorescence intensity and lifetime of tris(2-phenylpyridine) iridium doped in the fluorescent material TDP. *Physical Review B* **72**, 125109 (2005).

[141] Hu, H., Koochesfahani, M. & Lum, C. Molecular tagging thermometry with adjustable temperature sensitivity. *Experiments in Fluids* **40**, 753–763 (2006).

[142] Heyes, A. L., Seefeldt, S. & Feist, J. P. Two-colour phosphor thermometry for surface temperature measurement. *Optics & Laser Technology* **38**, 257–265 (2006).

[143] Kaholek, M., Hrdlovic, P. & Bartos, J. Singlet probes based on coumarin derivatives substituted in position 3; spectral properties in solution and in polymer matrices. *Polymer* **41**, 991–1001 (2000).

[144] Walker, G. W. *et al.* Quantum-dot optical temperature probes. *Applied Physics Letters* **83**, 3555–3557 (2003).

[145] Dibbern-Brunell, D., de Oliveira, M. G. & Atvars, T. D. Z. Temperature dependence of the photobleaching process of fluorescein in poly(vinyl alcohol). *Journal of Photochemistry and Photobiology A: Chemistry* **85**, 285–289 (1995).

[146] Coolen, M. C. J., Kieft, R. N., Rindt, C. C. M. & van Steenhoven, A. A. Application of 2-D LIF temperature measurements in water using a Nd : YAG laser. *Experiments in Fluids* **27**, 420–426 (1999).

[147] Banin, U. *et al.* Evidence for a thermal contribution to emission intermittency in single cdse/cds core/shell nanocrystals. *Journal of Chemical Physics* **110**, 1195–1201 (1999).

[148] Kuno, M., Fromm, D. P., Hamann, H. F., Gallagher, A. & Nesbitt, D. J. "on"/"off" fluorescence intermittency of single semiconductor quantum dots. *Journal of Chemical Physics* **115**, 1028–1040 (2001).

[149] Tang, J. & Marcusa, R. A. Mechanisms of fluorescence blinking in semiconductor nanocrystal quantum dots. *Journal of Chemical Physics* **123**, 054704 (2005).

[150] Hohng, S. & Ha, T. Near-complete suppression of quantum dot blinking in ambient conditions. *Journal of American Chemical Society* **126**, 1324–1325 (2004).

[151] Wong, F. H. C., Banks, D. S., Abu-Arish, A. & Fradin, C. A molecular thermometer based on fluorescent protein blinking. *Journal of American Chemical Society* **129**, 10302–10303 (2007).

[152] Liu, T.-C. *et al.* Temperature-dependent photoluminescence of water-soluble quantum dots for a bioprobe. *Analytica Chimica Acta* **559**, 120–123 (2006).

[153] Allison, S. W., Gillies, G. T., Rondinone, A. J. & Cates, M. R. Nanoscale thermometry via the fluorescence of yag:ce phosphor particles: measurements from 7 to 77 c. *Nanotechnology* **14**, 859–863 (2003).

[154] Coppeta, J. & Rogers, C. Dual emission laser induced fluorescence for direct planar scalar behavior measurements. *Experiments in Fluids* **25**, 1–15 (1998).

[155] Lavieille, P., Lemoine, F., Lavergne, G., Virepinte, J. F. & Lebouché, M. Temperature measurements on droplets in monodisperse stream using laser-induced fluorescence. *Experiments in Fluids* **29**, 429–437 (2000).

[156] Lavieille, P., Delconte, A., Blondel, D., Lebouché, M. & Lemoine, F. Non-intrusive temperature measurements using three-color laser-induced fluorescence. *Experiments in Fluids* **36**, 706–716 (2004).

[157] Sakakibara, J. & Adrian, R. J. Whole field measurement of temperature in water using two-color laser induced fluorescence. *Experiments in Fluids* **26**, 7–15 (1999).

[158] Sakakibara, J., Hishida, K. & Maeda, M. Measurements of thermally stratified pipe flow using image-processing techniques. *Experiments in Fluids* **16**, 82–96 (1993).

[159] Seuntiëns, H. J., Kieft, R. N., Rindt, C. C. M. & van Steenhoven, A. A. 2d temperature measurements in the wake of a heated cylinder using lif. *Experiments in Fluids* **31**, 588–595 (2001).

[160] Van Keuren, E., Littlejohn, D. & Schrof, W. Three-dimensional thermal imaging using two-photon microscopy. *Journal of Physics D: Applied Physics* **37**, 2938–2943 (2004).

[161] Benninger, R. K. P. *et al.* Quantitative 3d mapping of fluidic temperatures within microchannel networks using fluorescence lifetime imaging. *Analytical Chemistry* **78**, 2272–2278 (2006).

[162] de Camargo, A. S. *et al.* Infrared to visible frequency upconversion temperature sensor based on er^{3+}–doped plzt transparent ceramics. *Solid State Communications* **137**, 1–5 (2006).

[163] Wade, S. A., Muscat, J. C., Collins, S. F. & Baxter, G. W. Nd^{3+}–doped optical fiber temperature sensor using the fluorescence intensity ratio technique. *Review of Scientific Instruments* **70**, 4279–4282 (1999).

[164] Schrum, K. F., Williams, A. M., Haerther, S. A. & Ben-Amotz, D. Molecular fluorescence thermometry. *Analytical Chemistry* **66**, 2788–2190 (1994).

[165] Ross, D. & Locascio, L. E. Microfluidic temperature gradient focusing. *Analytical Chemistry* **74**, 2556–2564 (2002).

[166] Alig, A. R. G., Gourdon, D. & Israelachvili, J. Properties of confined and sheared Rhodamine B films studied by SFA-FECO spectroscopy. *Journal of Physical Chemistry B* **111**, 95–106 (2007).

[167] Erickson, D., Sinton, D. & Li, D. Joule heating and heat transfer in poly(dimethylsiloxane) microfluidic systems. *Lab on a Chip* **3**, 141–149 (2003).

[168] Sakakibara, J., Hishida, K. & Maeda, M. Vortex structure and heat transfer in the stagnation region of an impinging plane jet (simultaneous measurements of velocity and temperature fields by digital particle image velocimetry and laser-induced fluorescence). *Int. J. Heat Mass Transfer* **40**, 3163–3176 (1997).

[169] Ferguson, J. & Mau, A. W.-H. Spontaneous and stimulated emission from dyes. spectroscopy of the neutral molecules of acridine orange, proflavine, and rhodamine b. *Australian Journal of Chemistry* **26**, 1617–1624 (1973).

[170] Bindhu, C. V. *et al.* Measurement of the absolute fluorescence quantum yield of rhodamine b solution using a dual-beam thermal lens technique. *Journal of Physics D: Applied Physics* **29**, 1074–1079 (1996).

[171] Pernthaler, A. & Amann, R. Simultaneous fluorescence in situ hybridization of mRNA and rRNA in environmental bacteria. *Applied and Environmental Microbiology* **70**, 5426–5433 (2004).

[172] Zhang, Q. & Guo, L.-H. Multiple labeling of antibodies with dye/DNA conjugate for sensitivity improvement in fluorescence immunoassay. *Bioconjugate Chemistry* **18**, 1668–1672 (2007).

[173] Liu, G. L., Kim, J., Lu, Y. & Lee, L. P. Optofluidic control using photothermal nanoparticles. *Nature Materials* **5**, 27–32 (2006).

[174] Bruchez Jr., M., Moronne, M., Gin, P., Weiss, S. & Alivisatos, A. P. Semiconductor nanocrystals as fluorescent biological labels. *Science* **281**, 2013–2016 (1998).

[175] Costa-Fernandez, J. M., Pereiro, R. & Sanz-Medel, A. The use of luminescent quantum dots for optical sensing. *Trends in Analytical Chemistry* **25**, 207–218 (2006).

[176] Michalet, X. *et al.* Quantum dots for live cells, in vivo imaging, and diagnostics. *Science* **307**, 538–544 (2005).

[177] Chan, W. C. W. & Nie, S. Quantum dot bioconjugates for ultrasensitive nonisotopic detection. *Science* **281**, 2016–2018 (1998).

[178] Lin, C.-A. J. *et al.* Bioanalytics and biolabeling with semiconductor nanoparticles (quantum dots). *Journal of Materials Chemistry* **17**, 1343–1346 (2007).

[179] Alexson, D. *et al.* Semiconductor nanostructures in biological applications. *Journal of Physics: Condensed Matter* **17**, R637–R656 (2005).

[180] Parak, W. J., Pellegrino, T. & Plank, C. Labelling of cells with quantum dots. *Nanotechnology* **16**, R9–R25 (2005).

[181] Alivisatos, P. The use of nanocrystals in biological detection. *Nature Biotechnology* **22**, 47–52 (2004).

[182] Klimov, V. Nanocrystal quantum dots - from fundamental photophysics to multicolor lasing. *Los Alamos Science* **28**, 214–220 (2003).

[183] Valerini, D. *et al.* Temperature dependence of the photoluminescence properties of colloidal cdse/zns core/shell quantum dots embedded in a polystyrene matrix. *Physical Review B* **71**, 235409 (2005).

[184] Wuister, S. F., van Houselt, A., Donegá, C. d. M., Vanmaekelbergh, D. & Meijerink, A. Temperature antiquenching of the luminescence from capped cdse quantum dots. *Angewandte Chemie International Edition* **43**, 3029–3033 (2004).

[185] Wuister, S. F., Donegá, C. d. M. & Meijerink, A. Luminescence temperature antiquenching of water-soluble cdte quantum dots: Role of the solvent. *Journal of American Chemical Society* **126**, 10397–10402 (2004).

[186] Joshi, A., Narsingi, K. Y., Manasreh, M. O., Davis, E. A. & Weaver, B. D. Temperature dependence of the band gap of colloidal cdse/zns core/shell nanocrystals embedded into an ultraviolet curable resin. *Applied Physics Letters* **89**, 131907 (2006).

[187] Chen, W., Joly, A. G., Malm, J.-O., Bovin, J.-O. & Wang, S. Full-color emission and temperature dependence of the luminescence in poly-p-phenylene ethynylene-ZnS/Mn^{2+} composite particles. *Journal of Physical Chemistry B* **107**, 6544–6551 (2003).

[188] Zohar, O. *et al.* Thermal imaging of receptor-activated heat production in single cells. *Biophysical Journal* **74**, 82–89 (1998).

[189] Bhaumik, M. L. Quenching and temperature dependence of fluorescence in rare-earth chelates. *Journal of Chemical Physics* **40**, 3711–3715 (1964).

[190] Alencar, M. A. R. C., Maciel, G. S., de Araújo, C. B. & Patra, A. Er^{3+}–doped $BaTiO_3$ nanocrystals for thermometry: Influence of nanoenvironment on the sensitivity of a fluorescence based temperature sensor. *Applied Physics Letters* **84**, 4753–4755 (2004).

[191] Aizawa, H. *et al.* Fluorescence thermometer based on the photoluminescence intensity ratio in Tb doped phosphor materials. *Sensors and Actuators A* **126**, 78–82 (2006).

[192] Li, D. *et al.* Thermal conductivity of individual silicon nanowires. *Applied Physics Letters* **83**, 2934–2936 (2003).

[193] Li, D., Wu, Y., Fan, R., Yang, P. & Majumdar, A. Thermal conductivity of Si/SiGe superlattice nanowires. *Applied Physics Letters* **83**, 3186–3188 (2003).

[194] Livi, R. & Lepri, S. Heat in one dimension. *Nature* **421**, 327 (2003).

[195] Cahill, D. G. *et al.* Nanoscale thermal transport. *Journal of Applied Physics* **93**, 793–818 (2003).

[196] Graf, M., Jurischka, R., Barrettino, D. & Hierlemann, A. 3D nonlinear modeling of microhotplates in CMOS technology for use as metal-oxide-based gas sensors. *Journal of Micromechanics and Microengineering* **15**, 190–200 (2005).

[197] Berthoumieux, H., Jullien, L. & Lemarchand, A. Response to a temperature modulation as a signature of chemical mechanisms. *Physical Review E* **76**, 056112 (2007).

[198] Toriyama, T. & Sugiyama, S. Single crystal silicon piezoresistive nano-wire bridge. *Sensors and Actuators A* **108**, 244–249 (2003).

[199] Gao, Z. *et al.* Silicon nanowire arrays for label-free detection of DNA. *Analytical Chemistry* **79**, 3291–3297 (2007).

[200] Kedzierski, J., Bokor, J. & Kisielowski, C. Fabrication of planar silicon nanowires on silicon-on-insulator using stress limited oxidation. *Journal of Vacuum Science and Technology B* **15**, 2825–2828 (1997).

[201] Pennellia, G. & Piotto, M. Fabrication and characterization of silicon nanowires with triangular cross section. *Journal of Applied Physics* **100**, 054507 (2006).

[202] Stern, E. *et al.* Label-free immunodetection with CMOS-compatible semiconducting nanowires. *Nature* **445**, 519–522 (2007).

[203] Møartensson, T., Borgström, M., Seifert, W., Ohlsson, B. J. & Samuelson, L. Fabrication of individually seeded nanowire arrays by vapour-liquid-solid growth. *Nanotechnology* **14**, 1255–1258 (2003).

[204] Wu, Y. *et al.* Controlled growth and structures of molecular-scale silicon nanowires. *Nano Letters* **4**, 433–436 (2004).

[205] Cui, Y., Lauhon, L. J., Gudiksen, M. S., Wang, J. & Lieber, C. M. Diameter-controlled synthesis of single-crystal silicon nanowires. *Applied Physics Letters* **78**, 2214–2216 (2001).

[206] Huang, Y., Duan, X. & Lieber, C. M. Nanowires for integrated multicolor nanophotonics. *Small* **1**, 142–147 (2005).

[207] Cui, Y. & Lieber, C. M. Functional nanoscale electronic devices assembled using silicon nanowire building blocks. *Science* **291**, 851–853 (2001).

[208] Cui, Y., Zhong, Z., Wang, D., Wang, W. U. & Lieber, C. M. High performance silicon nanowire field effect transistors. *Nano Letters* **3**, 149–152 (2003).

[209] Boote, J. J. & Evans, S. D. Dielectrophoretic manipulation and electrical characterization of gold nanowires. *Nanotechnology* **16**, 1500–1505 (2005).

[210] Nicewarner-Peña, S. R. *et al.* Submicrometer metallic barcodes. *Science* **294**, 137–141 (2001).

[211] Qin, L., Park, S., Huang, L. & Mirkin, C. A. On-wire lithography. *Science* **309**, 113–115 (2005).

[212] Park, S., Lim, J.-H., Chung, S.-W. & Mirkin, C. A. Self-assembly of mesoscopic metal-polymer amphiphiles. *Science* **303**, 348–351 (2004).

[213] Wildt, B., Mali, P. & Searson, P. C. Electrochemical template synthesis of multisegment nanowires: Fabrication and protein functionalization. *Langmuir* **22**, 10528–10534 (2006).

[214] Lew, K.-K., Reuther, C., Carim, A. H., Redwing, J. M. & Martin, B. R. Template-directed vapor-liquid-solid growth of silicon nanowires. *Journal of Vacuum Science and Technology B* **20**, 389–392 (2002).

[215] Lew, K.-K. & Redwing, J. M. Growth characteristics of silicon nanowires synthesized by vapor-liquid-solid growth in nanoporous alumina templates. *Journal of Crystal Growth* **254**, 14–22 (2003).

[216] Aslam, M. & Hatfield, J. V. Fabrication of thin film microheater for gas sensors on polyimide membrane. *Proc. IEEE* **1**, 389–392 (2003).

[217] Rossi, C. *et al.* Matrix of 10x10 addressed solid propellant microthrusters: Review of the technologies. *Sensors and Actuators A* **126**, 241–252 (2006).

[218] Rossi, C., Temple-Boyer, P. & Estève, D. Realization and performance of thin SiO_2/SiN_x membrane for microheater applications. *Sensors and Actuators A* **64**, 241–245 (1998).

[219] Sandre, O. *Pores transitoires, adhesion et fusion des vesicules geantes*. Ph.D. thesis, Université Paris 6 (2000).

[220] Löw, P., LePioufle, B., Kim, B. & Bergaud, C. Assembly of cdse/zns nanocrystals on microwires and nanowires for temperature sensing. *Sens. Actuat. B* **in Press** (2007).

[221] Arata, H. F., Noji, H. & Fujita, H. Motion control of single F1-ATPase rotary biomolecular motor using microfabricated local heating devices. *Applied Physics Letters* **88**, 083902 (2006).

[222] Ren, Q., Zhao, Y.-P., Yue, J. C. & Cui, Y. B. Biological application of multicomponent nanowires in hybrid devices powered by F1-ATPase motors. *Biomedical Microdevices* **8**, 201–208 (2006).

[223] Kawaguchi, K. & Ishiwata, S. Thermal activation of single kinesin molecules with temperature pulse microscopy. *Cell Motility and the Cytoskeleton* **49**, 41–47 (2001).

[224] Kawaguchi, K. & Ishiwata, S. Temperature dependence of force, velocity, and processivity of single kinesin molecules. *Biochemical and Biophysical Research Communications* **272**, 895–899 (2000).

[225] Böhm, K. J., Stracke, R., Baum, M., Zieren, M. & Unger, E. Effect of temperature on kinesin-driven microtubule gliding and kinesin ATPase activity. *FEBS Letters* **466**, 59–62 (2000).

[226] Kato, H., Nishizaka, T., Iga, T., Kinosita Jr., K. & Ishiwata, S. Imaging of thermal activation of actomyosin motors. *Proceedings of the National Academy of Science* **96**, 9602–9606 (1999).

[227] Schmidt, R. H., Mosbach, K. & Haupt, K. A simple method for spin-coating molecularly imprinted polymer films of controlled thickness and porosity. *Advanced Materials* **16**, 719–722 (2004).

[228] Karg, M., Pastoriza-Santos, I., Pérez-Juste, J., Hellweg, T. & Liz-Marzán, L. M. Nanorod-coated pnipam microgels: Thermoresponsive optical properties. *Small* **3**, 1222–1229 (2007).

[229] Mao, H., Li, C., Zhang, Y., Bergbreiter, D. E. & Cremer, P. S. Measuring LCSTs by novel temperature gradient methods: Evidence for intermolecular interactions in mixed polymer solutions. *Journal of American Chemical Society* **125**, 2850–2851 (2003).

[230] Mitsuishi, M. *et al.* Nanoscale actuation of thermoreversible polymer brushes coupled with localized surface plasmon resonance of gold nanoparticles. *Langmuir* **23**, 7472–7474 (2007).

[231] He, Q., Küller, A., Grunze, M. & Li, J. Fabrication of thermosensitive polymer nanopatterns through chemical lithography and atom transfer radical polymerization. *Langmuir* **23**, 3981–3987 (2007).

[232] Park, S., Chung, S.-W. & Mirkin, C. A. Hybrid organic-inorganic, rod-shaped nanoresistors and diodes. *Journal of American Chemical Society* **126**, 11772–11773 (2004).

[233] Gudiksen, M. S., Lauhon, L. J., Wang, J., Smith, D. C. & Lieber, C. M. Growth of nanowire superlattice structures for nanoscale photonics and electronics. *Nature* **415**, 617–620 (2002).

[234] Bur, A. J., Vangel, M. J. & Roth, S. Temperature dependence of fluorescent probes for applications to polymer materials processing. *Applied Spectroscopy* **56**, 174–181 (2002).

[235] Bai, F. & Melton, L. A. High-temperature, oxygen-resistant molecular fluorescence thermometers. *Applied Spectroscopy* **51**, 1276–1280 (1997).

[236] Bur, A. J. & Roth, S. Fluorescence temperature measurements: Methodology for applications to process monitoring. *Polymer Engineering and Science* **44**, 898–908 (2004).

[237] Bur, A. J. *et al.* Measuring resin temperature during extrusion using a fluorescence technique. In *ANTEC*, vol. 1, 3341–3345 (2003).

[238] Amao, Y. & Okura, I. Optical molecular thermometer based on the fluorescence of fullerene dispersed in poly(methyl methacrylate) film. *Bulletin of the Chemical Society of Japan* **75**, 389–391 (2002).

[239] Sangmin, J., Turner, J. & Granick, S. Noncontact temperature measurement in microliter-sized volumes using fluorescent-labeled dna oligomers. *Journal of the American Chemical Society* **125**, 9908–9909 (2003).

[240] Tashiro, R. & Sugiyama, H. A nanothermometer based on the different π stackings of B- and Z-DNA. *Angewandte Chemie International Edition* **42**, 6018–6020 (2003).

[241] Lupton, J. M. A molecular thermometer based on long-lived emission from platinum octaethyl porphyrin. *Applied Physics Letters* **81**, 2478–2480 (2002).

[242] Biju, V. *et al.* Temperature-sensitive photoluminescence of cdse quantum dot clusters. *Journal of Physical Chemistry B* **109**, 13899–13905 (2005).

[243] Filevich, O. & Etchenique, R. 1d and 2d temperature imaging with a fluorescent ruthenium complex. *Analytical Chemistry* **78**, 7499–7503 (2006).

[244] Mills, A., Tommons, C., Bailey, R. T., Tedford, M. C. & Crilly, P. J. Luminescence temperature sensing using poly(vinyl alcohol)-encapsulated ru(bpy)$_3{}^{2+}$ films. *Analyst* **131**, 495–500 (2006).

[245] Liebsch, G., Klimant, I. & Wolfbeis, O. S. Luminescence lifetime temperature sensing based on sol-gels and poly(acrylonitrile)s dyed with ruthenium metal-ligand complexes. *Advanced Materials* **11**, 1296–1299 (1999).

[246] Lee, J., Govorov, A. O. & Kotov, N. A. Nanoparticle assemblies with molecular springs: A nanoscale thermometer. *Angew. Chem.* **117**, 7605–7608 (2005).

[247] Govorov, A. O. *et al.* Exciton-plasmon interaction and hybrid excitons in semiconductor-metal nanoparticle assemblies. *Nano Letters* **6**, 984–994 (2006).

[248] Li, D. *et al.* Thermosensitive nanostructures comprising gold nanoparticles grafted with block copolymers. *Adv. Funct. Mater.* **17**, 3134–3140 (2007).

[249] Chen, Y., Gautrot, J. E. & Zhu, X. X. Synthesis and characterization of core-shell microspheres with double thermosensitivity. *Langmuir* **23**, 1047–1051 (2007).

[250] Richards, C. D. & Richards, R. F. Transient temperature measurements in a convectively cooled droplet. *Experiments in Fluids* **25**, 392–400 (1998).

[251] Nozaki, T., Mochizuki, T., Kaji, N. & Mori, Y. H. Application of liquid-crystal thermometry to drop temperature measurements. *Experiments in Fluids* **18**, 137–144 (1995).

[252] Gumkowski, S., Wierzbowski, M. & Stasiek, J. Visualization of heat transfer from an oblique impinging jets on flat plate using liquid crystal thermography. In *Proc. 9th International Symposium on Flow Visualization*, 115 (2000).

[253] Azar, K., Benson, J. R. & Manno, V. P. Liquid crystal imaging for temperature measurement of electronic devices. In *Proc. 7th Annual IEEE Semiconductor Thermal Measurement and Management Symposium*, 23–33 (1991).

[254] Csendes, A., Székely, V. & Rencz, M. Thermal mapping with liquid crystal method. *Microelectronic Engineering* **31**, 281–290 (1996).

[255] Wei, Y., Smith, B. G. & Chalamala, B. R. An improved method for detecting hot spots in field emission cathode arrays. *Review of Scientific Instruments* **70**, 3889–3891 (1999).

[256] Gascoyne, P. R. C. & Vykoukal, J. V. Dielectrophoresis-based sample handling in general-purpose programmable diagnostic instruments. *Proceedings of the IEEE* **92**, 22–42 (2004).

[257] Suzuki, M. *et al.* Dielectrophoretic micropatterning with microparticle monolayers covalently linked to glass surfaces. *Langmuir* **20**, 11005–11011 (2004).

[258] Costanzo, P. J., Liang, E., Patten, T. E., Collins, S. D. & Smith, R. L. Biomolecule detection via target mediated nanoparticle aggregation and dielectrophoretic impedance measurement. *Lab on a Chip* **5**, 606–610 (2005).

[259] Green, N. G., Ramos, A., Gonzalez, A., Morgan, H. & Castellanos, A. Fluid flow induced by nonuniform ac electric fields in electrolytes on microelectrodes. i. experimental measurements. *Physical Review E* **61**, 4011–4018 (2000).

[260] Gascoyne, P. R. C. & Vykoukal, J. Particle separation by dielectrophoresis. *Electrophoresis* **23**, 1973–1983 (2002).

PUBLICATIONS

Journal publications

[1] **P. Löw**, B.J. Kim, N. Takama & C. Bergaud, "High spatial resolution surface temperature mapping using fluorescent thermometry", *Small*, accepted for publication (2007).

[2] **P. Löw**, B. Le Pioufle, B. J. Kim & C. Bergaud, "Assembly of CdSe/ZnS nanocrystals on microwires and nanowires for temperature sensing", *Sensors & Actuators B*, accepted for publication (2007).

[3] B. Samson, L. Aigouy, **P. Löw**, C. Bergaud, B. J. Kim & M. Mortier, "ac thermal imaging of nanoheaters using a scanning fluorescent probe", *Applied Physics Letters*, **92**, 023101 (2008).

[4] B. Samson, L. Aigouy, G. Tessier, **P. Löw**, B. J. Kim, C. Bergaud & M. Mortier, "Thermal imaging of nickel wires with a fluorescent nanoprobe" *Journal of Physics: Conference Series* **92**, 012089 (2007).

[5] H. F. Arata, **P. Löw**, K. Ishizuka, C. Bergaud, B. J. Kim, H. Noji & H. Fujita, "Temperature distribution measurement on microfabricated thermodevice for single biomolecular observation using fluorescent dye", *Sensors and Actuators B* **117**, 339-345 (2006).

International conferences

[1] **P. Löw**, "High spatial resolution thermometry using fluorescent nanoprobes in dry and liquid media", *The 7th France-Japan Workshop on Nanosciences and Nanomaterials*, 2007, Bischoffsheim, France, October 24 - 26.

[2] B. Samson, L. Aigouy, G. Tessier, **P. Löw**, B. J. Kim, C. Bergaud & M. Mortier, "Thermal imaging of nickel wires with a fluorescent nanoprobe", *Phonons*, Paris, France, July 15-20, 2007.

[3] **P. Löw**, B. J. Kim & C. Bergaud, "Using dried Rhodamine B fluorescence for temperature characterization of sub-micron scale devices", *14th International*

Conference on Solid State Sensors, Actuators and Microsystems, Transducers'07, Lyon, France, June 10-14, 2007.

[4] **P. Löw**, N. Takama, B. J. Kim & C. Bergaud, "Measurement of the Temperature Distribution on Resistively Heated Nanowires using CdSe/ZnS Nanocrystals", *MRS Fall Meeting*, Boston, Massachusetts, USA, November 27 – December 1, 2006.

[5] **P. Löw**, B. LePioufle, B. J. Kim & C. Bergaud, "Electric field assembly of quantum dots on nanowires for temperature sensing", *IMCS 11*, Brescia, Italy, July 16-19, 2006.

TITLE :

High spatial resolution fluorescent thermometry:

Thermal characterization of submicrometer

structures in dry and liquid conditions

ABSTRACT

This thesis presents the development of an improved fluorescent thermometry approach for the thermal characterization of Joule-heated submicrometer wires in dry and liquid conditions. The design parameters of the wire systems are studied by the use of finite element modeling (FEM) in order to optimize their thermal behavior. A high spatial confinement of the temperature changes is experimentally demonstrated when using a nickel submicrometer wire on a silicon substrate as a heat source. The thermal time constants of the wire systems are shown to lie below one millisecond. The results of this thesis are of great interest in the development of new tools for the sensing, recognition and fundamental studies of molecules, (for instance the folding of proteins and DNA) based on fast temperature modulation.

KEYWORDS

Fluorescence, thermometry, submicrometer analysis, nanowires, FEM analysis, temperature modulation, lab-on-a-chip.

AUTEUR : Peter LÖW

TITRE : Thermométrie submicrométrique par fluorescence: Caractérisation de micro et nanostructures en milieux sec et liquide

DIRECTEUR DE THESE : Christian BERGAUD

LIEU ET DATE DE SOUTENANCE : Toulouse, le 22 février 2008

RESUME

Ce travail concerne le développement et l'optimisation de la thermométrie par fluorescence en milieu sec et liquide pour caractériser thermiquement des fils de dimensions submicrométriques dont l'échauffement est obtenu par effet Joule. En utilisant des simulations en éléments finis, les paramètres des fils sont étudiés afin d'optimiser leur comportement thermique. Un fort confinement spatial de la température autour des fils en nickel sur un substrat de silicium est observé grâce à des mesures en fluorescence. Concernant le temps de réponse, des constantes de temps thermiques en dessous de la milliseconde sont obtenues expérimentalement. Les résultats présentés dans cette thèse sont d'un grand intérêt pour le développement de nouveaux outils pour la détection, la reconnaissance et l'étude fondamentale des molécules (dépliement et repliement de protéines et d'ADN par exemple) sous modulation thermique rapide.

MOTS-CLES

Fluorescence, thermométrie, analyse submicrométrique, nanofils, simulation en éléments finis, modulation thermique, laboratoire-sur-puce.

DISCIPLINE

Sciences de la Matière

Laboratoire d'Analyse et d'Architecture des Systèmes du CNRS

7 avenue du Colonel Roche - 31077 Toulouse Cedex 4